



**HAL**  
open science

# Air-sea interactions in Southeast Asia: evaluating the impact of ENSO/ENSO Modoki on rainfall variability and characterizing historical and future surface air-sea heat exchanges

Hue Thi Thanh Nguyen

► **To cite this version:**

Hue Thi Thanh Nguyen. Air-sea interactions in Southeast Asia: evaluating the impact of ENSO/ENSO Modoki on rainfall variability and characterizing historical and future surface air-sea heat exchanges. Ocean, Atmosphere. Université Paul Sabatier - Toulouse III, 2023. English. NNT : 2023TOU30379 . tel-04637038

**HAL Id: tel-04637038**

**<https://theses.hal.science/tel-04637038>**

Submitted on 5 Jul 2024

**HAL** is a multi-disciplinary open access archive for the deposit and dissemination of scientific research documents, whether they are published or not. The documents may come from teaching and research institutions in France or abroad, or from public or private research centers.

L'archive ouverte pluridisciplinaire **HAL**, est destinée au dépôt et à la diffusion de documents scientifiques de niveau recherche, publiés ou non, émanant des établissements d'enseignement et de recherche français ou étrangers, des laboratoires publics ou privés.

Université Fédérale



Toulouse Midi-Pyrénées

# THÈSE

**En vue de l'obtention du  
DOCTORAT DE L'UNIVERSITÉ DE TOULOUSE  
Délivré par l'Université Toulouse 3 - Paul Sabatier**

---

**Présentée et soutenue par  
Hue Thi Thanh NGUYEN**

Le 18 décembre 2023

**Interactions air-mer en Asie du Sud-Est: Évaluation de l'impact  
d'ENSO canonique et/ENSO Modoki sur la variabilité des  
précipitations et caractérisation des échanges thermiques air-  
mer sur les périodes historiques et futures**

---

Ecole doctorale : **SDUZE - Sciences de l'Univers, de l'Environnement et de  
l'Espace**

Spécialité : **Océan, Atmosphère, Climat**

Unité de recherche :

**LEGOS - Laboratoire d'Etudes en Géophysique et Océanographie Spatiale**

Thèse dirigée par  
**Marine HERRMANN et Thanh NGO DUC**

Jury

**M. Jérôme VIALARD**, Rapporteur

**Mme Faye Abigail T. CRUZ**, Rapporteur

**M. Yves MOREL**, Examineur

**M. Tan PHAN VAN**, Examineur

**Mme Marine HERRMANN**, Directrice de thèse

**M. Thanh NGO-DUC**, Co-directeur de thèse



# Acknowledgements

I am deeply grateful to my supervisors, Marine Herrmann, and Thanh Ngo-Duc, for their unwavering guidance, patience, and expertise. Marine, an exceptionally conscientious supervisor, taught me lessons about always taking care of the tiniest details and making everything self-contained and easy to understand. Her constructive criticisms and candid feedback during the research process played a pivotal role in enhancing the quality of the papers and this thesis. Thanh, my second supervisor, has been a cornerstone in shaping both the direction and the quality of this work. Their insightful feedback and encouragement were indispensable in every stage of this research.

I extend my heartfelt thanks to the members of my thesis defense committee, who generously devoted their time to read and provide invaluable comments on this document. My gratitude also extends to the French Embassy for their financial support, which enabled me to conduct this research at LEGOS.

My profound appreciation goes to Tung and Nadia, who offered their support from the moment I arrived in Toulouse. I am grateful to my dear friends Margot, Juliette, Elisa, Adrien, and Quentin, my first friends in Toulouse, who stood by me with support and encouragement.

I wish to thank my family for their support in my life and for always encouraging me to pursue the way of studying and doing research. Without them, I would not have had such a day as today. I would also like to thank Hanh, Trung, and Minh Tri for helping me have the most wonderful experience in Toulouse.

Last but not least, my deepest thanks go to my husband -Trung, who has been a constant source of strength and support in every circumstance. Without him, I would never have been able to start and finish this work. I'm also grateful to my sons Kien and Nguyen who gave me motivation in everything and who reminded me of balancing between work and life.

# Contents

Contents .....	i
List of Figures .....	vi
List of Tables .....	xi
List of acronyms .....	xiii
Résumé.....	1
Abstract.....	3
Introduction générale .....	5
General introduction .....	9
Chapter 1. Introduction .....	13
1.1 Air-sea interactions .....	15
1.1.1 General schematic of air in -sea interactions.....	15
1.1.2 Coupled atmospheric-oceanic phenomena. ....	18
<i>1.1.2.1 El Niño-Southern Oscillation (ENSO)</i> .....	18
<i>1.1.2.2 ENSO Modoki</i> .....	20
1.1.3 Air-sea heat flux .....	21
1.2 Southeast Asia regional climate system.....	24
1.2.1 Southeast Asia physical Geography .....	24
1.2.2 Southeast Asia monsoon system.....	26
<i>1.2.2.1 Summer monsoon</i> .....	27
<i>1.2.2.2 Winter monsoon</i> .....	27

1.2.3 Southeast Asia climatic characteristics.....	29
1.2.3.1 <i>Surface temperature</i> .....	29
1.2.3.2 <i>Rainfall</i> .....	30
1.2.3.3. <i>Tropical cyclones</i> .....	31
1.3 Ocean circulation around and in SEA.....	33
1.3.1 Western boundary currents (WBC): Kuroshio and Mindanao currents .....	33
1.3.2 South China Sea Throughflow (SCSTF) .....	35
1.3.3 Indonesian Throughflow (ITF).....	36
1.3.4 Effect of ENSO on ocean circulation in the SEA region .....	37
1.4 Thesis Objectives and Structure.....	38
1.4.1 Effect of ENSO and ENSO Modoki on SEA Climate.....	38
1.4.2 Air-sea heat exchanges in SEA .....	39
1.4.3 Thesis main scientific questions .....	40
1.4.4 Thesis structure.....	40
Chapter 2. Impacts of ENSO and ENSO Modoki on rainfall variability.....	43
Article summary.....	44
2.1 Introduction.....	46
2.2 Study domain, data, and method.....	48
2.2.1 Study domain.....	48
2.2.2 Data.....	49
2.2.3 Method.....	49
2.3 The two types of ENSO and associated rainfall .....	52

2.3.1 EOF analysis.....	52
2.3.2 Rainfall variations in ENSO and ENSO Modoki events .....	54
2.3.2.1 Relationship between SST and rainfall over SEA .....	54
2.3.2.2 Rainfall anomaly patterns .....	56
2.3.2.3 Rainfall anomaly averaged over the 20 SEA sub-regions.....	58
2.4 Possible mechanisms responsible for the rainfall variations .....	61
2.4.1 Vertically Integrated Moisture Flux .....	61
2.4.2 Associated circulation cells .....	63
2.5 Chapter’s conclusions .....	68
Chapter 3. Quantifying air-sea heat fluxes over Southeast Asia: intercomparison of available datasets and sensitivity ocean simulations .....	72
3.1. Introduction.....	74
3.2 Data and Method.....	76
3.2.1 The ocean model SYMPHONIE .....	76
3.2.2 Computation of heat fluxes in SYMPHONIE .....	78
3.2.2.1 Method 1: bulk method.....	79
3.2.2.2 Method 2: flux method.....	80
3.2.3 Experimental design .....	80
3.2.4 Heat flux datasets and data for model evaluation.....	82
3.2.5 Statistical methods.....	85
3.3. Characteristics of heat fluxes in distributed dataset.....	85
3.3.1 Spatial variability.....	86
3.3.2 Seasonal cycle.....	88

3.4 Results of sensitivity simulations.....	90
3.4.1 SST spatial distribution .....	90
3.4.2 Surface temperature temporal evolution.....	92
3.4.3 Relationship between temperature differences and heat flux .....	94
3.5 Extending our conclusions over longer periods.....	97
3.5.1 Comparison between heat flux computed from SYMPHONIE and ECMWF products over 2009-2018 .....	97
3.5.2 Extension to other heat flux datasets .....	98
3.6. Chapter’s conclusion.....	100
Chapter 4. CMIP6 analysis: heat fluxes estimation and the role of the climate change..	103
4.1 Introduction.....	104
4.2. Data and method .....	107
4.2.1 CMIP6 GCMs.....	107
4.2.2 Observations and Reanalysis datasets .....	107
4.2.3 Methods .....	107
4.3. Seasonal and spatial variability of heat fluxes .....	110
4.3.1 Spatial distribution.....	110
4.3.2 Seasonal cycle.....	114
4.4 Future projections .....	118
4.4.1 Future projections in the multi-model ensemble mean .....	118
4.4.2 Future projections in low and high warming groups .....	121
4.5 Models’ sensitivity to the magnitude of SST change .....	123
4.6. Conclusions of chapter.....	127

Chapter 5. Conclusions and perspectives.....	130
5.1 Conclusions.....	131
5.1.1 Impact of ENSO/ENSO Modoki on rainfall variability .....	132
5.1.2 Estimation, variability, and evolution of air-sea heat fluxes .....	133
5.1.2.1 <i>Estimating air-sea heat fluxes over the SEA region.</i> .....	133
5.1.2.2 <i>Representation and climate projection of SEA air-sea heat fluxes in CMIP6 models.</i> .....	134
5.2 Perspectives.....	135
CONCLUSION GÉNÉRALE.....	140
I. Conclusions .....	140
I.1 Impact d'ENSO/ENSO Modoki sur la variabilité des précipitations .....	141
I.2 Estimation, variabilité et évolution des flux de chaleur air-mer .....	142
I.2.1 <i>Estimation des flux de chaleur air-mer sur la région SEA</i> .....	142
I.2.2 <i>Représentation et projection climatique des flux de chaleur air-mer de l'ESE dans les modèles CMIP6</i> .....	143
II. Perspectives.....	145
Reference .....	147
Appendix A.....	183
Supplemental Tables.....	183
Supplemental Figures .....	187

# List of Figures

<b>Figure 0.1</b> The Southeast Asia domain. Topography over SEA (shaded) is obtained from the General Bathymetric Chart of the Oceans (GEBCO), available from <a href="https://www.gebco.net">https://www.gebco.net</a> . .....	10
<b>Figure 1.1.</b> Air-sea interaction’s schematic. Source: <a href="https://www.ecmwf.int/">https://www.ecmwf.int/</a> .....	15
<b>Figure 1.2</b> Map of major ocean currents and gyres (De Blij et al, 2004) .....	17
<b>Figure 1.3</b> Anomalous conditions in the tropical Pacific:(a) El Niño event, (b) El Niño Modoki (c, d) The opposite (La Niña) phases of the El Niño and El Niño Modoki respectively (Ashok and Yamagata 2009). .....	19
<b>Figure 1.4</b> SEA population density map (black box) in 2019. Source: <a href="https://ourworldindata.org/grapher/population-density?time=2019&amp;region=Asia">https://ourworldindata.org/grapher/population-density?time=2019&amp;region=Asia</a> .....	25
<b>Figure 1.5</b> Climatological mean fields of precipitation and low-level winds at 850 hPa during (a) July–August and (b) January–February based on merged CMAP-GPCP data (Wang et al. 2014). Orange: actual monsoon precipitation domain. Blue: approximate regional monsoon boxes. Red: domains where the Asian summer monsoon and Australian summer monsoon low-level circulation (U850(1), U850(2)) indices are defined.....	28
<b>Figure 1.6</b> (a) Annual mean and (b) seasonal cycle of temperature over SEA for the APHRODITE dataset (1979-2015).....	30
<b>Figure 1.7</b> Climatological seasonal mean precipitation (mm.day) for the APHRODITE dataset (period 1970-2005) in (a) annual, (b) DJF, and (c) JJA (Ngai et al. 2022). .....	30
<b>Figure 1.8</b> Western North Pacific (WNP) tropical cyclone track density map at 0.25-degree resolution from the Joint Typhoon Warning Center (Tran et al. 2022). The yellow and red rectangles indicate the WNP and SEA domains, respectively.....	32
<b>Figure 1.9</b> Topographic and boundary current systems in the Northwest Pacific. Depths shallower than 2,000 m are color shaded. Grey shading indicates depths shallower than 50 m. The main currents, integrated from 1,000 m to the surface, are indicated by light blue arrows; red straight arrows indicate the main surface-trapped counter currents; purple arrows indicate undercurrents. Abbreviations used include KC for Kuroshio Current, NEC for North Equatorial Current, MC for Mindanao Current, NECC for North Equatorial Counter Current, LUC for	

Luzon Undercurrent, MUC for Mindanao Undercurrent, NGCC for New Guinea Coastal Current, NEUC for North Equatorial Undercurrent, SEC for South Equatorial Current (Hu et al. 2015). .....34

**Figure 1.10** Schematic diagram showing circulations and major straits of the SEA seas (Tozuka et al. 2009) .....36

**Figure 2.1.** The Southeast Asia domain and its 20 sub-regions were used for the assessment (delineated by black boxes). Topography over SEA (shaded) is obtained from the Global 30 Arc-Second Elevation (GTOPO30) data set. ....48

**Figure 2.2.** EOF patterns of the HadISST anomalies (1979–2019) for (a) the 1st mode, corresponding to a typical EN, (b) the 2nd mode, corresponding to a typical EM; and time series of (c) the PC1 and Niño3, Niño3.4, and Niño4 indices, and (d) the PC2 and EMI. Locations of the Niño3 (5°S–5°N, 150°W–90°W), Niño3.4 (5°S–5°N, 170°W–120°W), and Niño4 (5°S–5°N, 160°E–150°W) regions are indicated in (a). Boxes A (10°S–10°N, 165°E–140°W), B (15°S–5°N, 110°–70°W), and C (10°S–20°N, 125°–145°E) in (b) are used for computing the EMI. The numbers in parentheses in (c) and (d) indicate the correlations between the corresponding indices with the PC1 and PC2 series, respectively. ....53

**Figure 2.3.** Spatial distribution of correlations between monthly rainfall anomalies and (a) the Niño-3 index and (b) the EMI. The dot pattern indicates areas where the correlations are statistically significant at 90% based on the student’s t-test.....56

**Figure 2.4.** Composites of JJA and DJF rainfall anomalies (units: mm/day) for (a, b) EN, (c, d) EM, and (e, f) the differences between EN and EM. The dot pattern indicates areas where differences are statistically significant at 90% based on the bootstrap test. ....57

**Figure 2.5.** As in Fig. 2.4 but for LN and LM. ....59

**Figure 2.6.** Box plots of average JJA and DJF rainfall anomaly over 20 sub-regions for (a, b) EN (red) and EM (blue), (c, d) LN (yellow) and LM (green). Units in mm/day. The subregions where the differences between EN and EM (and between LN and LM) mean values are within 0.5–1mm/day and above 1mm/day are highlighted in black dashed line and solid line boxes, respectively. ....60

**Figure 2.7.** VIMF (vector, unit:  $\text{kg m}^{-2}\text{s}^{-1}$ ) and its divergence (shading, unit  $10^{-5} \text{ kg m}^{-2}\text{s}^{-1}$ ) for JJA and DJF of the neutral years (a, b), anomalies of the composites of EN (c, d) and EM (e, f) and differences between EM and EN (g, h) during JJA and DJF. The dot patterns in (c–h)

indicate areas where differences are statistically significant at 90% based on the bootstrap test. .....	62
<b>Figure 2.8.</b> As in Fig. 2.7(c–h) but for LN and LM. ....	64
<b>Figure 2.9.</b> Mean of 200 hPa velocity potential (shading; units: $10^6 \text{ m}^2\text{s}^{-1}$ ) and divergent wind (arrow, unit: $\text{ms}^{-1}$ ) for the neutral years during (a, b) JJA and DJF. Anomalous velocity potential and divergent wind at the 200 hPa for (c, d) EN and (e, f) EM events and (g, h) the differences between EN and EM anomalies during JJA and DJF. Shading in (c–h) indicates areas where differences are statistically significant at 90% based on the bootstrap test. ....	65
<b>Figure 2.10.</b> As in Figure 2.9(c–h) but for LN and LM. ....	66
<b>Figure 2.11.</b> Mean of pressure vertical velocity for the neutral years during (a) JJA and (b) DJF, and composites of pressure vertical velocity anomalies for (c, d) EN, (e, f) EM, (g, h) LN, and (i, j) LM during JJA (left) and DJF (right). The average between 13°S and 29.5°N is computed. Units in $\text{Pas}^{-1}$ . The hatch patterns in (c–j) indicate areas where differences are statistically significant at 90% based on the bootstrap test. ....	67
<b>Figure 3.1</b> The Arakawa staggered C-grid. The indices $i, j, k$ refer to grid points in $x, y$ and $z$ direction, respectively. Scalar quantities $\phi$ are defined at the center of the grid volume, whereas velocities are defined at the edges of the grid volumes (Piton 2019). ....	77
<b>Figure 3.2</b> Bathymetry and domain of the SEA configuration .....	81
<b>Figure 3.3</b> Annual mean of net heat flux and its four components from ECMWF, MERRA-2, CFSv2, JRA-55, CTL, and ERA5 for the period 2017-2018. Unit: $\text{W}\cdot\text{m}^{-2}$ .....	87
<b>Figure 3.4</b> Seasonal variability of (a) QNET, (b) SW, (c) LW, (d) LH, and (e) SH over the SEA. The positive means downward flux, while the negative represents the upward. ....	89
<b>Figure 3.5</b> Annual mean of SST obtained from six SYMPHONIE simulations compared with the observation data from OSTIA for 2018. Annual mean errors (bias) and daily Pearson correlation coefficients obtained from six simulations compared to OSTIA SST. ....	91
<b>Figure 3.6</b> Daily time series of (a) the SST bias of six SYMPHONIE simulations and (b) the change of the temperature of the 0 - 100m layer ( $T_{0-100\text{m}}$ ) compared to the initial condition (i.e., temperature of the first day of simulation). ....	93
<b>Figure 3.7</b> Scatterplot of SST bias and $T_{0-100}$ change over 2018 versus $Q_{\text{net}}$ averaged over SEA and 2017-2018 for the five SYMPHONIE flux simulations, and corresponding linear regression analysis (black dotted line). The Pearson correlation coefficient between the	

temperature and heat flux is denoted as  $r$  with  $p$ -value  $<0.01$ , except  $r$  between SST bias and LW with  $p$ -value  $<0.1$ . .....96

**Figure 3.8** Yearly time series of SST bias in SYMPHONIE simulations and heat fluxes computed from SYMPHONIE “bulk” simulations, ECMWF analysis and ERA5 reanalysis.98

**Figure 4.1.** Projected SST changes over SEA for individual models under SSP1.2-6 (orange color), SSP2.4-5 (gray color) and SSP5.8-5 (green color) for the period 2015–2099 relative to the baseline 1995–2014. .... 110

**Figure 4.2.** Annual mean of (a, b) Qnet, (d, e) SW, (g, h) LW, (j, k) LH and (m, n) SH from CMIP6 MME (left) and ERA5 (middle) (Unit:  $W.m^{-2}$ ). The value in the black box indicates the spatial correlation coefficient between ERA5 and CMIP6 MME ( $p$ -value  $<0.01$ ). Bias between CMIP6 MME and ERA5 (c, f, i, h, p) (right, unit:  $W.m^{-2}$ ). The dot and hatch pattern indicates areas where differences are statistically significant at 95% based on the student’s  $t$ -test. .... 112

**Figure 4.3.** Zonal mean values of Qnet, SW, LW, LH and SH computed from the annual and four seasons (December-February, DJF; March-May, MMA; June-August, JJA; September-November, SON) means of CMIP6 MME (red line) and ERA5 (black line) for the period 1995–2014 (Unit:  $W.m^{-2}$ ). The gray lines indicate the zonal mean profile of 30 individual models from CMIP6, and dashed black lines show the range of interannual variability in ERA5 based on  $\pm 1$  standard deviation. .... 113

**Figure 4.5.** Projected annual Qnet changes from CMIP6 MME under SSP1-2.6 (left), SSP 2-4.5 (middle) and SSP5-8.5 (right) for the mid-century (upper panel) and the end-century (lower panel) relative to the baseline period. Shading indicates areas where changes are statistically significant at a 95% confidence level based on the student’s  $t$ -test. The value in the black box shows the average projected change in heat flux over the entire area. .... 119

**Figure 4.6.** As in Figure 4.5, but for SW, LW, LH, and SH. .... 120

**Figure 4.7.** Time series of projected changes in yearly heat fluxes spatially averaged over the study domain relative to the baseline period 1995-2014 under SSP1-2.6 (blue), SSP2-4.5 (green), and SSP5-8.5 scenario (red) for the low warming group (**L**, dotted line), high warming group (**H**, dashed line) and the ensemble mean of the 30 CMIP6 models (**MME**, solid line). The black solid and color lines depict historical and future heat flux anomalies, respectively. These lines were obtained using the locally estimated scatterplot smoothing technique

(LOESS) (Cleveland et al. 1988). The gray lines indicate the ensemble mean values for each group prior to the use of the LOESS technique. .... 122

**Figure 4.8.** Projected changes in  $Q_{net}$  and its four components and of  $Q_a$ ,  $W$ ,  $\Delta q = q_a - q_s$ , and  $\Delta T = T_a - T_s$  versus changes in SST by the end of the century compared to the baseline period. Filled upward-pointing triangles represent the high warming (H) group, and non-filled downward-pointing triangles represent the low warming (L) group. Blue, green, and red colors correspond to the scenarios SSP1-2.6, SSP2-4.5, and SSP5-8.5, respectively. Solid and dash-dotted lines represent trend lines for the H group and the L group, respectively. The Pearson correlation coefficient between changes for the L group and  $\Delta SST$  is denoted as  $r_L$ , while the correlation coefficient between changes for the H group and  $\Delta SST$  is denoted as  $r_H$ , where bold values with p-value  $<0.01$ , bold and italic values with p-value  $<0.05$ , and italic values p-value  $>0.1$ . Values of  $m_L$  and  $m_H$  are slopes for components that show a statistically significant linear relationship (p-value  $<0.01$ ), for group L and H, respectively. .... 126

**Figure 5.1.** Scatter plots showing the relationships of (a)  $Q_{net}$ , (b) SW, (c) LW, (d) LH, (e) SH, and (f) W vs. SST for the period 1995–2014. Each dot on the plot represents a distinct grid point in the study domain. The curves fitted through the set of data points were obtained using the LOESS technique. The vertical dashed line corresponds to SST at 28 °C. .... 137

**Figure 5.2.** Same as Figure 5.1 for the L (dashed curve) and H (solid curve) groups under SSP1-2.6 (blue color), SSP2-4.5 (green color), and SSP5-8.5 (red color) scenarios for the period 2081–2099. .... 139

**Figure 2.A1.** Differences between climatology and neutral values for (a) JJA and (b) DJF. Units in mm/day. The dot pattern indicates areas where differences are statistically significant at 90% based on the Student’s t-test. .... 187

**Figure 2.A2** Composites of SON and MAM rainfall anomalies (units: mm/day) for (a, b) EN, (c, d) EM, and (e, f) the differences between EN and EM. The dot pattern indicates areas where differences are statistically significant at 90% based on the bootstrap test. .... 188

# List of Tables

**Table 2.1.** List of EN, LN, EM, LM, and neutral years over the period of 1979–2019. The number in parentheses indicates the total number of years for each type of event. ....55

**Table 3.1** Values of net heat flux and its four components averaged over the SEA region (2017-2018) for ERA5 and 6 SYMPHONIE simulations. Blue texts indicate the heat flux forcing (HFF) dataset used to drive the model. \* Indicates that the value is equal to the mean heat fluxes value of ECMWF.  $\alpha$  values are calculated based on individual heat flux products compared to ECMWF. The values of SEA-averaged SST bias values and 0-100 m layer temperature changes (compared with 1st day of simulation) for the periods 2017-2018, 2018 and for the last day of simulation (30/12/2018) for the 6 simulations are also indicated.....83

**Table 3.2** Average over SEA of Qnet, SW, LW, LH, SH estimated from different datasets for the period 2009-2018, except CMIP6 multi model ensemble (CMIP6 MME) (2009-2014). This data set is presented in detail in chapter 4, section 4.2.1. Differences compared to SYM(0918) are indicated in italics. Positive (negative) differences are highlighted in blue (red). Unit: W.m- .....99

**Table 4.1.** List of CMIP6 GCMs used in this study. The superscript next to each model’s name indicates the model group, i.e., L or H (defined in sub-section 4.2.3), to which the model belongs in each specific scenario: <sup>1</sup>L1-2.6, <sup>2</sup>L2-4.5, <sup>3</sup>L5-8.5, <sup>4</sup>H1-2.6, <sup>5</sup>H2-4.5, <sup>6</sup>H5-8.5..... 108

**Table 4.2.** Annual and seasonal means of Qnet, SW, LW, LH, and SH averaged over SEA along with their respective interannual standard deviations of the CMIP6 MME yearly values for the period 1995–2014 (mean  $\pm$  deviation), and biases compared with ERA5. Units are in W.m<sup>-2</sup>..... 116

**Table 2.A1.** List of ENSO and ENSO Modoki months over the period of 1979–2019. Results are obtained with the Niño3 index. Slightly different results obtained with the Niño3.4 index are indicated in the parentheses. The last row shows the total number of months for each event. .... 183

**Table 4.A1.** Annual mean value of SST, Qnet and its four components for individual models in CMIP6 during baseline 1995-2014 over the SEA region. .... 184

<b>Table 4.A2.</b> Annual mean value of SST, Qnet and its four components for individual models in CMIP6 under SSP1-2.6 during 2015-2099. $\Delta$ SST is the difference in SST during the period 2015-2099 compared to the baseline period 1995-2014.....	185
<b>Table 4.A3</b> As the same Table 4.A2 but for SSP2-4.5.....	185
<b>Table 4.A4</b> As the same Table 4.A2 but for SSP5-8.5.....	186

# List of acronyms

APHRODITE	Asian Precipitation-Highly Resolved Observational Data Integration Towards Evaluation of the Water Resources
CFSv2	Climate Forecast System version 2
CMIP	Coupled Model Intercomparison Projects
CRU	Climate Research Unit
CTL	Control
ECMWF	European Center for Medium-Range Weather Forecasts
EM	El Niño Modoki
EN	El Niño
ENSO	El Niño – Southern oscillation
EOF	Empirical orthogonal function
ERA5	European Centre for Medium-Range Weather Forecasts reanalysis
EXP	Experiment
GCM	Global Climate Models
GPCC	Global Precipitation Climatology Centre
ITCZ	Intertropical Convergence Zone
ITF	Indonesian throughflow
LH	Latent heat flux
LM	La Niña Modoki
LN	La Niña

LW	Longwave radiation
ME	mean error
MERRA-2	Modern-Era Retrospective Analysis for Research and Applications version 2
NCAR	National Center for Atmospheric Research
NCEP	National Centers for Environmental Prediction
OSTIA	Operational Sea Surface Temperature and Sea Ice Analysis
PC	Principal component
Qnet	Net heat flux
RMSE	Root Mean Square Error
SCS	South China Sea
SCSTF	South China Sea throughflow
SEA	Southeast Asia
SH	Sensible heat flux
SST	Sea surface temperature
SW	Shortwave radiation
TC	Tropical cyclone
VIMF	Vertically integrated moisture flux
WBC	Western boundary currents
WNP	Western North Pacific

# Résumé

L'Asie du Sud-Est (SEA pour *Southeast Asia*) regroupe 10% de la population mondiale et est soumise à un large éventail de facteurs et aléas climatiques: typhons, mousson, Oscillation Australe El Niño (ENSO), changement climatique... A l'interface entre l'Océan Indien, l'Océan Pacifique et l'atmosphère, cette région, qui comprend le continent maritime, est de plus un élément clé du fonctionnement de la circulation océanique et atmosphérique globale. L'objectif général de cette thèse est de mieux comprendre le fonctionnement et l'impact des interactions air-mer dans le climat d'Asie du Sud-Est. Ceci est d'une importance primordiale pour une connaissance approfondie et une meilleure capacité de prédiction de la variabilité climatique à toutes les échelles dans la région, depuis les événements extrêmes et la variabilité interannuelle jusqu'aux projections futures, mais aussi pour mieux comprendre, modéliser et prévoir le climat global. Nous nous sommes concentrés sur deux processus qui jouent un rôle important dans le climat d'Asie du Sud-Est: ENSO et les échanges de chaleur à l'interface air-mer.

Tout d'abord, l'impact d'ENSO et de sa variante, ENSO Modoki, sur la variabilité des précipitations dans la région SEA a été étudié pour la période 1979-2019. La diminution (augmentation) observée des précipitations sur la SEA pendant les événements Modoki par rapport aux événements ENSO canoniques a été expliquée par une réduction (augmentation) du transport d'humidité dans la région et un affaiblissement (renforcement) de la branche ascendante de la circulation de Walker.

Deuxièmement, nous avons analysé les jeux de données observationnelles et numériques disponibles et effectué des simulations de sensibilité afin d'explorer la gamme d'estimations des flux de chaleur air-mer dans la région SEA. Cela a révélé une énorme incertitude dans ces estimations, avec des valeurs de flux de chaleur net allant de  $-30$  à  $+40$   $\text{W.m}^{-2}$ . Le modèle numérique SYMPHONIE a été utilisé avec deux méthodes de forçage des flux de chaleur de surface (formules bulk vs. flux prescrits à partir de jeux de données atmosphériques) pour étudier la sensibilité de la température de surface de la mer simulée à ces flux. Les résultats ont fourni une estimation de  $+12.5$   $\text{W.m}^{-2}$  du gain net de chaleur pour l'océan sur la période 2009-2018, et ont suggéré qu'ERA5, la cinquième génération de réanalyse de l'ECMWF ("European Centre for Medium-Range Weather Forecasts"), peut être utilisée comme référence bien qu'elle surestime légèrement le flux net de chaleur.

Enfin, les flux air-mer produits par 30 modèles issus des simulations de la phase 6 du “Coupled Model Intercomparison Project” (CMIP6) ont été évalués par rapport à ERA5. Sur la période historique, la moyenne d'ensemble CMIP6 reproduit bien la variabilité spatiale des flux de chaleur, mais sous-estime de deux tiers le gain net de chaleur océanique par rapport à ERA5. Les principaux facteurs contribuant à ce biais sont le rayonnement en ondes courtes (SW) et le flux de chaleur latente (LH). Le gain de chaleur net devrait augmenter au cours du XXIème siècle, en raison d'une augmentation du gain de SW et de la perte de LH et d'une diminution des pertes du rayonnement de grande longueur d'onde (LW) et de chaleur sensible (SH). Les modèles et scénarios qui prévoient un réchauffement plus intense de la surface de la mer présentent des changements plus importants dans les flux de chaleur, qui devraient changer le plus dans le cadre du scénario SSP5-8.5 (+3,7, +1,0, -8,4, +9,2, et +1,9 W.m<sup>-2</sup>, respectivement pour Qnet, SW, LH, LW, et SH). Les résultats montrent une relation linéaire entre le réchauffement de surface de l'océan et le changement de Qnet, LW, LH et SH. L'effet thermodynamique lié aux changements d'humidité et de température pilote les changements de LH et SH, tandis que le terme dynamique lié au changement de l'intensité du vent est négligeable.

# Abstract

Southeast Asia (SEA) gathers 10% of the world population and is subject to a wide range of climate factors and hazards: typhoons, monsoon, El Niño Southern Oscillation (ENSO), climate change, etc. At the interface between the Indian Ocean, the Pacific Ocean and the atmosphere, the SEA region, which includes the maritime continent, is moreover key to the functioning of global oceanic and atmospheric circulation. The general objective of this thesis is to better understand the functioning and impact of air-sea interactions in the SEA climate. This is of primary importance for an in-depth knowledge and a better prediction capacity of climate variability at all scales in the region, from extreme events and interannual variability to future projections, but also to better understand, model and forecast global climate. We focused on two processes that play an important role in SEA climate: El Niño Southern Oscillation (ENSO) and air-sea heat exchanges.

First, the impact on SEA rainfall variability of ENSO and its variant, ENSO Modoki, were investigated for the period 1979-2019. The observed decrease (increase) in rainfall over SEA during Modoki events compared to the canonical ENSO events was explained by a reduced (enhanced) moisture transport into the region and a weakening (strengthening) of the ascending branch of the Walker circulation.

Second, we analyzed available observational and numerical datasets and conducted sensitivity simulations to explore the range of estimates of air-sea heat fluxes in the SEA region. This revealed huge uncertainty in those estimates, with values of net heat flux varying from  $-30$  to  $+40$   $\text{W}\cdot\text{m}^{-2}$ . The SYMPHONIE numerical model was used with two methods of surface heat flux forcing (bulk formulae versus prescribed fluxes from atmospheric datasets) to investigate the sensitivity of the simulated sea surface temperature to those fluxes. Results provided a  $+12.5$   $\text{W}\cdot\text{m}^{-2}$  estimate of net heat gain for the ocean over 2009-2018, and suggested that ERA5, the fifth generation of the European Centre for Medium-Range Weather Forecasts reanalysis, can be used as a reference though a slight overestimation of net heat flux.

Third, air-sea fluxes produced by 30 models from the Coupled Model Intercomparison Project Phase 6 (CMIP6) simulations were evaluated against ERA5. Over the historical period, the CMIP6 ensemble average reproduces well the spatial variability of heat fluxes but underestimates the net heat gain for the ocean by two-third compared to ERA5. The primary

contributors to the net bias are shortwave radiation (SW) and latent heat flux (LH). The net heat gain is projected to increase during the XXIst century, resulting from an increase of SW gain and LH loss and a decrease of longwave radiation (LW) and sensible heat (SH) losses. Models with higher projected sea surface warming exhibit larger changes in heat fluxes, which are predicted to change the most under the SSP5-8.5 scenario (+3.7, +1.0, -8.4, +9.2, and +1.9  $\text{W.m}^{-2}$ , respectively for Qnet, SW, LH, LW, and SH). Results show a linear relationship between the change of SST and the change of Qnet, LW, LH and SH. The thermodynamic effect related to changes of humidity and temperature with a warming sea surface drive the changes of LH and SH, while the dynamic term related to change of wind intensity is negligible.

# Introduction générale

L'océan et l'atmosphère échangent chaleur, eau douce et quantité de mouvement à la surface de la mer. Une meilleure compréhension de ces échanges est essentielle pour mieux comprendre comment atmosphère et océan interagissent (Cayan 1992a). Ces échanges impliquent un large éventail de processus à différentes échelles spatiales et temporelles, depuis les cyclones tropicaux (Ma et al. 2015, Li et al. 2022) ou la formation d'eau dense (Millot et Taupier-Letage 2005, Gutjahr et al. 2022) jusqu'aux moussons saisonnières et aux oscillations interannuelles à multidécennales à grande échelle telles que l'oscillation australe El Niño (ENSO) (Wang et al. 2011, Yan et al. 2020, Huang et Xie 2015).

L'un des principaux mécanismes par lesquels l'océan libère la chaleur absorbée par rayonnement solaire est le flux turbulent de chaleur, sous la forme de flux de chaleur latente (LH) et sensible (SH). Yu et Weller (2007) ont montré que les flux de chaleur induisent des changements dans la température de surface de la mer (SST), le vent et l'humidité spécifique de l'air. En outre, l'apport d'énergie fourni par les flux de chaleur latente et sensible de l'océan vers l'atmosphère modifie le mélange vertical et a le potentiel de moduler l'atmosphère (Xie et al. 2004) et la couche limite atmosphérique marine (Tokinaga et al. 2005). À leur tour, ces échanges de chaleur à la surface de l'océan influencent fortement la température des couches supérieures océaniques ainsi que leur dynamique (Carton et Zhou 1997, Duvel et al. 2004). Par conséquent, il est essentiel de mieux comprendre la variabilité temporelle et spatiale des flux de chaleur air-mer et de mieux représenter ces interactions air-mer dans les modèles océaniques, atmosphériques et climatiques pour étudier et comprendre les variations climatiques sur un large éventail d'échelles de temps et d'espace. Cependant, la fiabilité des estimations des flux de chaleur a été mise en question, en raison de la dispersion des biais importants dans les valeurs provenant des différents produits disponibles (Brunke et al. 2003, Zhang et al. 2004, Yu et al. 2004). Les estimations des modèles climatiques comportent des erreurs liées à un certain nombre de facteurs, notamment leur physique, les paramétrisations, les conditions initiales et limites, etc., qui peuvent les éloigner des observations (Cao et al. 2015, Zhang et al. 2018).

Des études antérieures ont montré l'importance des interactions air-mer en termes d'oscillations atmosphère-océan telles que ENSO canonique (Kleeman et al. 1999, Mizuta et al. 2014) et ENSO Modoki, un type distinct de réchauffement/refroidissement de la SST dans

le Pacifique tropical caractérisé par ses anomalies maximales de réchauffement/refroidissement dans le centre du Pacifique équatorial (Ashok et al. 2007; Weng et al. 2007, 2009). ENSO a un impact significatif sur le climat et les schémas météorologiques en Asie du Sud-Est. Bien que les impacts exacts puissent varier en fonction du lieu et de l'intensité des événements El Niño/La Niña, on considère généralement qu'il s'agit d'un facteur majeur de la variabilité climatique dans la région. En outre, les caractéristiques d'ENSO ont changé au cours des dernières décennies (Behera et al. 2021), affectant non seulement ses caractéristiques spatiales et temporelles, mais aussi le climat de régions éloignées par le biais de téléconnexions dans l'atmosphère et les océans. Il est donc extrêmement important de comprendre les impacts d'ENSO ainsi que les impacts distincts d'ENSO Modoki sur les composantes du climat. L'élaboration de connaissances détaillées sur les conditions océaniques et climatiques passées, présentes et futures, influencées par les effets de ce phénomène couplé air-mer, peut en effet contribuer à atténuer les risques et à mettre en œuvre des mesures d'adaptation appropriées dans le contexte de la variabilité et du changement climatiques.

L'Asie du Sud-Est (SEA, Fig. 0.1) est une sous-région tropicale de l'Asie située entre les océans Pacifique et Indien, qui comprend l'Asie du Sud-Est continentale et le Continent Maritime. Le climat de cette région est principalement tropical et humide avec des températures élevées, et influencé par les moussons asiatiques, avec une forte saisonnalité (Yoneyama & Zhang, 2020). En raison de la répartition complexe des terres et des mers (on y dénombre plus de 22 000 îles), la région SEA est le siège de fortes interactions terre-air-mer locales: brises terre-mer, cyclones tropicaux connus sous le nom de typhons, convection atmosphérique profonde, mousson... (Xue et al. 2020). Les extrêmes climatiques tels que les fortes précipitations, les sécheresses et les inondations sont courants dans la plupart des régions de SEA et ont été identifiés comme des facteurs contribuant aux principaux risques liés au changement climatique dans cette région (Hijioka et al., 2014, Ngo-Duc et al., 2017). La SEA est également influencée par des phénomènes couplés océan-atmosphère à grande échelle. Parmi ceux-ci, ENSO a un impact majeur sur le climat et la circulation océanique de la région: les événements El Niño affectent la fréquence des cyclones tropicaux (Landsea, 2000) et la variabilité des précipitations (Matsumoto 1997, Francisco et al. 2006), et induisent un affaiblissement de la mousson d'été qui se traduit par un réchauffement de la surface de la mer et un affaiblissement de la circulation océanique en SEA, y compris des upwellings côtiers (Chao et al., 1996, Wang et al., 2006, Da et al., 2019). La région SEA est également le lieu de passage des eaux de surface de la circulation thermohaline mondiale entre les océans Indien et Pacifique (le "Indonesian Throughflow", ITF et le "South China Sea Throughflow", SCSTF, Qu

et al. 2004, Susanto et Song 2015, Kannad et al. 2020). Au cours de cette traversée, ces eaux océaniques gagnent en chaleur et en eau douce grâce aux apports atmosphériques et continentaux, et sont fortement modifiées par le mélange océanique induit par les marées (Hein 2008, Chen et al. 2012). Ces interactions à différentes échelles entre l'océan et l'atmosphère jouent un rôle important dans la détermination des régimes météorologiques et climatiques ainsi que dans la dynamique océanique dans la région SEA.

L'impact d'ENSO sur la circulation et le climat de l'atmosphère et de l'océan en SEA a fait l'objet de plusieurs études qui ont examiné, par exemple, l'influence d'ENSO sur les phénomènes météorologiques extrêmes, la sécheresse et les inondations (Ward et al. 2014, Villafuerte et Matsumoto 2015), la variabilité des précipitations (Nguyen-Thanh et al. 2023) et l'échange d'eau océanique (Qu et al. 2005). Cependant, la plupart de ces études se sont concentrées sur l'ENSO canonique, et l'impact distinct d'ENSO Modoki reste encore à mieux caractériser, quantifier et expliquer. De plus, la plupart des études numériques portant sur l'influence d'ENSO, mais plus généralement sur le fonctionnement, la variabilité et l'évolution à long terme du système climatique SEA océan-atmosphère-continent, ont été réalisées à l'aide de modèles uniquement atmosphériques ou océaniques, afin d'étudier respectivement la réponse de l'atmosphère ou de l'océan à divers facteurs de variabilité. A notre connaissance, très peu d'études ont été réalisées à l'aide de modèles couplés (Xue et al. 2020), et la compréhension et la quantification des interactions air-mer dans la région SEA, en particulier des échanges de chaleur, restent encore à explorer.

Dans ce contexte, l'objectif général de ce travail est d'améliorer notre connaissance du fonctionnement, de la variabilité et de l'influence des interactions air-mer dans le système climatique de la région SEA, et de leur réponse au changement climatique. Dans cette thèse, nous étudions d'abord l'impact des deux types d'ENSO sur la variabilité des précipitations dans la région SEA. Nous nous concentrons ensuite sur les échanges de chaleur air-mer, dans le but d'explorer leurs estimations et les incertitudes associées à partir d'ensembles de données numériques et d'observation disponibles, et d'évaluer leur réponse au changement climatique.

La thèse est organisée en cinq chapitres. Le chapitre 1 présente une vue d'ensemble de la région SEA et de son climat, discute des connaissances liées aux interactions air-mer, présente les questions scientifiques de la thèse et décrit sa structure. Le chapitre 2 étudie l'impact des deux types d'ENSO sur les précipitations dans la région SEA. Le chapitre 3 se concentre sur l'analyse des flux de chaleur air-mer en SEA à travers les ensembles de données disponibles et

les simulations de sensibilité océanique. Le chapitre 4 évalue les estimations des flux de chaleur dans les modèles CMIP6 et examine leurs tendances futures. Enfin, le chapitre 5 conclut la thèse et suggère des orientations pour les travaux futurs.

# General introduction

The ocean and atmosphere systems exchange heat, freshwater, and momentum at the sea surface. A better understanding of these exchanges is essential for advancing our comprehension of how the atmosphere and oceans interact (Cayan 1992a). They involve a wide range of processes, at very different spatial and temporal scales, from tropical cyclones (Ma et al. 2015, Li et al. 2022) or dense water formation (Millot et Taupier-Letage 2005, Gutjahr et al. 2022) to seasonal monsoons and large-scale interannual to multi-decadal oscillations such as El Niño-Southern Oscillation (ENSO) (Wang et al. 2011, Yan et al. 2020, Huang and Xie 2015).

One of the primary mechanisms for the ocean to release the heat absorbed from solar radiation is through turbulent heat exchange, in the form of latent (LH) and sensible (SH) heat fluxes. Yu and Weller (2007) showed that heat fluxes induce changes in SST, wind, and air-specific humidity. Moreover, the energy input provided by LH and SH from the ocean to the atmosphere modifies the vertical mixing and has the potential to modulate the atmosphere (Xie 2004) and the marine atmospheric boundary layer (Tokinaga et al. 2005). In turn, those heat exchanges at the ocean surface strongly drive the temperature of the oceanic upper layers as well as their dynamics (Carton and Zhou 1997, Duvel et al. 2004). Therefore, gaining insight into the temporal and spatial variability of air-sea heat fluxes, and better representing those air-sea interactions in ocean, atmosphere, and climate models, is crucial for understanding climate variations over a wide range of time and space scales. However, questions have been raised about the reliability of heat flux estimates due to the large spread and bias of values from different products (Brunke et al. 2003, Zhang et al. 2004, Yu et al. 2004). Estimates from climate models also have errors related to a number of factors including model physics, parameterizations, initial and boundary conditions, etc., that can cause them to drift away from observations (Cao et al. 2015, Zhang et al. 2018).

Previous studies showed the importance of air-sea interactions in terms of atmosphere-ocean oscillations such as canonical ENSO (Kleeman et al. 1999, Mizuta et al. 2014) and ENSO Modoki, a distinct type of tropical Pacific Sea surface temperature (SST) warming/cooling pattern characterized by its maximum warm/cool anomalies in the central equatorial Pacific (Ashok et al. 2007; Weng et al. 2007, 2009). ENSO has a significant impact on climate and weather patterns in Southeast Asia. While the exact impacts may vary depending on the

location and severity of the El Niño/La Niña events, it is generally considered to be a major driver of climate variability in the region. Moreover, the characteristics of ENSO have undergone changes in recent decades (Behera et al. 2021), affecting not only its spatial and temporal characteristics but also remote regions' climate through teleconnections in the atmosphere and oceans. Therefore, understanding the impacts of ENSO as well as the distinct impacts of ENSO Modoki on climate components is extremely important. Building a detailed understanding about past, present, and future oceanic and climate conditions influenced by the coupled effects of this sea-air phenomena, can indeed aid in mitigating risks and implementing appropriate adaptation measures within the context of climate variability and change.

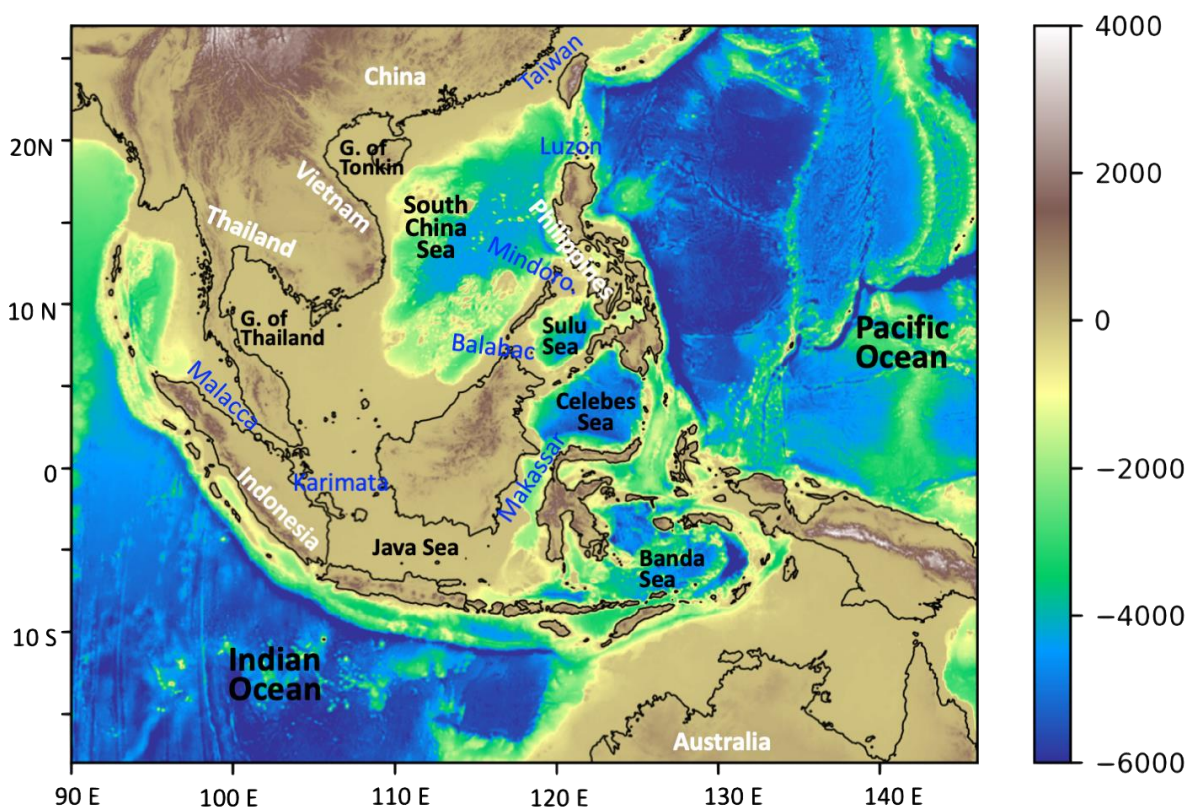


**Figure 0.1** The Southeast Asia domain. Topography over SEA (shaded) is obtained from the General Bathymetric Chart of the Oceans (GEBCO), available from <https://www.gebco.net>.

Southeast Asia (SEA, Fig. 0.1) is a tropical sub-region of Asia located between the Pacific and Indian Oceans and including Mainland Southeast Asia and the Maritime Continent. The climate in this region is mainly tropical with high temperatures, humid, and influenced by the Asian monsoons, with a strong seasonality (Yoneyama & Zhang, 2020). Due to the complex distribution of land and sea (there are more than 22000 islands), the SEA region experiences strong local land-air-sea interactions, including land-sea breezes, tropical cyclones known as

typhoons, deep atmospheric convection, and monsoon... (Xue et al. 2020). Climate extremes such as heavy rainfall, droughts, and floods are common in most parts of SEA, and have been identified as contributing factors to major climate change risks in this region (Hijioka et al., 2014, Ngo-Duc et al., 2017). SEA is also influenced by large scale coupled ocean-atmosphere phenomena. Among these, ENSO has a major impact on the region's climate and ocean circulation: El Niño events affect tropical cyclone frequencies (Landsea, 2000) and rainfall variability (Matsumoto 1997, Francisco et al. 2006), induce a weakening of SEA summer monsoon that results in sea surface warming and ocean circulation weakening, including coastal upwellings (Chao et al., 1996, Wang et al., 2006, Da et al., 2019). The SEA region also hosts the passage of surface waters of the global thermohaline circulation between the Indian and Pacific Oceans (the Indonesian throughflow, ITF and South China Sea throughflow, SCSTF, Qu et al. 2004, Susanto and Song 2015, Kannad et al. 2020). During this crossing, these oceanic waters gain heat and freshwater from atmospheric and continental inputs and are strongly modified by ocean mixing induced by tides (Hein 2008, Chen et al. 2012). These interactions at different scales between ocean and atmosphere play an important role in determining weather and climate patterns as well as ocean dynamics in the SEA region.

The impact of ENSO on SEA atmosphere and ocean circulation and climate was the subject of several studies that examined for example ENSO influence on extreme weather, drought and floods (Ward et al. 2014, Villafuerte and Matsumoto 2015), rainfall variability (Nguyen-Thanh et al. 2023) and oceanic water exchange (Qu et al. 2005). However, most of those studies focused on canonical ENSO, and the distinct impact of ENSO Modoki still remains to be better characterized, quantified and explained. Moreover, most of the numerical studies investigating ENSO influence, but more generally the functioning, variability, and long-term evolution of SEA ocean-atmosphere-continent climate system, were done using atmospheric only or oceanic only models, to respectively study the answer of atmosphere or ocean to various factors of variability. To our knowledge, only very few studies were done using coupled models (Xue et al. 2020), and the understanding and quantification of air-sea exchanges of the SEA region, in particular of heat exchanges, still remains to be explored.

In this context, the general objective of this work is to improve our knowledge of the functioning, variability and influence of air-sea interactions in the SEA climate system and of their response to climate change. In this thesis we first investigate the impact of the two types of ENSO on precipitation variability in the SEA region. We then focus on air-sea heat exchanges, with the goal to explore their estimates and related uncertainties from available

observational and numerical datasets and evaluate their answer to climate change.

The thesis is organized into five chapters. Chapter 1 provides an overview of the SEA region and climate, discusses the underlying knowledge of air-sea interaction, presents the scientific questions of the thesis, and outlines its structure. Chapter 2 investigates the impact of the two types of ENSO on rainfall in SEA. Chapter 3 focuses on the analysis of air-sea heat fluxes in SEA across available datasets and ocean sensitivity simulations. Chapter 4 evaluates heat flux estimates in CMIP6 models and examines their future trends. Finally, Chapter 5 concludes the thesis and suggests directions for future work.

# Chapter 1. Introduction

## Contents

1.1 Air-sea interactions .....	15
1.1.1 General schematic of air in -sea interactions.....	15
1.1.2 Coupled atmospheric-oceanic phenomena. ....	18
<i>1.1.2.1 El Niño-Southern Oscillation (ENSO)</i> .....	18
<i>1.1.2.2 ENSO Modoki</i> .....	20
1.1.3 Air-sea heat flux .....	21
1.2 Southeast Asia regional climate system.....	24
1.2.1 Southeast Asia physical Geography .....	24
1.2.2 Southeast Asia monsoon system.....	26
<i>1.2.2.1 Summer monsoon</i> .....	27
<i>1.2.2.2 Winter monsoon</i> .....	27
1.2.3 Southeast Asia climatic characteristics.....	29
<i>1.2.3.1 Surface temperature</i> .....	29
<i>1.2.3.2 Rainfall</i> .....	30
<i>1.2.3.3. Tropical cyclones</i> .....	31
1.3 Ocean circulation around and in SEA.....	33
1.3.1 Western boundary currents (WBC): Kuroshio and Mindanao currents .....	33
1.3.2 South China Sea Throughflow (SCSTF) .....	35

## Chapter 1. Introduction

1.3.3 Indonesian Throughflow (ITF).....	36
1.3.4 Effect of ENSO on ocean circulation in the SEA region .....	37
1.4 Thesis Objectives and Structure.....	38
1.4.1 Effect of ENSO and ENSO Modoki on SEA Climate.....	38
1.4.2 Air-sea heat exchanges in SEA .....	39
1.4.3 Thesis main scientific questions .....	40
1.4.4 Thesis structure.....	40

This chapter presents a literature review that leads to the main questions of this PhD thesis. We first present the general existing knowledge about air-sea interactions, with a focus on the coupled atmospheric-oceanic phenomena, in particular the El Niño Southern Oscillation (ENSO) phenomenon and air-sea heat fluxes. Subsequently, we focus on the current knowledge about Southeast Asia (SEA): its geographical features, climate characteristics, functioning and variability, including monsoons, tropical cyclones, ocean circulation and ENSO influence. We then explore the unresolved aspects in ongoing research concerning the effects of ENSO and heat exchanges in the SEA region, leading to the main scientific questions and the structure of this thesis.

### 1.1 Air-sea interactions

#### 1.1.1 General schematic of air in -sea interactions

The atmosphere and ocean are key drivers of the heat, momentum, and water budget of the climate system. The associated processes play important roles not only in transporting the heat and momentum but also developing modes of climate variations that are very important for terrestrial and marine ecosystems. The interaction between the atmosphere and the ocean is a complex and highly nonlinear turbulent process that involves a large number of feedback and is fundamental to the motions of both systems (Pond 1971). The winds blowing over the surface of the ocean transfer momentum and mechanical energy to the water, generating waves and currents, while the ocean gives off energy through latent heat (phase change), sensible heat, and longwave radiation (Fig 1.1).

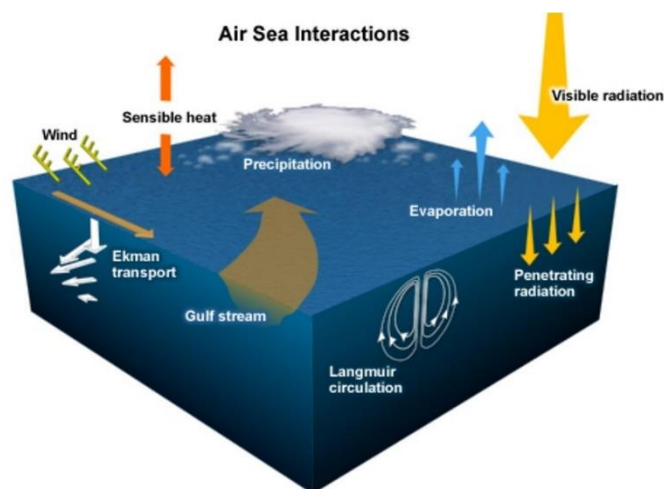


**Figure 1.1.** Air-sea interaction's schematic. Source: <https://www.ecmwf.int/>

## Chapter 1. Introduction

The thermal regime that controls the atmosphere plays an important role in maintaining the energy balance and forming weather phenomena on Earth. The major source of this thermal energy is the Sun, which provides heat directly and indirectly (through the oceans) in the form of shortwave solar radiation. Of all the solar radiation reaching Earth, 30% is reflected in space and 70% is absorbed by the Earth (47%) and atmosphere (23%) (Stephens et al. 2012). The heat absorbed by the land and oceans is exchanged with the atmosphere through conduction, radiation, and latent heat (Trenberth et al. 2009, Wild et al. 2013a, b). The tropical regions are considerably warmer than the mid- and high latitudes. That temperature difference drives the atmospheric and oceanic circulations that in turn help in maintaining the Earth's energy balance. Because of those circulations and associated energy transports, the Earth is approximately in energetic balance on an annual average and the net energy loss in the polar regions is roughly balanced with the net energy gain in the tropical regions.

One of the most important roles of ocean currents is in governing Earth's weather and climate (Bressan and Constantin 2019) by transporting and redistributing the heat stored in the upper ocean around the planet. This in turn governs wind patterns, air temperature, and precipitation, both locally and globally. Most ocean surface circulations are wind driven. On a large scale, winds in the tropics and the subtropics give rise to large upper ocean circulations known as subtropical gyres (Ganopolski 2008, Boyd 2018). Five permanent subtropical gyres are found in the major ocean basins – two in the Atlantic, two in the Pacific and one in the Indian Ocean – rotating clockwise in the Northern Hemisphere and counterclockwise in the Southern (Fig. 1.2). The gyres have equatorial westward currents driven by easterly winds and strong western boundary currents such as the Kuroshio in the northwest Pacific and the Gulf Stream in the northwest Atlantic. These gyres help to carry heat along their western boundaries through the strong western boundary currents in both hemispheres and bring cold waters from higher latitudes to the tropics along the interior and eastern boundaries of the oceans (De Blij et al, 2004).

Oceans also play an important role in the heat budget of the atmosphere and its heat transport. In the long term, the convergence and divergence resulting from oceanic heat transfers act as sources and sinks of heat for the atmosphere, significantly impacting Earth's climate. Moreover, at the air-sea interface, the oceans engage in complex exchanges with the atmosphere, involving gases, water vapor, suspended particles, momentum, and energy. These exchanges are often associated with the friction at the sea surface and the associated turbulence caused by surface winds. Consequently, these heat transfers are commonly classified as

turbulent energy to distinguish them from radiative energy.

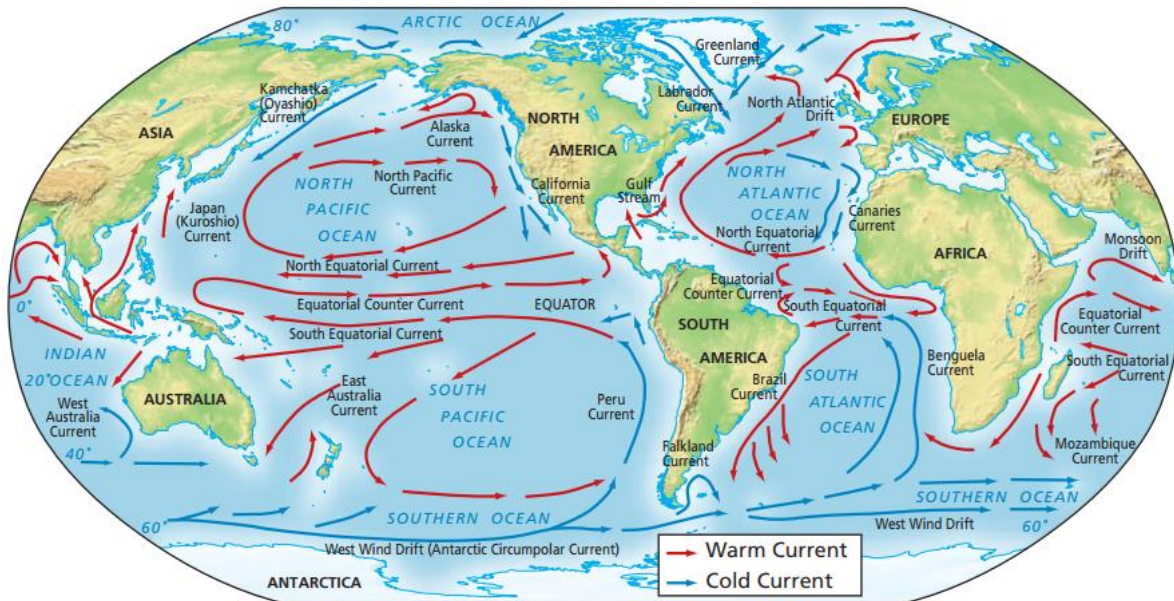


**Figure 1.2** Map of major ocean currents and gyres (De Blij et al, 2004)

The surface wind induces a force on the ocean called wind stress and its effect reduces with the depth owing to greater friction (Welander 1957, Stern 1965). Together with the Coriolis force (due to Earth's rotation) and friction, the wind stress causes water to upwell through a process called Ekman pumping (Chelton 1982, Wang et al 2013). The direction of wind-induced ocean currents also changes with depth, changing from around 45 degrees to the right (left) in the Northern Hemisphere (Southern Hemisphere) at the surface to the opposite direction at the bottom of the Ekman layer because of the effect of Coriolis and frictional forces. Therefore, along the eastern boundaries of the oceans, the equatorward winds push upper ocean water away from coasts, causing cooler subsurface water to upwell from below to replenish the offshore-moving surface water. The equatorial region, especially in the eastern Pacific, also experiences upwelling driven by the trade winds on either side of the equator, which drive surface water away from the equator, inducing cooler subsurface water to rise (Chiang and Bitz 2005, Pennington et al. 2006). The coastal upwelling as explained earlier causes zonal differences in the ocean basins (Stommel and Arons 1959, Longhurst 1993). As subsurface waters are cooler than surface waters, regions experiencing upwelling exhibit cooler SSTs. While both western and eastern sides of these basins receive similar amounts of solar radiation, the SSTs in the eastern sides are much cooler due to upwelling (Xie et al. 2003).

### 1.1.2 Coupled atmospheric-oceanic phenomena.

The Earth's climate is strongly influenced by several large-scale air-sea coupled phenomena that particularly affect Southeast Asia's climate.

#### 1.1.2.1 *El Niño-Southern Oscillation (ENSO)*

The El Niño-Southern Oscillation, ENSO, is the most typical ocean-atmosphere coupled phenomenon in the climate system at the interannual time scale. It refers to the abnormal ocean warming/cooling that develops in the tropical Pacific Ocean and is linked to variations in atmospheric circulations and oceanic conditions (Wang and Picaut 2004).

The warm phase of ENSO (El Niño) is characterized by higher SST in the center and eastern tropical Pacific resulting in a weaker SST gradient between the Western Pacific warm-pool region and the Eastern equatorial Pacific (Fig. 1.3a). The opposite condition is referred to as La Niña, with the SST in the central and eastern Pacific becoming cooler than average (Fig. 1.3b).

The Pacific Walker circulation is a large-scale zonal overturning circulation in the atmosphere, which is characterized by rising motion and deep convection over the equatorial western Pacific and Maritime Continent, and strong easterly surface winds over the equatorial Pacific (Bjerknes 1969, Lau and Yang 2003). On interannual time scales, variations in the Walker circulation are tightly connected to ENSO (Rasmusson and Carpenter 1982, Tanaka et al. 2004), impacting global climate through atmospheric teleconnections (Lau and Yang 2003, Power et al. 1999). The Western Pacific and Maritime Continent experience drier conditions during El Niño owing to the downdrafts of the anomalous Walker circulation associated with the event (Weng et al. 2009). At this time, anomalously wet conditions are observed east of the dateline due to the updrafts of the anomalous Walker circulation. The weakening of the Walker Circulation thus causes widespread drought in Indonesia/Maritime Continent and in northeastern Brazil, severe floods in Peru, Ecuador, southeastern Brazil, and northern Argentina (Lau and Yang 2003). Moreover, the western coasts of the United States receive increased rainfall associated with the El Niño teleconnections. Besides, regions of anomalously warm SSTs are linked with enhanced tropical convection, which affects atmospheric circulation patterns and weather conditions, producing large-scale ecological and social impacts (Dilley and Hayman 1995).

Regarding the opposite phase, with a stronger Walker circulation, intensified upwelling along the Southamerican coast, and colder SSTs in the eastern Pacific, La Niña's effects on global weather variability are roughly (though not exactly) opposite to those of El Niño (Halpert and Ropelewski 1992). La Niña typically brings increased rainfall in southern Africa northeastern Brazil and in the monsoon regions of India, Indonesia and Northern Australia. La Niña is often linked to drier-than-normal conditions over equatorial East Africa, southern Brazil, and Uruguay (McPhaden 2002).

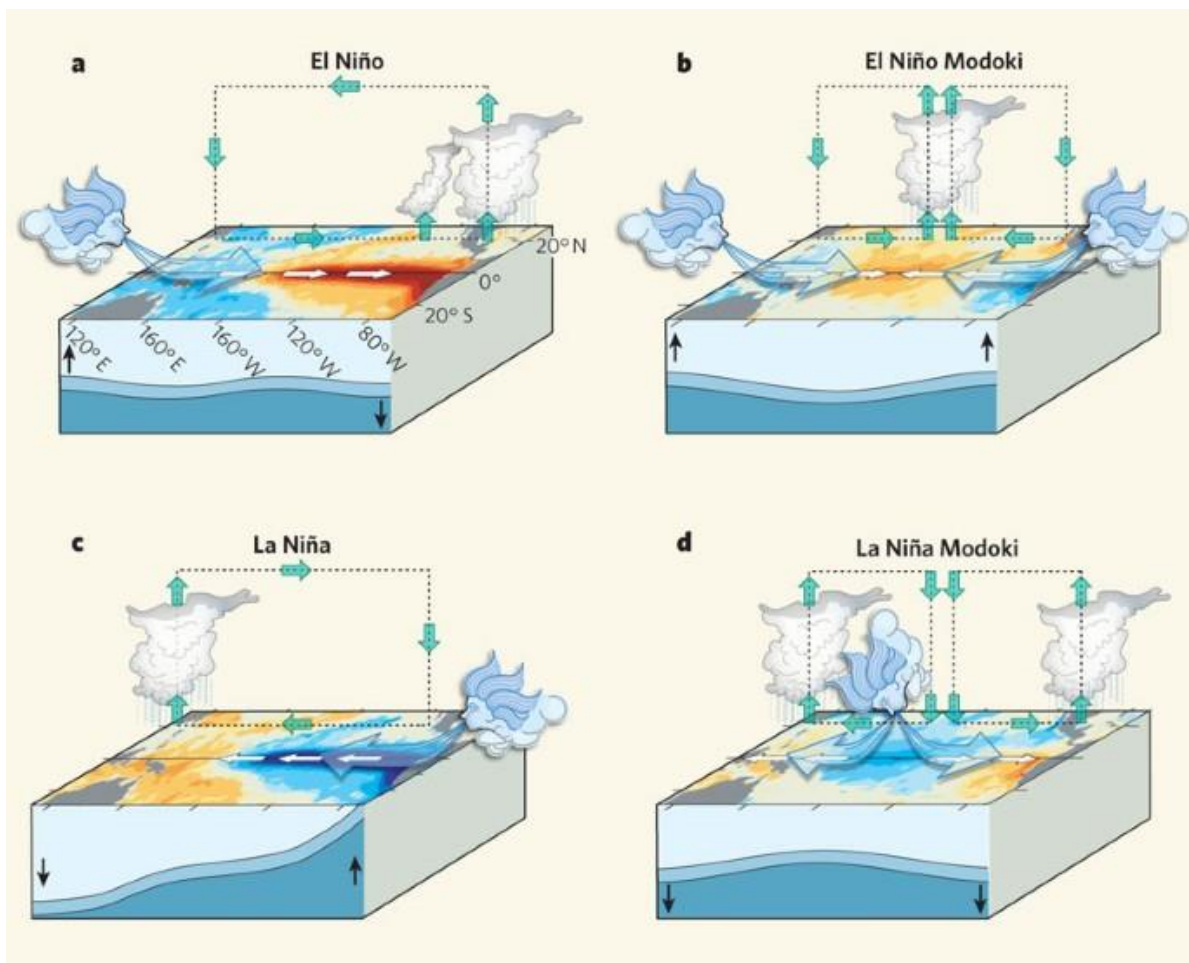


**Figure 1.3** Anomalous conditions in the tropical Pacific: (a) El Niño event, (b) El Niño Modoki (c, d) The opposite (La Niña) phases of the El Niño and El Niño Modoki respectively (Ashok and Yamagata 2009).

In addition to affecting adjacent landmasses and remote regions of the globe by bringing changes in seasonal Walker and Hadley circulations or through atmospheric teleconnections, ENSO also has the capacity to modulate extreme weather events such as tropical cyclones, heat waves, and floods (Rasmusson and Carpenter 1982, Trenberth et al.1998). ENSO is linked to

tropical cyclone variability in the northwestern Pacific: it has been suggested that the region of typhoon genesis shifts eastward (westward) during El Niño (La Niña) years (Chan 2000, Wang and Chan 2002), and the lifespan of tropical cyclones in El Niño years tends to be longer (Camargo and Sobel 2005). Over the Atlantic basin, El Niño suppresses Atlantic hurricane activity through enhanced vertical wind shear (Bell and Chelliah 2006). The teleconnections and influences associated with La Niña generally stand in contrast to those of El Niños. However, these teleconnections exhibit inherent nonlinearity, and asymmetries are also observed between El Niño and La Niña events (Behera et al. 2021).

### 1.1.2.2 ENSO Modoki

Central Pacific El Niño events, also known as El Niño Modoki (Ashok et al. 2007) or warm pool El Niño (Kug et al. 2009), present an anomalous condition of a distinctly different kind with a warm SST anomaly located in the central equatorial Pacific, flanked by colder waters to the east and west (Fig. 1.3b). They are associated with distinct patterns of atmospheric convection. Since the 1990s, the frequency of emergence of El Niño Modoki events, and their cold counterparts, La Niña Modoki (Fig. 1.3d), has increased (Yu and Kao 2007, Ashok et al. 2007). Hereinafter, we use the term El Niño Modoki (EM) and La Niña Modoki (LM) for these new types of SST warming and cooling patterns to differentiate them from the canonical El Niño (EN) and La Niña (LN).

In contrast to the traditional ENSO, the ENSO Modoki has new features in many aspects, including the spatial distribution and intensity of SST anomaly, the mechanism of development and evolution, etc. During EN, a broad region from Myanmar through eastern China to Northern central China receives reduced summer rainfall but experiences opposite conditions during EM, except in some portions of coastal China. Japan experiences a substantial deficit in rainfall during EM summers, in contrast to the anomalously surplus summer rainfall during EN. These findings for East Asia are in broad conformation with earlier studies such as Weng et al. (2007), Ashok et al. (2007), Kim et al. (2012), Preethi et al. (2015), Feng et al. (2011), Cai and Cowan (2009), Taschetto et al. (2009). EN summers are associated with anomalously positive (negative) rainfall in northern (eastern and southern) Australia. Notably, during EM summers, entire Australia suffers below-normal rainfall (Taschetto and England 2009).

During EM, we observe strong negative rainfall anomalies in subtropical southern Africa (Preethi et al. 2015). India receives above-normal rainfall during Modoki winters. The rainfall

patterns over India and China during canonical EN are opposite to the signals during EM. While anomalously deficit rainfall occurs, in general, in the northern hemispheric region of South America during EN summers, a zone of anomalously surplus precipitation extends from southern Columbia to Ecuador and Northern Peru during EM. These findings are consistent with earlier studies such as [Weng et al. \(2007\)](#), [Ashok et al. \(2007\)](#), and [Yu et al. \(2012\)](#). Additionally, [Magee et al. \(2017\)](#) discovered that ENSO Modoki has a significant impact on the location of tropical cyclone genesis, with the EM/LM phase leading to a north/south shift in TC activity ([Chen and Tam 2010](#); [Pradhan et al., 2011](#); [Kim et al., 2009](#)).

Beside ENSO, the Indian Ocean Dipole (IOD) mode, emerging within the Indian Ocean basin, also gives rise to global teleconnections ([Saji et al. 1999](#)). Like ENSO, IOD involves an irregular oscillation of SST across the Indian Ocean, and the change in water temperature gradients results in rising and descending moisture and air in specific regions ([Webster et al. 1999](#)). While ENSO and IOD dominate on interannual scales, a remarkable feature of the atmosphere-ocean coupled mode on the intraseasonal scale is the Madden–Julian Oscillation (MJO). The MJO is characterized by equatorially trapped eastward-propagating convective variability in boreal winter ([Madden and Julian 1994](#)). Within the framework of this thesis, the emphasis will be primarily on investigating the impact of ENSO, rather than of IOD or MJO, on the SEA climate.

### 1.1.3 Air-sea heat flux

The ocean interacts with the atmosphere by exchanging momentum, heat, water, gases, and particles at the air–sea interface. This participates in driving the energy and mass balance of the ocean-atmosphere coupled climate system and, consequently, the ocean’s role in the regional and global climate system at all spatial and temporal scales ([Myhre et al. 2014](#), [Jordà et al. 2017](#)). These fluxes are direct indicators of the way the ocean impacts climate and weather, including their extremes, and how the atmosphere forces ocean variability. The strength of this coupling depends on ocean and atmospheric differences in several factors (e.g., temperature, current, and wind speeds) and therefore has a broad range of spatiotemporal variability scales ([Sea-Air Interactions, 2017](#)), from the daily to the multi-decadal scale and from the local and regional to the global scale.

The net heat flux (hereafter  $Q_{net}$ ) at the air-sea interface is the sum of sensible heat flux (SH), latent heat flux (LH), net shortwave radiation (SW), and net longwave radiation (LW)

([Large and Yeager 2004](#), [Huang 2015](#)). In the following, a positive (negative) flux corresponds to a gain (loss) of heat by the ocean. The short wave, or solar radiation refers to the incoming energy from the sun in the form of shortwave electromagnetic radiation and is always positive ([Large and Yeager 2004](#)). Longwave radiation refers to the infrared radiation emitted by the surface and the atmosphere, that is generally negative because the upward radiation from the sea surface is usually greater than the downward. The sensible heat flux is the transfer of heat caused by the difference in temperature between the sea and the air ([Taylor, 2015](#)): when air is warmer than the sea, heat is transferred from the sea to the air. Latent heat flux involves the transfer of heat associated with phase changes, particularly the evaporation and condensation of water. When water evaporates from the sea surface, it absorbs latent heat, cooling the ocean surface. Conversely, when water vapor condenses in the atmosphere, it releases latent heat, warming the surrounding air.

Latent and sensible heat fluxes are the primary mechanism through which the ocean transfers a portion of the absorbed solar radiation back to the atmosphere. Both fluxes cannot be directly observed by space sensors, but can be estimated from wind speed and sea–air humidity/temperature differences using the following bulk parameterization ([Cayan 1992](#), [Large and Yeager 2004](#))

There are numerous research directions related to air-sea heat flux, including:

- 1) Improving understanding of the physical processes that govern air-sea heat flux ([Konda et al. 2010](#), [Chronis et al. 2011](#), [Papadopoulos et al. 2012](#), [Jacob et al. 2020](#)). This includes understanding how factors such as wind speed, air temperature, humidity, and SST affect the exchange of heat between the ocean and the atmosphere.

- 2) Developing new methods for measuring air-sea heat flux ([Yu 2009](#), [Cronin et al. 2019](#)). Existing methods for measuring air-sea heat flux are limited in their accuracy and spatial resolution. Thus, new methods that can provide more accurate and detailed measurements are needed.

- 3) Understanding the spatiotemporal variability of air-sea heat flux ([Mayer et al. 2023](#), [Huang et al. 2023](#), [Jin et al. 2022](#)), and its impact on ocean's temperature, salinity, and circulation and on the Earth's climate.

- 4) Modeling air-sea heat flux in coupled models ([Fang et al. 2010](#), [Kudryavtsev et al. 2014](#), [Barr et al. 2023](#)). Coupled model systems are used to project future changes in Earth's

climate. However, there remain uncertainties in the simulations of air-sea heat flux by existing models (Robertson et al. 2020). New methods are needed to improve the representation of air-sea heat flux in these coupled models.

The accurate determination of  $Q_{net}$ , either retrieved from satellites or modeling, is essential for an accurate assessment of the total heat budget and for understanding long-term climate changes and their related responses, both on global and regional scales (Tomita et al 2021). However, previous studies showed that global mean estimates based on satellite data exhibited a positive bias (i.e., heating the ocean), while reanalysis-based estimates had a negative bias (Park et al 2005, Valdivieso et al 2017). For instance, Song et al 2013 estimated  $Q_{net}$  and showed that reanalysis products, including NCEP1, NCEP2, ERA-40, and ERA-Interim, provided global heat flux estimates in the lower range (ranging from 1 to 11  $W m^{-2}$ ), while estimates based on observations spanned the upper range (ranging from 25  $W m^{-2}$  by NOCSv2.0, a ship-based product, to 30  $W m^{-2}$  by OAFflux and ISCCP, both satellite-based products).

Some studies focused on specific regions. Over the Mediterranean Sea, the annual  $Q_{net}$  is obtained by averaging nine  $Q_{net}$  climatologies over the basin, resulting in a value of  $2 \pm 12 W m^{-2}$  (Song and Yu 2017). By examining the nine climatologies, it is found that the Western Pacific Ocean receives 18  $W m^{-2}$  for the low net heat flux group consisting of five members, and 49  $W m^{-2}$  for the high net heat flux group comprising four members (Song and Yu 2013). The results show that CFSR, MERRA, NOCSv2.0, and OAFflux+ISCCP are warm-biased not only in the western Pacific warm pool but also in the Mediterranean Sea. Conversely, CORE.2 exhibits a cold bias in both regions. NCEP 1, 2, and ERA-Interim show a cold bias over the warm pool yet exhibits a warm bias in the Mediterranean Sea (Song and Yu 2013, 2017).

Although previous studies have demonstrated the superiority of hybrid flux products as compared to the reanalysis flux products (Yu et al. 2006, 2007, Farmer 2012; Liu et al. 2015) for the net heat flux estimation, uncertainties still remain notably significant. Pokhrel et al. (2020) examined the uncertainties of widely used heat flux products, including four reanalyses (NCEP-2, MERRA, CFSR, and ERA5) and two blended products (OAFflux and TropFlux), over the Indian Ocean region for the 10-year period from 2000 to 2009. They indicated that both new generation reanalyses, ERA5 and CFSR, exhibit better agreement with buoy observations in comparison to the older generation NCEP-2 reanalysis. The blended product TropFlux also closely aligns with observations. Among these products, ERA5 consistently

outperforms the others in most cases with the highest correlation (0.89 at 15°N, 90°E; 0.74 at 8°S, 67°E; and 0.86 at 18°N, 89°E), the lowest RMSE, and the most explained variance with respect to in situ values. The time series analysis clearly shows that five flux products (ERA5, CFSR, MERRA, OAFlux, and TropFlux) can capture observed variations with reasonable accuracy. However, NCEP-2 is unable to replicate observed variations, particularly during winter and summer (Pokhrel et al. 2020).

Net heat flux and its four components can also be estimated using model outputs. Macdonald and Wunsch (1996) developed and used a global ocean model to estimate both global ocean circulation and heat fluxes. Their work indicated net heat losses in the North Atlantic and Pacific oceans, heat gain around equatorial regions, and overall losses throughout much of the Southern Ocean. More recently, state-of-the-art global climate models participating in the Coupled Model Intercomparison Project phase 6 (CMIP6) were used to investigate the representation of the global energy balance (Wild 2020). The results of the study demonstrated a significant inter-model variability in the magnitudes of heat flux components within the individual CMIP6 models, with a range of 10–20 W.m<sup>-2</sup>.

### 1.2 Southeast Asia regional climate system

#### 1.2.1 Southeast Asia physical Geography

Located within the geographical coordinates of approximately 12.5°S - 30°N latitude and 90° - 142°E longitude (Fig. 0.1), Southeast Asia (SEA) lies between two oceans (the Pacific to the east and the Indian to the west) and two continental regions of Asia and Australia and includes the Maritime Continent. SEA is considered the world's largest archipelago (Chang et al. 2005). It covers an area of approximately 4.5 million km<sup>2</sup>, which accounts for ~3% of Earth's total land area and gathers about 9% of the world's population (662 million based on the latest United Nations estimates in January 2019), with the majority living in low elevated areas that are vulnerable to climatic hazards (Fig. 1.4). The region is known for its rich cultural and ethnic diversity, with hundreds of languages spoken by different ethnic groups (Norman, 1968).

SEA combines low elevated deltas and plains and mountainous areas, in particular in Myanmar and Indonesia, where elevations can reach up to 4000 m above sea level (Fig. 0.1). The region comprises eleven countries and is made up of two main regions: Mainland and Maritime Continent. The mainland region gathers Vietnam, Laos, Cambodia, Thailand, and

Myanmar. The Maritime region comprises Malaysia, Singapore, Brunei, Indonesia, East Timor, and the Philippines, characterized by numerous island chains – the Malay and Philippine archipelagoes, as well as the Indonesian archipelago, known as one of the most active volcanic regions in the world (Bani et al 2022).

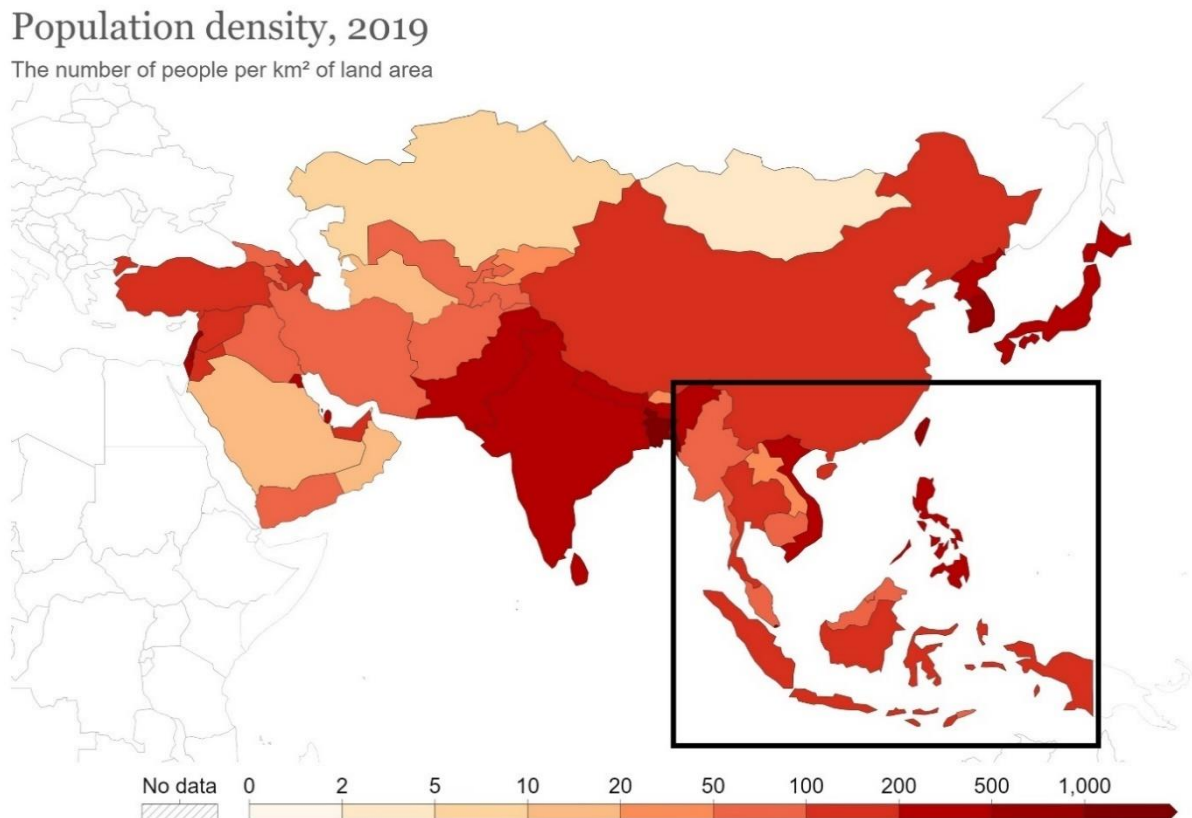


**Figure 1.4** SEA population density map (black box) in 2019. Source: <https://ourworldindata.org/grapher/population-density?time=2019&region=Asia>

The SEA region is characterized by a tropical hot and humid climate with abundant rainfall (Khan et al. 2019, Yang et al. 2021). Most of the region is marked by alternating wet and dry seasons driven by seasonal changes in the winds (Mandapaka et al. 2017) and often experiences extreme weather phenomena. The main seas in SEA, including South China Sea and Indonesian Seas, are interconnected with surrounding seas as well as the Pacific and Indian Oceans through several straits (Wyrcki 1961, Qu et al. 2005, 2006, Wang et al. 2006). These straits will be described in detail in Section 1.3.

### 1.2.2 Southeast Asia monsoon system

SEA is generally characterized by a tropical monsoon climate, related to the region's proximity to the equator and the surrounding oceans. The major controlling factor of a tropical monsoon climate is its relationship to the monsoon circulation which is a 'large-scale seasonal reversal of the wind regime' (Loo et al. 2014). Because of its geographic location and unique monsoon characteristics, SEA has become one of the foci of monsoon research (Lim et al. 2007, Loo et al. 2014, Tangang et al. 2020).

The SEA region is located within the conflict zone of several monsoon systems, including the South Asian monsoon, the East Asian Monsoon and the Asian–Australian monsoon (Wang and LinHo, 2002). The South Asian monsoon is characterized by dry winters and wet summers, with rainfall occurring from May (in southern India and southeastern Asia) to July (in northwestern India). The East Asian monsoon presents more contrasted seasons with cold and dry winters due to the presence of the Siberian High and hot and wet summers with rainfall maxima from May (southeastern China) to July (northeastern China). The Asian–Australian monsoon, exemplified in the northern hemisphere by the mostly oceanic western North Pacific monsoon, results from the seasonal migration of the Intertropical Convergence Zone (ITCZ) and generates rainfall from April to August (over southeastern Asia and the western Pacific) and from November to February (over Indonesia and northern Australia) (Chuan 2005). The Asian–Australian monsoon system also has an asymmetrical nature, with the region of maximum convection shifting from the northern parts during the summer monsoon to the southern parts during the winter monsoon (Chang et al. 2005; Robertson et al. 2011; Waliser and Gautier 1993). Previous studies show that the Bay of Bengal, the Indochina Peninsula, and the Philippines experience a wet (dry) monsoon during boreal summer (winter), while the Maritime Continent experiences the opposite pattern (Fig. 1.5).

The SEA region therefore resides among different monsoon systems, which, to a large extent, influence the rainfall characteristics of the region as a whole. Myanmar, Vietnam, Thailand, Laos, Cambodia, and the Philippines (except for a few island areas) are largely influenced by the South Asian summer monsoon system that brings heavy rainfall from May to September. Conversely Malaysia, Singapore, Indonesia, and Papua New Guinea regions receive heavy rainfall over boreal winter monsoon, mostly from November to March (Johnson 1987, Feng et al. 2010; Tyrlis et al. 2013, Xavier et al. 2014, Ngo-Duc et al. 2017). For both summer and winter monsoons, the rainfall distribution in the SEA region is to a large extent

influenced by the region's topographical features, including mountains and islands (Robertson et al. 2011).

### *1.2.2.1 Summer monsoon*

An important feature of SEA summer monsoon is the monsoon trough, a region of low pressure extending from the West Pacific across Southeast Asia to the Bay of Bengal (Lau and Yang 1997, Sikka and Narasimha 1995, Wang 2004). The trough is also a heat source characterized by wet and windy weather and closely linked to the monsoon disturbances that produce significant precipitation in summer in Southeast Asia (Kiguchi and Matsumoto 2005; Kiguchi et al., 2016). The onset of the summer monsoon in Southeast Asia coincides with the disappearance of the northern hemisphere near-equatorial trough and the formation of the summer monsoon trough over the Vietnam–Cambodia–Laos region, allowing the equatorial westerlies to penetrate northward. Earlier studies have documented the progression of the onset of the Asian monsoon, with the earliest onset occurring first in the eastern Bay of Bengal and the Indochina Peninsula in the middle of May, followed by that over the South China Sea in late May (Tanaka, 1994, Webster et al. 1998, Chang et al. 2004, Qian and Yang 2000). Other studies have also suggested that heavy rainfall typically begins over the Indochina Peninsula in early May, about 10–15 days earlier than over the South China Sea (Lau and Yang 1997; Matsumoto 1997, Webster et al. 1998, Wu and Zhang 1998, Wu and Wang 2000). During boreal summer, the interaction between the southwest monsoon wind and terrain strongly affects the distribution of summer monsoon rainfall, with maximum rainfall occurring on the windward side of terrain in the Indian Ocean, the Indochina Peninsula, and the South China Sea (Fig. 1.5a).

### *1.2.2.2 Winter monsoon*

The onset of the winter monsoon usually occurs in mid-November along the east coast of Peninsular Malaysia, in early December towards the south of the peninsula, and in late December in northern Borneo (Lau and Chan 1983, Tanaka 1994).

The retreat of the monsoon from Peninsular Malaysia varies interannual between early February and the end of March (Chang et al. 2006). Three key features are recognized as being associated with the onset of this monsoon. First, a large-scale monsoon trough moves southward from its location in late summer, around September, in the northern South China

Sea. Secondly, a cold surge precedes the onset of the winter monsoon in Peninsular Malaysia by a day or two. Thirdly, a reversal of the easterly winds to westerly winds happens at the 200 hPa level over southern China owing to the reversal of the north-south temperature gradient across the Asian continent (Chuan 2005).

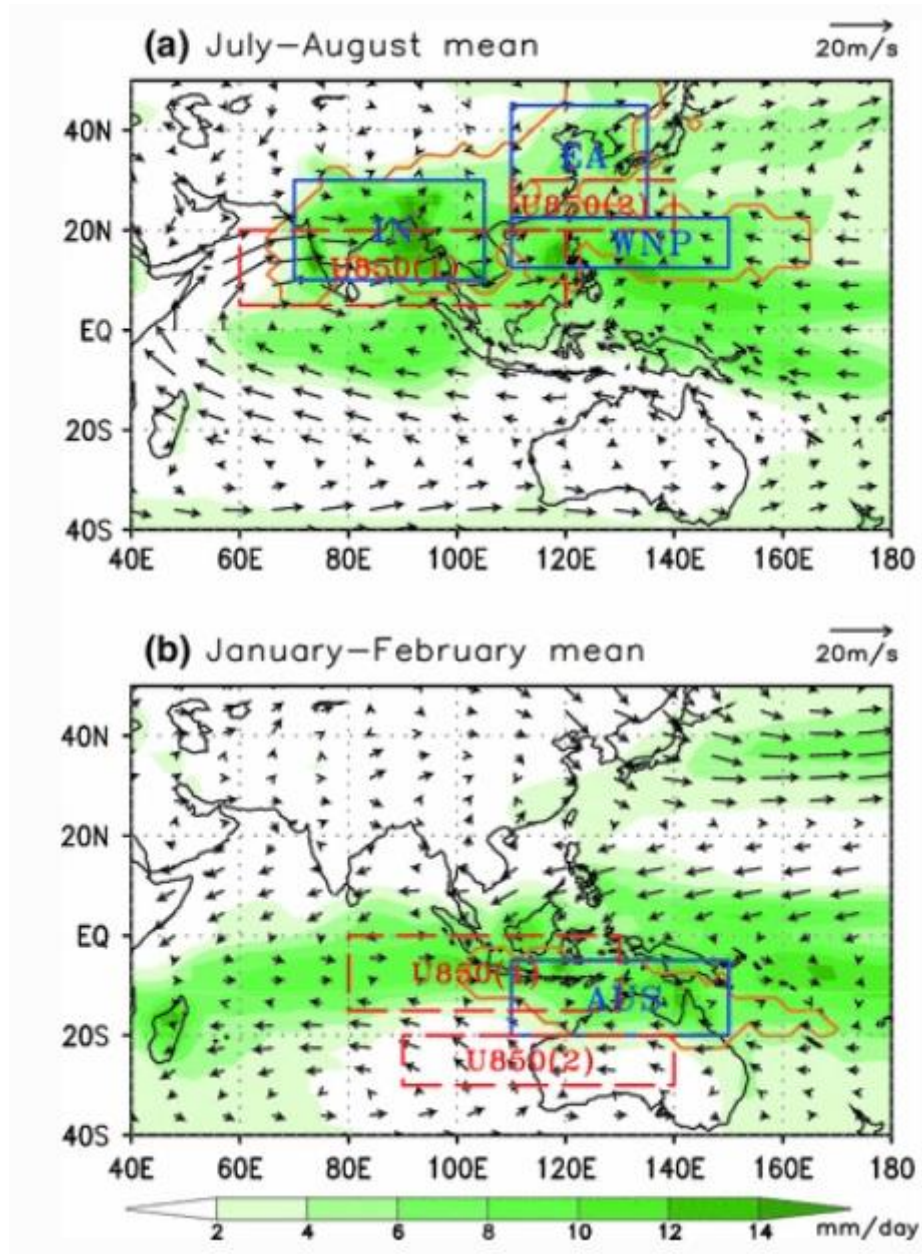


**Figure 1.5** Climatological mean fields of precipitation and low-level winds at 850 hPa during (a) July–August and (b) January–February based on merged CMAP-GPCP data (Wang et al. 2014). Orange: actual monsoon precipitation domain. Blue: approximate regional monsoon boxes. Red: domains where the Asian summer monsoon and Australian summer

monsoon low-level circulation (U850(1), U850(2)) indices are defined.

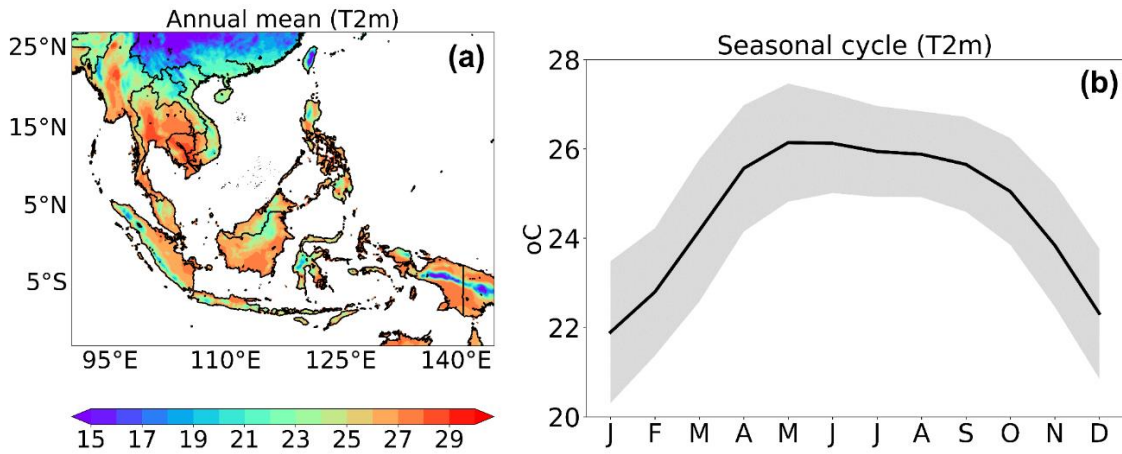
During the winter monsoon, most of the northern SEA region experiences dry weather especially north of 10°N and west of the Philippines (Lim et al. 2007). In contrast, Australia and southern SEA receive large amounts of rainfall during winter monsoon, often leading to extreme rainfall events and floods (Johnson and Chang 2007, Wu et al. 2007, Tangang et al. 2008, Pullen et al. 2015). For instance, higher rainfall is observed over the ocean west of Sumatra, northern Borneo, and the eastern Philippines (Fig. 1.5b). Especially in February, most heavy rainfall events tend to occur around western Java and the southeastern Philippines (Wang et al. 2014). Due to intense outbursts of cold air from mainland Asia interacting with cyclonic systems near the Maritime Continent in boreal winter, heavy rainfall occurs over Malaysia (Lim and Samah 2004, Juneng et al. 2007, Tanganget al. 2008, Ooi et al. 2017) and flooding occurs over the east coast states of Peninsular Malaysia, southeastern Thailand, and western Sarawak (Chen et al. 2013, Chenoli et al. 2022).

### 1.2.3 Southeast Asia climatic characteristics

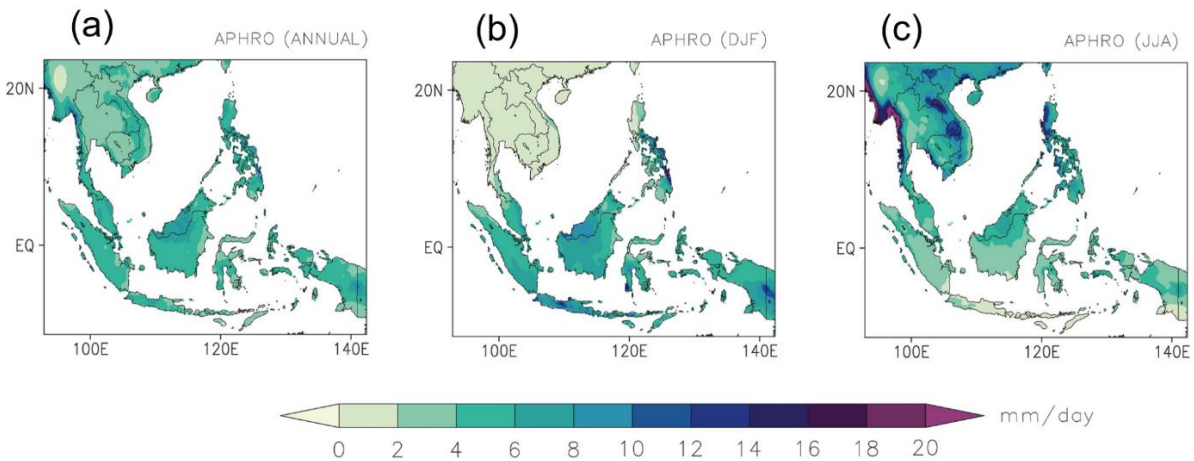
#### 1.2.3.1 Surface temperature

Figure 1.6 shows the annual mean and seasonal cycle of land surface temperatures over SEA from the APHRODITE dataset (Yatagai et al. 2012) for the 1979-2015 period. Temperatures range from 15°C in high-altitude mountain regions (Southern China over mainland SEA, and Papua New Guinea in the Maritime Continent) to 28°C in low-altitude regions like Thailand (Fig. 1.6a).

Temperature seasonally varies from 22°C on average during the winter months (December, January, and February, DJF) to 26°C in May, Jun, and July (Fig. 1.6b). The seasonal variability in temperature over the mainland SEA region is higher than in the equatorial, maritime area. Cruz et al. (2017) showed that the average regional mean temperature over land is 24.8°C, with lower temperatures observed in the northern part of Indochina and high-elevation areas during the winter. During the summer months (June to August, JJA), temperatures are higher, with a regional mean value of 26.2°C over land, reaching as high as 30.5°C locally.



**Figure 1.6** (a) Annual mean and (b) seasonal cycle of temperature over SEA for the APHRODITE dataset (1979-2015).



**Figure 1.7** Climatological seasonal mean precipitation (mm.day) for the APHRODITE dataset (period 1970-2005) in (a) annual, (b) DJF, and (c) JJA (Ngai et al. 2022).

### 1.2.3.2 Rainfall

Overall, the climate in SEA is highly complex, characterized by a complex distribution of land, sea, and terrain resulting in significant spatiotemporal variability of rainfall patterns (Chang et al. 2005, Loo et al., 2015). Figure 1.7a shows the annual precipitation averaged over the 36-year period of 1970–2005, with a range from 1 to 14 mm/day. There is high precipitation over the equatorial region and along the western coast of the mainland region, as well as in parts of Laos, Vietnam, and the Philippines (Ngai et al. 2022). During DJF, low rainfall is depicted over Indochina, while high rainfall occurs over the Maritime Continent with strong

spatial variability (Fig 1.7b) (e.g., over Borneo, southern Sumatra, and Java, [Tangang et al. 2020](#)). The high rainfall over the Maritime Continent is associated with the monsoonal winds that transport moisture from the South China Sea and enhanced convergence. During JJA, rainfall is high over Indochina, especially along the coast of Myanmar due to the boreal summer monsoonal winds that transport moisture from the Indian Ocean and Bay of Bengal (Fig. 1.7c). Furthermore, there is high rainfall in the mountainous region over Laos and Vietnam due to the topographic effect ([Chang et al. 2005](#)).

The spatial and temporal distribution of rainfall in the SEA region is a function of several factors, including the prevailing monsoon, orographic influence, the distribution of land and sea, and the seasonal migration of the ITCZ ([Chang et al. 2005](#), [Waliser and Gautier 1993](#)). [Ratna et al. \(2017\)](#) showed that the peak season for average monthly rainfall varies among subregions. Precipitation in the mainland region peaks during the months of boreal summer, whereas regions such as Malaysia, Singapore, Brunei, and western Indonesia have peaks mostly in the boreal winter months ([Tangang et al. 2020](#)). The Philippines have a slightly longer rainy season compared to the mainland region, though the peak in both regions occurs during the boreal summer. The seasonality is relatively weak in the eastern Indonesia region, with slightly higher precipitation in the boreal winter and boreal spring seasons.

The spatial distribution of rainfall is influenced by topography that enhances rainfall amounts ([Chuan 2005](#)). In general, annual rainfall increases from sea level up to about 1000–1500 m and decreases beyond this altitude. For example, in Indonesia, the maximum annual rainfall is 7069 mm in Central Java, at an elevation of 700 m, while the minimum is 574 mm in Sulawesi at sea level. [Hamed et al. 2022](#) also showed that southern Papua experiences the highest annual rainfall, while the lowest can be found in central Myanmar during 1979-2005.

Over the past decades, many studies revealed complex variations in the annual cycle of rainfall over SEA ([Aldrian and Dwi Susanto 2003](#), [Juneng and Tangang 2005](#), [Lau and Wang 2006](#)). Previous studies have examined the interactions between wind-terrain-rainfall and monsoon circulations ([Wang and Chang 2012](#), [Misra and DiNapoli 2014](#)), and others have explored the impact of climate change at both local and large scales ([IPCC 2013](#), [Loo et al. 2015](#), [Lu et al. 2015](#), [Singh et al. 2019](#), [Raghavan et al. 2017](#)).

### *1.2.3.3. Tropical cyclones*

Southeast Asia is located in the western North Pacific (WNP), which is the most active

tropical cyclone (TC) basin, accounting for 30% of the global total (Woodruff et al. 2013). TCs are often accompanied by extreme winds, torrential rains, and storm surges, potentially causing extensive coastal and inland flooding, associated landslides, and damages (Acosta et al. 2016, Chen et al. 2020, Mei and Xie 2016, Mori et al. 2014). Over the period 1997 to 2016, TCs produced an enormous toll in Southeast Asian countries, resulting in a substantial loss of human lives (178,500) and economic losses (nearly 32 billion USD) (APEC Climate Center, 2017).

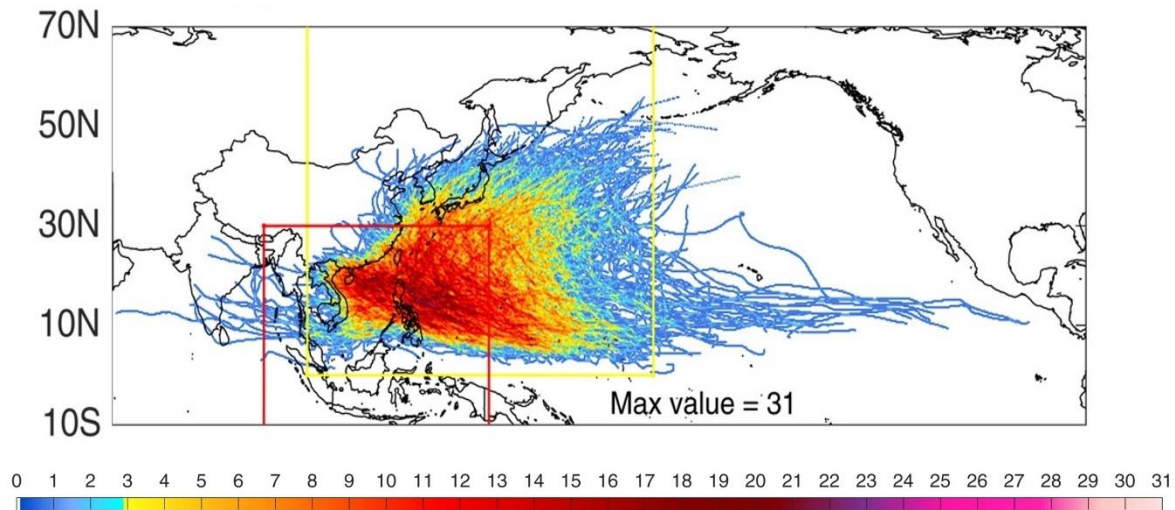


**Figure 1.8** Western North Pacific (WNP) tropical cyclone track density map at 0.25-degree resolution from the Joint Typhoon Warning Center (Tran et al. 2022). The yellow and red rectangles indicate the WNP and SEA domains, respectively.

Following Tran et al. (2022), for the 1970 - 2019 period, approximately half of the TCs that developed in the WNP made landfall in SEA. Most TCs make landfall first in island nations such as the Philippines before moving over the South China Sea then making landfall on the Asian mainland. The peak TC landfall period is from July to October, matching the seasonal peak of TC activity in the WNP (Wang and Chan 2002). The most common TC landfall locations in SEA include the northern and central Philippines, southern China including Hainan Island, Taiwan, and the northern coast of Vietnam (Liu and Chan 2003, Goh and Chan 2010). Landfall locations shift seasonally northward through the summer, from low latitudes in the spring to northern SEA (Taiwan, southern China, and northern Vietnam) (Liu and Chan 2003, Wu et al. 2004). In September, the pattern reverses, and by December TC landfalls mostly concentrate over South Vietnam, the Philippines, and equatorial countries. More WNP TCs make landfall in SEA during LN and Neutral years compared with EN years, with a widespread landfalling area in all subregions in La Niña years (Tran et al. 2022).

### 1.3 Ocean circulation around and in SEA

Ocean circulation is a key component of the SEA climate system: SEA seas exchange heat and water with the atmosphere, the continent and the surrounding seas and oceans. Water masses of the global thermohaline ocean circulation transit from the Pacific Ocean to the Indian ocean through the SEA seas, crossing numerous straits (e.g. Luzon, Mindoro, Makassar, Karimata, Figure 1.6) and flowing through the South China Sea (the South China Sea throughflow, SCSTF, [Qu et al. 2004](#)) and the Indonesian Seas (the Indonesian throughflow, ITF, [Susanto and Song 2015](#), [Kannad et al. 2020](#)). The ITF has long been recognized for its significant role in the world's climate ([Gordon and Fine 1996](#)), transmitting the ENSO signal from the Pacific to the Indian Ocean via changes in internal energy transport ([Tillinger and Gordon 2010](#)) and affecting the Indian monsoon ([Gordon 2005](#)). The SCSTF transforms the cold, salty water of northwest Pacific origin that inflows through the Luzon Strait into warm fresh water out-flowing through the Mindoro and the shallow southern Karimata straits ([Qu et al. 2000](#), [Qu et al. 2009](#), [Fang et al. 2009](#), [Du and Qu 2010](#)). Besides, the South China Sea (SCS) and the Indonesian Seas are also affected by the tropical western Pacific through two Western Boundary Currents (WBCs) ([Takaura et al. 2020](#)).

#### 1.3.1 Western boundary currents (WBC): Kuroshio and Mindanao currents

Western boundary currents (WBC) constitute the largest channel in the ocean for transporting heat poleward and thus play an important role in establishing and maintaining the global heat balance ([Imawaki et al. 2013](#), [Hu et al. 2015](#)). These currents, found in all major oceanic gyres, are swift, narrow, and are the primary conduits for heat exchange between equatorial regions, where heat is added to the oceans, and polar regions, where it is removed ([Hogg and Johns 1995](#)). Within the SEA region, the subtropical gyre WBCs include the Kuroshio Current in the Northern Hemisphere and tropical belt WBCs include the Mindanao Current in the Northern Hemisphere ([Fig. 1.9](#)). Much of modern wind-driven ocean circulation theory was developed in an effort to understand these Pacific Ocean currents ([Hu et al. 2015](#)).

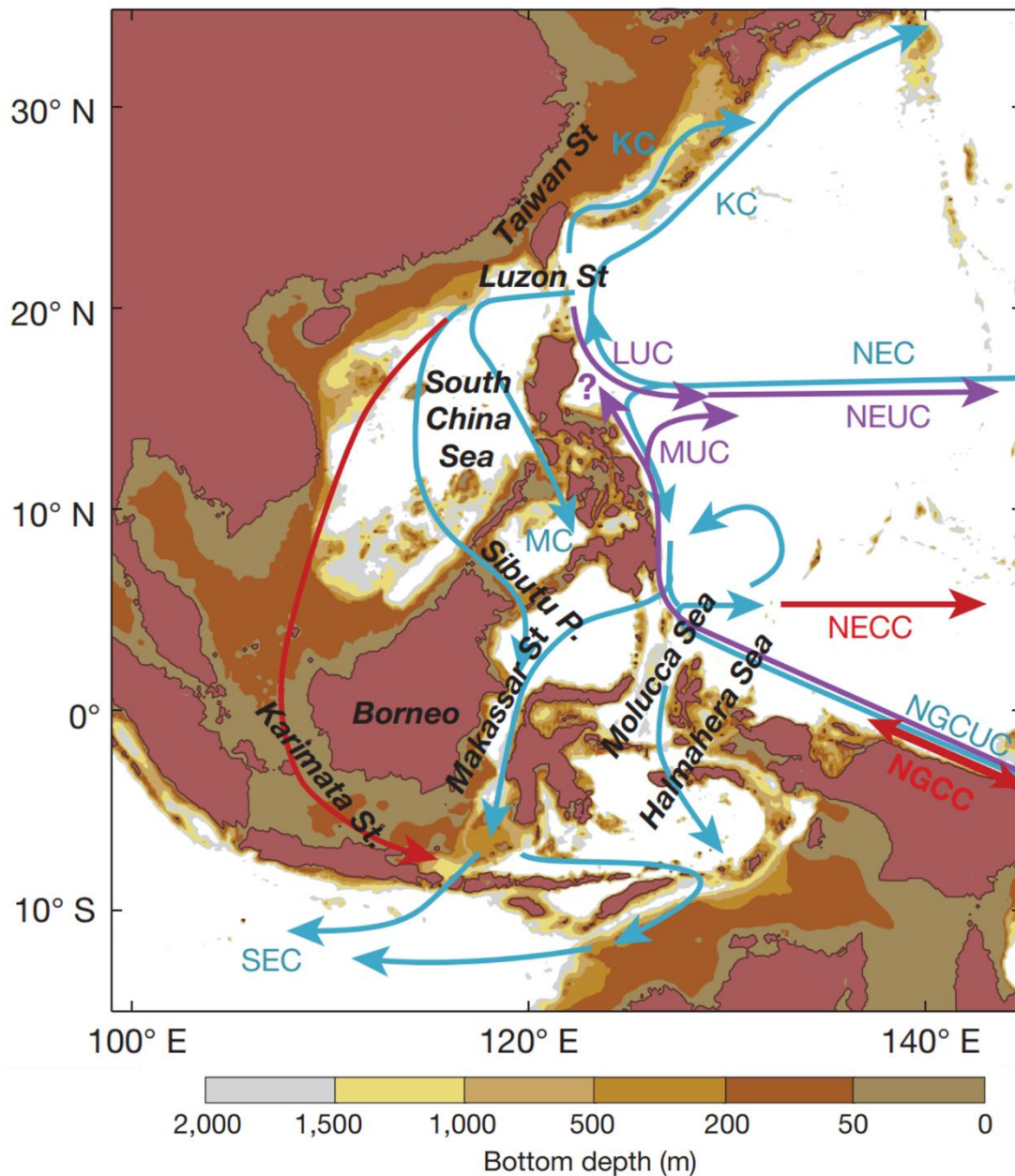


**Figure 1.9** Topographic and boundary current systems in the Northwest Pacific. Depths shallower than 2,000 m are color shaded. Grey shading indicates depths shallower than 50 m. The main currents, integrated from 1,000 m to the surface, are indicated by light blue arrows; red straight arrows indicate the main surface-trapped counter currents; purple arrows indicate undercurrents. Abbreviations used include KC for Kuroshio Current, NEC for North Equatorial Current, MC for Mindanao Current, NECC for North Equatorial Counter Current, LUC for Luzon Undercurrent, MUC for Mindanao Undercurrent, NGCC for New Guinea Coastal Current, NEUC for North Equatorial Undercurrent, SEC for South Equatorial Current (Hu et al. 2015).

The SEA region is influenced by the Kuroshio Current east of the Philippines and the Mindanao Current (Fig. 1.9), both of which originate from the separation and bifurcation of the westward-flowing North Equatorial Current (NEC) around 15°N. Off the Philippine coast, the principal branch of the NEC turns northward, forming the Kuroshio. The other branch turns southward as the Mindanao Current, which feeds the North Equatorial Counter Current and the Indonesian Throughflow into the Indian Ocean via the Celebes Sea. The Mindanao Current transport varies between 25 Sv and 35 Sv, while the Kuroshio has a mean volume transport of 21.5 Sv east of Taiwan (Lee et al. 2001, Fieux 2017).

### 1.3.2 South China Sea Throughflow (SCSTF)

The SCS is a region of strong seasonal reversals of surface circulation driven by the East Asian monsoon: southwest summer monsoon winds (warm and humid) and northeast winter monsoon winds (cool and dry) (Wang 2004). In general, winter monsoon northeast winds cause southward and southwestward currents along the mainland coast. These currents reverse direction when the summer monsoon's southwest winds prevail (Mitsuguchi et al. 2007). The SCS is connected to neighboring bodies of water through six straits: the Taiwan Strait leading into the East China Sea, the Luzon Strait to the Philippine Sea, the Mindoro Strait and the Balabac Strait to the Sulu Sea, the Karimata Strait to the JavaSea, and the Strait of Malacca to the Andaman Sea (Fig. 1.7) (Qu et al. 2009, Tozuka et al. 2009). Among these, the Luzon Strait, having a width of about 350 km and a sill depth of 2500 m, is much larger than the other five straits and connects the SCS directly to the open Pacific Ocean (Wyrski 1961). Recent extensive studies have shown that, on the long-term average, the heat and freshwater gain from the atmosphere can only be balanced by horizontal advection. This balance involves the inflow of cold and salty water through the Luzon strait and the outflow of warm and freshwater through the Mindoro and Karimata straits (Qu et al. 2005, 2006, Wang et al. 2006, Yu et al. 2007, Trinh et al. 2023). This circulation has been referred to as the South China Sea throughflow (SCSTF).

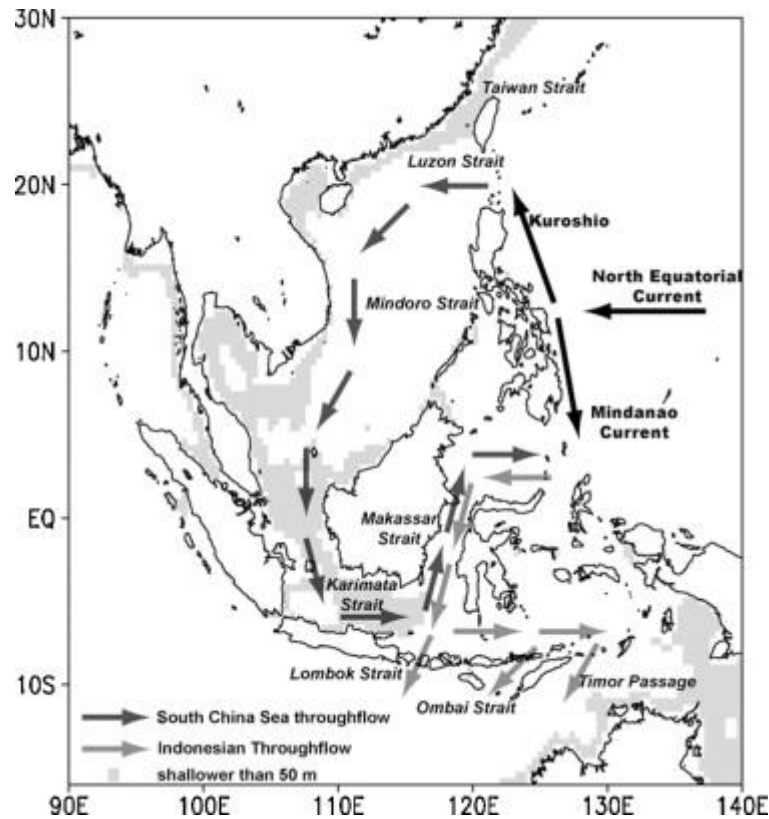


**Figure 1.10** Schematic diagram showing circulations and major straits of the SEA seas (Tozuka et al. 2009)

### 1.3.3 Indonesian Throughflow (ITF)

The Indonesian seas, with their complex coastline geometry and narrow passages (Fig. 1.10), provide the only pathway for low-latitude Pacific water to flow into the Indian Ocean, which is known as the Indonesian throughflow (ITF) (Wyrtki 1961). The main input is through the Makassar Strait, Halmahera Sea, and Molucca Sea (Fig. 1.10). The ITF then flows out to the Indian Ocean from the Lombok Strait, or from the Ombai Strait and Timor Passage after the waters' mixing in the Banda Sea (Gordon et al. 2010, Susanto et al. 2012, Pang et al. 2021). The ITF plays an important role in global ocean thermohaline circulation and directly impacts the basin mass, heat, and freshwater budgets of the Pacific and Indian Oceans with possible influence of ENSO and Asian-Australian monsoon climate phenomena (Bryden and Imawaki 2001, Sprintall et al. 2014).

### 1.3.4 Effect of ENSO on ocean circulation in the SEA region

The Mindanao Current and the Kuroshio Current undergo seasonal and interannual variations depending on the strength of the winds (Kashino et al. 2009, Qiu and Chen 2010, Fieux 2017). Due to the seasonal movement of trade winds, the NEC bifurcation latitude moves from 15°N in boreal summer, to 17°N in boreal winter (Qu and Lukas 2003). During boreal summer, this leads to an increase in the tropical water transport into the North Pacific subtropical gyre. As such, these currents tend to migrate southward with increased transport in summer (June/July) and shift northward with reduced transport in winter (November/December) (Hu et al. 2015). At the interannual scale, ENSO strongly affects the NEC bifurcation latitude and its partitioning into the Mindanao Current and the Kuroshio Current. The Kuroshio originates at a more northern latitude and has a weaker volume transport during EN years, but the Mindanao Current is stronger (Kim et al. 2004, Kashino et al. 2005).

SCS circulation and water characteristics are significantly affected by ENSO. Water exchange between the SCS and the Pacific Ocean through the Luzon Strait plays a crucial role in conveying the impacts of ENSO into the SCS (Wyrtki 1961). Qu et al. (2005) studied SCSTF interannual variations and indicated that flow through the Luzon Strait increases during EN years. This is because the NEC bifurcation (see Fig. 1.6) shifts northward, resulting in a weaker Kuroshio Current to the east of the Philippines, as explained above. These conditions are more favorable for Pacific water to enter the SCS during El Niño events (Tozuka et al. 2002, Kim et al. 2004; Wang et al. 2006). The opposite pattern occurs during LN events. Recent studies have further shown that SST in the SCS has two peaks in the year following EN: one around February and another around August (Wang et al. 2006). During these two phases, changes in atmospheric circulation alter temperature and humidity, leading to an enhanced surface heat flux that warms the sea surface. The warming may also be due to the mixed layer dynamics of the ocean (Shaw et al. 1999). The mixed layer depth variation in the SCS is closely related to the heat transport of the SCSTF (Gan et al., 2006; Qu et al., 2007). The mixed layer depth shoals during and after the EN maturation phase due to the weakening of the northeast monsoon, leading to reduced penetration of the surface heat flux, contributing to a warmer SST (Wang et al. 2006).

Previous studies demonstrated the impact of ENSO on the ITF (Meyers 1996, England and Huang 2005, Qu et al. 2005). The ITF's transport is indeed strongly correlated with ENSO, with strong throughflow during La Niña and weak throughflow during EN (van Sebille et al.

2014, Hu and Sprintall 2016). The observed ITF means transport is  $11.6 \pm 3.2$  Sv southward, varying from 5.6 Sv during the strong 1997 EN to 16.9 Sv during the 2007 LN period (Susanto and Song 2015). The Walker circulation weakens during EN, associated with anomalously warm SST in the central-eastern equatorial Pacific. This leads to lower-than-normal sea levels in the western Pacific, consequently reducing the interbasin pressure gradient that drives the ITF. The reverse occurs during LN. As LN develops, the ITF transport increases due to stronger easterly trade winds which induces an increased pressure gradient between the West Pacific and the eastern Indian Ocean, while the Mindanao Current and SCSTF weaken (Qu et al. 2006, Gordon et al. 2012).

Moreover, the ITF and SCSTF possibly reciprocally influence ENSO through the atmosphere (Qu et al. 2005, 2006, Gordon et al. 2012). For example, in the Makassar Strait route, tropical Pacific surface water is blocked by South China Sea surface water entering the Indonesian Sea through the Sibutu Passage during the EN period (Gordon et al. 2012). However, transport through the Sibutu Passage cannot compensate for all the blocked Pacific surface water. Although the entry of the surface layer to the Makassar Strait is reduced, the transport in subsurface thermocline water is increased, leading to the cooler temperature transport of the ITF. During the LN period, the contribution of South China Sea transport decreases, allowing surface water from the Pacific Ocean to enter the Makassar Strait, resulting in warmer Makassar Strait transport (Gordon et al. 2012). These changes lead to differences in the SST pattern in the western tropical Pacific and may introduce a significant difference in the air-sea coupled system under the presence of the Indo-Pacific warm pool (Yamagata and Masumoto 1992, Tozuka et al. 2007).

### 1.4 Thesis Objectives and Structure

In this context, the general objective of this thesis is to contribute to improving our knowledge of the air-sea interactions in the SEA climate.

#### 1.4.1 Effect of ENSO and ENSO Modoki on SEA Climate

ENSO impacts on weather and climate over the world through atmospheric teleconnections even modulating extreme weather events (Rasmusson and Carpenter 1982, Trenberth et al. 1998). While the teleconnections and influences associated with La Niña are mostly opposite to those of El Niños, they exhibit nonlinear behavior among the events and show asymmetries

in the teleconnections (Behera et al. 2021). However, changes in the character of ENSO, as well as alterations in the ocean mean state, have led to modifications in ENSO teleconnections in terms of precipitation and temperature (Cai et al. 2020). The SEA region, in particular, is demonstrated to be highly vulnerable to ENSO influence, with effects like extreme weather, droughts, and floods (Ward et al. 2014, Villafuerte and Matsumoto 2015, Sun et al. 2015, Räsänen et al. 2016, Kondo et al. 2018, Li et al. 2018). Many wet and dry extreme events over SEA occur during ENSO events, especially from March to May (Räsänen et al. 2016).

In recent decades, ENSO Modoki and its teleconnections have been demonstrated to exhibit notable differences compared to those of conventional ENSO events (Ashok et al. 2007, Weng et al. 2009). However, the impact of ENSO Modoki on rainfall in SEA has not been fully addressed. For example, the impact on rainfall during boreal summer has only been studied for the surrounding regions of SEA such as South China (Karori et al. 2013) and/or the Pacific rim (Weng et al. 2007) and not for the entire SEA region. Feng et al. (2010) showed a negative rainfall anomaly during EM; however, the coarse resolution dataset they used did not allow an adequate representation of the heterogeneity of the rainfall pattern over the SEA region. The studies moreover focused only on the impact of EM and not of LM (Salimun et al. 2013, Feng et al. 2010). Feng et al. (2010) and Salimun et al. (2013) analyzed rainfall during boreal winter only. Thus, it is crucial to obtain a more precise quantification of the effects of ENSO Modoki over Southeast Asia and how these impacts are different from those of traditional ENSO events.

Therefore, the first objective of the thesis is to investigate the impact of ENSO and ENSO Modoki on rainfall over the SEA region in the past decades. The attribution of different spatial distributions of SST anomalies between the two types of ENSO on regional rainfall variations can provide a deeper understanding of the impact of air-sea interaction in SEA.

### 1.4.2 Air-sea heat exchanges in SEA

Although there are numerous heat flux products available, estimates of air-sea heat fluxes still show large uncertainties, both at the global and regional scales. Most of the research about air-sea exchanges in the SEA region focuses on the SCS area (Qu et al. 2004, Fang et al. 2009, Wang Yan et al. 2019) as pointed out in Trinh's thesis (2020), and a detailed characterization and quantification of air-sea exchanges, in particular heat exchanges, over the SEA region still remains to be done. This requires a better examination of their spatial and temporal variability at different scales, from seasonal variations to long-term evolution related to climate change.

## Chapter 1. Introduction

As explained in section 1.1.3 above, several numerical and observational datasets are distributed and available to study air-sea heat flux, including satellite products, hybrid products, analysis and reanalysis, global simulations, etc... In particular, numerical modeling has become an integral component of the study of air-sea heat flux, especially in the current global warming context. Therefore, the second objective of the thesis is to establish a methodology to build benchmark values of air-sea heat flux in the SEA region that can be used to assess the various available datasets of air-sea heat fluxes.

Last, understanding how heat flux as well as its components change across different temporal and spatial scales for long-term periods as well as in the future is extremely important for detecting and comprehending the consequences of climate variability and climate change (Trenberth et al. 2009). The last objective of the thesis is to evaluate Qnet, and its four components produced by the latest CMIP6 climate models and estimate their projected change and response to climate change.

### 1.4.3 Thesis main scientific questions

Following the above objectives, the primary scientific questions we aim to address include the following:

1. How do ocean surface anomalies, particularly SST anomalies related to ENSO and ENSO Modoki events, impact precipitation, temperature, and circulation in the SEA region?
2. Can we establish a methodology to build benchmark estimates of SEA air-sea heat flux over periods of interest, that can serve as a reference for assessing the uncertainty and errors in heat flux estimates from various observational and numerical products?
3. How do the latest CMIP6 climate models estimate surface heat fluxes in the SEA region and simulate the response of heat fluxes to climate change?

### 1.4.4 Thesis structure

The chapters of this thesis correspond to the main research questions detailed above.

## **Chapter 1. Introduction**

### **Chapter 2. Impacts of ENSO and ENSO Modoki on rainfall variability**

Chapter 2 investigates the distinct impacts of the two types of ENSO, conventional ENSO and ENSO Modoki, on rainfall variability in the SEA region. It also assesses the mechanism responsible for these rainfall variations via an analysis of moisture transport and circulation during these events.

### **Chapter 3. Quantifying air-sea heat fluxes over Southeast Asia: intercomparison of available datasets and sensitivity ocean simulations**

In this chapter, a series of simulations were first carried out using the SYMPHONIE ocean model to assess the sensitivity of simulated SST to prescribed heat flux values and establish a benchmark value of heat flux over the SEA region for the studied period. Values provided by this method were then used to evaluate heat fluxes from other widely distributed products.

### **Chapter 4. CMIP6 analysis: heat fluxes estimation and the role of the climate change**

Chapter 4 first presents the assessment of the representation of air-sea heat fluxes, i.e.  $Q_{net}$  and its four components, over SEA in an ensemble of CMIP6 models, in terms of regional climatological estimates, spatial patterns, seasonal cycles, and future trends. Second, we study the projected changes in air-sea heat fluxes over SEA in simulations from those CMIP6 models for 3 scenarios. In particular, we investigate the relationship between SST and heat flux components and their changes.



# Chapter 2. Impacts of ENSO and ENSO Modoki on rainfall variability

## Contents

Article summary.....	44
2.1 Introduction.....	46
2.2 Study domain, data, and method.....	48
2.2.1 Study domain.....	48
2.2.2 Data.....	49
2.2.3 Method.....	49
2.3 The two types of ENSO and associated rainfall .....	52
2.3.1 EOF analysis.....	52
2.3.2 Rainfall variations in ENSO and ENSO Modoki events .....	54
2.3.2.1 Relationship between SST and rainfall over SEA .....	54
2.3.2.2 Rainfall anomaly patterns .....	56
2.3.2.3 Rainfall anomaly averaged over the 20 SEA sub-regions.....	58
2.4 Possible mechanisms responsible for the rainfall variations .....	61
2.4.1 Vertically Integrated Moisture Flux .....	61
2.4.2 Associated circulation cells .....	63
2.5 Chapter’s conclusions .....	68

## Chapter 2. Impacts of ENSO and ENSO Modoki on rainfall variability

The study of the influence of the ENSO and ENSO Modoki was the subject of an article published in the *Climate Dynamics* journal (Nguyen-Thanh et al., 2023). This chapter consists of a summary of this article, then of the article itself.

### Article summary

The El Niño Southern Oscillation (ENSO) is an important climate phenomenon that affects precipitation patterns across Southeast Asia (SEA) through atmospheric teleconnections. A distinction is made between the canonical ENSO and a more recently discovered type of ENSO, ENSO Modoki. Besides, to date, the impact of ENSO Modoki on rainfall in SEA has not been fully investigated. Therefore, this study aims to use up-to-date datasets to assess the impacts of ENSO and ENSO Modoki on rainfall variability over SEA and its sub-regions. We focus particularly on the distinct impacts of Modoki events compared to conventional ENSO and on the associated circulation mechanisms.

We analyze the impacts of ENSO and ENSO Modoki on rainfall in both December - January - February (DJF) and June - July - August (JJA), which are the main rainy seasons over the southeastern part and the northern part of SEA, respectively. For that, rainfall dataset obtained from the Global Precipitation Climatology Centre (GPCC) and circulation variables from the European Center for Medium-Range Weather Forecasts (ECMWF) Reanalysis version 5 (ERA5) dataset were used. The vertically integrated moisture flux (VIMF) and velocity potential were estimated based on monthly mean values computed from ECMWF reanalysis dataset to analyze the possible physical mechanisms associated with the two types of ENSO. The monthly SST data from the Hadley Centre Global Sea Ice and Sea Surface Temperature (HadISST) was used to identify ENSO and ENSO Modoki events. For the period 1979–2019, seven El Niño (EN), six La Niña (LN), five El Niño Modoki (EM), and five La Niña Modoki (LM) events were identified.

In the boreal summer (JJA) and winter (DJF) of EN events, rainfall reduction occurs over the Maritime Continent and the Philippines except for West Philippines in JJA and West Kalimantan in DJF. Similar patterns but with enhanced drier/wetter conditions are detected during EM.

During LN, rainfall increases in most sub-regions except for West Philippines and parts of mainland Indochina in JJA and in DJF in some southern areas such as South Sumatra, West Kalimantan, and Papua. Compared to LN, LM generally exhibits less wet/drier conditions in

## Chapter 2. Impacts of ENSO and ENSO Modoki on rainfall variability

JJA over most sub-regions and wetter conditions in DJF over a major part of the Maritime Continent.

The decrease (increase) in rainfall over SEA during Modoki events compared to the canonical ENSO events is explained by a reduced (enhanced) moisture transport into the region and a weakening (strengthening) of the ascending branch of the Walker circulation. For instance, under EN, the negative anomalies of the ascending branch of the Walker circulation are located over the southwest and southeast of SEA in JJA and DJF, respectively, thus suppressing rainfall and leading to drier conditions in the region. The negative anomalies of the ascending branch are weaker under EM, resulting in a weaker rainfall reduction compared to EN over the Philippines and Papua during JJA and over the southwestern SEA during DJF. The LM rainfall deficit compared to LN in JJA comes from a shortage of moisture transport into the north of SEA and from the strong anomalous convergence at the upper level that leads to a weakening of the ascending motion beneath, hence rainfall suppression. Meanwhile, the LM rainfall increase compared to LN in DJF in the southern subregions is attributed to more enhanced moisture transport by the Pacific easterlies and the equatorial westerlies into the region, hence the rainfall surplus. This study was the subject of an article published in the *Climate Dynamics* journal ([Nguyen-Thanh et al., 2023](#)).

### PUBLISHED ARTICLE CLIMATE DYNAMIC

doi: <https://doi.org/10.1007/s00382-023-06673-2>

**The distinct impacts of the two types of ENSO on rainfall variability over Southeast Asia**

**Authors: Hue Nguyen-Thanh, Thanh Ngo-Duc, Marine Herrmann**

#### 2.1 Introduction

The El Niño Southern Oscillation (ENSO) is one of the most important climate phenomena that affect temperature and precipitation patterns across the globe via atmospheric teleconnections (Trenberth et al. 1998; Deser et al. 2017; Timmermann et al. 2018). Many studies focused on ENSO to predict its onset or investigate its impacts on weather and climate (Wang et al. 2011; Yan et al. 2020; Huang and Xie 2015). More recently, a new type of tropical Pacific Sea surface temperature (SST) warming pattern, with maximum warm anomalies in the central equatorial Pacific and cooler conditions in the eastern and western parts, has been discussed widely (Ashok et al. 2007; Weng et al. 2007; Marathe et al. 2015). This phenomenon differs from the canonical El Niño, which refers to anomalous warmings in the eastern equatorial Pacific (Rasmusson and Carpenter 1983). The new type of SST warming patterns was alternatively referred to as dateline El Niño (Larkin and Harrison 2005), central Pacific El Niño (Kao and Yu 2009), warm pool El Niño (Kug et al. 2009), or El Niño Modoki (Ashok et al. 2007; Weng et al. 2007, 2009). The opposite phase, with a cold sea surface temperature anomaly (SSTA) occurring in the central equatorial Pacific and warm SSTA in the eastern and western parts, is called La Niña Modoki (Ashok et al. 2007; Shinoda et al. 2011). Hereinafter, we use the terms El Niño Modoki (EM) and La Niña Modoki (LM) for the new types of SST warming and cooling patterns to differentiate them from the canonical El Niño (EN) and La Niña (LN). EN and EM have different impacts on the spatial patterns of atmospheric and ocean variables (Kug et al. 2009). Those different impacts, particularly on precipitation, were investigated in numerous previous studies. EN events are generally associated with a reduction of rainfall over the western Pacific from the Philippines to West Australia, while a large area from the center to the eastern Pacific receives excess rainfall (Trenberth et al. 1998; McPhaden et al. 2006). Indeed, Ashok (2007) showed that during EM winters, the eastern Pacific experienced below-average rainfall. Moreover, the Philippines, South Thailand, and South India, along with some parts of North India, Sri Lanka, and East Africa, experienced abnormally dry conditions, whereas New Zealand, Pakistan, and Kazakhstan received excess

## Chapter 2. Impacts of ENSO and ENSO Modoki on rainfall variability

rainfall.

Southeast Asia (SEA) comprises islands and the mainland of eleven countries: Cambodia, Laos, Vietnam, Thailand, Brunei, Philippines, Myanmar, Timor-Leste, Indonesia, Singapore, and Malaysia (Fig. 1). It has a tropical marine climate with high temperatures and abundant precipitation and is affected by monsoons (Räsänen et al. 2016; Tangang et al. 2020). Both rainfall and temperature display strong seasonality over most of SEA (Juneng and Tangang 2005; Phan et al. 2009; Juneng et al. 2016; Cruz et al. 2017; Alsepan and Minobe 2020). The rainfall season in the northern part of SEA, i.e., the Indochina peninsula and West Philippines, occurs mostly in the boreal summer (Matsumoto 1997; Francisco et al. 2006; Juneng et al. 2016; Tangang et al. 2020) while it mainly occurs in the boreal winter in the southern part and some specific locations of SEA, such as the Maritime Continent and East Philippines (Aldrian and Susanto 2003; Juneng et al. 2007; Juneng et al. 2016). The rainfall variations in SEA depend strongly on ENSO (Page et al. 2002; Wang et al. 2000; Hendon 2003; Wu et al. 2003; Juneng and Tangang 2005; Nguyen-Thi et al. 2012; Alsepan and Minobe 2020).

To date, the impact of ENSO Modoki on rainfall in SEA has not been fully addressed. Feng et al. (2010) studied the impact of EM on boreal winter rainfall in SEA for the period 1979–2008 using a coarse resolution dataset of 2.5°. They showed a negative rainfall anomaly during EM; however, the coarse resolution dataset they used did not allow an adequate representation of the heterogeneity of the rainfall pattern over the region. Salimun et al. (2013) also indicated the boreal winter rainfall deficit during EM, but their study domain was limited to Malaysia and the period 1950–2009. Alsepan and Minobe (2020) showed that EM conversely increases precipitation in West Indonesia in the wet season (November–April) compared to EN, but again, their study was limited to Indonesia and the period 1960–2007. The above studies moreover focused only on the impact of EM and not of LM. Feng et al. (2010) and Salimun et al. (2013) analyzed rainfall during boreal winter only. Last, the impact on rainfall during boreal summer has only been studied for the surrounding regions of SEA such as South China (Karori et al. 2013) and/or the Pacific rim (Weng et al. 2007) and not for the entire SEA region.

Besides the gaps highlighted above, more up-to-date datasets are now available, motivating the need to revisit or newly assess the impacts of ENSO and ENSO Modoki on rainfall variability over this landmass and its sub-regions. Moreover, we aim to explore the role of associated circulation conditions for the two types of ENSO in both boreal summer and winter months based on up-to-date reanalysis datasets. To sum up, our aim in this study is to use up-to-date datasets to assess the impacts of ENSO and ENSO Modoki on rainfall variability over

## Chapter 2. Impacts of ENSO and ENSO Modoki on rainfall variability

SEA and all its sub-regions. We focus particularly on the distinct impacts of Modoki events compared with conventional ENSO and on the associated circulation mechanisms. This paper is composed of four sections. The study domain, datasets, and methods of analysis are described in section 2.2. We analyze our results in Section 2.3, where we examine with the most recent available data the impact of ENSO/ENSO Modoki on rainfall variability in different SEA sub-regions over a 41-year period (1979–2019). Section 2.4 investigates possible physical mechanisms responsible for the rainfall variations over the region. Conclusions are presented in Section 2.5.

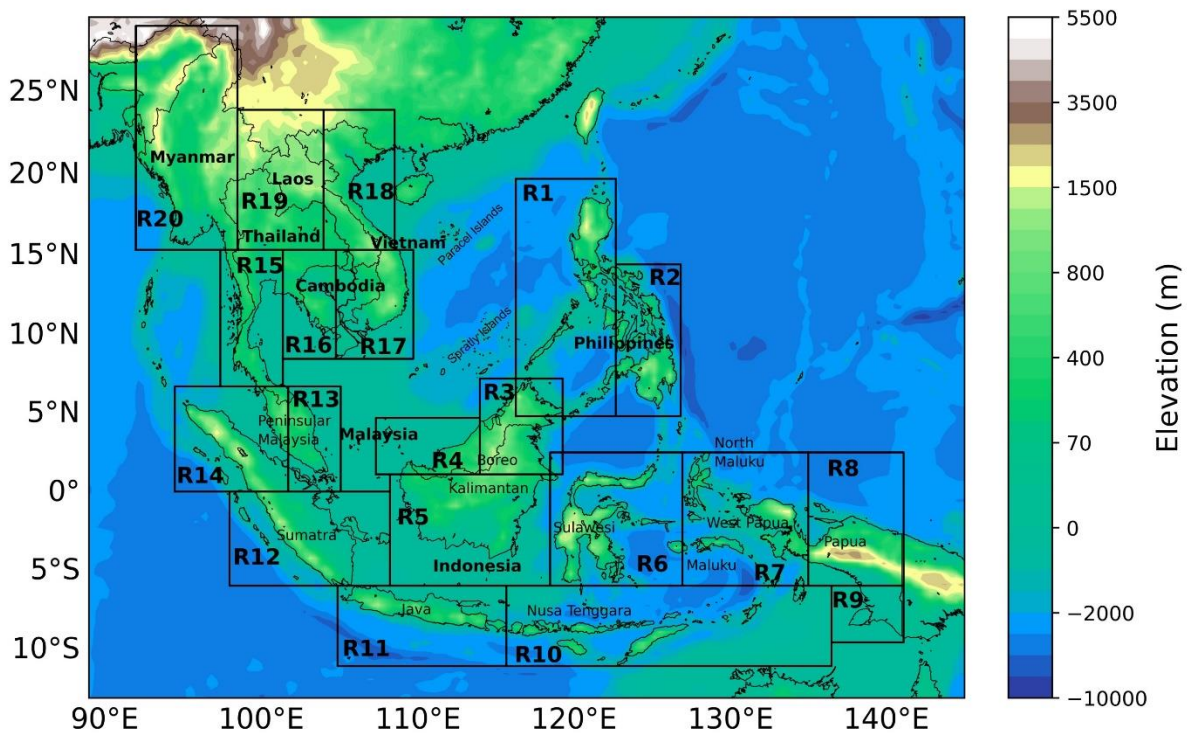


**Figure 2.1.** The Southeast Asia domain and its 20 sub-regions were used for the assessment (delineated by black boxes). Topography over SEA (shaded) is obtained from the Global 30 Arc-Second Elevation (GTOPO30) data set.

### 2.2 Study domain, data, and method

#### 2.2.1 Study domain

Figure 2.1 displays the SEA study domain and its 20 sub-regions defined by Juneng et al. (2016) under the framework of the Southeast Asia Regional Climate Downscaling/Coordinated Regional Climate Downscaling Experiment- Southeast Asia (SEACLID/CORDEX-SEA)

## Chapter 2. Impacts of ENSO and ENSO Modoki on rainfall variability

project (Tangang et al. 2020). These 20 sub-regions were identified based on previous studies focusing on rainfall characteristics in SEA (Aldrian and Susanto 2003; Juneng and Tangang 2005; Francisco et al. 2006; Juneng et al. 2007; Chokngamwong and Chiu 2008; Nguyen-Thi et al. 2012; Salimun et al. 2013). In the following, the impacts of the two types of ENSO on rainfall will be examined over the whole SEA area as well as over these sub-regions.

### 2.2.2 Data

To identify ENSO and ENSO Modoki events, we used monthly SST data from the Hadley Centre Global Sea Ice and Sea Surface Temperature (HadISST) (Rayner et al. 2003). This dataset has a spatial resolution of  $1^{\circ} \times 1^{\circ}$  and covers the period 1979–2019.

The rainfall dataset is obtained from the Global Precipitation Climatology Centre (GPCC) version 2020 (Rudolf et al. 1994). Here we used the monthly land dataset for the period 1979–2019 at a resolution of  $0.25^{\circ} \times 0.25^{\circ}$ .

To analyze the possible physical mechanisms explaining the impacts of the two types of ENSO on rainfall in SEA, the European Center for Medium-Range Weather Forecasts (ECMWF) Reanalysis version 5 (ERA5) dataset (Hersbach et al. 2020) was used. The ERA5 data used in this study has a horizontal resolution of  $0.25^{\circ} \times 0.25^{\circ}$ . The variables include specific humidity ( $q$ ), meridional wind ( $v$ ), zonal wind ( $u$ ), and vertical velocity ( $\omega$ ), which are provided on 23 pressure levels between 1000 hPa and 200 hPa, and the vertical integral of moisture flux divergence ( $\text{div}$ ).

Furthermore, to examine the sensibility of the obtained results to the choice of datasets, we also perform the analysis with other rainfall and reanalysis datasets, including the Climate Research Unit (CRU) rainfall data (version TS v. 4.05; Harris et al. 2020), and the National Centers for Environmental Prediction (NCEP)/National Center for Atmospheric Research (NCAR) Reanalysis-1 (hereafter called NCEP1; Kalnay et al. 1996) data. The horizontal resolutions of the CRU and NCEP1 are  $0.5^{\circ} \times 0.5^{\circ}$  and  $2.0^{\circ} \times 2.0^{\circ}$ , respectively. They all cover the study period 1979–2019.

### 2.2.3 Method

In this study, an EN (LN) event is identified when the normalized 3-month running mean of the SST anomalies (SSTAs) in the Niño3 region ( $5^{\circ}\text{S}$ – $5^{\circ}\text{N}$ ,  $150^{\circ}\text{W}$ – $90^{\circ}\text{W}$ ; Fig. 2.2a)

## Chapter 2. Impacts of ENSO and ENSO Modoki on rainfall variability

exceeds  $0.5^{\circ}\text{C}$  (is lower than  $-0.5^{\circ}\text{C}$ ) for at least five consecutive months, as implemented in previous studies (e.g. Trenberth 1997; Yeh et al. 2009; Shukla et al. 2011). An ENSO event usually begins in boreal summer, peaks in boreal winter, and decays in the following spring (Rasmusons and Carpenter 1982; An and Wang 2001; Chen and Jin 2020). For a year (denoted as Year0) where an EN or LN event is detected in the boreal winter months, the seasonal rainfall averages of that ENSO event are thus computed for four seasons: June-July-August (JJA) of YEAR0, September-October-November (SON) of YEAR0, December-January-February (DJF) with December of YEAR0 and January-February of the following year (denoted as YEAR+1), and March-April-May (MAM) of YEAR+1.

To identify ENSO Modoki events, we use the El Niño Modoki index (EMI) defined by Ashok et al. (2007) and used in previous studies (e.g., Weng et al. 2009; Yu et al. 2012, 2013):

$$\text{EMI} = [\text{SSTA}]_A - 0.5 \times [\text{SSTA}]_B - 0.5 \times [\text{SSTA}]_C \quad (\text{Eq. 2.1})$$

Brackets in Eq. 2.1 represent the area average over the central Pacific region A ( $10^{\circ}\text{S}$ – $10^{\circ}\text{N}$ ,  $165^{\circ}\text{E}$ – $140^{\circ}\text{W}$ ), the Eastern Pacific region B ( $15^{\circ}\text{S}$ – $5^{\circ}\text{N}$ ,  $110^{\circ}$ – $70^{\circ}\text{W}$ ), and the Western Pacific region C ( $10^{\circ}\text{S}$ – $20^{\circ}\text{N}$ ,  $125^{\circ}$ – $145^{\circ}\text{E}$ ), as shown in Fig. 2.2b. An EM (LM) event is identified when the normalized 3-month running mean of the EMI is larger than  $0.7 \times \sigma$  (smaller than  $-0.7 \times \sigma$ ), where  $\sigma$  is the standard deviation of the EMI, for at least five consecutive months. Similar to ENSO, for a year where an EM or LM event is detected in the boreal winter months, the seasonal rainfall averages of that ENSO Modoki event are computed for the four seasons JJA, SON, DJF, and MAM.

Previous studies for the SEA region focused on the EM impacts on DJF rainfall (Feng et al. 2010; Salimun et al. 2013). In this study, we analyze the ENSO and ENSO Modoki impacts on rainfall in both DJF and JJA, which are mainly the rainy seasons over the southeastern part (subregions R2–14 shown in Fig. 2.1) and the northern part (subregions R1, R15–20) of SEA, respectively. To avoid repetitive texts and figures, the impacts on SON and MAM rainfall are displayed in supplemental figures (Fig. 2.A2, Fig. 2.A3).

To quantify the impact of the two types of ENSO on seasonal rainfall, e.g., the impact of EM on DJF rainfall, we compute the difference between the average of DJF rainfall for all EM years (5 years, see Table 2.1) and the average of DJF rainfall for all neutral years (16 years, see Table 2.1). For simplicity, the term “anomaly” used in the text corresponds to this difference. Previous studies did not compute the DJF rainfall of the neutral years but computed the climatological DJF rainfall, i.e., the average DJF rainfall for the whole study period. The

## Chapter 2. Impacts of ENSO and ENSO Modoki on rainfall variability

drawback of using the climatological values is that they might be influenced by the dominant signal of one of the four ENSO or ENSO Modoki modes, which was the most active during the study period. Indeed, over the study period of 1979–2019, the difference between the neutral values and the climatological values of rainfall (Fig. 2.A1) displays similar patterns as the difference between the EN/EM values and the neutral values, particularly in DJF over the whole domain and in JJA over the Indochinese Peninsula (cf. Fig. 2.4). Moreover, with the choice of neutral years, we can estimate the significant level of the impacts by using the bootstrapping technique detailed by Efron and Tibshirani (1993). 1000 bootstrap replications of size  $n_{EM}=5$  ( $n_{EN}=7$ ,  $n_{LM}=5$ ,  $n_{LN}=6$ , see Table 2.1) and  $n_{neutral\ years}=16$  is generated to estimate the difference between EM (EN, LM, LN) and the neutral years.

To analyze the possible physical mechanisms associated with the two types of ENSO, the vertically integrated moisture flux (VIMF) and velocity potential were estimated based on monthly mean values computed from the reanalysis dataset.

The VIMF  $\vec{Q}$  (units:  $\text{kg m}^{-1} \text{s}^{-1}$ ) was calculated by:

$$\vec{Q} = -\frac{1}{g} \int_{p_s}^{p_t} q \vec{V} dp \quad (\text{Eq. 2.2})$$

where  $g$  is the gravity acceleration ( $9.8 \text{ m s}^{-2}$ ),  $q$  the specific humidity,  $\vec{V}$  the horizontal wind vector,  $p_s$  the surface pressure, and  $p_t$  the pressure at the top of the atmosphere. Since most of the water vapor in the atmosphere is located below 200 hPa (Li et al. 2011) and the specific humidity above 200 hPa has a minimal effect on the VIMF (Kalnay et al. 1996; Fasullo and Webster 2003), the VIMF in this study was calculated with the pressure data from the surface to the 200 hPa level. We have also computed the VIMF for the whole atmospheric column by integrating the data from the surface to the 01 hPa level and obtained almost identical results with those below the 200 hPa level (not shown).

The potential velocity scalars were estimated by decomposing the horizontal wind into the rotational and divergent components according to the Helmholtz theorem (Helmholtz 1867). Finally, vertical velocity ( $\omega$ ) from 1000 to 200 hPa were used to describe the intensity and spatial extent of the convection processes in the region. Negative (positive) vertical velocity anomalies denote ascending (descending) vertical motion enhancements.

### 2.3 The two types of ENSO and associated rainfall

#### 2.3.1 EOF analysis

The purpose of this section is to re-examine the ENSO and ENSO Modoki patterns and identify the months in which those events occurred during the period 1979–2019 in order to confirm and update previous findings (e.g., [Ashok et al. 2007](#)) with more recent SST data.

An empirical orthogonal function (EOF) analysis was performed on the monthly mean SSTA over the domain of 100°E–80°W, 30°S–30°N to obtain the principal modes of SST variability over the tropical Pacific and to distinguish the two types of EN events. The first EOF mode (EOF1) corresponds to the EN pattern. It is characterized by a strong anomalous warming in the central-eastern equatorial Pacific and an anomalous cooling in the western tropical Pacific ([Fig. 2.2a](#)). This pattern, associated with its principal component (PC1, [Fig. 2.2c](#)), explains about 42% of the tropical Pacific SST variability for the study period 1979–2019. Similarly, [Xu et al. \(2017\)](#) and [Bo and Ren \(2019\)](#) found that 52% and 48% of the SST variability were explained by the EOF1 for the periods 1950–1999 and 1979–2016, respectively. The correlations between the PC1 and the Niño3, Niño3.4, and Niño4 indices reach highly significant values of 0.97, 0.96, and 0.93, respectively ([Fig. 2.2](#)).

The second EOF (EOF2), with an explained variance of 11%, is characterized by a zonal tripole pattern with warmer-than-normal SST in the central equatorial Pacific and colder SST in the eastern and western tropical Pacific ([Fig. 2.2b](#)). It corresponds to the EM patterns. Similarly, [Ashok et al. \(2007\)](#) and [Bo and Ren \(2019\)](#) found that 12% and 11% of the SST variability were explained by the EOF2 for the period 1979–2004 and 1979–2016, respectively. The slight difference between those studies can be attributed to the differences in the analysis periods or the SST data used. The EOF2 of the SSTA pattern, associated with the positive phase of its principal component (PC2, [Fig. 2.2d](#)), is consistent with the EM pattern previously identified ([Ashok et al. 2007](#); [Yu and Kao 2007](#)). The PC2 series correlates well with the EMI, with a correlation value of 0.78 ([Fig. 2.2](#)).

## Chapter 2. Impacts of ENSO and ENSO Modoki on rainfall variability

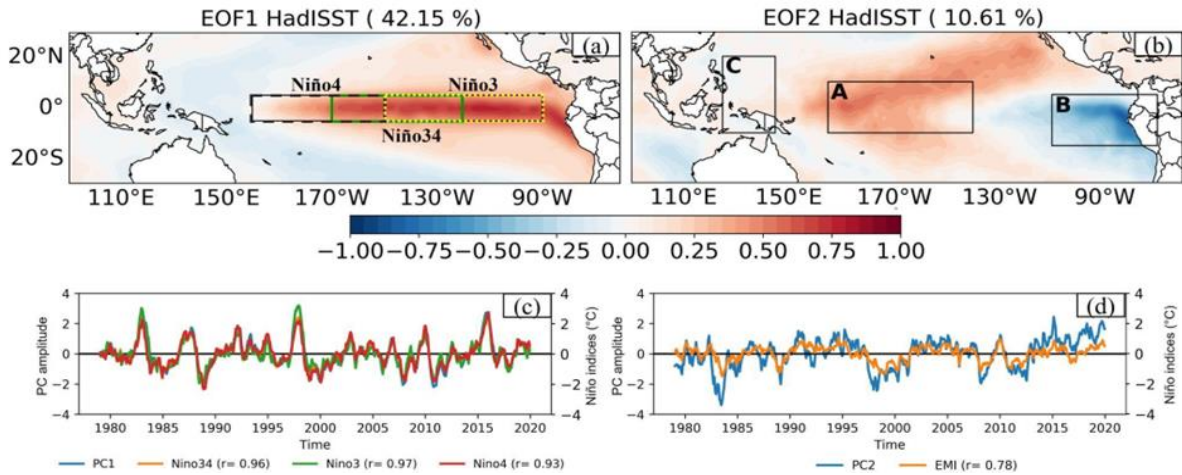


**Figure 2.2.** EOF patterns of the HadISST anomalies (1979–2019) for (a) the 1st mode, corresponding to a typical EN, (b) the 2nd mode, corresponding to a typical EM; and time series of (c) the PC1 and Niño3, Niño3.4, and Niño4 indices, and (d) the PC2 and EMI. Locations of the Niño3 (5°S–5°N, 150°W–90°W), Niño3.4 (5°S–5°N, 170°W–120°W), and Niño4 (5°S–5°N, 160°E–150°W) regions are indicated in (a). Boxes A (10°S–10°N, 165°E–140°W), B (15°S–5°N, 110°–70°W), and C (10°S–20°N, 125°–145°E) in (b) are used for computing the EMI. The numbers in parentheses in (c) and (d) indicate the correlations between the corresponding indices with the PC1 and PC2 series, respectively.

The high correlations between the PC series and the Niño and EMI indices indicate that the first two modes of SSTA over the tropical Pacific, i.e., the ENSO and Modoki patterns, can be well represented by the Niño and EMI indices. Since the correlation between the PC1 and the Niño3 index reaches the highest value of 0.97, the Niño3 index is used in this study to identify canonical ENSO events. Nevertheless, it is worth mentioning that using the Niño3.4 index provides almost identical ENSO years except for the weak El Niño year 1987/1988 that was detected by the Niño3.4 index but not by the Niño3 index (Table 2.A1). There are also minor differences of +/- 1 month in the starting/ending time of some ENSO events if we use the Niño3.4 index instead of the Niño3. Note that the Niño4 region (5°S–5°N, 160°E–150°W) was not chosen for detecting ENSO events in this study because it is more in the central Pacific compared to the Niño3 and Niño3.4 regions, hence it could reflect variations of both Modoki and canonical ENSO events (Weng et al. 2009). The correlations between the Niño4 index and the PC2 and the EMI are 0.21 and 0.60, respectively, reaching the highest values when compared with the results of the Niño3 and Niño3.4 indices.

Using the criteria defined in Section 2.2.3, seven EN, six LN events, five EM and five LM

## Chapter 2. Impacts of ENSO and ENSO Modoki on rainfall variability

events were identified over the study period of 1979–2019 (Table 2.1). 16 years are classified as neutral years (Table 2.1). The ENSO events generally started in the fall (Table 2.A1). However, there were five early-onset events that started from April to June, including the two El Niño events of 04/1982–06/1983 and 05/1997–05/1998, and the three La Niña events of 04/1988–10/1988, 06/1999–03/2000, and 06/2010–05/2011. The timing of these events is confirmed by cross-checking with the historical ENSO episodes provided by the Climate Prediction Center (CPC) of the National Oceanic and Atmospheric Administration (NOAA) (NOAA-CPC, 2022).

Among the 16 neutral years in Table 2.1, 1979/1980 and 1990/1991 were classified as EM years in some previous studies (Feng et al. 2010; Salimun et al. 2013); 1987/1988 was classified as an EN year (Salimun et al. 2013). The differences between those studies and our study can be attributed to the different indices, dataset periods, or thresholds used to detect those three-weak EN and EM events. We have conducted an additional analysis (not shown) that considers 1979/1980 and 1990/1991 as EM years and 1987/1988 as EN years. This analysis confirms that the results shown in the following subsections stay robust regardless of the classification of those three years.

### 2.3.2 Rainfall variations in ENSO and ENSO Modoki events

#### 2.3.2.1 Relationship between SST and rainfall over SEA

To examine and confirm the relationship between SST and rainfall over SEA, we compute the correlation coefficient between Niño-3 and EMI indices and monthly rainfall anomalies, using 3-month running averages of each dataset (Fig. 2.3). The annual cycle was removed from the time series before computing the correlations.

Figure 2.3a shows significant negative correlations between monthly rainfall anomalies and the Niño-3 index over all SEA subregions, with values varying from -0.5 to -0.2. In the areas of South Philippines (R2), East Borneo (R3), Maluku, and West Papua (R7), the correlation between rainfall and the Niño-3 index reaches the largest value of -0.45, while it is positive in Southeast China (0.5). The negative correlation pattern implies that a warm (cold) SST in the Niño-3 region, corresponding to an EN (LN) phase, leads to a decrease (increase) in rainfall over SEA. Similar results were shown in the study of Hendrawan et al. (2019): an increase in SST leads to a decrease in rainfall over the Indonesian region (R5–12, R14). Harger (1995) also showed that EN events are generally associated with decreased rainfall over the

## Chapter 2. Impacts of ENSO and ENSO Modoki on rainfall variability

Philippines and Indonesia.

**Table 2.1.** List of EN, LN, EM, LM, and neutral years over the period of 1979–2019. The number in parentheses indicates the total number of years for each type of event.

EN (7)	LN (6)	EM (5)	LM (5)	Neutral (16)
1982/1983	1984/1985	1991/1992	1983/1984	1979/1980
1986/1987	1995/1996	1994/1995	1988/1989	1980/1981
1997/1998	1999/2000	2002/2003	1998/1999	1981/1982
2006/2007	2007/2008	2004/2005	2008/2009	1985/1986
2014/2015	2010/2011	2009/2010	2011/2012	1987/1988
2015/2016	2017/2018			1990/1991
2018/2019				1992/1993
				1993/1994
				1996/1997
				2000/2001
				2001/2002
				2003/2004
				2005/2006
				2012/2013
				2013/2014
				2016/2017

The correlation coefficient between rainfall anomalies and the EMI is also negative in most of SEA, with absolute values usually less than 0.35 (Fig. 2.3b). Those correlations are weaker and less significant than correlations with Niño-3, and areas with correlation reaching statistical significance are also smaller. The correlation is insignificant in North Laos (R18–19), North Vietnam (R18), Myanmar (R20), and South Sumatra (R12). The correlation coefficient is significantly positive in the central part of the southeastern China region, while the remaining southern areas have small correlation values that do not reach the significance level ( $|r| < 0.2$ ). Overall, the correlation between the average rainfall over the entire SEA and the Niño-3 and the EMI is 0.66 and 0.60, respectively.

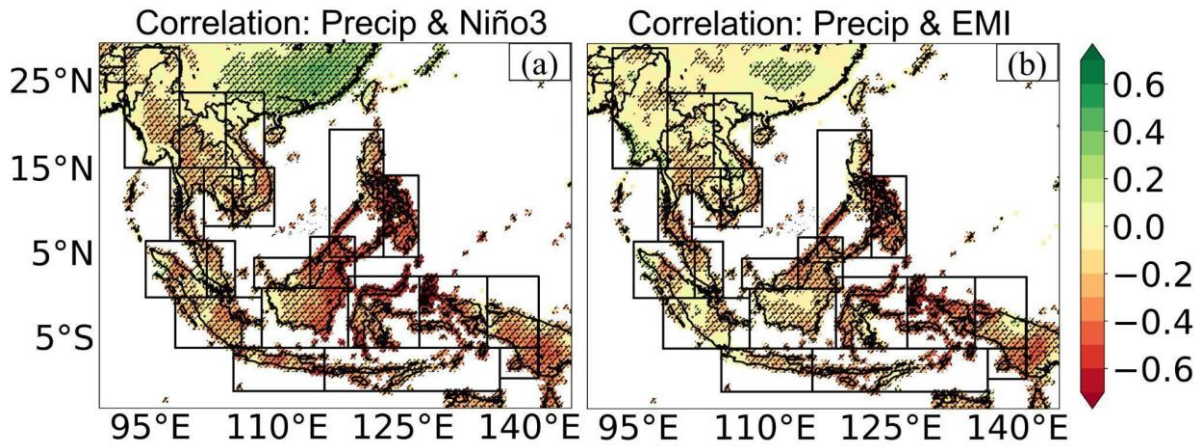


**Figure 2.3.** Spatial distribution of correlations between monthly rainfall anomalies and (a) the Niño-3 index and (b) the EMI. The dot pattern indicates areas where the correlations are statistically significant at 90% based on the student's t-test.

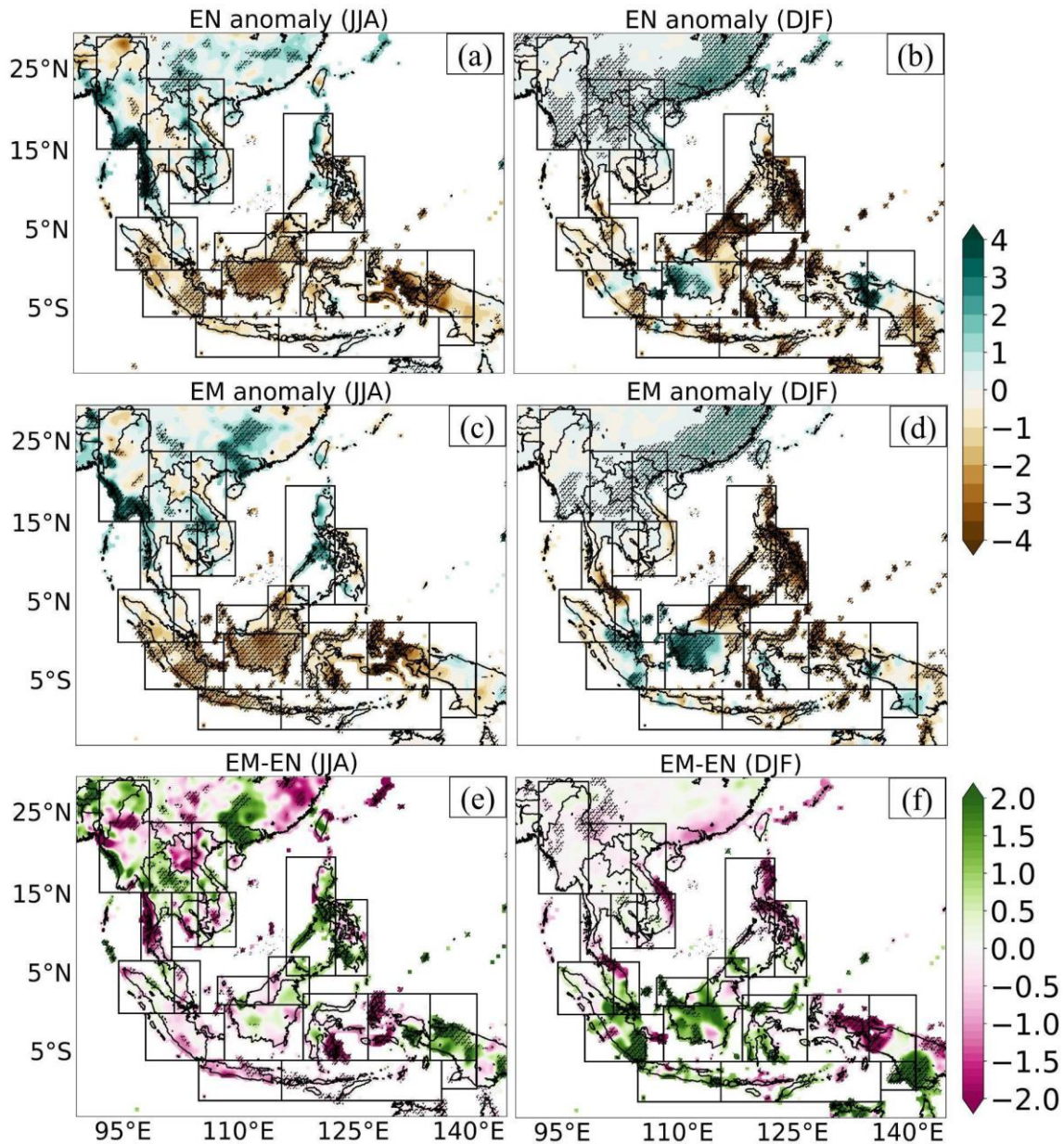
### 2.3.2.2 Rainfall anomaly patterns

Figure 2.4 displays the spatial distribution over the SEA domain of the JJA and DJF composites of rainfall anomalies for the EN and EM years and the differences between them, i.e., EM minus EN. Rainfall reduction occurs throughout most sub-regions from 5°N southward (R3–13) and Southeast Philippines (R2) in JJA of EN events (Fig. 2.4a). A significant rainfall reduction of about 2–3.5 mm/day is observed over Kalimantan (R5), Maluku and West Papua (R7), Java (R11), and South Sumatra (R12). However, the EN impacts on JJA rainfall over the Indochinese Peninsula (R16–20) are insignificant, with alternating drier and wetter conditions from -1 to 1 mm/day. In DJF of EN events, while larger rainfall reduction compared to JJA is seen over Southeast Philippines (R2), East Borneo (R3), and Maluku (R7), there is a significant rainfall enhancement of about 1–3 mm/day over West Kalimantan (R5) and part of the Indochinese Peninsula (R18–R20) (Fig. 2.4b). The rainfall reduction during EN identified here is in agreement with previous findings in the region, e.g., Salimun et al. (2013) for Peninsular Malaysia and North Borneo, and Juneng and Tangang (2005) for Southeast Asia. Besides, although the Southeast China region is outside the study area, it is noteworthy to mention that the rainfall increase (~1–2.5 mm/day) over this area during EN conditions is consistent with previous studies (Feng and Hu 2004; Xue and Liu 2008; Karori et al. 2013).

The general anomaly patterns of EM (Fig. 2.4c, d) are very similar to those of EN (Fig. 2.4a, b) for both JJA and DJF. However, the anomaly magnitudes are not the same (Fig. 2.4e,

## Chapter 2. Impacts of ENSO and ENSO Modoki on rainfall variability

f). Generally, EM shows enhanced drier/wetter conditions compared to EN. In JJA, EM produces more rainfall than EN does in the eastern side of the domain and less rainfall in the southwestern part. The opposite is found in DJF, i.e., EM produces less rainfall than EN does in the eastern side and more rainfall in the southwestern part. In Section 2.4, we will discuss the mechanism of these systematic seasonal differences.



**Figure 2.4.** Composites of JJA and DJF rainfall anomalies (units: mm/day) for (a, b) EN, (c, d) EM, and (e, f) the differences between EN and EM. The dot pattern indicates areas where differences are statistically significant at 90% based on the bootstrap test.

Rainfall increase occurs throughout most sub-regions in JJA of LN events except for West

## Chapter 2. Impacts of ENSO and ENSO Modoki on rainfall variability

Philippines and some specific locations in the Indochinese Peninsula where the rainfall reduction is usually not statistically significant (Fig. 2.5a). Significant rainfall increases of about 2–3.5 mm/day are observed during LN over Borneo (R4), Kalimantan (R5), Sulawesi (R6), and Maluku and West Papua (R7). Similar to EN, the LN impacts on JJA rainfall over the Indochinese Peninsula (R16–20) are not homogeneously significant, with alternating drier and wetter conditions from -1 to 1 mm/day (Fig. 2.5a). In DJF of LN events, while larger rainfall compared to JJA is seen over southeastern Philippines (R2), there is a rainfall depletion of about 1–1.5 mm/day over some areas in the southern part of SEA, such as South Sumatra (R12), West Kalimantan (R5), and Papua (R8) (Fig. 2.5b). The rainfall increase over the western part of Indochina in the dry months DJF during LN is statistically significant although the increased amount is relatively small (less than 0.5 mm/day).

The main anomaly patterns of LM (Fig. 2.5c, d) are similar to those of LN (Fig. 2.5a, b). For JJA, LM also displays increased rainfall over the Maritime Continent and North Thailand, and reduced rainfall over West Philippines (Fig. 2.5c). For DJF, LM exhibits increased rainfall over the northern Maritime Continent and the Philippines, while showing alternating drier and wetter conditions over the Indochinese Peninsula and the southern rim of the SEA domain. Nevertheless, the anomaly magnitudes are not the same (Fig. 2.5e, f). In JJA, LM generally shows less wet/drier conditions than LN, particularly in Central Vietnam (R17–18) and the coastal regions of Myanmar (R15 and R20) (Fig. 2.5e). Some exceptions can be found over some specific locations such as Southeast Philippines (R2) and North Sumatra (R14) where LM produces more rainfall compared to LN. In DJF, compared to LN, LM exhibits more rainfall over a major part of the Maritime Continent while generally displaying less rainfall over Indochina (R15–20), Southeast Philippines (R2), and part of Sulawesi (R6).

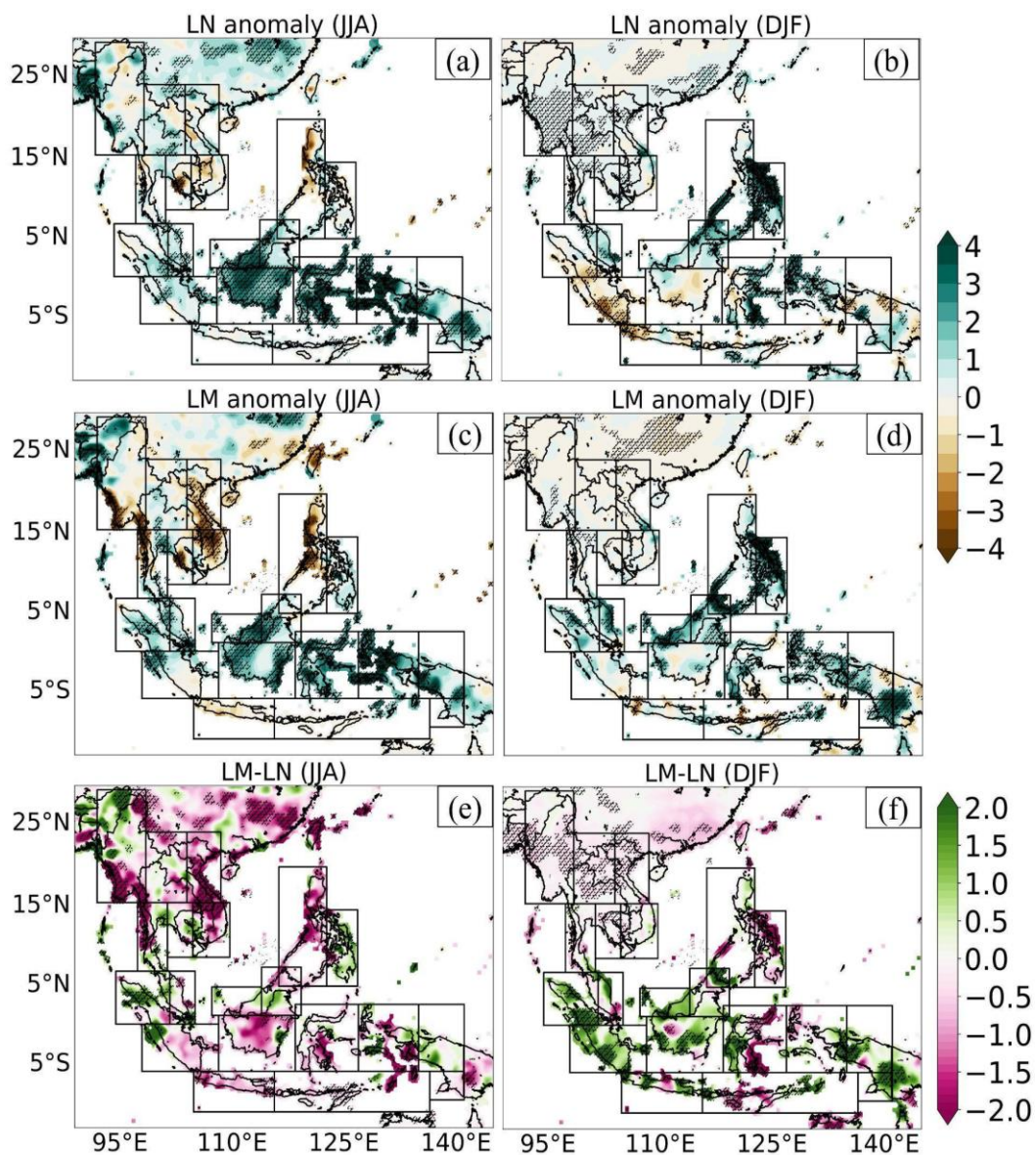
### *2.3.2.3 Rainfall anomaly averaged over the 20 SEA sub-regions.*

Figure 2.6 summarizes the detailed changes in rainfall over the 20 SEA sub-regions. As seen above, rainfall in JJA in the eastern rim of SEA (i.e., R1, R2, R8, and R18) is less reduced during EM compared to EN, while the remaining subregions generally experience more rainfall reduction during EM (Fig. 2.6a, b). In contrast, less rainfall in the eastern rim and more rainfall in the southern subregions (R4–6, R9–14) is obtained in DJF of EM compared to EN. The highest rainfall deficit during EN occurs in R2–3 in DJF (~2.5 mm/day) and in R7 in JJA (~2 mm/day) and can lead to significant drought conditions over these areas (Saji et al. 1999; Webster et al. 1999; D'Arrigo and Smerdon 2008; Lestari et al. 2016). Droughts during EM

## Chapter 2. Impacts of ENSO and ENSO Modoki on rainfall variability

are thus expected to be less severe than during EN in almost all subregions, except for some parts of Indonesia (R6–7, R10–R12) during JJA.

During LN, the largest rainfall increase occurs over the east of the Philippines (R2) in DJF and part of Indonesia (R5–7) in JJA, with a rainfall increase exceeding 2.5–3 mm/day on average (Fig. 2.5c, d). In JJA, LM shows drier characteristics than LN for almost all subregions as also indicated in Fig 2.4e. In DJF, LM generally exhibits more rainfall than LN over subregions R3–14, i.e., over the Maritime Continent. LN could induce severe floods in the region in DJF (Tangang et al 2017), that could thus be worsened in LM.



**Figure 2.5.** As in Fig. 2.4 but for LN and LM.

## Chapter 2. Impacts of ENSO and ENSO Modoki on rainfall variability

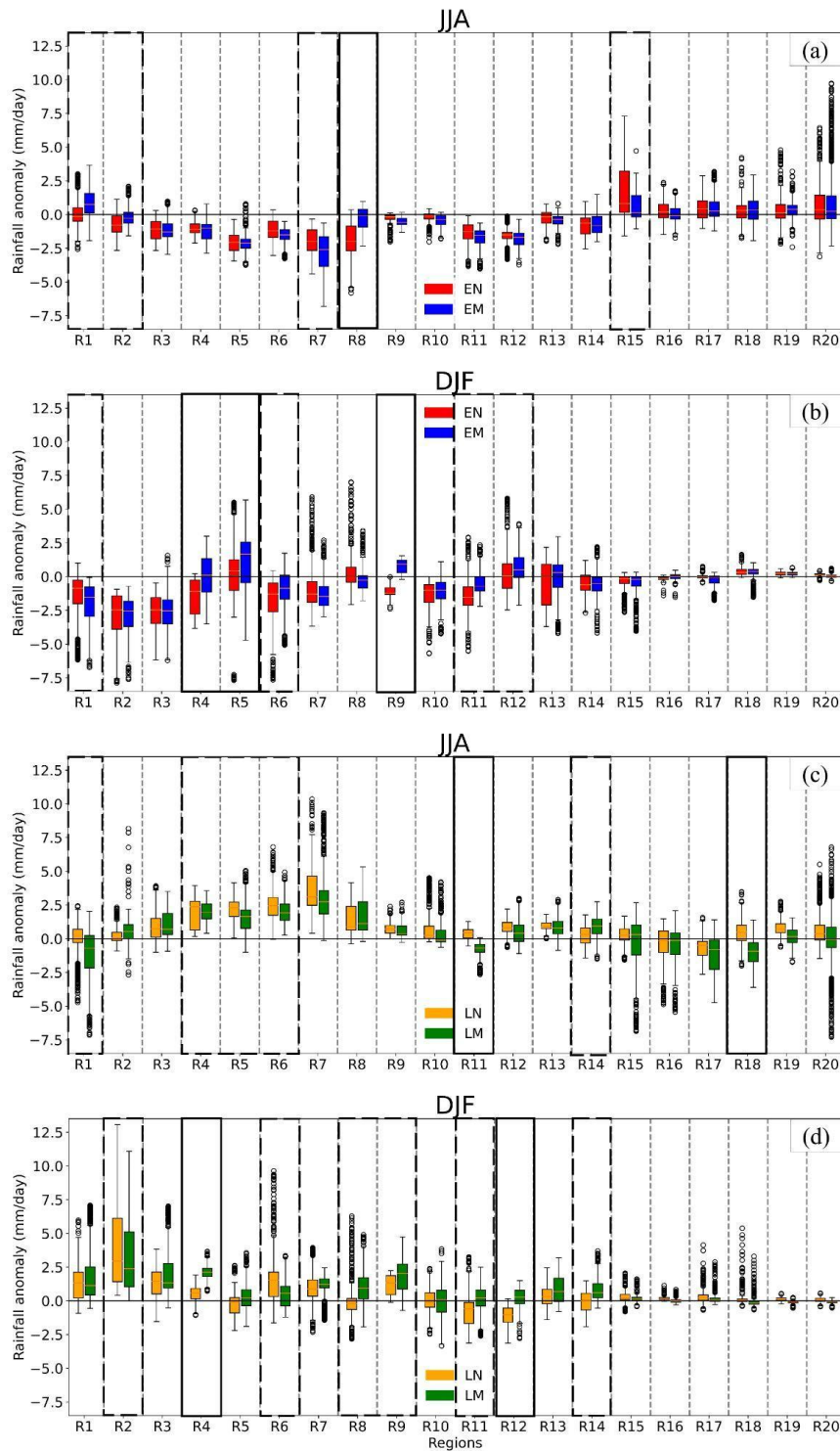


**Figure 2.6.** Box plots of average JJA and DJF rainfall anomaly over 20 sub-regions for (a, b) EN (red) and EM (blue), (c, d) LN (yellow) and LM (green). Units in mm/day. The subregions where the differences between EN and EM (and between LN and LM) mean values are within 0.5–1mm/day and above 1mm/day are highlighted in black dashed line and solid line boxes, respectively.

### 2.4 Possible mechanisms responsible for the rainfall variations

#### 2.4.1 Vertically Integrated Moisture Flux

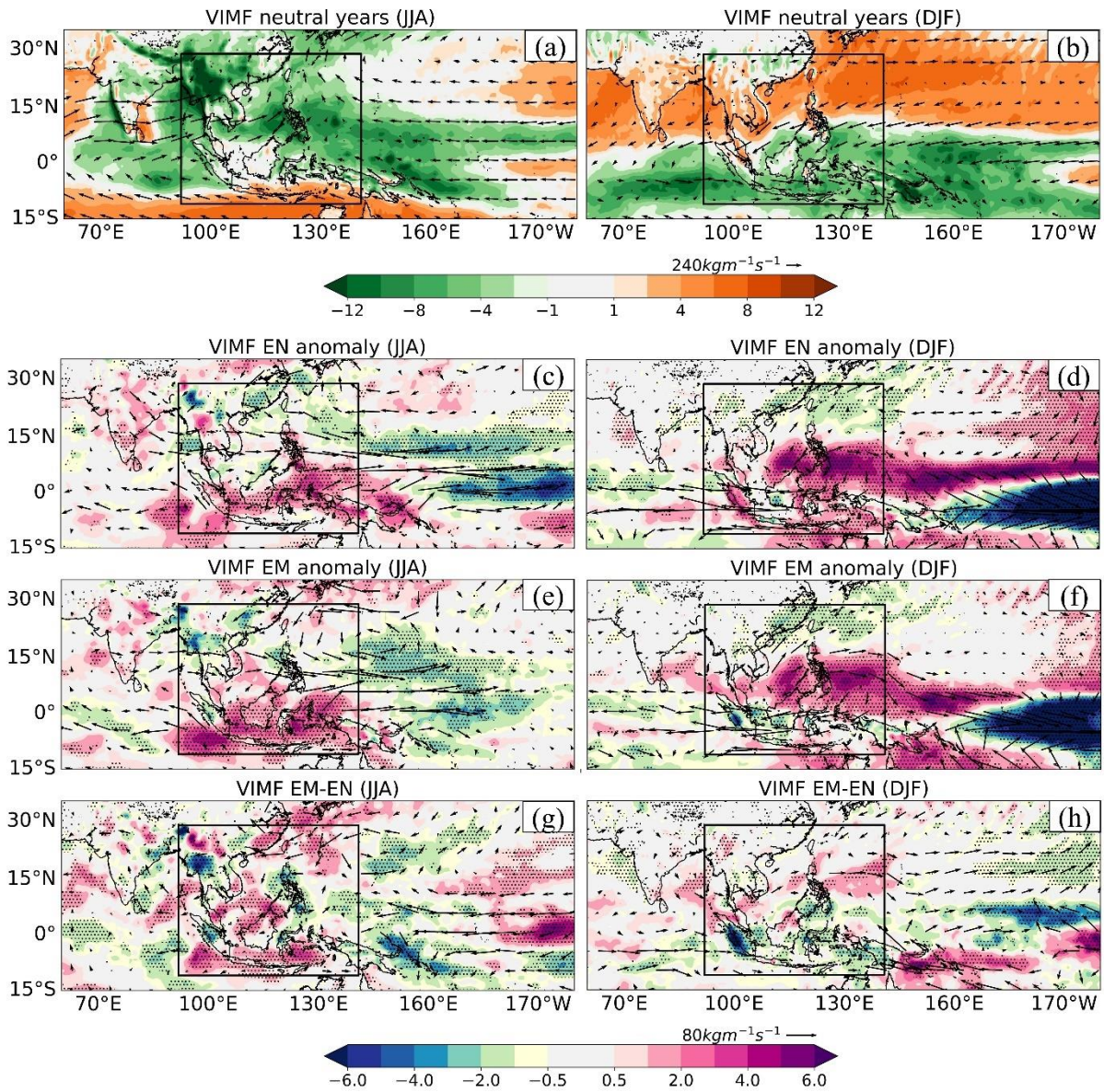
The transport direction and origins of VIMF are associated with rainfall anomaly patterns (Zhou and Yu 2005). The VIMF anomaly allows identifying the areas of divergence (positive values) and convergence (negative values) of the moisture fluxes that correspond to rainfall decrease or increase, respectively.

Figure 2.7a, b displays the VIMF and its divergence over the SEA domain for the neutral JJA and DJF composites. The wet conditions in JJA over the northern domain, i.e., Indochina and the Philippines, mainly originate from the moisture transport by the southwest monsoon from the Bay of Bengal in the Indian Ocean to the west of the domain, and by the Pacific easterlies to the east of the domain. Most of the Maritime Continent experiences dry conditions because of a lack of moisture supply to the region in JJA. In DJF, the SEA domain is well separated into a northern dry area and a southern wet area. The moisture transport to the Maritime Continent in DJF originates from the equatorial westerlies in the southern hemisphere, and from the Pacific easterlies in the northern hemisphere.

Figures 2.7c–f show both in EN and EM events a decrease in moisture transport from the Pacific in both JJA and DJF as well as from the equatorial easterlies in the southern hemisphere to parts of SEA in DJF. The moisture deficit in EM is larger (smaller) than that in EN over the Maritime Continent in JJA (DJF) (Fig. 2.7g, h). Anomalous divergent conditions (positive values in Fig. 2.7c–f) prevail noticeably over the Maritime Continent in JJA and the northern part of the Maritime Continent and the Philippines in DJF in both EN and EM, inducing an inhibition, i.e., deficit, of rainfall over these subregions. This is in agreement with the results discussed above and shown in Fig. 2.5a. In EN, weak anomalous convergences are observed in Southeast China, part of Indochina (R19, R20), and North Sumatra (R14) in both seasons, and South Borneo (R4) in DJF. Furthermore, relatively strong anomalous convergences in the coastal region of Myanmar (part of R15, R20) in JJA and West Sumatra (part of R12, R14) in DJF are observed in EM, resulting in increased rainfall over this region. The anomalous convergence regions in EN and EM could be explained by enhanced moisture transport from the Bay of Bengal in JJA, e.g., in Indochina, or by the redistribution of the moisture budget within the regions in DJF, e.g., in Sumatra. Values corresponding to anomalous divergence (convergence) conditions in JJA (DJF) during EM are generally larger than those during EN

## Chapter 2. Impacts of ENSO and ENSO Modoki on rainfall variability

over the Maritime Continent, causing and explaining the stronger rainfall decrease (increase) during EM than during EN in this region as shown in Fig. 2.4.



**Figure 2.7.** VIMF (vector, unit:  $\text{kg m}^{-2} \text{ s}^{-1}$ ) and its divergence (shading, unit  $10^{-5} \text{ kg m}^{-2} \text{ s}^{-1}$ ) for JJA and DJF of the neutral years (a, b), anomalies of the composites of EN (c, d) and EM (e, f) and differences between EM and EN (g, h) during JJA and DJF. The dot patterns in (c–h) indicate areas where differences are statistically significant at 90% based on the bootstrap test.

Figure 2.8 displays the VIMF anomaly in LN and LM and the differences between LM and LN. Under LM conditions, moisture north of  $10^{\circ}\text{N}$  (from the Bay of Bengal and Northwest Pacific Ocean) is considerably reduced in JJA, mainly due to a deficit in the moisture transport

## Chapter 2. Impacts of ENSO and ENSO Modoki on rainfall variability

by summer monsoon into the west, and by the Pacific easterlies into the northeast of the domain (Fig. 2.8c). On the other hand, moisture in LM increases over the southern SEA region (5°N–15°S, 100°E–150°E) in both JJA and DJF because of enhanced moisture transport into the east of the domain by the Pacific easterlies in both seasons, and into the west of the domain by the equatorial westerlies in DJF (Fig. 2.8c, d). As a result, rainfall in LM decreases sharply in JJA in the subregions from 10°N northward such as Vietnam (R17, R18) and West Philippines (R1), and generally increases in the southern subregions in both seasons (Fig. 2.5c, d). The VIMF anomaly, as well as its anomalous divergence/convergence conditions, show similar patterns under LN with some differences in magnitude compared to LM. In JJA, LN exhibits less reduced (more enhanced) moisture transport than LM over the northern (southern) subregions (Fig. 2.8e), leading to less rainfall over these subregions, respectively (cf. Fig. 2.5e). In DJF, LM shows enhanced convergence compared to LN in most of the southern subregions (Fig. 2.8f), explaining the rainfall enhancement over these regions during LM (cf. Fig. 2.5f).

For the identification of atmospheric circulation cells associated with the two types of ENSO, we employ three variables: velocity potential, divergent wind, and pressure vertical velocity. Velocity potential and divergent wind, i.e., the Laplacian of velocity potential, are assessed at the atmosphere's upper level (200 hPa). Generally, regions of positive (negative) velocity potential at 200 hPa have converging (diverging) winds and subsidence (ascending motion) beneath. Values of velocity potential at 200 hPa also show information regarding the intensity of atmospheric circulation (Weng et al. 2007). The convergence (divergence) in the upper level corresponds to divergence (convergence) in the lower level (Wang 2002). The descending and ascending regions are specifically illustrated by vertical velocity. Wang (2002) described the vertical velocity's structure associated with the Walker circulation cell across the equatorial Pacific Ocean under EN.

### 2.4.2 Associated circulation cells

Figure 2.9a, b shows that the maximum value of velocity potential at 200 hPa for a neutral year is about  $15 (\times 10^6 \text{ m}^2 \text{ s}^{-1})$ , located in South Atlantic and South Africa during JJA and in North Atlantic and North Africa during DJF. The minimum is observed in the northwestern Pacific and Southeast Asia around 90°E–170°E during JJA and in the western equatorial Pacific during DJF, with a value of  $-15 (\times 10^6 \text{ m}^2 \text{ s}^{-1})$ . The wind at 200 hPa diverges from the location of minimum velocity potential to the place of higher velocity potential, such as the eastern Pacific and Africa. The divergence at the upper level is connected with a strong upward

## Chapter 2. Impacts of ENSO and ENSO Modoki on rainfall variability

motion associated with the ascending branch of the Walker circulation over the western Pacific, notably over the northwestern Pacific (100°E-180°E) in JJA and the western equatorial Pacific (130°E-140°W) in DJF (Fig. 2.11a, b).

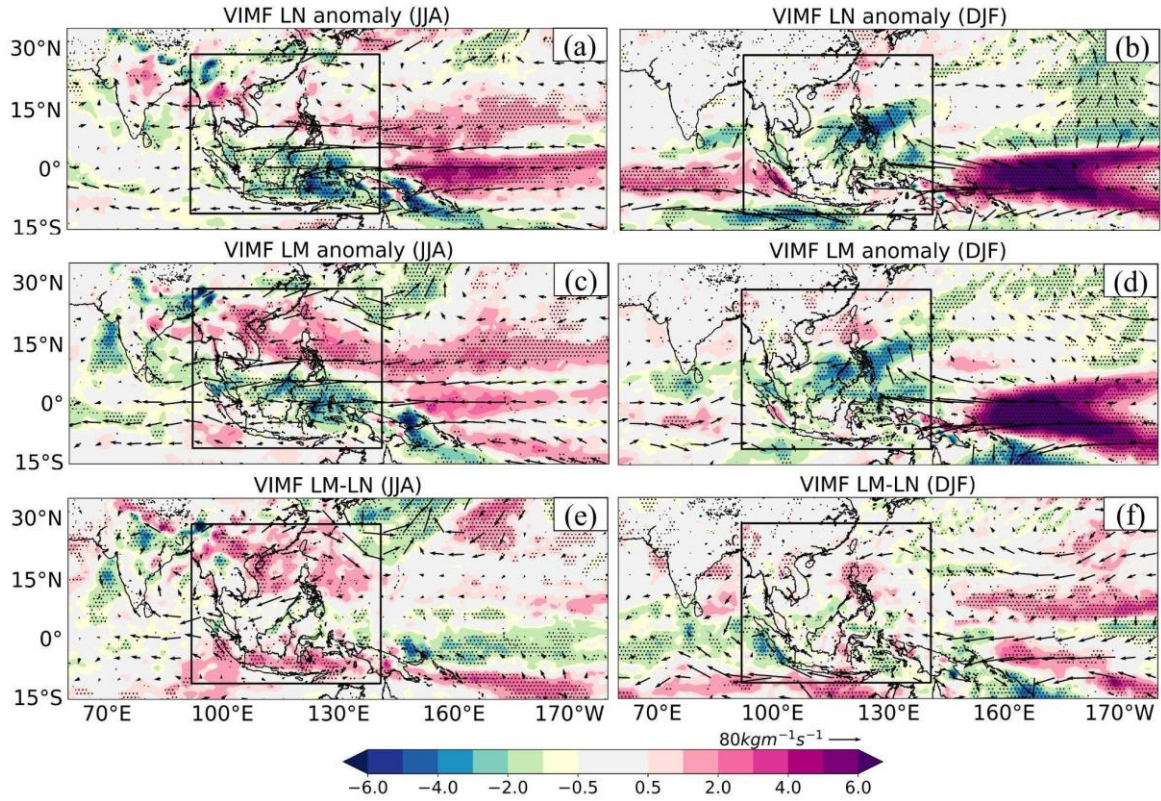


**Figure 2.8.** As in Fig. 2.7(c-h) but for LN and LM.

Previous studies have shown that differences in the patterns of SSTA in the Pacific Ocean can lead to a shift in the position and intensity of the Walker circulation. For example, under EN in both JJA and DJF, there is a typical positive SSTA in the central and eastern Pacific, and the sea level pressure difference between the East and western Pacific Oceans decreases markedly, leading to a weakening of the Walker circulation (Julian and Chervin 1978; Vecchi et al. 2007; Power and Smith 2007). The equatorial region in the western Pacific Ocean often shows a westerly wind anomaly, due to the weakening of the Walker circulation under EN, in contrast to the easterly anomaly in the eastern Indian Ocean. Thus, this region becomes a divergent zone in the low level under EN (Hosking et al. 2012).

Under EN conditions, the positive values of the composite velocity potential and divergent wind anomalies indicate upper-level anomalous convergences (Fig. 2.9c, d). The upper-level anomalous convergence center is located around [110°E, -20°S] over the tropical Indian Ocean

## Chapter 2. Impacts of ENSO and ENSO Modoki on rainfall variability

–a part of the Maritime Continent–Australia region in JJA (Fig. 2.9c). In DJF, the anomalous center is shifted northeastward to around [120°E, 0°N] (Fig. 2.9d). Conversely, there exist upper-level anomalous divergences over the eastern and equatorial central Pacific, where SSTA is positive (Fig. 2.2). The areas of maximum velocity potential in the eastern Pacific and minimum in the western Pacific are shifted to West under EN for both JJA and DJF, and the magnitudes decrease to 12 and  $-10 (\times 10^6 \text{ m}^2 \text{ s}^{-1})$ , compared to the neutral years' means of  $\sim 15$  and  $-15 (\times 10^6 \text{ m}^2 \text{ s}^{-1})$ , respectively. These changes correspond to reduced descending motions, due to anomalous warming, in the central and eastern Pacific between 160°W and 100°W (120°W and 80°W) in JJA (DJF), along with weaker upward motions west of 160°E (160°W) in JJA (DJF) (Fig. 2.11c, d). The weaker upward motions in the ascending branch of the Walker circulation led to rainfall decrease over the major part of SEA under EN (cf. Fig. 2.4a, b).

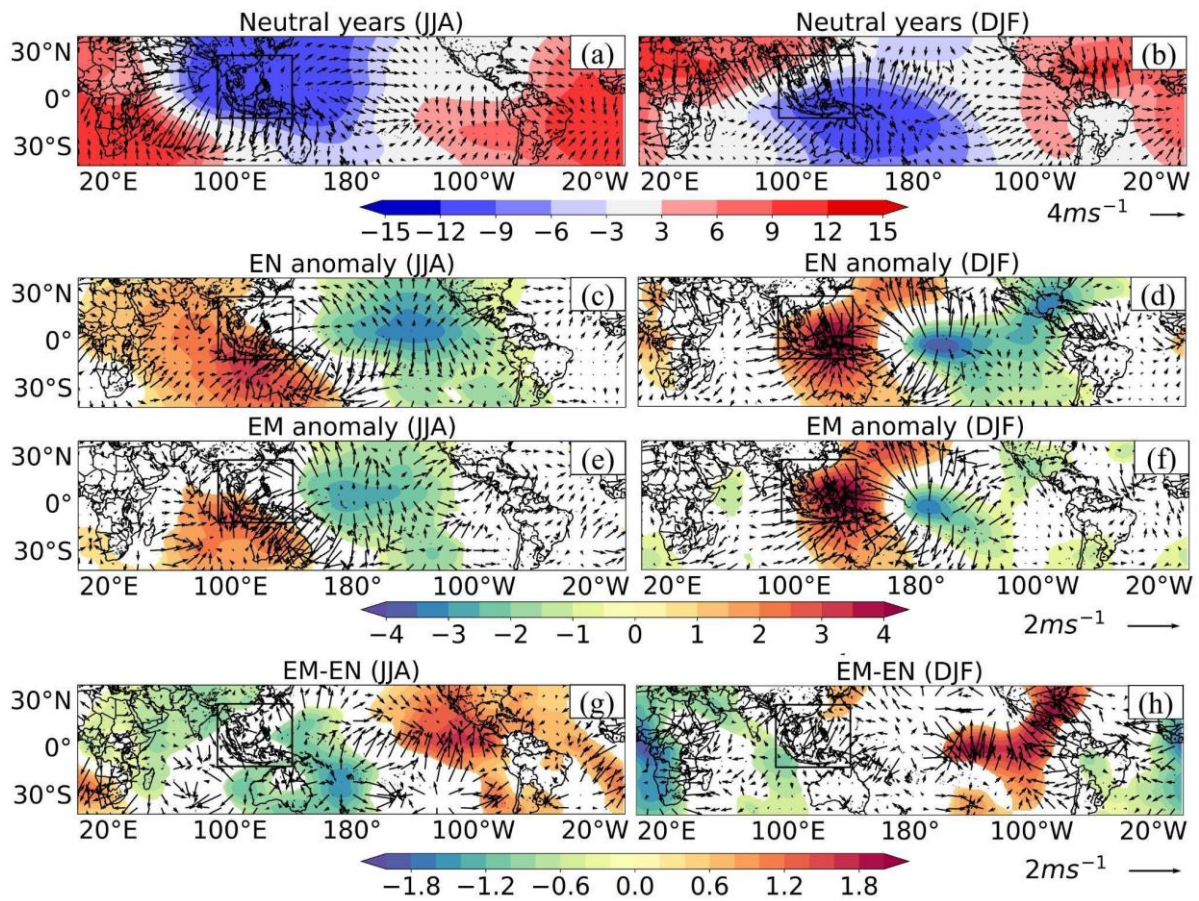


**Figure 2.9.** Mean of 200 hPa velocity potential (shading; units:  $10^6 \text{ m}^2 \text{ s}^{-1}$ ) and divergent wind (arrow, unit:  $\text{ms}^{-1}$ ) for the neutral years during (a, b) JJA and DJF. Anomalous velocity potential and divergent wind at the 200 hPa for (c, d) EN and (e, f) EM events and (g, h) the differences between EN and EM anomalies during JJA and DJF. Shading in (c–h) indicates areas where differences are statistically significant at 90% based on the bootstrap test.

## Chapter 2. Impacts of ENSO and ENSO Modoki on rainfall variability

For EM conditions, an upper-level anomalous divergence is located over the central Pacific around 180°W in both seasons, while an anomalous convergence center is found over the southwestern (southeastern) part of SEA in JJA (DJF) (Fig. 2.9e, f). Compared to EN, the EM convergence and divergence anomalies are generally weaker in terms of magnitude; however, the differences are not significant over most of SEA (Fig. 2.9e, f). The significantly less positive velocity potential anomaly of EM compared to EN over the southeastern part of SEA (15°N, 150°E) in JJA (Fig. 2.9g) and over the southwestern part in DJF (Fig. 2.9h) indicates stronger upward motions over these areas during EM than EN. These areas belong to the ascending branch of the Walker circulation. The less reduced upward motion in EM compared to EN can be observed between 150°E and 180°E (60°E and 120°E) in JJA (DJF) (Fig. 2.11). This explains the significantly weaker rainfall deficit in EM compared to EN over the Philippines (R1,2) and Papua (R8) during JJA, and over the southwestern SEA during DJF (cf. Fig. 2.4e, f).

Our analysis above partly follows that of Weng et al. (2007), who focused on the impacts of EM and EN on rainfall in the Pacific rim (China, Japan and the USA) during boreal summer. The analysis is, however, performed here for the first time over the entire SEA for the recent period 1979–2019, for both boreal summer and winter, and with up-to-date datasets. Moreover, the features during LN and LM, which were not examined in Weng et al. (2007), are presented in the following.

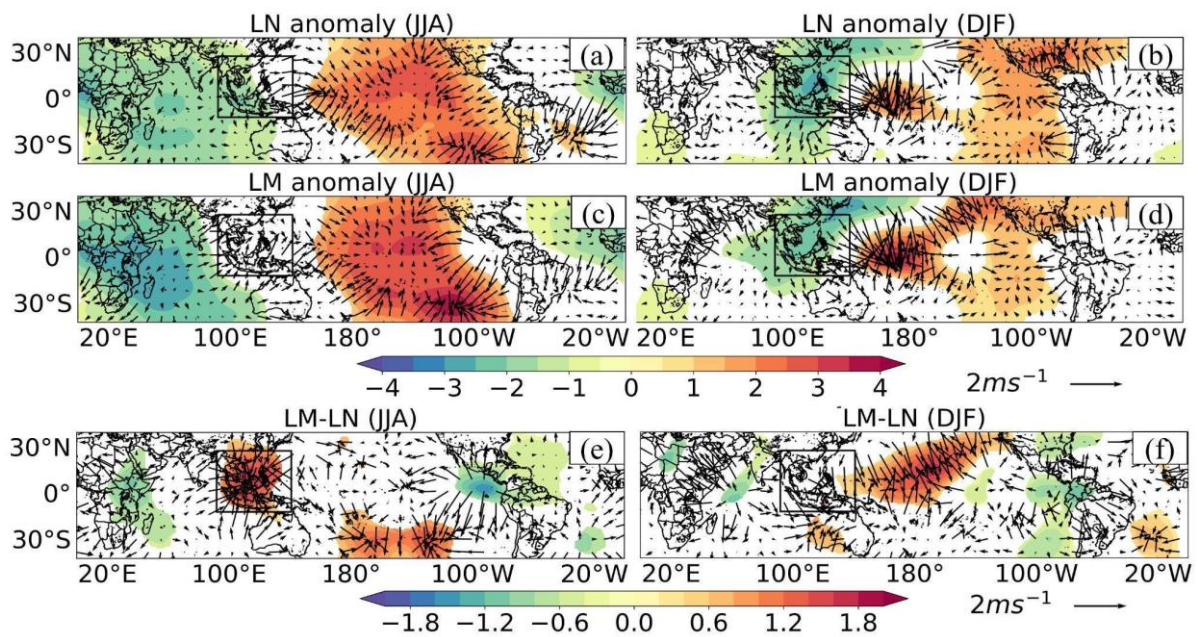


**Figure 2.10.** As in Figure 2.9(c–h) but for LN and LM.

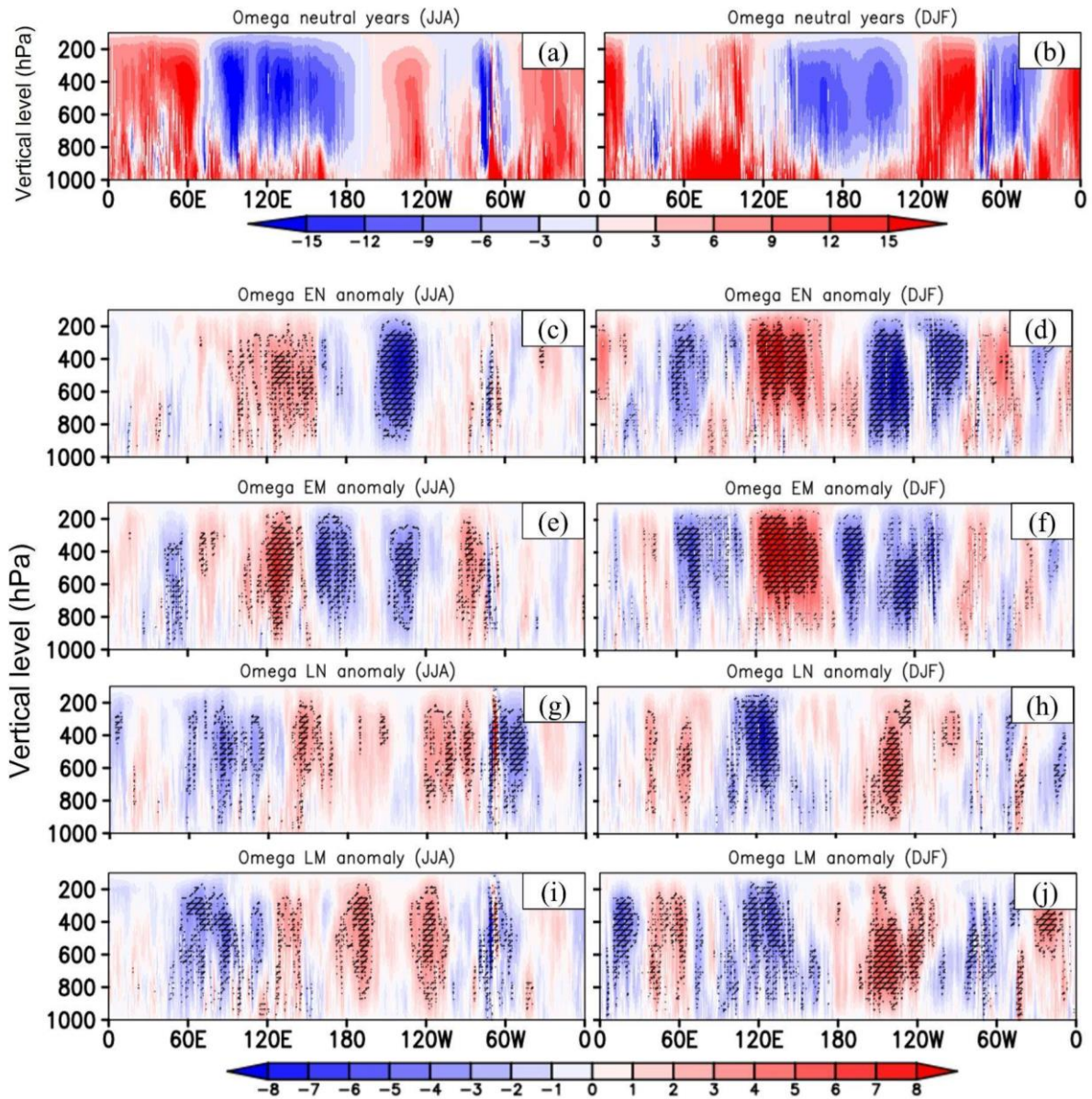


**Figure 2.11.** Mean of pressure vertical velocity for the neutral years during (a) JJA and (b) DJF, and composites of pressure vertical velocity anomalies for (c, d) EN, (e, f) EM, (g, h) LN, and (i, j) LM during JJA (left) and DJF (right). The average between 13°S and 29.5°N is computed. Units in  $\text{Pas}^{-1}$ . The hatch patterns in (c–j) indicate areas where differences are statistically significant at 90% based on the bootstrap test.

The anomalous potential velocity and divergent wind values in LN and LM show opposite patterns compared to those in EN and EM, respectively (Fig. 2.10). Convergence and divergence are both enhanced compared to the neutral years' means in LM and, to a lesser extent in LN, in both seasons (Fig. 2.10a–d). In LN, an anomalous divergence at the upper level occurs over the southwest of SEA during JJA and over the entire SEA domain during DJF,

## Chapter 2. Impacts of ENSO and ENSO Modoki on rainfall variability

corresponding to an intensification of the ascending branch of the Walker circulation over these areas (Fig. 2.11g, h), hence explaining the increase in rainfall over parts of SEA (cf. Fig. 2.5a, b). In DJF, there is no significant difference over SEA between LM and LN in terms of potential velocity, divergent wind (Fig. 2.10f), and pressure vertical velocity (Fig. 2.11h, j). In JJA, the difference between LM and LN shows a significant anomalous convergence center at the upper level over the SEA domain (Fig. 2.10e), corresponding to a reduced upward motion between 100°E–140°E (Fig. 2.11i), thus explaining the weaker rainfall increase or drier conditions over SEA in LM compared to LN (cf. Fig. 2.5e).

It is of interest to recognize that the location and strength of the anomalous circulation patterns of each type of ENSO event (Figs. 2.9–11) correspond to the location and strength of the SSTA maximum (Fig. 2.A4). Previous studies also indicated that atmospheric teleconnections are strongly influenced by different SSTA configurations in the equatorial regions (Capotondi et al. 2015; Abid et al. 2020; Ma et al. 2022). Thus, the differences in the precipitation response between the two types of ENSO events, resulting from the differences in the atmospheric circulations, are linked to the SSTA spatial pattern and intensity. Note that the largest differences in the precipitation response lie in the amplitude rather than the spatial pattern (Figs. 2.4, 5). These differences appear more likely to be related to the SSTA zonal location during JJA, while the different SSTA amplitudes play a more important role during DJF (Figs. 2.9–11, and Fig. 2.A4).

### 2.5 Chapter's conclusions

This study depicts, for the first time, the detailed and distinct impacts of ENSO and ENSO Modoki on rainfall over Southeast Asia and its 20 sub-regions during the last 40 years. The EMI and Niño 3 indices were used to identify the Modoki and the classic ENSO events, respectively. Results showed that within the study period of 1979–2019, there were seven EN, six LN events, five EM, and five LM events; and 16 years were classified as neutral years.

Based on the up-to-date GPCP version 2020 dataset at 0.25° resolution, changes in rainfall under ENSO and ENSO Modoki conditions were estimated and associated with the SSTA in the Pacific Ocean and the atmospheric circulation. In JJA under canonical EN conditions, rainfall reduction occurs over most of the southern SEA domain and Southeast Philippines, while alternating drier and wetter conditions occur over Indochina. In DJF of EN events, larger rainfall reduction compared to JJA is seen over Southeast Philippines, East Borneo, and Maluku, while significant rainfall enhancements are observed over West Kalimantan and parts

## Chapter 2. Impacts of ENSO and ENSO Modoki on rainfall variability

of the Indochinese Peninsula. Similar rainfall anomaly patterns are obtained in EM, though EM shows enhanced drier/wetter conditions compared to EN. In both EN and EM, the reduction in moisture transport from the Pacific in both JJA and DJF and from the equatorial easterlies in the southern hemisphere in DJF to the SEA region causes a decrease in rainfall over the Maritime Continent in JJA and the northern part of the Maritime Continent and the Philippines in DJF. They are associated with a weakening and westward shift of the ascending and descending branches of the Walker circulation. Under EN, the negative anomalies of the ascending branch of the Walker circulation are located over the southwest and southeast of SEA in JJA and DJF, respectively, thus suppressing rainfall and leading to drier conditions in the region. The negative anomalies of the ascending branch are weaker under EM, resulting in a weaker rainfall reduction compared to EN over the Philippines and Papua during JJA and over the southwestern SEA during DJF.

The impacts of LN and LM on rainfall in Southeast Asia are noticeably different from those of EN and EM. Under LN, rainfall increases in most sub-regions except for the West Philippines and some specific locations in Indochina in JJA, and some areas in the southern part of SEA in DJF. Although having the same anomaly patterns, LM generally shows less wet/drier conditions than LN in JJA. In DJF, LM produces more rainfall than LN over most of the Maritime Continents while generally displaying less rainfall over the eastern part of SEA. The LM rainfall deficit compared to LN in JJA comes from a shortage of moisture transport into the north of SEA and from the strong anomalous convergence at the upper level that leads to a weakening of the ascending motion beneath, hence rainfall suppression. Meanwhile, the LM rainfall increase compared to LN in DJF in the southern subregions is attributed to more enhanced moisture transport by the Pacific easterlies and the equatorial westerlies into the region, hence the rainfall surplus.

Our results suggest that droughts in EM could be less severe than in EN in almost all subregions during JJA, while floods in LM could be worsened compared to LN in the southern part of SEA during DJF.

We have performed the sensitivity analysis with other rainfall and reanalysis datasets, i.e. the CRU rainfall and the NCEP1 reanalysis datasets. This confirmed the robustness of the obtained results discussed above (not shown). In the present work, the role of heat transfer was not investigated. As latent and sensible heat fluxes were shown to have a close connection with rainfall (Gao et al. 2015; Juneng et al. 2016), the results obtained in this study thus highlight the importance of examining the impacts of both types of ENSO on air-sea heat fluxes across

## **Chapter 2. Impacts of ENSO and ENSO Modoki on rainfall variability**

the SEA region. The ability of regional models to reproduce both types of ENSO and their impacts would also deserve to be carefully investigated in a future study.



# Chapter 3. Quantifying air-sea heat fluxes over Southeast Asia: intercomparison of available datasets and sensitivity ocean simulations

## Contents

3.1. Introduction.....	74
3.2 Data and Method.....	76
3.2.1 The ocean model SYMPHONIE .....	76
3.2.2 Computation of heat fluxes in SYMPHONIE .....	78
3.2.2.1 Method 1: bulk method.....	79
3.2.2.2 Method 2: flux method.....	80
3.2.3 Experimental design .....	80
3.2.4 Heat flux datasets and data for model evaluation.....	82
3.2.5 Statistical methods.....	85
3.3. Characteristics of heat fluxes in distributed dataset.....	85
3.3.1 Spatial variability.....	86
3.3.2 Seasonal cycle.....	88
3.4 Results of sensitivity simulations.....	90
3.4.1 SST spatial distribution .....	90
3.4.2 Surface temperature temporal evolution.....	92
3.4.3 Relationship between temperature differences and heat flux .....	94

**Chapter 3. Quantifying air-sea heat fluxes over Southeast Asia: intercomparison of available datasets and sensitivity ocean simulations**

3.5 Extending our conclusions over longer periods.....97

    3.5.1 Comparison between heat flux computed from SYMPHONIE and ECMWF products over 2009-2018.....97

    3.5.2 Extension to other heat flux datasets .....98

3.6. Chapter’s conclusion..... 100

## Chapter 3. Quantifying air-sea heat fluxes over Southeast Asia: intercomparison of available datasets and sensitivity ocean simulations

In this chapter, our goal is to establish a benchmark estimate of air-sea heat fluxes in Southeast Asia. We begin by introducing the problem, followed by a description of the SYMPHONIE hydrodynamic ocean model, its configuration for the SEA region, and the experimental designs used in this study. Subsequently, we describe satellite observations and in-situ data analysis, as well as the reanalysis datasets used for model validation. We also introduce the climate indices used for analyzing simulation results. Through the ocean simulations, we evaluate the sensitivity of the modeled sea surface temperature (SST) and temperature from 0 to 100m layers profiles to prescribed surface heat flux values and deduce from this an estimate of errors in the heat flux values provided by the popular reanalysis datasets.

### 3.1. Introduction

The ocean interacts with the atmosphere through exchanges of momentum, heat, and mass (Myhre et al. 2014). These air-sea exchanges constitute the ocean-surface energy and water budgets, which define the ocean's role in Earth's climate and its variability on both short and long timescales. Knowledge of these exchanges is essential for understanding and modeling several physical processes at appropriate spatial and temporal scales, spanning various scales of atmospheric and oceanic motions, as explained in Chapter 1 (Introduction). Despite the development of heat flux products and improved parameterizations, existing datasets still do not fully close the surface energy budget (L'Ecuyer et al. 2015) and the uncertainty in the flux estimates remains very large (Rhein et al. 2013). In addition, ocean observing buoys and stations are also limited. Nevertheless, heat fluxes are a key element of ocean-atmosphere interactions, and an essential ingredient for ocean simulations.

Atmospheric sea surface fields, specifically heat fluxes, water fluxes, momentum fluxes (wind stress) and scalar forcing (air temperature, pressure, shortwave, and longwave radiation at the ocean surface), are commonly used to study sea surface atmospheric dynamics, including air-sea fluxes, and their variability, and to provide input data for ocean model simulations (Wallcraft et al. 2008). These fields are typically obtained from models. Atmospheric products such as the Modern-Era Retrospective analysis for Research and Applications, Version 2 (MERRA-2; Gelaro et al. 2017), the European Centre for Medium-Range Weather Forecasts (ECMWF) product ([www.ecmwf.int](http://www.ecmwf.int)) or the Japanese 55-year Reanalysis (JRA-55; Kobayashi et al. 2015) are available to force ocean models. They compute air-sea fluxes from bulk

### Chapter 3. Quantifying air-sea heat fluxes over Southeast Asia: intercomparison of available datasets and sensitivity ocean simulations

formulae using both atmospheric and oceanic variables such as wind, air temperature, and humidity (Mahrt et al. 2023, Bonino et al. 2022). Those atmospheric products are designed to provide the most realistic representation of the atmosphere by assimilating conventional and satellite-based observations into a modeling framework (Molod et al. 2015).

Estimates of air-sea heat fluxes still show large uncertainties, both at the global and regional scales. For example, global net heat flux is estimated to range from 1 to 30  $\text{W}\cdot\text{m}^{-2}$  (Song and Yu 2013). NCEP1 (Kalnay et al. 1996) provides the lowest estimate, while OAFflux+ISCCP (Yu and Weller 2007, Zhang et al. 2004) gives the highest estimate. Net heat flux estimates over the northwestern Pacific region vary from 15  $\text{W}\cdot\text{m}^{-2}$  (CFSR, Saha et al. 2010) to 54  $\text{W}\cdot\text{m}^{-2}$  (ERA-40, Uppala et al. 2005) (Song and Yu 2013). Song and Yu (2017) demonstrated that the Mediterranean Sea is a region of heat gain, with  $Q_{\text{net}}$  ranging from 1  $\text{W}\cdot\text{m}^{-2}$  in NCEP1 to 21  $\text{W}\cdot\text{m}^{-2}$  in MERRA (Bosilovich et al. 2008, Rienecker et al. 2011). In contrast, results with JRA-55 and CORE2 (Large and Yeager 2009) indicate that the Mediterranean Sea is a region of heat loss, with  $Q_{\text{net}}$  of -12 and -19  $\text{W}\cdot\text{m}^{-2}$ , respectively. Estimates of  $Q_{\text{net}}$  for the South China Sea (SCS) range from 18 to 25  $\text{W}\cdot\text{m}^{-2}$  (Wang et al. 1997, Yang et al. 1999, Fang et al. 2002, Qu et al. 2006, 2006). It is noteworthy that uncertainties of air-sea heat flux estimates are caused by many factors, including errors in the models, in the formulas used, and in SST (Brunke et al. 2002, Kubota et al. 2008, Valdivieso et al. 2017) among others. Moreover, most atmospheric products are created without coupled ocean-atmosphere interaction, in which the air-sea fluxes are calculated using prescribed SST, which can lead to errors in air-sea fluxes due to the inconsistency between the prescribed SST and the simulated atmosphere (Kalnay et al. 1996, Dee et al. 2011, Kobayashi et al. 2015).

The use of climate estimates of total heat flux to force an ocean model can result in unrealistic SSTs in the ocean simulation, due to inconsistencies between the imposed surface fluxes and the SST computed by the ocean model (Barnier et al. 1995, Hughes and Weaver 1996, Wallcraft et al. 2008). Additionally, ocean models themselves have errors, related to several factors including the model's physics and parameterisations, initial and boundary conditions, etc, which can lead them to drift from ocean observations, even when they are forced by accurate surface fluxes (Hughes and Weaver 1996). A common approach to adjust the bias due to the inconsistency between the prescribed fluxes and the ocean model SST is to use bulk formulae in the ocean model, using oceanic variables computed by the ocean model (Maltrud et al. 1998, Wallcraft et al. 2008, Strobach et al. 2018). It indeed allows the model to

## **Chapter 3. Quantifying air-sea heat fluxes over Southeast Asia: intercomparison of available datasets and sensitivity ocean simulations**

take into account the feedback from the ocean to the atmosphere, allowing latent and sensible heat fluxes, longwave radiation and wind stress to vary as functions of the predicted SST and surface current of the ocean model (Reeves et al. 2021, Bonino et al 2022). A positive (negative) downward heat flux to the ocean will indeed cause an increase (decrease) in SST, which will in turn cause an increase (decrease) in the upward heat flux into the atmosphere. The use of reanalysis dataset as input to the bulk formulas helps to ensure more realistic and accurate results for air-sea flux calculations. (Strobach et al. 2018). Therefore, this method is a useful compromise and is the most widely used today for ocean-only simulations.

Previous studies demonstrated the importance of SST in air-sea interactions through surface heat flux in the SEA region (Zhang et al. 1995, Kumar et al. 2017). SST also plays a key role in long-term climate variability, particularly in relation to ENSO and ENSO Modoki (Jiang et al. 2022, Nguyen-Thanh et al. 2023, Kido et al., 2023). In addition, it is used in bulk formulas to estimate heat flux (Kara et al. 2000). Furthermore, SST is one of the best-observed variables of the upper ocean (Schopf and Loughe 1995). This makes SST simulated from ocean models easily verifiable.

The goal of the present chapter is to establish a set of benchmark values of air-sea heat flux in the SEA region. These benchmarks will serve as a reference for assessing the performance of various heat flux datasets, including those from analysis, reanalysis, model simulations, and observations. To achieve this goal, we investigate the sensitivity of SSTs produced by an ocean model to the prescribed surface heat flux. We first perform an ocean simulation that produces realistic SSTs over the period 2017–2018 using bulk formulae, which we refer to as the Control (CTL) simulation. Next, we conducted five sensitivity tests using the same configuration, but without bulk formulae and prescribing instead different values of heat fluxes to test the sensitivity of the ocean model SST to these values. The results obtained from this sensitivity analysis are used to establish a realistic estimate of air-sea heat flux over the SEA region.

### **3.2 Data and Method**

#### **3.2.1 The ocean model SYMPHONIE**

SYMPHONIE is a 3-D hydrostatic ocean circulation model developed by the SIROCCO group (LEGOS, CNES, CNRS, IRD, Université de Toulouse, France) (Marsaleix et al. 2006,

### Chapter 3. Quantifying air-sea heat fluxes over Southeast Asia: intercomparison of available datasets and sensitivity ocean simulations

2008, 2009, 2012). This model has been used and validated in a number of previous studies, covering a wide range of regions and processes, including: the formation and variability of continental shelves and dense water masses in the open ocean (Herrmann and Somot 2008, Herrmann et al. 2008, Waldman et al. 2016, Estournel et al. 2016), internal waves and wave-current interactions (Auclair et al. 2011, Michaud et al. 2011, Marsaleix et al. 2019). Recently, there have been studies and applications of the SYMPHONIE model in the calculation of hydrodynamic processes in the SCS (Nguyen-Duy et al. 2021, To Duy et al. 2022, Herrmann et al. 2023). Trinh (2020) and Trinh et al. (2023) used the model in particular to investigate the water, salt, and heat budget over the SCS, examining the respective contributions of surface, river, and lateral fluxes to this budget.

SYMPHONIE is built based on the Navier–Stokes primitive equations under the hydrostatic equilibrium hypothesis, incompressibility hypothesis, and Boussinesq approximations. The equations are based on six state variables: three velocity components ( $u$ ,  $v$ ,  $w$ ), the temperature  $T$ , the salinity  $S$ , and the sea surface elevation  $\eta$ . The model equations are solved using the finite difference method on the Arakawa staggered C-grid (Harlow and Welch 1965, Arakawa and Lamb 197, Arakawa and Suarez 1983), where scalar quantities (temperature, salinity, surface elevation) are defined at the center of each grid cell, whereas velocity components ( $u$ ,  $v$ ) are shifted by half a grid cells (Fig 3.1).

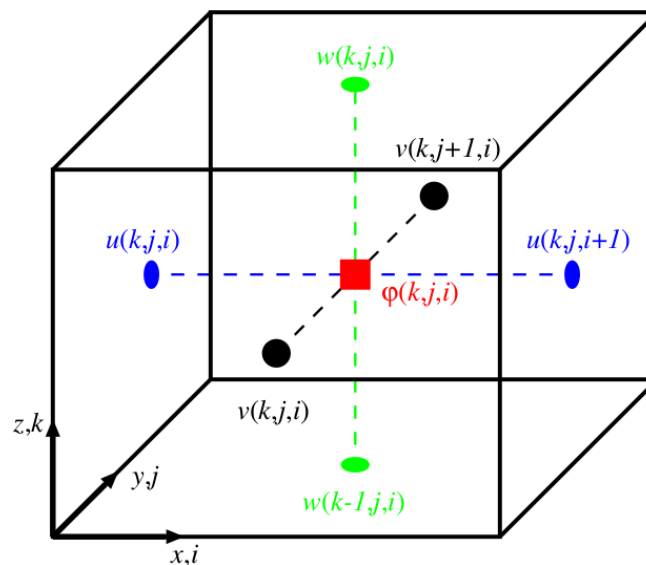


**Figure 3.1** The Arakawa staggered C-grid. The indices  $i, j, k$  refer to grid points in  $x, y$  and  $z$  direction, respectively. Scalar quantities  $\varphi$  are defined at the center of the grid volume, whereas velocities are defined at the edges of the grid volumes (Piton 2019).

### Chapter 3. Quantifying air-sea heat fluxes over Southeast Asia: intercomparison of available datasets and sensitivity ocean simulations

SYMPHONIE uses the QUICKEST scheme (Leonard, 1979) for horizontal advection and diffusion of temperature and salinity. Each horizontal advection and momentum diffusion is computed with the fourth-order central-differencing scheme. Vertical advection is computed using the central scheme. The vanishing quasi-sigma (VQS) vertical coordinate concept system (Dukhovskoy et al. 2009) is used in SYMPHONIE. VQS coordinates represent depth well and avoid hydrostatic inconsistency in computing pressure gradients for strong slopes. It also helps to limit the number of vertical levels in very shallow regions, while maintaining accurate representation in deep regions and reducing sigma coordinate-related truncation error (Siddorn et al. 2013). The governing equations, bottom, and lateral boundaries, as well as tides and rivers, are comprehensively documented in the studies of Trinh (2020), To Duy (2022), and Nguyen Duy (2022). In the context of this thesis, we exclusively present the formulas pertaining to the surface boundary, with particular emphasis on heat flux, which constitutes the focal point of our investigation.

The heat flux at the ocean-atmosphere boundary is computed from 4 components: Shortwave radiation flux (SW), longwave radiation flux (LW), latent heat flux (LH) and sensible heat (SH):

$$Q_{net} = SW + LW + LH + SH \quad (\text{Eq. 3.1})$$

where all fluxes and their components are defined as positive downwards, such that the fluxes into the ocean are positive. SW is consistently positive, while LW is generally negative because the upward radiation from the surface is typically greater than the downward radiation from the colder clear sky and cloud. Turbulent heat fluxes are represented by SH and LH. LH is directly related to the vapor component of freshwater fluxes, and its value is typically negative.

#### 3.2.2 Computation of heat fluxes in SYMPHONIE

In this study, we use two methods to perform simulations using the SYMPHONIE model: one is a simulation with feedback from the ocean to the atmosphere using bulk flux formulae, along with atmospheric variables computed by an atmospheric model. The other is a simulation without feedback from the ocean (no bulk), using directly fluxes computed by the atmospheric model.

## Chapter 3. Quantifying air-sea heat fluxes over Southeast Asia: intercomparison of available datasets and sensitivity ocean simulations

### 3.2.2.1 Method 1: bulk method

*Using bulk formulae to include feedback from the ocean to the atmosphere.*

When using bulk formulae, we use atmospheric variables computed by an atmospheric model and oceanic variables computed by the ocean model SYMPHONIE: SW, wind components at 10 m, air temperature at 2 m, precipitation, surface pressure and relative humidity data are sourced in our case from ECMWF analyses ([www.ecmwf.int](http://www.ecmwf.int)). The computation of wind stress  $\tau_s$ , LW, turbulent heat fluxes (LH and SH), and evaporation ( $E$ , deduced from LH) relies on atmospheric variables and on SST simulated by SYMPHONIE, applying the bulk formulae developed by [Large and Yeager \(2004\)](#).

$$E = \rho C_E W (q_a - q_s) \quad (\text{Eq. 3.2})$$

$$LH = L_v E \quad (\text{Eq. 3.3})$$

$$SH = \rho C_p C_H W (T_a - T_s) \quad (\text{Eq. 3.4})$$

where  $W$ ,  $q_a$ , and  $T_a$  represent the 10-m wind speed, specific humidity, and air temperature at 2m above sea surface, respectively;  $\rho$  is the near surface air density ( $\approx 1.22 \text{ kg m}^{-3}$ );  $L_v$  is the latent heat of vaporization ( $2.5 \times 10^6 \text{ J kg}^{-1}$ );  $C_E = 1.3 \times 10^{-3}$  and  $C_H = 0.83 \times 10^{-3}$  (stable condition) are the transfer coefficients for latent heat and sensible heat, respectively, which are functions of height, atmospheric stability, and wind speed. The formulations were detailed in the study of [Large and Yeager \(2004\)](#);  $C_p$  is the specific heat of air at a constant pressure, which is assumed to be constant at  $1.005 \times 10^3 \text{ J kg}^{-1} \text{ K}^{-1}$ ; and  $q_s$  and  $T_s$  are the saturation specific humidity and sea surface temperature, respectively. Wind stress ( $\tau_s$ ) refers to the force exerted by the wind per unit area on a surface. As the wind blows across the surface of the ocean, it imparts a force on the water, causing it to move. The magnitude of the wind stress depends on the speed of the wind and the roughness of the ocean surface. The direction of the wind stress is parallel to the direction of the wind.

The net longwave radiation (LW) at the ocean surface is estimated by combining upward ocean surface radiation and downward atmospheric radiation. The LW heat flux component

### Chapter 3. Quantifying air-sea heat fluxes over Southeast Asia: intercomparison of available datasets and sensitivity ocean simulations

associated with the ocean surface radiation is negative, as the ocean loses heat. This heat flux is expressed as  $-\epsilon\sigma(SST)^4$ , where  $\sigma = 5.67 \times 10^{-8} \text{ Wm}^{-2}\text{K}^{-4}$  denotes the Stefan-Boltzmann constant and  $\epsilon$  represents the surface emissivity. Additionally, the ocean absorbs longwave energy from the atmosphere, which is provided by ECMWF, denoted as  $Q_a$ , thereby contributing to the net longwave radiation (LW).

$$LW = Q_a - \epsilon\sigma(SST)^4 \quad (\text{Eq. 3.5})$$

Where the emissivity  $\epsilon$  is taken to be 1.0 to account for the small, reflected fraction of  $Q_a$  (Lind and Katsaros 1986). The total heat flux (Eq. 3.1) is therefore expressed as a polynomial function of the model SST.

As can be seen in equations 3.4 and 3.5, using bulk formulae therefore allows to take into account the feedback from the ocean, namely through the impact of SST on SH and LW.

#### 3.2.2.2 Method 2: flux method

*Prescribing fluxes from the atmospheric model, i.e. not including feedback from the ocean.*

In this approach, not only heat flux components (SW, LW, LH, and SH) but also the water flux (evaporation minus precipitation) and momentum flux (wind stress) needed to force the model are provided directly by the atmospheric ECMWF analysis. It is noteworthy that this ECMWF analysis also uses bulk formulae but does not use the SST from the ocean model).

#### 3.2.3 Experimental design

The SYMPHONIE model was used to perform simulations for the entire SEA region. The grid covers the domain shown in Fig. 3.2 with a horizontal 4 km resolution, 1199 x 974 grid points, and 50 vertical levels with depths reaching 8000 m. The simulated period goes from January 2017 to December 2018.

The initial and open lateral boundary conditions for temperature, salinity, current velocities, and sea level were obtained from the daily reanalysis of the Copernicus Marine Systems (GLORYS 12v1), with a resolution of  $1/12^\circ$  and 50 regular depth levels. The tidal surface elevation and current at lateral boundaries were prescribed from the tidal atlas FES2014 (Lyard

### Chapter 3. Quantifying air-sea heat fluxes over Southeast Asia: intercomparison of available datasets and sensitivity ocean simulations

et al. 2021).

The CTL reference simulation is performed using method 1 (bulk method) with 3-hourly atmospheric forcing from the ECMWF analysis. This dataset is indeed widely used for ocean modeling since it is one of the most accurate and high-resolution available products. It has a spatial resolution of  $1/8^\circ$  and can provide atmospheric variables required for bulk formulae (see 3.2.1.1), including wind, precipitation, atmospheric temperature, dew point temperature, surface pressure, shortwave radiation, and humidity.

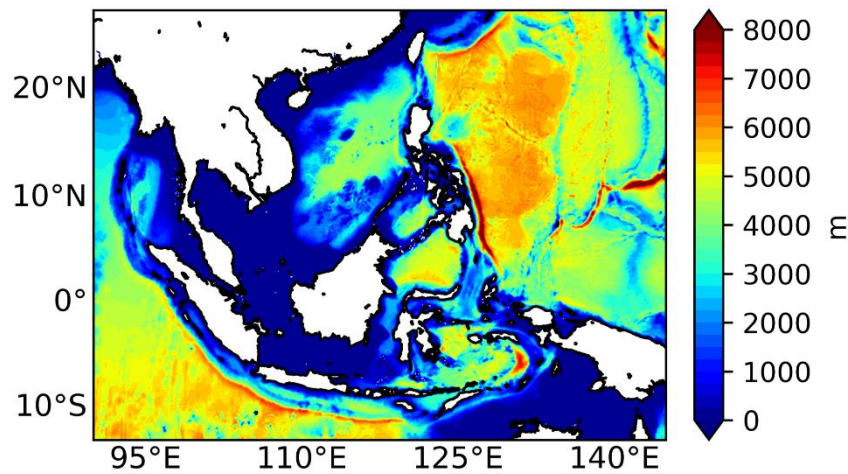


**Figure 3.2** Bathymetry and domain of the SEA configuration

In addition, we perform five simulations using this flux method to evaluate the sensitivity of simulated SST to heat flux forcing. In these simulations, the model was run with different prescribed heat fluxes forcing (SW, LW, LH, SH), while maintaining the same conditions for other inputs, such as wind stress and precipitation, as in the CTL simulation.

In this study, our goal is to evaluate the sensitivity of the simulated SST to the value of prescribed surface heat fluxes, but not to other parameters, such as the resolution of the forcing dataset. We thus created different heat flux datasets with the same grid characteristics as ECMWF but varying heat flux values. For that, we compared to ECMWF heat flux - five datasets (the identical ECMWF dataset, MERRA-2, CFS, JRA-55, and CTL, due to their availability over the study period, see 3.2.4), as well as the heat flux computed by the ocean model bulk formulae in the CTL simulation. For each heat flux component of each dataset, we calculated its ratio  $\alpha$  relative to ECMWF:

### Chapter 3. Quantifying air-sea heat fluxes over Southeast Asia: intercomparison of available datasets and sensitivity ocean simulations

$$\alpha = \frac{X_i}{X_{ECMWF}} \quad (\text{Eq. 3.6})$$

Where  $X$  is the mean of the heat flux component (SW, LW, LH, and SH) over the entire region and period, and  $i$  denotes the dataset (ECMWF, MERRA-2, CFSv2, JRA-55, and CTL).

Hence, for each dataset, we obtained a coefficient  $\alpha$  associated with each component of the heat flux (Table 3.1). Obviously, we have  $\alpha_{ECMWF}=1$ . We then multiplied ECMWF heat flux fields by  $\alpha$  to create new datasets with modified heat fluxes, namely ECMWF-ECMWF, ECMWF-MERRA-2, ECMWF-CFSv2, ECMWF-JRA-55, and ECMWF-CTL. Each of these new datasets has the same average over the entire region and period as the ECMWF dataset, while preserving the spatial and temporal variability found in the original fields. Information about these experiments is shown in Table 3.1.

#### 3.2.4 Heat flux datasets and data for model evaluation

- Heat flux datasets

##### ECMWF

As already explained, we use 3-hourly atmospheric forcing (atmospheric variables and fluxes) from ECMWF analysis, available on [www.ecmwf.int](http://www.ecmwf.int) at a spatial resolution of  $1/8^\circ$ .

##### MERRA-2

The Modern-Era Retrospective Analysis for Research and Applications version 2 (MERRA-2, Gelaro et al. 2017) is a global atmospheric reanalysis dataset produced by the NASA Global Modeling and Assimilation Office (GMAO). The heat flux from the MERRA-2 data set is available over the period 1981-present at a spatial resolution of  $0.25^\circ \times 0.25^\circ$ . It is updated every 6 hours.

### Chapter 3. Quantifying air-sea heat fluxes over Southeast Asia: intercomparison of available datasets and sensitivity ocean simulations

**Table 3.1** Values of net heat flux and its four components averaged over the SEA region (2017-2018) for ERA5 and 6 SYMPHONIE simulations. Blue texts indicate the heat flux forcing (HFF) dataset used to drive the model. \* Indicates that the value is equal to the mean heat fluxes value of ECMWF.  $\alpha$  values are calculated based on individual heat flux products compared to ECMWF. The values of SEA-averaged SST bias values and 0-100 m layer temperature changes (compared with 1st day of simulation) for the periods 2017-2018, 2018 and for the last day of simulation (30/12/2018) for the 6 simulations are also indicated.

Name And method	Atmospheric dataset	SW	LW	LH	SH	Qnet	SST bias			$\Delta(T - T(\text{initial}))$ (0-100m)		
							2017-2018	2018	30/12/2018	2017-2018	2018	30/12/2018
	<b>ERA5*</b>	210.7	-50.6	-132.9	-12	15.2						
<b>CTL, bulk</b>	<b>ECMWF</b>	211.8	-49.1	-142.7	-11.7	8.3	-0.25	-0.28	-0.34	-0.09	-0.1	-0.12
<b>EXP-01, flux</b>	<b>ECMWF -ECMWF</b>	<b>211.8*</b>	<b>-50.0*</b>	<b>-136.0*</b>	<b>-11.2*</b>	<b>14.6*</b>	0.83	1.05	1.10	0.42	0.43	0.49
	$\alpha$	1.000	1.000	1.000	1.000	1.000						
<b>EXP-02, flux</b>	<b>ECMWF -MERRA-2</b>	<b>190</b>	<b>-54.8</b>	<b>-133.4</b>	<b>-9.6</b>	<b>-7.8</b>	-0.91	-1.13	-1.42	-0.38	-0.59	-0.85
	$\alpha$	0.901	1.100	0.981	0.850	-0.534						
<b>EXP-03, flux</b>	<b>ECMWF -CFSv2</b>	<b>222.7</b>	<b>-50.5</b>	<b>-121.6</b>	<b>-7.2</b>	<b>43.4</b>	3.43	4.46	4.67	1.39	1.79	1.89
	$\alpha$	1.051	1.010	0.890	0.640	2.972						
<b>EXP-04, flux</b>	<b>ECMWF -JRA-55</b>	<b>200.0</b>	<b>-53.8</b>	<b>-153.4</b>	<b>-20.2</b>	<b>-27.4</b>	-2.07	-2.59	-2.97	-1.00	-1.43	-1.75
	$\alpha$	0.944	1.076	1.128	1.801	-1.876						
<b>EXP-05 flux</b>	<b>ECMWF -CTL</b>	<b>211.8</b>	<b>-49.1</b>	<b>-142.7</b>	<b>-11.7</b>	<b>8.3</b>	0.31	0.39	0.45	0.21	0.22	0.23
	$\alpha$	1.000	0.982	1.049	1.045	0.568						

### **Chapter 3. Quantifying air-sea heat fluxes over Southeast Asia: intercomparison of available datasets and sensitivity ocean simulations**

#### **CFSv2**

The heat flux dataset from the Climate Forecast System version 2 (CFSv2) Operational Analysis is produced by the National Center for Atmospheric Research (NCAR) and is available from 2011 to the present day with hourly frequency and a  $0.5^\circ$  horizontal resolution (approximately 56 km). CFSv2 analysis is based on a numerical weather prediction model that assimilates observations from a variety of sources, including satellites, weather stations, and buoys, to produce an estimate of the state of the atmosphere. Operational real-time CFSv2 model data are available on: <https://www.ncei.noaa.gov/products/weather-climate-models/climate-forecast-system>

#### **JRA-55**

JRA-55 reanalysis uses the four-dimensional variational data assimilation (4DVar) system of the Japan Meteorological Agency (JMA) (Kobayashi et al. 2015). It uses SST from the Centennial in Situ Observation-Based Estimates of the Variability of SSTs and Marine Meteorological Variables (Ishii et al. 2005). The global model used for the analysis has a TL319 spectral horizontal resolution (approximately 60 km) and 60 vertical levels in a hybrid coordinate. The heat flux dataset of JRA-55 is available from 1991 to 2020.

#### **ERA5**

Data from the fifth generation of the European Centre for Medium-Range Weather Forecasts (ECMWF) reanalysis, ERA5 (Hersbach and Dee 2016), are used as the reference dataset for the four heat flux components. ERA5 offers a higher spatial resolution ( $0.25^\circ$  versus  $0.75^\circ$ ) compared to its predecessor ERA-Interim (Dee et al. 2011) and has a revised data assimilation system and improved model physics (Josey et al. 2019). ERA5 accurately captures the magnitude and variability of near-surface air temperature and wind regimes: its higher spatial and temporal resolution effectively reduces the cold coastal biases identified in ERA-Interim, while also enhancing the accuracy of wind direction and wind speed in the escarpment (Tetzner et al. 2019). Additionally, ERA5 has been demonstrated to provide accurate air-sea heat flux estimates in specific regions worldwide (Pokhrel et al. 2020, Mayer et al 2023).

- **OSTIA sea surface temperature (SST)**

The Operational Sea Surface Temperature and Sea Ice Analysis (OSTIA), provided daily

### Chapter 3. Quantifying air-sea heat fluxes over Southeast Asia: intercomparison of available datasets and sensitivity ocean simulations

SST data at <https://data.nodc.noaa.gov/ghrsst/L4/GLOB/UKMO/OSTIA/> with a high resolution ( $1/20^\circ$  - approx. 6 km). OSTIA is used to evaluate the SST produced by each SYMPHONIE simulation over the simulated period 2017-2018. OSTIA, run over the global ocean by the Met Office in the United Kingdom, uses satellite data provided by the Global Heat Budget and Climate Experiment (GHRSSST) project together with in-situ observations. More details about the OSTIA system are found in Donlon et al. (2011).

#### 3.2.5 Statistical methods

The relationship between the simulated dataset  $S$  and observational dataset  $O$  (of the same element number  $n$ ) is investigated using three statistical parameters: the bias (mean error - ME), Root Mean Square Error (RMSE) and the Pearson correlation coefficient  $r$ .

We keep the same convention for the three-statistic formula:  $S_i$ ,  $O_i$ : the simulation series and observation series.

$$ME = \underline{S} - \underline{O} \quad (\text{Eq. 3.7})$$

$$RMSE = \sqrt{\frac{\sum_{i=1}^n (S_i - O_i)^2}{n}} \quad (\text{Eq. 3.8})$$

$$r = \frac{\sum_{i=1}^n (O_i - \underline{O})(S_i - \underline{S})}{\sqrt{\sum_{i=1}^n (O_i - \underline{O})^2 \sum_{i=1}^n (S_i - \underline{S})^2}} \quad (\text{Eq. 3.9})$$

To quantify the statistical significance of a correlation, we moreover compute for each correlation coefficient the associated p-value, defined as the probability that the null hypothesis (there is no relationship between the two variables being studied) is true. The smaller the p-value, the stronger the evidence that the null hypothesis is rejected. If p-value < 0.05, resp. 0.01, the correlation coefficient is called statistically significant at 95% (significant), resp. 99% (highly significant).

#### 3.3. Characteristics of heat fluxes in distributed dataset

In this chapter, a positive heat flux indicates that the flux is directed downwards into the ocean (heat gain for the ocean), while a negative sign indicates that the flux is directed upwards into the atmosphere (loss for the ocean). Figure 3.3 shows the annual mean spatial distribution

### Chapter 3. Quantifying air-sea heat fluxes over Southeast Asia: intercomparison of available datasets and sensitivity ocean simulations

of the net heat flux  $Q_{net}$  and its four components over the SEA region from all products described above. Table 3.1 provides for each dataset and each component the heat flux values averaged over the SEA region and over 2017-2018. SEA is a heat gain region for the ocean on an annual mean basis according to ERA5, ECMWF, CFSv2, and CTL products, although the precise  $Q_{net}$  value varies according to the dataset. Meanwhile, SEA is a heat loss region for the ocean in MERRA-2 and JRA-55. Figure 3.5 also shows that the primary term that balances the incoming SW into the ocean is LH loss, followed by LW loss, then SH loss which is much smaller.

#### 3.3.1 Spatial variability

The similarity between the spatial patterns of the annual mean  $Q_{net}$  in the five products, except for JRA-55, is quite striking. In particular, there is a high annual net heat loss in the northern part of the study area in all datasets, and a net heat gain over most of the equatorial region (10S -10N) in all datasets except for MERRA-2 and JRA-55. ERA5 has an annual mean net heat gain over the region of about  $15.2 \text{ W.m}^{-2}$ , close to the ECMWF  $Q_{net}$  value of  $14.6 \text{ W.m}^{-2}$  (Table 3.1). Both datasets produce similar spatial patterns, which is expected since they are produced from the same group of models and based on the same tools. CFSv2, on the other hand, produces a much stronger  $Q_{net}$  with a value of  $43.4 \text{ W.m}^{-2}$ , while JRA-55 and MERRA-2 produce (unrealistic) negative  $Q_{net}$  values ranging between  $-27.4 \text{ W.m}^{-2}$  and  $-7.8 \text{ W.m}^{-2}$ . CTL produces an intermediate  $Q_{net}$  value of  $8.6 \text{ W.m}^{-2}$ .

Overall, the distribution of SW heat gain is nearly identical in ERA5 ( $210.7 \text{ W.m}^{-2}$  on average over the period and region, Table 3.1) and ECMWF ( $211.8 \text{ W.m}^{-2}$  in the CTL simulation which uses SW from ECMWF), with the largest values of  $220 \text{ W.m}^{-2}$  in the southern hemisphere (from  $5^{\circ}\text{S}$ ), and the lowest SW values of less than  $170 \text{ W.m}^{-2}$  in the northern regions, where the Kuroshio current flows. MERRA-2 ( $190.0 \text{ W.m}^{-2}$ ) and JRA-55 ( $200.0 \text{ W.m}^{-2}$ ) show smaller SW values and CFSv2 displays higher SW ( $222.7 \text{ W.m}^{-2}$ ). This higher CFSv2 SW value may contribute to the high positive net heat flux in CFSv2 compared to other flux products.

Chapter 3. Quantifying air-sea heat fluxes over Southeast Asia: intercomparison of available datasets and sensitivity ocean simulations

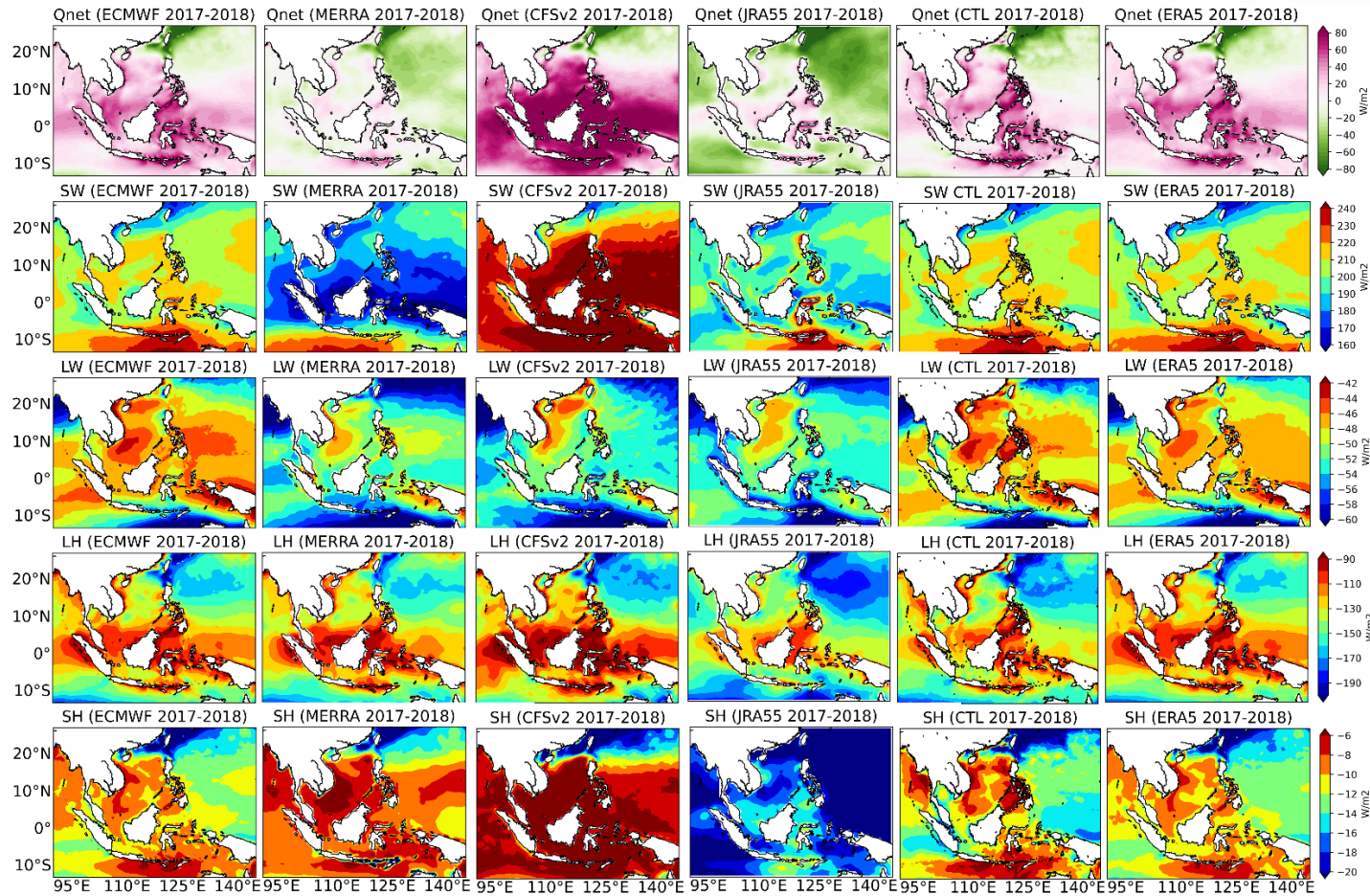


Figure 3.3 Annual mean of net heat flux and its four components from ECMWF, MERRA-2, CFSv2, JRA-55, CTL, and ERA5 for the period 2017-2018. Unit:  $W.m^{-2}$

### Chapter 3. Quantifying air-sea heat fluxes over Southeast Asia: intercomparison of available datasets and sensitivity ocean simulations

LW, LH and SW are systematically associated with heat losses for the SEA seas (Fig. 3.3 and 3.4). In the case of LW, although the magnitudes are different, all products indicate a minimum heat loss of 40 - 45  $\text{W.m}^{-2}$  over the 10°S-10°N equatorial region, including the entire South China Sea, while the region from 10 °S southward and the 90-95°E, 10-20°N region show the highest LW heat loss ( $> 60 \text{ W.m}^{-2}$ ). The average LW over the region shows a small variability among the datasets. ERA5, ECMWF, and CFSv2 have a LW heat loss of around 50  $\text{W.m}^{-2}$ , while the CTL simulation has the lowest LW loss (-49.1  $\text{W.m}^{-2}$ ) and JRA-55 and MERRA-2 produce higher LW losses 53.8 and 54.8  $\text{W.m}^{-2}$ , Fig. 3.3, Table 3.1).

The spatial pattern of LH loss distribution is similar in all products. The LH values of ERA5, ECMWF, and MERRA-2 vary around -133.0  $\text{W.m}^{-2}$ . JRA-55 has the highest LH loss in the northern Philippine Sea, while CFSv2 has the weakest loss in the equatorial region. Both datasets also exhibit the highest loss (-153.4  $\text{W.m}^{-2}$ ) and lowest loss (-121.6  $\text{W.m}^{-2}$ ) in the average LH over the entire SEA region compared to the other datasets. Therefore, the negative value of  $Q_{\text{net}}$  in JRA-55 could be explained by a lower SW gain and higher LH loss.

The weak heat loss due to SH varies around 10  $\text{W.m}^{-2}$  for all datasets, except for JRA-55 with SH values twice larger compared to other products (Fig. 3.3 and Table 3.1).

#### 3.3.2 Seasonal cycle

To further examine the differences between the six products, seasonal variations of  $Q_{\text{net}}$  and its four components were averaged over the SEA region (Fig. 3.4). Despite differences in magnitudes, the semi-annual cycle of  $Q_{\text{net}}$  over the SEA region is clearly described by all six products, with a primary maximum in April and a secondary maximum in September (Fig. 3.4a). CFSv2 has the highest values for all months, while JRA-55 has the lowest values, consistently with the analysis of spatial variability and average above.

The semi-annual cycle in  $Q_{\text{net}}$  is determined by the SW cycle (Fig. 3.4b), which peaks in April and September during the equinox. There are significant differences in SW, of 60  $\text{W.m}^{-2}$  between the largest (CFSv2) and smallest (MERRA-2) in June.

LH in most products exhibits a seasonal cycle with a minimum loss in April and a maximum loss in December and January (Fig. 3.4d). CFSv2 has a semi-annual cycle with a secondary peak in October, which is distinct from other products. JRA-55 produces the strongest LH loss

### Chapter 3. Quantifying air-sea heat fluxes over Southeast Asia: intercomparison of available datasets and sensitivity ocean simulations

from the ocean, and its average magnitude is more than  $30 \text{ W m}^{-2}$  weaker than CFSv2.

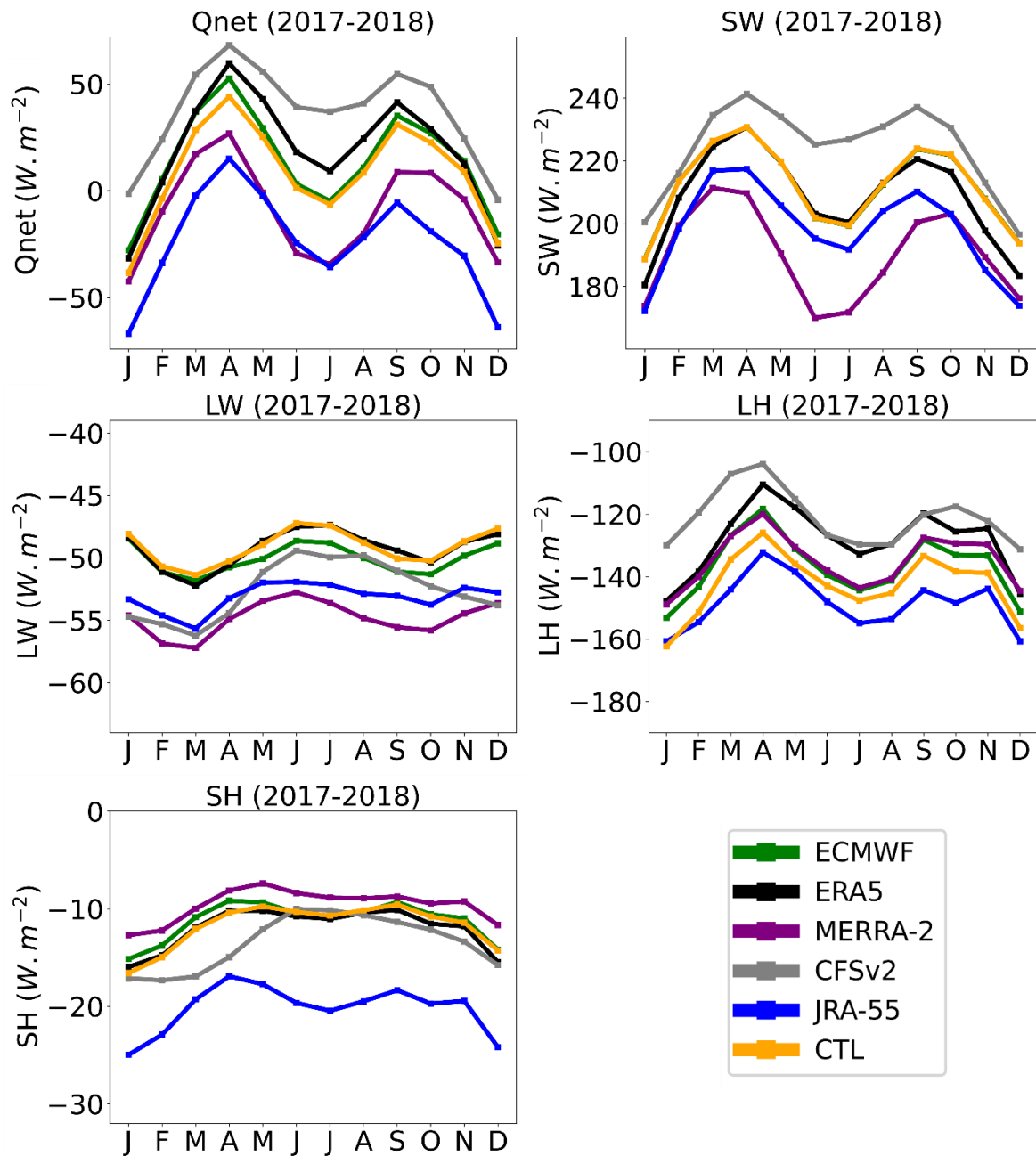


**Figure 3.4** Seasonal variability of (a) QNET, (b) SW, (c) LW, (d) LH, and (e) SH over the SEA. The positive means downward flux, while the negative represents the upward.

A weak semi-annual cycle is observed in LW (Fig. 3.4c). The LW cycle of CTL is similar to ERA5 in both magnitude and pattern. CFSv2 LW has the largest difference between March and June (about  $7.0 \text{ W.m}^{-2}$ ). SH is weak, about 10% of LH (Fig 3.4e). However, there is one

### **Chapter 3. Quantifying air-sea heat fluxes over Southeast Asia: intercomparison of available datasets and sensitivity ocean simulations**

notable feature: JRA-55 SH has a significantly stronger magnitude than all products.

Net heat flux  $Q_{net}$  is the balance between net downward SW and net upward LW, LH, and SH, thus compensating for the differences in the four flux components. In general, the lower  $Q_{net}$  products (MERRA-2 and JRA-55) are due to weaker SW and stronger LH loss, while the higher  $Q_{net}$  products (ERA5, ECMWF, CFSv2, and CTL) are due to stronger SW and potentially less LH loss (CFSv2). To see this more clearly, the annual means of  $Q_{net}$  and the four flux components contributing to the following heat flux products are listed in [Table 3.1](#). In conclusion, the differences between SW and LH are the two main sources of differences in  $Q_{net}$ , followed by differences in LW.

#### **3.4 Results of sensitivity simulations**

Chapter 1 of the thesis has overviewed the high uncertainty in the estimation of heat fluxes (which depends on the data source and bulk formulas) affects the simulation of SST from ocean models. In this section, we investigate the sensitivity of SST from SYMPHONIE simulations to different heat flux forcings and heat flux computation methods (bulk or flux). The spatial and temporal distribution of SST is evaluated against OSTIA satellite data. Additionally, the difference in sea water temperature of the 0 to 100 m layer from the initial condition is also presented.

##### **3.4.1 SST spatial distribution**

[Figure 3.5](#) shows the spatial distribution of SST from the model and OSTIA observations averaged for the year 2018. The maps of bias and temporal correlation coefficient between the daily simulated and observed SST are also presented. The SST bias and change of the 0-100m layer temperature over different periods is provided in [Table 3.1](#).

According to OSTIA observations, the annual mean SST for the entire region is about 28.39 °C. The equatorial region from -5°S to 10°N has the warmest SST, around 29-30°C. The northern Southeast Asia region from 20°N onwards has the colder SST, under 26°C.

Chapter 3. Quantifying air-sea heat fluxes over Southeast Asia: intercomparison of available datasets and sensitivity ocean simulations

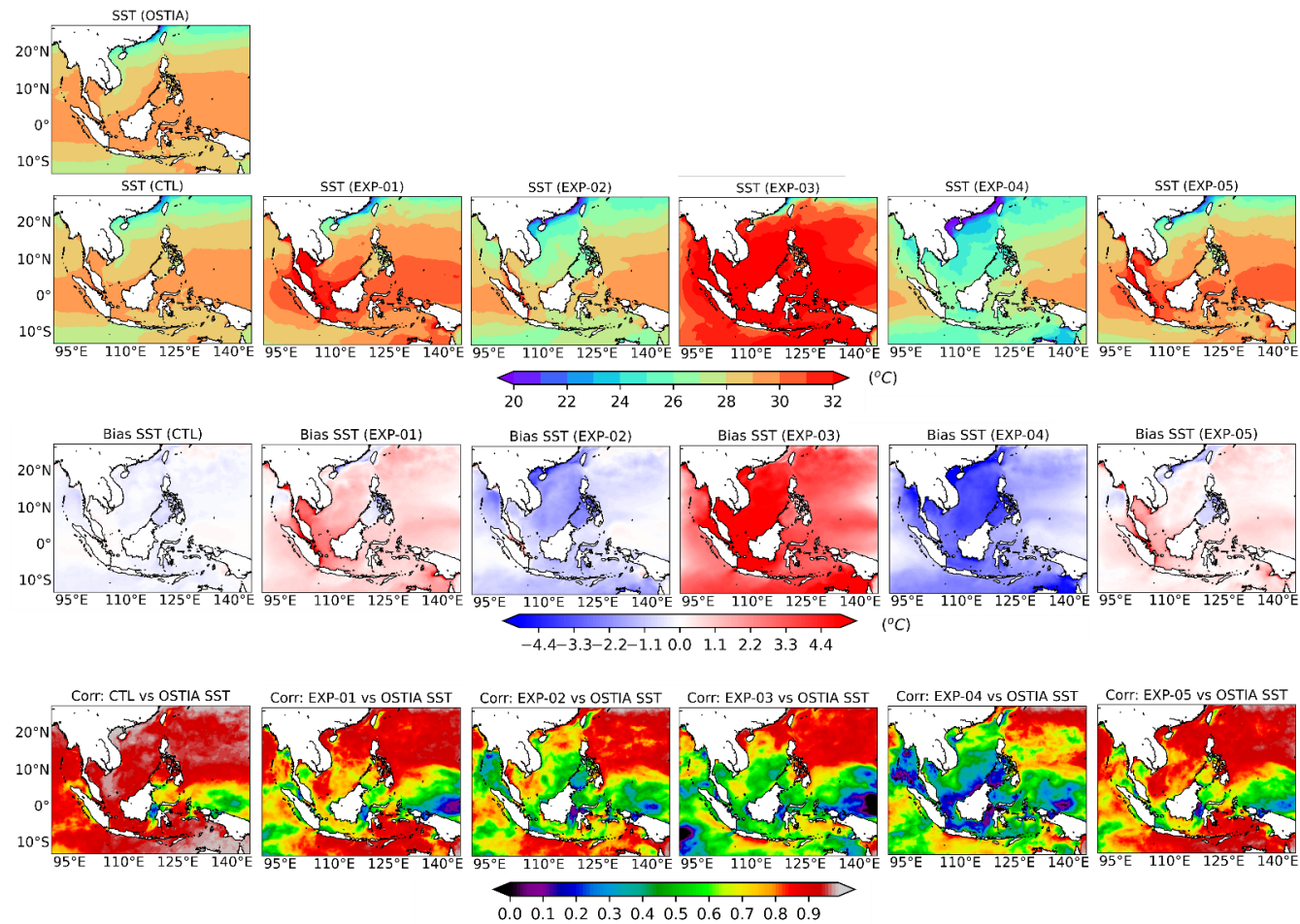


**Figure 3.5** Annual mean of SST obtained from six SYMPHONIE simulations compared with the observation data from OSTIA for 2018. Annual mean errors (bias) and daily Pearson correlation coefficients obtained from six simulations compared to OSTIA SST.

### **Chapter 3. Quantifying air-sea heat fluxes over Southeast Asia: intercomparison of available datasets and sensitivity ocean simulations**

The simulated SST pattern is similar for CTL and EXP-05 and quite close to OSTIA, with annual SEA mean values of 28.11°C and 28.86°C, i.e., bias of respectively -0.28°C and +0.39°C (Table 3.1). The positive bias between EXP-05 and observation occurs in most regions except the Sulu Sea, Andaman Sea, and the northern part of the region where the Kuroshio current is located, and hardly exceeds 0.5°C (Fig. 3.5). Meanwhile, the negative SST bias compared to OSTIA is very small (<0.5°C) for CTL for the entire region.

SST from the EXP-01 simulation also has a spatial distribution similar to observations but the SST values are higher in most areas, especially the waters of Malaysia. The annual SEA mean value of SST in the EXP-01 simulation is 29.49°C, with a corresponding error of 1.05°C.

CFSv2 produces a significantly higher SST simulation over the entire region, with an annual SEA mean value of 32.85°C over 2018. Meanwhile, EXP-02 and EXP-04 both produce colder SST than observations. The annual mean value for the entire region of EXP-02 is 27.25°C and EXP-04 is 25.79°C, i.e., biases of -1.13°C and -2.59°C. The negative error in these two simulations is observed over the entire study region.

#### **3.4.2 Surface temperature temporal evolution**

The correlation coefficient between simulated and observed daily SST time series was also calculated over the 2017-2018 period. In general, all models show a highly significant positive correlation ( $r > 0.9$ ,  $p\text{-values} < 0.01$ ) in the northern Southeast Asia region, from 20°N onwards, whereas the model and observations are much less correlated in the equatorial region from 115°E to 145°E, especially for EXP-03 and EXP-04. CTL has a strong positive correlation coefficient above 0.95 observed in most regions. EXP-02, EXP-03, and EXP-04 have low correlation coefficients and are not significantly correlated with OSTIA in the equatorial region.

The daily time series of SST bias between the model and observations over the period 2017-2018 shows results consistent with the spatial distribution (Fig. 3.6a). CTL has the smallest negative bias compared to the other five simulations for the entire period, with no significant SST drift. EXP-02 and EXP-04 have progressively increasing negative SST biases that exceed -1.5 °C and -3.0°C at the end of the simulation, respectively. Conversely, EXP-05 and EXP-02 both have positive biases throughout the time. EXP-03 has the largest SST bias, equal to 3.4°C over 2017-2018, and exceeding 4°C at the end of the simulation.

### Chapter 3. Quantifying air-sea heat fluxes over Southeast Asia: intercomparison of available datasets and sensitivity ocean simulations

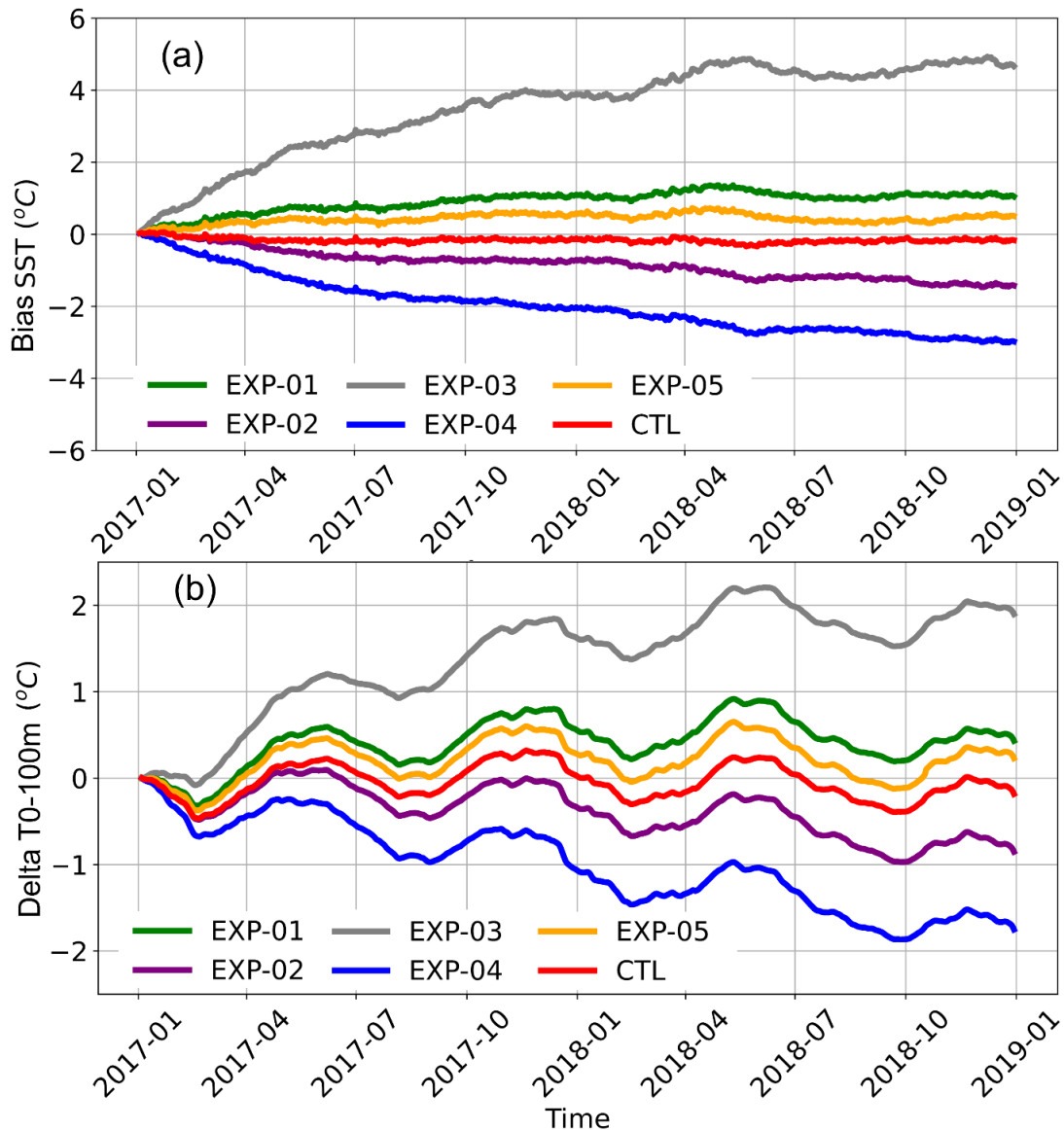


**Figure 3.6** Daily time series of (a) the SST bias of six SYMPHONIE simulations and (b) the change of the temperature of the 0 - 100m layer (T0-100m) compared to the initial condition (i.e., temperature of the first day of simulation).

The time series of the change in temperature of the 0 to 100m layer (T0-100m) compared to the initial value is shown in Fig. 3.6b. The T0-100m difference shows seasonal fluctuations in all simulations, related to the seasonal climate variability of the region, with two periods of maximum temperature during the year (May-June and October-November). EXP-03 has a positive T0-100m change for the entire time, and the difference compared to January 1st, 2017,

### **Chapter 3. Quantifying air-sea heat fluxes over Southeast Asia: intercomparison of available datasets and sensitivity ocean simulations**

reaches 1.9°C at the end of the simulation on December 31st, 2018. Conversely, EXP-04 has a negative change that exceeds -1.7°C after two years. CTL and EXP-05 are the two simulations with the smallest change from the initial condition value, of respectively -0.09 and 0.21°C after two years.

Both time series of SST bias and T0-100m change indicate that, except CTL and EXP-05, which have stable differences throughout the simulation period, all other simulations show increasing differences.

In summary, among the five simulations using flux method, EXP-05, which uses heat flux forcing computed from CTL, is the closest to observations. Moreover, the SST simulated from the CTL simulation, i.e., using the bulk method, is closer to observations than SST from all the simulations using the flux method. Using heat flux bulk formulae therefore provides the best SST simulation, as expected. Moreover, using CTL fluxes to force a simulation using flux method provides similar results as the CTL simulation itself, with a very small SST bias. Therefore, fluxes computed from SYMPHONIE using bulk formulae can be considered as a reference value for the evaluation of other datasets. Note that this relies on the assumption that SYMPHONIE realistically reproduces the ocean dynamics over the area, in particular the temperature distribution over the horizontal and vertical, if correct fluxes are prescribed, which seems justified from the analysis of SST above.

#### **3.4.3 Relationship between temperature differences and heat flux**

We assess the relationship between simulated SST and heat flux values by showing the scatter plot (Fig. 3.7) of the SST bias and the T0-100m change over 2018 against the corresponding heat flux forcing values over 2017-2018 for the five “flux” simulations and performing linear regression analysis between temperatures and fluxes.

Results show that the linear relationship between heat fluxes and seawater temperature, as well as the statistical significance at 95% of that relationship, is similar for both temperature factors (SST bias and T0-100 change). The statistical significance level of the relationship between seawater temperature and Qnet is the largest with correlation coefficient  $r=0.99$  with  $p$ -value  $<0.01$ , followed by SW and LH with  $r > 0.84$ , SH with  $r > 0.80$ , and finally, LW has the smallest  $r$  of about 0.65 with  $p$ -value  $<0.1$ . EXP-04 simulation using HFF from JRA-55 shows the largest negative seawater temperature difference, which is largely related to the

### **Chapter 3. Quantifying air-sea heat fluxes over Southeast Asia: intercomparison of available datasets and sensitivity ocean simulations**

strong values of LH and, to a lesser extent, SH losses in this dataset (columns 4 and 5 of [Fig. 3.7](#)), that explain the strongly negative value of Qnet (column 1). Conversely, the EXP-03 simulation (using HFF from CFSv2) shows the largest positive difference, related to weak values of LH and SH losses and strong value of SW gain that explain the strongly positive Qnet.

In summary, when the model uses the flux method, the simulated SST is positively correlated with provided heat fluxes. As a result, when the ocean receives a larger amount of heat (CFSv2) the model produces a larger positive SST bias, and it is the opposite when the ocean loses more heat (MERRA-2 and JRA-55). In the method, realistic surface fluxes are directly applied to the ocean model, and the SST is allowed to evolve freely without feedback between the ocean and the atmosphere, which can lead to large model errors, but allows to really explore the answer of the ocean model without any kind of relaxation toward observed SST. An anomalously positive downward heat flux can heat the ocean indefinitely without any release of the excess heat back into the atmosphere, whereas simulations using the bulk method, include feedback from the ocean to the atmosphere, which would lead to an adjustment of heat flux.

### Chapter 3. Quantifying air-sea heat fluxes over Southeast Asia: intercomparison of available datasets and sensitivity ocean simulations

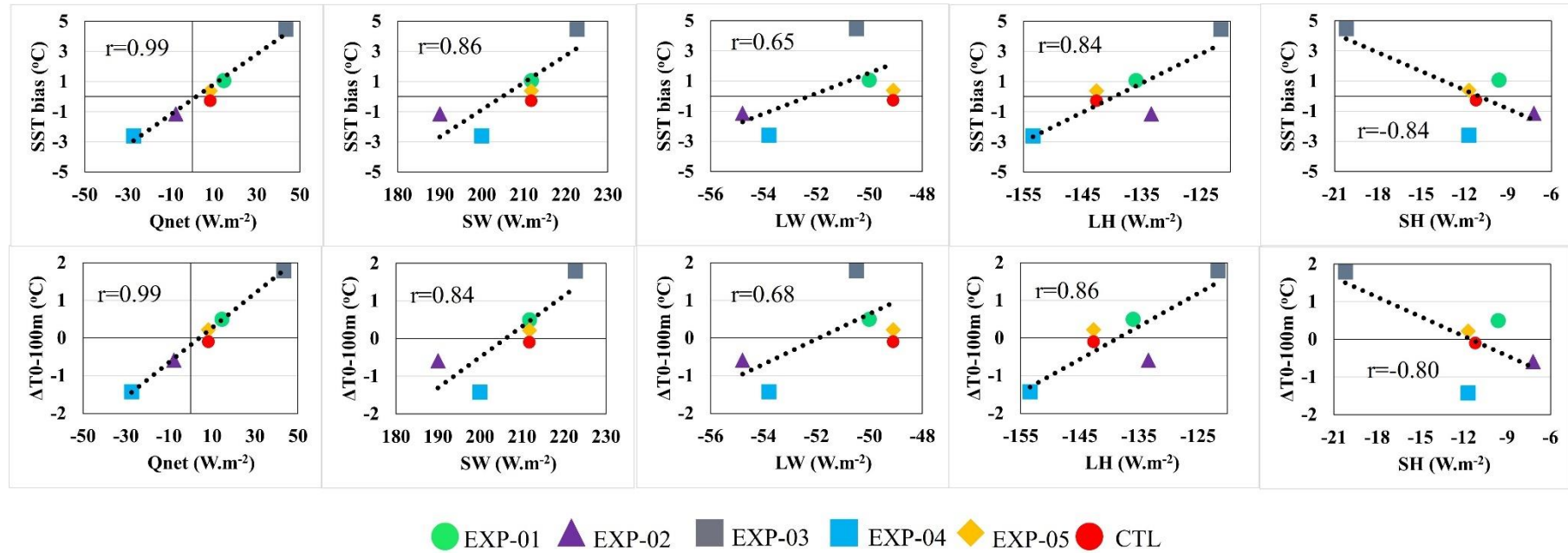


**Figure 3.7** Scatterplot of SST bias and T0-100 change over 2018 versus Qnet averaged over SEA and 2017-2018 for the five SYMPHONIE flux simulations, and corresponding linear regression analysis (black dotted line). The Pearson correlation coefficient between the temperature and heat flux is denoted as r with p-value <0.01, except r between SST bias and LW with p-value <0.1.

## **Chapter 3. Quantifying air-sea heat fluxes over Southeast Asia: intercomparison of available datasets and sensitivity ocean simulations**

### **3.5 Extending our conclusions over longer periods.**

We showed that a SYMPHONIE simulation using bulk formulae with atmospheric variables from ECMWF produces the closed SST to observations for the period 2017-2108. The annual mean Qnet for the entire region calculated from the model, which can be considered as a benchmark value, is  $8.3 \text{ W.m}^{-2}$ , lower than the ECMWF and ERA5 estimates of  $6.3 \text{ W.m}^{-2}$  and  $6.9 \text{ W.m}^{-2}$ , respectively (Table 3.1). In this section, we thus performed a simulation for the 2009-2018 10-year period (referred to as SYM(0918), again using the bulk method with atmospheric variables from ECMWF, to extend our benchmark estimates over a longer period. The annual time series of Qnet and its four components from the model output are first compared to the heat flux computed from ECMWF and ERA5 (Fig. 3.8) and the average values over the 2009-2018 period is then put into perspective in respect to other datasets (Table 3.2).

#### **3.5.1 Comparison between heat flux computed from SYMPHONIE and ECMWF products over 2009-2018**

SST simulated from SYM(0918) has a stable negative bias, equal on average to  $-0.21^\circ\text{C}$  and varying between  $-0.12^\circ\text{C}$  (in 2013) and  $-0.3^\circ\text{C}$  (in 2018), and with similar values as CTL in 2017 and 2018. The model produced the smallest SST error in the period 2011-2016 (Fig. 3.8a). The Qnet of SYM(0918) is also similar to CTL Qnet for the period 2017-2018 (Fig. 3.8b).

Despite an almost constant  $\sim -5.8 \text{ W.m}^{-2}$  difference, SYM(0918) Qnet has the same yearly chronology as ERA5 for the entire period, suggesting that ERA5 systematically overestimates Qnet by  $\sim 6 \text{ W.m}^{-2}$ . The chronology of ECMWF Qnet is also similar to SYM(0918), although larger differences occur over the 2011-2016, the period of the smallest SST bias in SYM(0918). The difference of LH and SH between the model and ECMWF as well as ERA5 are the two main components leading to the difference of Qnet between SYM(0918) and those datasets (Fig. 3.8e,f). This could be explained by the different bulk formulae used in SYMPHONIE and ECMWF models.

Those results show that the difference in net heat flux between the long SYMPHONIE simulation SYM(0918) and ECMWF and ERA5 is similar to the difference observed with the short simulation CTL, about  $6 \text{ W.m}^{-2}$ , and that SYMPHONIE simulation based on bulk formulae can be used to build realistic estimates of air-sea heat flux over SEA, which can serve

### Chapter 3. Quantifying air-sea heat fluxes over Southeast Asia: intercomparison of available datasets and sensitivity ocean simulations

as a benchmark for future studies.

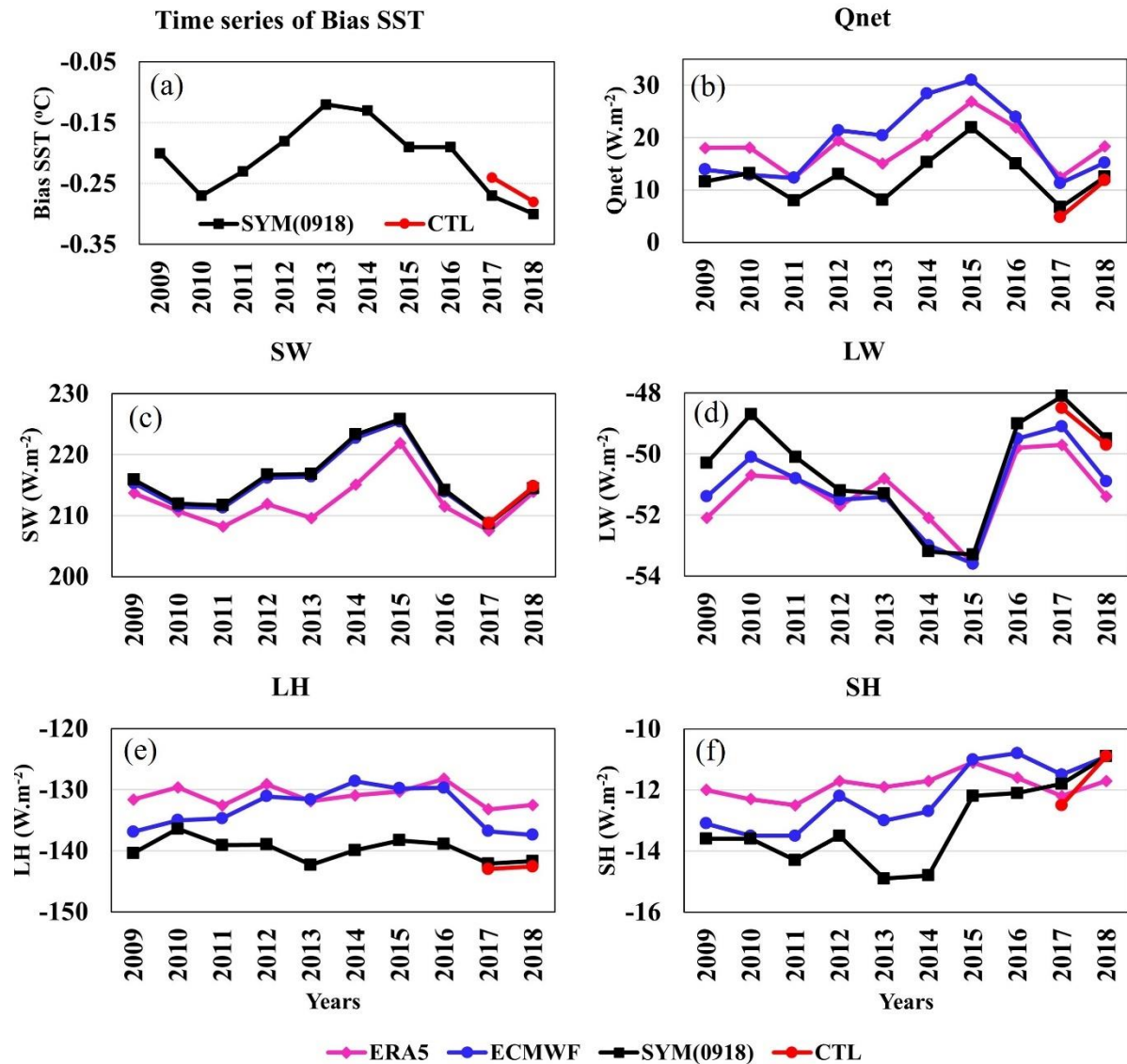


**Figure 3.8** Yearly time series of SST bias in SYMPHONIE simulations and heat fluxes computed from SYMPHONIE “bulk” simulations, ECMWF analysis and ERA5 reanalysis.

#### 3.5.2 Extension to other heat flux datasets

We analyzed the representation of heat flux in different distributed datasets in Section 3.3, showing that the estimation of heat flux over the SEA region for the period 2017-2018 is highly uncertain, with a range of  $Q_{net}$  values varying from  $-27.4 \text{ W.m}^{-2}$  to  $43.4 \text{ W.m}^{-2}$ . The two main sources of differences in  $Q_{net}$  are the differences in SW and LH, followed by errors in LW. To extend those conclusions over a longer period and to increase their robustness, the

### Chapter 3. Quantifying air-sea heat fluxes over Southeast Asia: intercomparison of available datasets and sensitivity ocean simulations

climatological means of Qnet and of the four heat flux components for the period 2009-2018 for 7 datasets, i.e. the 5 datasets studied above plus NCEP1 and NCEP2, are listed in Table 3.2 and compared with heat flux produced by SYM(0918).

**Table 3.2** Average over SEA of Qnet, SW, LW, LH, SH estimated from different datasets for the period 2009-2018, except CMIP6 multi model ensemble (CMIP6 MME) (2009-2014). This data set is presented in detail in chapter 4, section 4.2.1. Differences compared to SYM(0918) are indicated in italics. Positive (negative) differences are highlighted in blue (red). Unit: W.m<sup>-2</sup>

Models	Qnet	SW	LW	LH	SH
<b>SYM(0918)</b>	12.5	216.0	-50.5	-139.8	-13.2
<b>ECMWF</b>	18.7	216.0	-51.1	-133.2	-13.0
<i>Bias</i>	<u>6.2</u>	<u>0.0</u>	<u>-0.6</u>	<u>6.6</u>	<u>0.2</u>
<b>ERA5</b>	18.3	212.4	-51.3	-131.0	-11.9
<i>Bias</i>	<u>5.8</u>	<u>-3.6</u>	<u>-0.8</u>	<u>8.8</u>	<u>1.3</u>
<b>MERRA-2</b>	-7.8	188.1	-54.5	-131.9	-9.5
<i>Bias</i>	<u>-20.3</u>	<u>-27.9</u>	<u>-4.0</u>	<u>7.9</u>	<u>3.7</u>
<b>CFSv2</b>	42.2	234.0	-45.5	-129.0	-8.3
<i>Bias</i>	<u>29.7</u>	<u>18.0</u>	<u>5.0</u>	<u>10.8</u>	<u>4.9</u>
<b>JRA-55</b>	-24.1	199.6	-53.9	-149.5	-20.2
<i>Bias</i>	<u>-26.6</u>	<u>-16.4</u>	<u>-3.4</u>	<u>-9.7</u>	<u>-7.0</u>
<b>NCEP 1</b>	7.2	193.5	-50.3	-124.8	-11.2
<i>Bias</i>	<u>-5.3</u>	<u>-22.5</u>	<u>0.2</u>	<u>15.0</u>	<u>2.0</u>
<b>NCEP2</b>	-3.8	194.1	-47.0	-141.3	-9.6
<i>Bias</i>	<u>-16.3</u>	<u>-21.9</u>	<u>3.5</u>	<u>-1.5</u>	<u>3.6</u>
<b>CMIP6 MME</b>	6.5	208.4	-50.7	-137.8	-13.4
<i>Bias</i>	<u>-6.0</u>	<u>-7.6</u>	<u>-0.2</u>	<u>2.0</u>	<u>-0.2</u>

Qnet estimates are clustered into two groups, with positive values for the five-member group (CFSv2, ECMWF, ERA5, SYM(0918) and NCEP1) and negative values for the three-

### **Chapter 3. Quantifying air-sea heat fluxes over Southeast Asia: intercomparison of available datasets and sensitivity ocean simulations**

member group (MERRA-2, JRA-55 and NCEP2). For the positive net heat flux group, the SEA averaged  $Q_{net}$  is  $6.5 \text{ W.m}^{-2}$  by CMIP6 MME,  $7.2 \text{ W.m}^{-2}$  by NCEP1,  $12.5 \text{ W.m}^{-2}$  by SYM(0918),  $18.3 \text{ W.m}^{-2}$  by ERA5,  $18.7 \text{ W.m}^{-2}$  by ECMWF and  $42.2 \text{ W.m}^{-2}$  by CFSv2. It is apparent that the CFSv2 SW was the highest estimate and LH had a lower estimation.

For the negative net heat flux group, the SEA-averaged  $Q_{net}$  is  $-24.1 \text{ W.m}^{-2}$  by JRA-55,  $-7.8 \text{ W.m}^{-2}$  by MERRA-2, and  $-3.8 \text{ W.m}^{-2}$  by NCEP2. JRA-55 has an overestimated LH loss, and twice as much SH loss as the other datasets, explaining the large negative estimate of JRA-55  $Q_{net}$ .

Overall, based on SYM0918: CFSv2 clearly produces strong overestimation, MERRA-2 and JRA-55 and NCEP2 strong underestimation leading to even negative net heat fluxes. The closest datasets to SYM0918 are ECMWF and ERA5 ( $\sim +6 \text{ W.m}^{-2}$ ), NCEP1 ( $\sim -5 \text{ W.m}^{-2}$ ) and CMIP6 MME ( $\sim -6 \text{ W.m}^{-2}$ ). Note however that the low spatial resolution of NCEP1 makes it not very adapted to ocean model forcing. CMIP6 MME is a composite of 30 of the latest climate models. In the next chapter, we will use this dataset to assess estimates of heat flow over longer timescales and project future changes in them.

#### **3.6. Chapter's conclusion**

In this chapter, we used the 3-D hydrostatic ocean circulation model SYMPHONIE to perform six short simulations for the period 2017-2018 with two methods, bulk and flux, to examine the sensitivity of the model SST to different heat flux forcings.

First, the heat flux datasets used in the study, extracted from ECMWF and CFSv2 analysis and MERRA-2, JRA-55 and ERA5 reanalysis were examined in terms of spatial distribution, seasonal cycle, and annual mean values. SEA is a net heat gain region on an annual mean basis according to ERA5, ECMWF, CFSv2, although the exact amount of  $Q_{net}$  obtained from the basin varies by product, and a net heat loss region for MERRA-2 and JRA-55. In general, the low (and negative) net heat flux products (MERRA-2 and JRA-55) are due to weaker SW and stronger LH loss, while the high (and positive) net heat flux products (ERA5, ECMWF, CFSv2) are due to stronger SW and potentially less LH loss (especially CFSv2). The differences between SW and LH are the two main sources of differences in  $Q_{net}$ , followed by differences in LW.

We then evaluated based on OSTIA satellite data the spatial and temporal distribution of

### **Chapter 3. Quantifying air-sea heat fluxes over Southeast Asia: intercomparison of available datasets and sensitivity ocean simulations**

SST simulated in the sensitivity simulations based on the use of heat fluxes of similar spatiotemporal patterns but different average values built from 4 analyzed datasets (ECMWF, JRA55, MERRA-2 and CFSv2) and from a simulation using bulk formulae (CTL) (note that we did not perform a simulation based on ERA5 given its similarity with ECMWF analysis). SST patterns from simulation using fluxes computed by SYMPHONIE bulk formulae from ECMWF atmospheric variables were similar to the OSTIA pattern, with an annual mean bias of  $-0.28^{\circ}\text{C}$  over 2018. With simulations using the flux method, the positive SST bias from the simulation using CTL flux is the smallest ( $0.39^{\circ}\text{C}$  over 2018). SST from the flux simulation based on ECMWF values produced a slightly higher overestimation ( $1.05^{\circ}\text{C}$ ), and the simulation based on CFSv2 produced significant SST overestimation over the entire region ( $4.46^{\circ}\text{C}$ ). Simulations based on MERRA-2 and JRA-55 underestimated SST with biases of  $-1.13^{\circ}\text{C}$  and  $-2.59^{\circ}\text{C}$  for the SEA region over 2018. The simulation using bulk formulae had a highly significant temporal correlation coefficient ( $>0.95$ ) observed in most regions, and flux simulations based on MERRA-5, CFSv2 and JRA-555 had low correlation coefficients and were nearly uncorrelated in the equatorial region. The relationship between seawater temperature and net heat flux ( $Q_{\text{net}}$ ) has been shown to be strong and highly significant, explaining the differences of SST and surface layer temperature observed among the sensitivity simulations. SST simulated from heat fluxes computed from SYMPHONIE bulk formulae is therefore the closest to observations. This suggests that fluxes computed from SYMPHONIE bulk formulae can be used as benchmark values to evaluate other datasets.

We extended our analysis by running a 10-year simulation using bulk formulae. The  $\sim 6$   $\text{W}\cdot\text{m}^{-2}$  difference compared to ECMWF and ERA5 obtained for the 2017-2018 simulation remained the same for the 2009-2018 simulation. The main cause of this systematic  $Q_{\text{net}}$  difference is the difference of the LH and SH, which can be explained by the use of different bulk heat flux formulae as well. The model heat fluxes were finally compared to a variety of heat flux products, which revealed a large uncertainty in the estimation of air-sea exchange over the SEA region. ERA5 and ECMWF, despite a possible overestimation of  $\sim 6$   $\text{W}\cdot\text{m}^{-2}$ , appear as the best products in terms of air-sea heat flux values. Since the study region is an open ocean, and a key area for ocean thermohaline circulation (SCSTF and ITF), this study raises the question about the role of the air-sea exchange at the SEA in balancing the global energy budget. A physically consistent heat budget analysis over the SEA, as done by Trinh et al. (2023) over the SCS, would contribute to an improved understanding of heat fluxes and would help to achieve a globally balanced budget.



# Chapter 4. CMIP6 analysis: heat fluxes estimation and the role of the climate change

## Contents

Chapter 4. CMIP6 analysis: heat fluxes estimation and the role of the climate change ..	103
4.1 Introduction.....	104
4.2. Data and method .....	107
4.2.1 CMIP6 GCMs.....	107
4.2.2 Observations and Reanalysis datasets .....	107
4.2.3 Methods .....	107
4.3. Seasonal and spatial variability of heat fluxes .....	110
4.3.1 Spatial distribution.....	110
4.3.2 Seasonal cycle.....	114
4.4 Future projections .....	118
4.4.1 Future projections in the multi-model ensemble mean .....	118
4.4.2 Future projections in low and high warming groups .....	121
4.5 Models' sensitivity to the magnitude of SST change .....	123
4.6. Conclusions of chapter.....	127

## Chapter 4. CMIP6 analysis: heat fluxes estimation and the role of the climate change

### 4.1 Introduction

Air-sea net heat flux (hereafter  $Q_{net}$ ) is defined as the sum of shortwave radiation flux (SW), outgoing longwave radiation flux (LW), sensible heat flux (SH), and latent heat flux (LH) at the interface between the air and the ocean. A positive (negative value) of  $Q_{net}$  indicates a heat gain (loss) for the ocean: the SW gain is greater (less) than the LW, LH, and SH losses.  $Q_{net}$  plays an important role in air-sea interactions on various scales (Yu and Weller 2007). Solar radiation absorbed by the ocean not only promotes the movement of ocean water, but also supplies energy to the atmosphere to propel atmospheric circulation through processes like evaporation, long-wave radiation, and thermal induction of sensible heat flux (Kiehl and Trenberth 1997; Trenberth et al. 2009). Accurately determining  $Q_{net}$  across different spatial and temporal scales is crucial for correctly assessing the total heat budget and understanding long-term climate change and its related responses (Teray et al. 2012, Zhou et al. 2018). However, estimating  $Q_{net}$  still remains challenging due to large uncertainties: datasets of each heat flux component obtained from different sources (e.g satellite-based, ship-based, or reanalysis from numerical weather prediction) can show significant biases (Brunke et al. 2003, Zhang et al. 2004, Yu et al. 2004). Previous studies revealed that satellite estimates tend to exhibit a heating bias for the ocean, while reanalysis estimates tend to exhibit a cooling bias (Park et al 2005, Valdivieso et al 2017). Song and Yu (2013) indeed showed that the reanalysis group including NCEP1 (Kalnay et al. 1996), NCEP2 (Kanamitsu et al. 2002), and ERA-Interim (Dee et al. 2011) exhibited relatively low net heat flux values, with a globally averaged  $Q_{net}$  ranging from 1 to 11  $W.m^{-2}$ . In contrast, the ship-based product NOCSv2.0 (Berry and Kent 2009) yielded a  $Q_{net}$  of 25  $W.m^{-2}$ , while the satellite-based product OAFlux + ISCCP (Yu et al. 2008; Zhang et al. 2004) indicated a  $Q_{net}$  of 30  $W.m^{-2}$ .

The estimation of  $Q_{net}$  and its four components also relies on model outputs. Global Climate Models (GCMs) play a crucial role in providing and comparing climate projections across the different phases of the Coupled Model Intercomparison Projects (CMIP), including Phase 5 (CMIP5; Taylor et al. 2012) and Phase 6 (CMIP6; Eyring et al. 2016). These models are fundamental for understanding past, present, and future climate changes, forming the foundation of the Assessment Reports published by the Intergovernmental Panel on Climate Change (IPCC) (e.g. IPCC 2013; IPCC 2021). Ensuring an accurate representation of air-sea heat fluxes in these GCMs is needed for reliable climate projections, and estimating air-sea heat fluxes at the global and regional scales helps to evaluate and improve these models. Previous studies indicated that CMIP5 GCMs often overestimated LH in the tropics, although

## Chapter 4. CMIP6 analysis: heat fluxes estimation and the role of the climate change

they could effectively capture LH spatial and temporal patterns (Cao et al. 2015, Zhang et al. 2018). Wild (2020) demonstrated that the multi-model means of the latest CMIP6 GCMs produced a better global average of flux components compared to previous model generations, especially concerning surface downward SW and downward LW radiation.

Sea surface temperature (SST) is a critical parameter that determines the magnitude and direction of heat exchanges between the ocean and the atmosphere. Previous studies have extensively investigated its role in air-sea heat exchanges (Zhang and McPhaden 1995, Zhang et al. 1995, Barsugli and Battisti 1998, Wu et al. 2007, Nisha et al. 2012, Gao et al. 2013). SST contributes in particular to LH and SH, which are key components of air-sea heat flux spatial and temporal variability. An increase in SST results in increased evaporation, which in turn contributes to the transfer of heat from the ocean to the atmosphere by LH (Zhang and McPhaden 1995). However, the relationship between LH and SST is more complex than a simple monotonic increase. As shown by Zhang and McPhaden (1995), LH increases with SST up to a certain point, after which it levels off and tends to decrease when SST exceeds 28°C, despite the increase in humidity deficit. Cayan (1992), using marine observations from the Comprehensive Ocean-Atmosphere Data Set (COADS) dataset, found that typical flux anomalies of 50 W.m<sup>-2</sup> of LH and SH are associated with monthly SST changes of approximately 0.2°C. Additionally, in a study focusing on regional perspectives, Kumar et al. (2017) noted that at low SST, the change in LH and SST is primarily influenced by contributions from humidity deficit (thermodynamics), whereas at high SST, the change is dominated by contributions from wind (dynamics). This suggests that SST is a major driver of air-sea heat fluxes, and that even small changes in SST can have significant impacts on the global climate.

Southeast Asia (SEA) is located in the Western Pacific Warm Pool region, as depicted in Figure 4.1. The climatic conditions prevailing over the terrestrial expanse of SEA are primarily characterized by high temperatures and humidity, significantly influenced by the monsoonal circulation patterns. The climatic conditions over a specific land area of SEA are strongly affected by oceanic factors. This connection has been exemplified in prior research, highlighting the pivotal role of air-sea interactions in governing atmospheric and oceanic oscillations, such as El Niño-Southern Oscillation (ENSO) (Kleeman et al. 1999, Mizuta et al. 2014) and ENSO Modoki, a new type of tropical Pacific SST warming/cooling pattern, with maximum warm/cool anomalies in the central equatorial Pacific (Ashok et al. 2007, Weng et al. 2007, 2009). SST is related to the monsoon strength and patterns (Meehl 1994, Yang and

## Chapter 4. CMIP6 analysis: heat fluxes estimation and the role of the climate change

Lau 1998), and is consequently intricately interconnected with precipitation patterns (e.g. Chang et al. 2000, Wang et al. 2005, Xie et al. 2010, Roxy 2014, Nguyen-Le et al. 2015, Ngo-Thanh et al. 2018, Nguyen-Thanh et al. 2023). It is therefore extremely important to accurately represent the interactions between the atmosphere and the ocean in this region, specifically air-sea heat fluxes, in order to correctly understand the behaviors and changes of the SEA climate. However, determining the exact values of heat fluxes over the SEA remains challenging. Previous studies have indicated that this region is a heat gain area for the ocean, providing a considerable range of variation of  $Q_{net}$  estimates, especially over the South China Sea (SCS), ranging from 10 to 50  $W.m^{-2}$  (Qu et al. 2004, Qu et al. 2006, Song and Yu 2013, Valdivieso et al. 2017, Wang et al. 2019, Pokhrel et al. 2020). These  $Q_{net}$  estimates are specific to the areas and periods of study of each paper, and can vary depending on factors such as season, location, ocean currents, wind patterns, the characteristics of the methodology used (model resolution, in-situ sampling, satellite coverage...). Regarding future trends, previous studies over the SEA region have only focused on changes in individual variables in either the land/atmosphere or the ocean. For instance, Tangang et al. (2020) projected a decrease in future boreal summer rainfall over the region based on multiple regional experiments that dynamically downscaled CMIP5 GCMs to the Coordinated Regional Climate Downscaling Experiment-Southeast Asia (CORDEX-SEA) domain. Ngai et al. (2022) identified an increase in boreal winter rainfall over the Indochina Peninsula. Using the same set of CORDEX-SEA downscaling experiments, Supari et al. (2020) projected an increase in maximum daily rainfall over Indonesia and Northern Myanmar. Furthermore, Hermann et al. (2020) projected a general weakening in near-surface wind over the ocean in the region; however, the magnitude and direction of changes largely depend on the input global models, the regional model used for downscaling, as well as the seasonal characteristics of winds (Hermann et al. 2022). No study to date has quantified in detail air-sea heat fluxes over SEA and, particularly, their future trends under different scenarios.

In the present study we first examine and discuss the representation of the heat flux in the latest generation of climate models participating in CMIP6. This will provide a comprehensive reference for statistical quantities and characteristics of  $Q_{net}$  and its four components over SEA, such as regional climatological estimates, spatial patterns, seasonal cycles, and future trends. Second, we use CMIP6 models to examine future changes in heat fluxes in SEA based on SST changes, with a focus on groups of models with the highest and lowest warming. Last, this study aims to identify and understand how the dynamic processes of heat fluxes differ across a range of SST values.

## **Chapter 4. CMIP6 analysis: heat fluxes estimation and the role of the climate change**

### **4.2. Data and method**

#### **4.2.1 CMIP6 GCMs**

In this study, we selected 30 CMIP6 GCMs that were accessible at the time of data retrieval (list in [Table 4.1](#)) to conduct heat flux estimations over SEA. We selected the first ensemble member (r1i1p1f1) of the historical simulation derived from the pre-industrial control experiment of each model, and simulations for the future period 2015–2099 from the scenario experiments with specific Shared Socioeconomic Pathways (SSP), including SSP1-2.6, SSP2-4.5 and SSP5-8.5.

For comparison purposes, we regridded all model outputs to a  $1^\circ \times 1^\circ$  common grid using bilinear interpolation. A land–sea mask was applied to compute surface heat flux only on ocean regions.

#### **4.2.2 Observations and Reanalysis datasets**

##### **ERA5**

Descriptions of the ERA5 data set have been shown in detail in Chapter 3, Section 3.2.4.

##### **SST dataset**

We used monthly SST data at a  $1^\circ \times 1^\circ$  resolution from the Hadley Centre Global Sea Ice and Sea Surface Temperature (HadISST) ([Rayner 2003](#)) as the reference SST dataset.

#### **4.2.3 Methods**

For the evaluation of heat flux representation in CMIP6 GCMs, the spatial and temporal characteristics of air-sea heat fluxes in the CMIP6 multi-model ensemble (MME) are evaluated against the ERA5 reference dataset. The net heat flux ( $Q_{net}$ ) at the ocean surface is the sum of the four components: net downward SW, net downward LW, LH, and SH. The MME mean is calculated by mathematically averaging 30 models' simulations. The period 1995–2014 is designated as the baseline period of this study (2014 being the last year of the historical simulations) as done in previous studies (see [Tebaldi et al. 2021](#)), with detailed analysis on the climatological mean fields, seasonal variations, and zonal average.

## Chapter 4. CMIP6 analysis: heat fluxes estimation and the role of the climate change

For the study of climate change's impact on heat flux, heat flux projections in the CMIP6 MME are analyzed under three scenarios: SSP1-2.6, SSP2-4.5, and SSP5-8.5 scenarios, and referred to as MME1-2.6, MME2-4.5 and MME5-8.5, respectively. The timeframes considered are the mid-century (2041–2060) and the end-century (2081–2099), relative to the baseline period (1995–2014).

**Table 4.1.** List of CMIP6 GCMs used in this study. The superscript next to each model's name indicates the model group, i.e., L or H (defined in [sub-section 4.2.3](#)), to which the model belongs in each specific scenario: <sup>1</sup>L1-2.6, <sup>2</sup>L2-4.5, <sup>3</sup>L5-8.5, <sup>4</sup>H1-2.6, <sup>5</sup>H2-4.5, <sup>6</sup>H5-8.5.

Model	Institution /Country	Resolution	Model	Institution /Country	Resolution
ACCESS-CM2 <sup>4,5,6</sup>	Australia	1.875°x1.25°	FIO-ESM-2-0	China	1.25°x0.9°
ACCESS-ESM1-5 <sup>4,5</sup>	Australia	1.875°x1.25°	GFDL-ESM4 <sup>1,2,3</sup>	China	1.125°x1°
BCC-CSM2-MR <sup>1,2,3</sup>	China	1.125°x1.125°	IITM-ESM <sup>1,2,3</sup>	India	1.875°x1.875°
CAMS-CSM1-0 <sup>1,2,3</sup>	China	1.125°x1.125°	INM-CM4-8 <sup>1,2,3</sup>	USA	2°x1.5°
CanESM5 <sup>4,5,6</sup>	Canada	2.8°x2.8°	INM-CM5-0 <sup>1,2,3</sup>	Russia	2°x1.5°
CAS-ESM2-0 <sup>4,5</sup>	China	1.4°x1.4°	IPSL-CM6A-LR <sup>6</sup>	France	2.5°x1.3°
CESM2-WACCM <sup>4,5,6</sup>	USA	1.25°x0.9°	KACE-1-0-G <sup>4,5,6</sup>	Korea	1.875°x1.25°
CIESM <sup>5,6</sup>	China	1.25°x0.9°	MIROC6 <sup>1,2,3</sup>	Japan	1.4°x1.4°
CMCC-CM2-SR5	Italy	1.25°x0.9°	MPI-ESM 1-2-HR	Germany	0.94 × 0.94°
CMCC-ESM2 <sup>4,5</sup>	Italy	1.25°x0.9°	MPI-ESM 1-2-LR <sup>1</sup>	Germany	1.87 × 1.86°
EC-Earth3 <sup>4,5,6</sup>	Europe	0.7°x0.7°	MRI-ESM2-0 <sup>4</sup>	Japan	1.125°x1.125°
EC-Earth3-Veg <sup>6</sup>	EC-Earth consortium	0.7°x0.7°	NESM3 <sup>6</sup>	China	1.875°x1.875°
EC-Earth3-Veg-LR	EC-Earth consortium	1.125°x1.125°	NorESM2-LM <sup>2,3</sup>	Norway	2.5°x1.9°
FGOALS-f3-L <sup>1,2,3</sup>	China	1.25°x1°	NorESM2-MM	Norway	1.25°x0.9°
FGOALS-g3 <sup>1,2,3</sup>	China	2°x2°	TaiESM1 <sup>4,5,6</sup>	Taiwan	1.25°x0.9°

## Chapter 4. CMIP6 analysis: heat fluxes estimation and the role of the climate change

To assess the sensitivity of CMIP6 models at the regional scale concerning future sea surface temperature (SST) rise, we first classified CMIP6 models into two groups. One group comprises models projecting the lowest SST changes, while the other group comprises models projecting the highest SST changes in the future. The projected SST change (delta) was calculated using the following formula:

$$\Delta SST = \overline{F}(SST)_{i,j} - \overline{H}(SST)_{i,j} \quad (\text{Eq. 4.1})$$

where:

- $i$  represents three scenarios (SSP1.2-6, SSP2.4-5, and SSP 5.8-5),
- $j$  represents individual models of CMIP6 (30 models, [Table 4.1](#)),
- $\overline{F}$  is the mean value of SST for the entire SEA region during the period 2015-2099,
- $\overline{H}$  is the mean value of SST for the entire SEA region during the baseline period 1995-2014.

The values of Delta SST are detailed in [Fig. 4.1](#). For each scenario, we based on tercile classification of delta SST to select the group of models with the lowest projected change (33.33%) (hereafter referred to as group L) and the group of models with the highest projected change (33.33%) (hereafter referred to as group H). Therefore, with the three SSP scenarios, there are six model groups comprising 10 models each: L1-2.6, L2-4.5, L5-8.5, H1-2.6, H2-4.5, and H5-8.5. The models for each group are listed in [Table 4.1](#).

In addition, we will use the following bulk heat flux formulae ([Large and Yeager \(2004\)](#)) to calculate the control variables of the heat flux components:

$$LW = Q_a - \epsilon\sigma(SST)^4 \quad (\text{Eq. 4.2})$$

$$LH = \rho L_v C_E W (q_a - q_s) = \rho L_v C_E W \Delta q \quad (\text{Eq. 4.3})$$

$$SH = \rho C_p C_H W (T_a - T_s) = \rho C_p C_H W \Delta T \quad (\text{Eq. 4.4})$$

Where  $Q_a$  is downward of longwave radiation flux,  $\sigma = 5.67 \times 10^{-8} \text{ Wm}^{-2}\text{K}^{-4}$  denotes the Stefan-Boltzmann constant and  $\epsilon$  represents the surface emissivity is taken to be 1.0 to account for the small reflected fraction of  $Q_a$  ([Lind and Katsaros 1986](#));  $W$ ,  $q_a$ , and  $T_a$  represent the

## Chapter 4. CMIP6 analysis: heat fluxes estimation and the role of the climate change

10-m wind speed, specific humidity, and air temperature at 2m above sea surface, respectively;  $\rho$  is the air density at the observation level ( $\text{kg m}^{-3}$ );  $L_v$  is the latent heat of vaporization ( $2.44 \times 10^6 \text{ J kg}^{-1}$ );  $C_E$  and  $C_H$  are the transfer coefficients for latent heat and sensible heat, respectively;  $C_p$  is the specific heat of air at a constant pressure, which is assumed to be constant at  $1.005 \times 10^3 \text{ J kg}^{-1}\text{K}^{-1}$ ; and  $q_s$  and  $T_s$  are the saturation specific humidity and sea surface temperature, respectively.

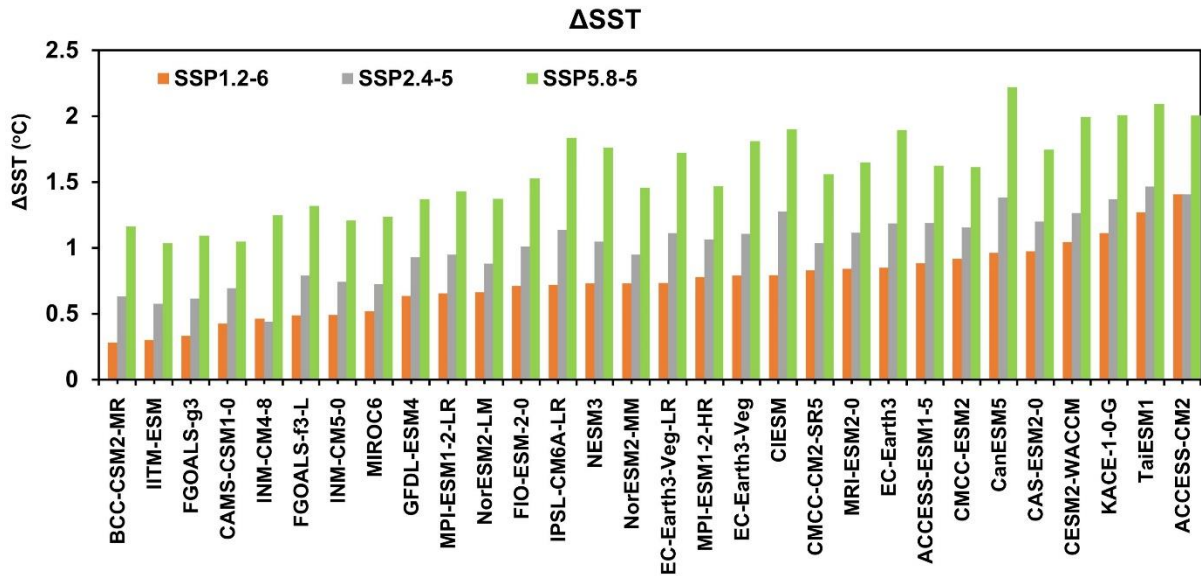


**Figure 4.1.** Projected SST changes over SEA for individual models under SSP1.2-6 (orange color), SSP2.4-5 (gray color) and SSP5.8-5 (green color) for the period 2015–2099 relative to the baseline 1995–2014.

### 4.3. Seasonal and spatial variability of heat fluxes

To evaluate the performance of CMIP6 models in representing heat fluxes, the spatial distribution (Fig. 4.2), zonal distribution (Fig. 4.3), annual and seasonal mean values (Table 4.2), and seasonal cycle (Fig. 4.4) of air-sea heat fluxes averaged over the SEA region during the period 1995–2014 were calculated for both CMIP6 and ERA5 products.

#### 4.3.1 Spatial distribution

Figure 4.2 shows the annual mean spatial distribution of  $Q_{net}$  and its four components over the SEA region of CMIP6 compared to ERA5. Despite the difference in magnitude, the spatial distribution of annual mean  $Q_{net}$  in the two products shows a remarkable similarity with a

## Chapter 4. CMIP6 analysis: heat fluxes estimation and the role of the climate change

correlation coefficient of 0.87 (p-value <0.01) (Fig. 4.2a-b). The northern part of the study area has a high annual Qnet loss, whereas most of the 10 °S–10 °N range shows a Qnet gain (Fig. 4.2a-b). The Qnet over SEA is estimated by ERA5 to be  $21.3 \pm 11.8 \text{ W.m}^{-2}$ . CMIP6 MME underestimates Qnet with an annual mean value of  $6.8 \pm 11.4 \text{ W.m}^{-2}$ , i.e., by  $-14.5 \text{ W.m}^{-2}$ , equivalent to about 2/3 of the ERA5 Qnet value (Table 4.2). A negative Qnet bias with 95% statistical significance is observed from the south of the region to 10 °N, while a small positive Qnet bias occurs around 90 °E–100 °E and 10 °N–20 °N (Fig. 4.2c).

Figure 4.2 (d–g) also shows the annual mean distribution of SW, LW, LH, and SH to study the role of each component in contributing to the net surface heat flux balance. The spatial correlation coefficient of LH is the largest among the four components ( $r=0.88$ ). This indicates that CMIP6 MME captures very well the spatial distribution of LH observed in ERA5. Both CMIP6 MME and ERA5 show significant LH loss, typically ranging from  $-85.0 \text{ W.m}^{-2}$  to  $-160.0 \text{ W.m}^{-2}$ , with maximum values exceeding  $-190 \text{ W.m}^{-2}$  in the western boundary currents around 18 °N–26 °N and 122 °E–125 °E (part of the Kuroshio Current) (Fig. 4.2i–k). CMIP6 MME generally overestimates LH loss, especially in the region 10 °S to 10°N (over the Indonesian Sea). The negative LH bias ranges from  $-25.0 \text{ W.m}^{-2}$  to  $-10.0 \text{ W.m}^{-2}$  depending on different basins (Fig. 4.2h). The regional mean annual LH error is around  $-11.4 \text{ W.m}^{-2}$  (Table 4.2).

CMIP6 models underestimate SW over the 105 °E–140 °E region, while accurately capturing the patterns over the Philippine Sea and north of 18°N, with a spatial correlation of 0.83 with ERA5 (Fig. 4.2d–f). Besides, the SW bias is positive over the regions of 90 °E–100 °E and 140 °E, 5 °S. However, the annual mean SW bias over the whole region is still negative, with a value of  $-1.8 \text{ W.m}^{-2}$  (Table 4.2).

Regarding LW (Fig. 4.2d–f), the annual mean shows a narrow range ( $-46 \text{ W.m}^{-2}$  to  $-52 \text{ W.m}^{-2}$ ) of spatial variability of LW over the region 10 °S–10 °N, primarily influenced by cloud cover variations (Berry et al. 2009). Some parts in the southern hemisphere and the seas of Myanmar (Bay of Bengal) observe significant LW losses ( $> 60 \text{ W.m}^{-2}$ ) (Fig. 4.2d–e). CMIP6 MME reproduces the spatial distribution of LW very well c, with no regional mean annual bias, and a spatial correlation coefficient  $r=0.87$  (Fig. 4.2f, Table 4.2).

SH loss is much smaller, only about 10% of LH loss, typically around  $-10 \text{ W.m}^{-2}$  (Fig. 4.2m–p). The largest annual mean SH loss, exceeding  $-30 \text{ W.m}^{-2}$ , is observed in western boundary current regions. SH errors with a statistical significance of 95% are present over most

## Chapter 4. CMIP6 analysis: heat fluxes estimation and the role of the climate change

of the study domain (Fig. 4.2p). The value of the mean annual bias for the entire region is  $-1.3 \text{ W.m}^{-2}$ .

The difference of  $-14.5 \text{ W.m}^{-2}$  in Qnet between CMIP6 MME and ERA5 is primarily due to the overestimation of LH loss (by  $-11.4 \text{ W.m}^{-2}$ ), and to a much lesser extent due to the underestimation of SW gain (by  $-1.8 \text{ W.m}^{-2}$ ) and the overestimation of SH loss (by  $-1.3 \text{ W.m}^{-2}$ ) by CMIP6 MME.

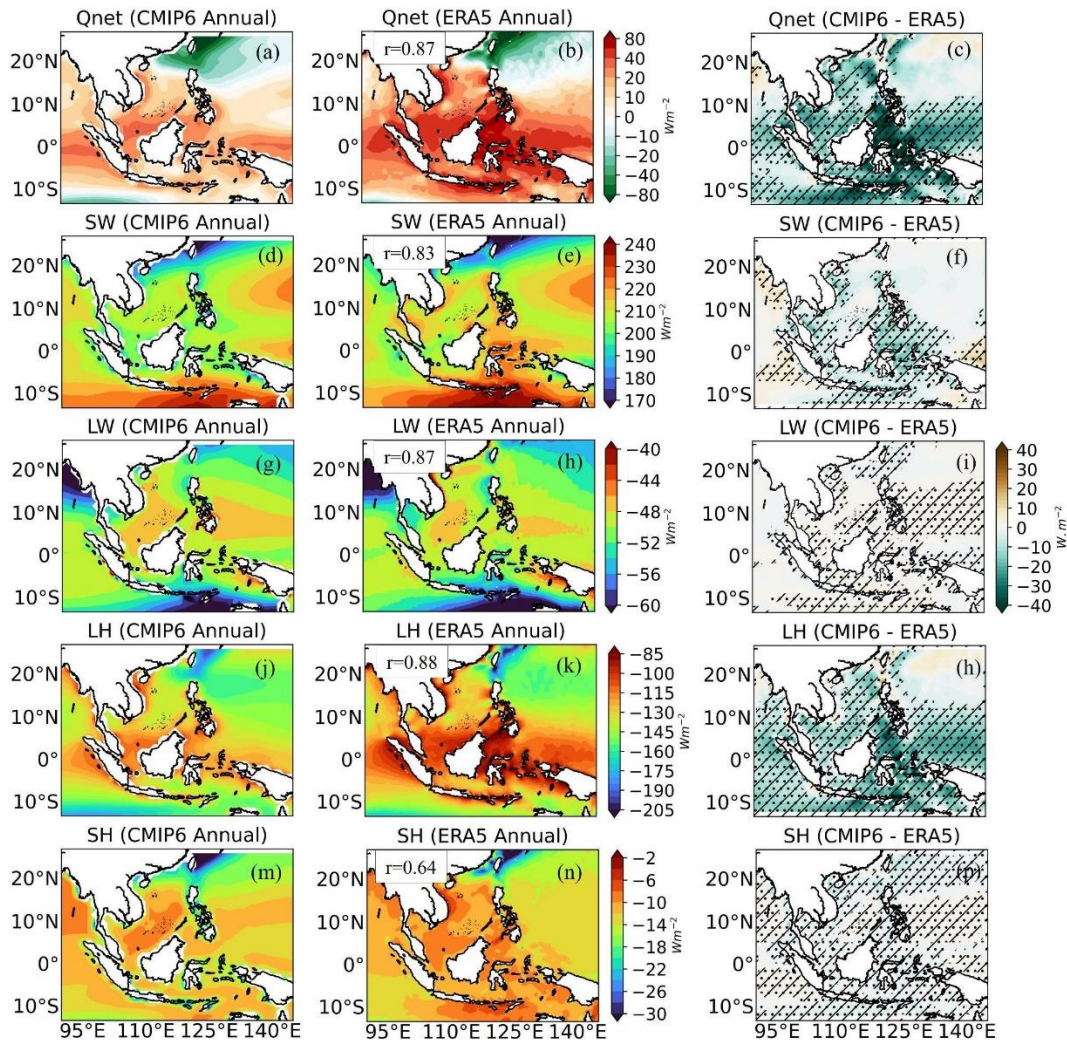


**Figure 4.2.** Annual mean of (a, b) Qnet, (d, e) SW, (g, h) LW, (j, k) LH and (m, n) SH from CMIP6 MME (left) and ERA5 (middle) (Unit:  $\text{W.m}^{-2}$ ). The value in the black box indicates the spatial correlation coefficient between ERA5 and CMIP6 MME (p-value  $<0.01$ ). Bias between CMIP6 MME and ERA5 (c, f, i, h, p) (right, unit:  $\text{W.m}^{-2}$ ). The dot and hatch pattern indicates areas where differences are statistically significant at 95% based on the student's t-test.

## Chapter 4. CMIP6 analysis: heat fluxes estimation and the role of the climate change

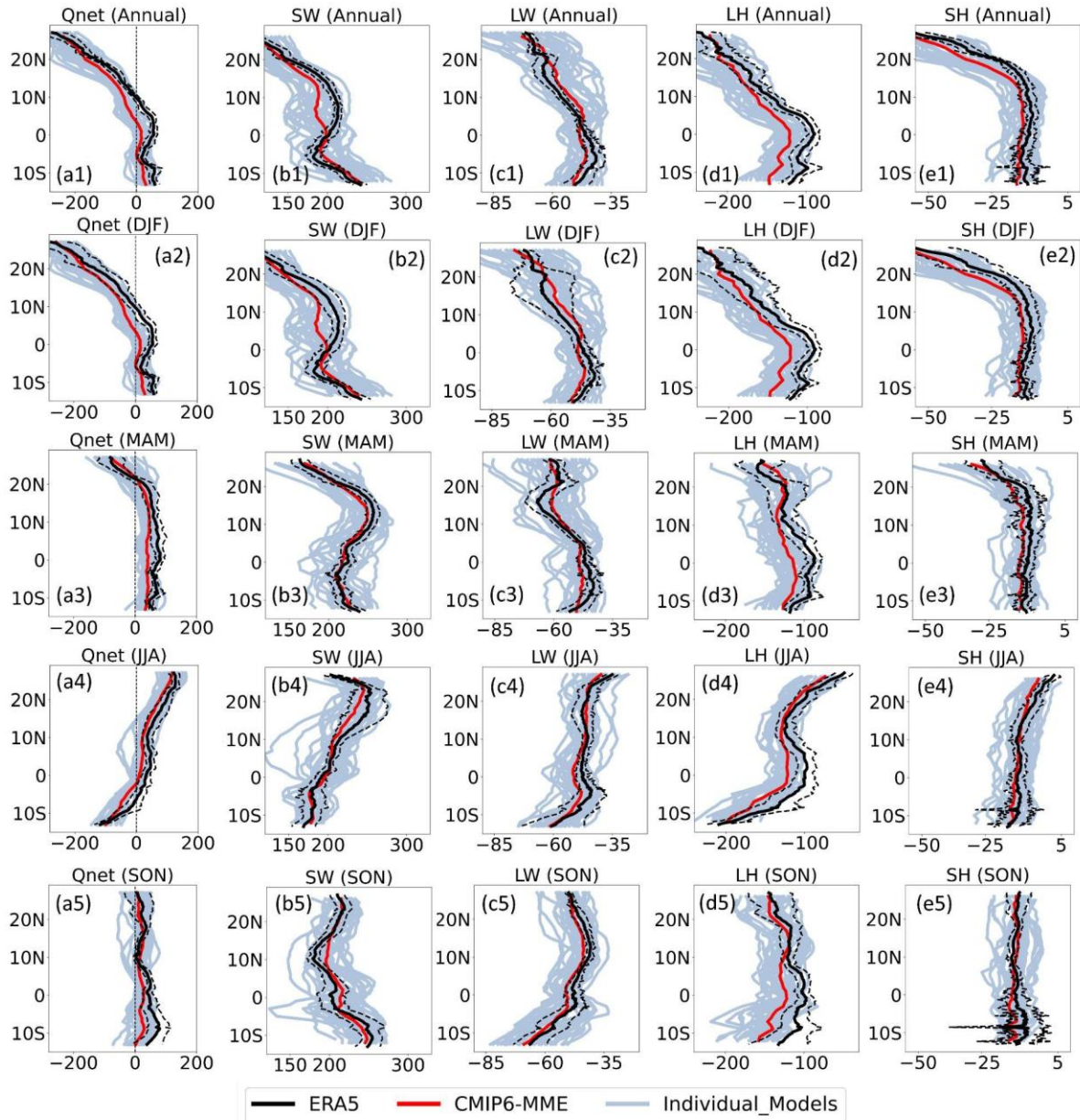


**Figure 4.3.** Zonal mean values of Qnet, SW, LW, LH and SH computed from the annual and four seasons (December-February, DJF; March-May, MAM; June-August, JJA; September-November, SON) means of CMIP6 MME (red line) and ERA5 (black line) for the period 1995–2014 (Unit:  $\text{W}\cdot\text{m}^{-2}$ ). The gray lines indicate the zonal mean profile of 30 individual models from CMIP6, and dashed black lines show the range of interannual variability in ERA5 based on  $\pm 1$  standard deviation.

Figure 4.3 presents the latitudinal profile of the zonally averaged annual mean and seasonal mean of Qnet and its four components from CMIP6 MME and ERA5. Despite the differences in magnitude, both products demonstrate a similar structure. The annual mean clearly shows a

## Chapter 4. CMIP6 analysis: heat fluxes estimation and the role of the climate change

Qnet gain zone from 12 °S to 10 °N, i.e. around the Equator, and thereafter a Qnet loss at higher latitudes (Fig. 4.3a1). The zonal average Qnet in CMIP6 MME is consistently smaller than ERA5 Qnet, with the largest bias  $\sim -50 \text{ W.m}^{-2}$  observed at approximately 2°N.

The annual zonal mean Qnet profile is primarily dictated by the SW profile. CMIP6 MME SW consistently remains lower than that from ERA5 between 0 to 20 °N, with the most significant bias  $\sim -25 \text{ W.m}^{-2}$  also observed around 2 °N (Fig. 4.3b1). The maximum bias in LH, of approximately  $-15 \text{ W.m}^{-2}$  to  $-20 \text{ W.m}^{-2}$ , occurs around the equator (Fig. 4.3d1). Although both LW and SH are well captured, the SH exhibits a minor bias of approximately  $-2 \text{ W.m}^{-2}$ , whereas the LW shows a negative bias (approximately  $-2 \text{ W.m}^{-2}$  –  $-1 \text{ W.m}^{-2}$ ) in the southern (below 10°S) and a small positive bias in the northern ( $\sim 2 \text{ W.m}^{-2}$ ), especially in the area from the equator to 10°N (Fig. 4.3c1, e1).

### 4.3.2 Seasonal cycle

In seasonal variation, CMIP6 MME well captures the ERA5 zonal mean profile of heat flux across all seasons (Fig. 4.3a2–e5). In more detail, Qnet exhibits pronounced seasonal variation at different latitudes, except for the equatorial region, especially the area above 20 °N. The biases in Qnet are highlighted in all seasons, particularly in the region between 10 °S and 10 °N. SW undergoes the most significant seasonal variations among the components of the heat flux, as it depends on the annual movement of the sun. The SW bias is strongest during winter (DJF), reaching  $-31 \text{ W.m}^{-2}$  around 5 °N, and weaker in other seasons (Fig. 4.3b2–b5). LW shows varying biases at each latitude depending on the season (Fig. 4.3c2–c5), with the largest bias observed during DJF between 5 °N and 20 °N.

For LH, strong zonal variations of LH loss are observed during DJF and JJA. The bias of LH loss is the most significant compared to other components, especially during SON from 10 °N to 10 °S, fluctuating between  $-30 \text{ W.m}^{-2}$  and  $-20 \text{ W.m}^{-2}$  (Fig. 4.3d2–d5).

The zonal variations of SH are prominently observed during winter in the northern hemisphere, above 20 °N. The bias between CMIP6 MME and ERA5 is negligible, except for the region in the Southern Hemisphere during autumn (Fig. 4.3e2–e5).

In summary, the zonal mean profile of heat fluxes during DJF determines the annual zonal mean profile (Fig. 4.3a2–e2). SW and LH exhibit the most significant latitudinal variations depending on different seasons. The substantial variability observed among individual models

## Chapter 4. CMIP6 analysis: heat fluxes estimation and the role of the climate change

within CMIP6 leads to disparities in the estimates of heat flux components between CMIP6 MME and ERA5.

These findings are further supported by comparing the climatological seasonal mean of CMIP6 MME and ERA5 (Table 4.2). We examine the role of each component in Qnet to pinpoint their relative importance in the surface heat budget on a seasonal basis, particular in LH loss. The SEA region experiences a total net heat gain in MAM, JJA and SON, and total net heat loss only during DJF. The strongest heat gain is observed in MAM, both in ERA5 and CMIP6 MME. CMIP6 MME consistently shows negative biases compared to ERA5 across all seasons, and for all components. The differences between the two products are lower during MAM and JJA ( $-12.4 \text{ W.m}^{-2}$  and  $-11.8 \text{ W.m}^{-2}$  for Qnet and  $-8.5 \text{ W.m}^{-2}$  and  $-7.5 \text{ W.m}^{-2}$  for LH, respectively), and higher in SON and DJF ( $-16.7 \text{ W.m}^{-2}$  and  $-20.6 \text{ W.m}^{-2}$  for Qnet and  $-13.0 \text{ W.m}^{-2}$  and  $-13.7 \text{ W.m}^{-2}$  for LH, respectively). It is of interest to note that the standard deviations of the CMIP6 heat flux components are comparable to those of ERA5.

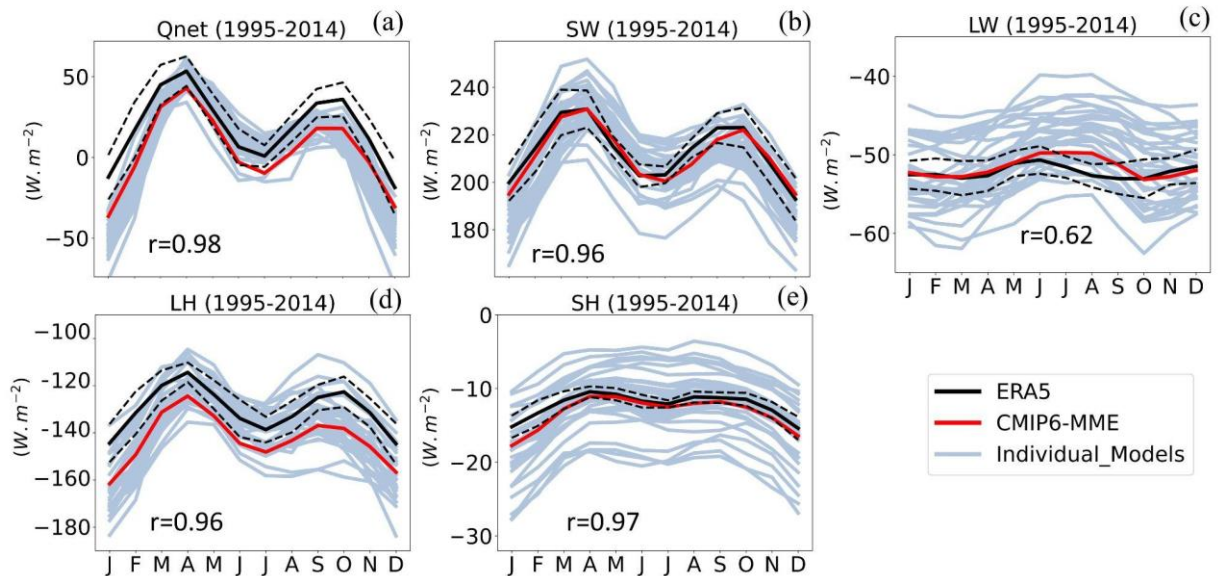


**Figure 4.4.** Seasonal cycle of (a) Qnet, (b) SW, (c) LW, (d) LH and (e) SH averaged over the SEA region from ERA5 (black line) and CMIP6 MME (red line) for the period 1995–2014 (Unit:  $\text{W.m}^{-2}$ ). The gray lines indicate the seasonal cycle of 30 individual models from CMIP6. Black dashed lines show the range of interannual variability in ERA5 based on  $\pm 1$  standard deviation. The  $r$  values indicate the temporal correlation coefficient between ERA5 and CMIP6 MME (p-value  $< 0.01$ ), except LW with p-value  $< 0.05$ .

## Chapter 4. CMIP6 analysis: heat fluxes estimation and the role of the climate change

**Table 4.2.** Annual and seasonal means of Qnet, SW, LW, LH, and SH averaged over SEA along with their respective interannual standard deviations of the CMIP6 MME yearly values for the period 1995–2014 (mean  $\pm$  deviation), and biases compared with ERA5. Units are in  $W.m^{-2}$ .

Heat fluxes	Annual			DJF			MAM			JJA			SON		
	CMIP6	ERA5	Bias	CMIP6	ERA5	Bias	CMIP6	ERA5	Bias	CMIP6	ERA5	Bias	CMIP6	ERA5	Bias
<b>Qnet</b>	6.8 $\pm 11.4$	21.3 $\pm 11.8$	<b>-14.5</b>	-31.6 $\pm 16.8$	-11.0 $\pm 16.8$	<b>-20.6</b>	37.0 $\pm 10.7$	49.4 $\pm 10.8$	<b>-12.4</b>	8.3 $\pm 8.7$	20.1 $\pm 8.9$	<b>-11.8</b>	10.3 $\pm 10.7$	27.0 $\pm 11.0$	<b>-16.7</b>
<b>SW</b>	209.0 $\pm 6.6$	210.8 $\pm 7.3$	<b>-1.8</b>	192.2 $\pm$ 7.7	195.5 $\pm 9.1$	<b>-3.3</b>	225.0 $\pm 6.8$	226.0 $\pm 7.7$	<b>-1.0</b>	205.0 $\pm 5.6$	209.3 $\pm 4.5$	<b>-4.3</b>	210.2 $\pm$ 7.8	212.5 $\pm 8.1$	<b>-2.3</b>
<b>LW</b>	-50.8 $\pm 1.7$	-50.8 $\pm 1.8$	<b>0.0</b>	-53.1 $\pm$ 1.9	-51.7 $\pm 2.0$	<b>-1.4</b>	-51.9 $\pm 1.8$	-51.3 $\pm 1.9$	<b>-0.6</b>	-49.4 $\pm$ 1.5	-49.8 $\pm 1.5$	<b>-0.4</b>	-51.3 $\pm 1.9$	-50.9 $\pm 2.0$	<b>-0.4</b>
<b>LH</b>	-137.8 $\pm 7.2$	-126.4 $\pm 6.9$	<b>-11.4</b>	-153.5 $\pm 10.2$	-139.8 $\pm 9.2$	<b>-13.7</b>	-123.9 $\pm 5.8$	-114.4 $\pm 5.6$	<b>-8.5</b>	-135.6 $\pm 5.9$	-128.1 $\pm 6.7$	<b>-7.5</b>	-135.7 $\pm 5.8$	-122.7 $\pm 6.2$	<b>-13.0</b>
<b>SH</b>	-13.6 $\pm 1.1$	-12.3 $\pm 1.1$	<b>-1.3</b>	-17.2 $\pm 2.0$	-15.0 $\pm 1.7$	<b>-2.2</b>	-12.2 $\pm 1.0$	-10.9 $\pm 0.9$	<b>-1.3</b>	-11.7 $\pm$ 0.6	-11.3 $\pm 0.7$	<b>-0.4</b>	-12.9 $\pm 0.8$	-11.9 $\pm 0.9$	<b>-1.0</b>

## Chapter 4. CMIP6 analysis: heat fluxes estimation and the role of the climate change

Monthly variations of  $Q_{net}$  and its four contributing heat flux components averaged over SEA are shown in Fig. 4.4. Although the magnitude differs, the semiannual cycle of  $Q_{net}$  is well depicted by CMIP6 individual models and MME with a first maximum in April and a second maximum in October ( $r=0.98$ ,  $p$ -value  $<0.01$ , Fig. 4.4a). CMIP6 MME shows lower  $Q_{net}$  values compared to ERA5 during the whole year, primarily due to the systematic overestimation of LH loss throughout the year (Fig. 4.4d), consistently with the results from Fig. 4.2, 4.3 and Table 4.2.

The semiannual cycle in  $Q_{net}$  is dictated by surface net SW (Fig. 4b). The SW peaks observed in April and October reflect the fact that the Sun crosses the Equator twice a year. Although there are significant discrepancies in SW values for August and September, with a difference of about  $4.5 \text{ W.m}^{-2}$  between the larger values (from ERA5) and the smaller values (from CMIP6), as also shown in Table 4.2, they still have a high spatial correlation coefficient of  $r=0.96$ , with a  $p$ -value  $<0.01$ . Overall, SW over the SEA is not solely controlled by the solar zenith angle but also by cloud radiative effects, given that the region often experiences strong deep convection, occurring predominantly in June–September (Webster and Stephens 1984, Chen et al. 2000, Wu and Chen 2021). While LW estimates exhibit a weaker semi-annual cycle, there remains a discrepancy of about  $1 \text{ W.m}^{-2}$  between CMIP6 MME and ERA5 from June to October (Fig. 4.4c). This is also reflected in the lower correlation coefficient ( $r=0.62$ ,  $p$ -value  $<0.01$ ) compared to other heat flux components.

Both CMIP6-MME and ERA5 show a seasonal cycle in LH characterized by a clear minimum LH loss in April, a secondary minimum in October, and a maximum LH loss in January with strong correlation coefficient  $r=0.96$ ,  $p$ -value  $<0.01$  (Fig. 4.43d). CMIP6 MME produces a stronger LH loss than ERA5, and its mean bias is more than  $-10 \text{ W.m}^{-2}$ . SH values are weak, representing approximately 10% of LH ( $r=0.97$ ,  $p$ -value  $<0.01$ , Fig. 4.43e). SH shows the strongest bias in winter, consistent with Fig 4.3 and Table 4.2.

In summary, the estimated net heat flux value in CMIP6 MME is approximately two-third lower than ERA5, attributable to LH loss overestimation and SW slight underestimation. Results indicate a wide performance range for each individual model within CMIP6 for each heat flux component. Some models accurately estimate one component but exhibit high inaccuracy with other components, leading to significant discrepancies in  $Q_{net}$  (Table A1). For instance, models like INM-CM4-0 and INM-CM5-0 have SW estimates close to ERA5 (approximately  $210.0 \text{ W.m}^{-2}$ , compared to ERA5's  $210.8 \text{ W.m}^{-2}$ ) but overestimate LH loss

## Chapter 4. CMIP6 analysis: heat fluxes estimation and the role of the climate change

significantly ( $\sim 142.0 \text{ W.m}^{-2}$ , compared to ERA5's  $126.4 \text{ W.m}^{-2}$ ). Conversely, models like CAS-ESM2-0 and EC-Earth-Veg-LR, despite reasonably accurate LH loss estimates compared to ERA5, underestimate SW (approximately  $203.9 \text{ W.m}^{-2}$  and  $194.6 \text{ W.m}^{-2}$ , respectively).

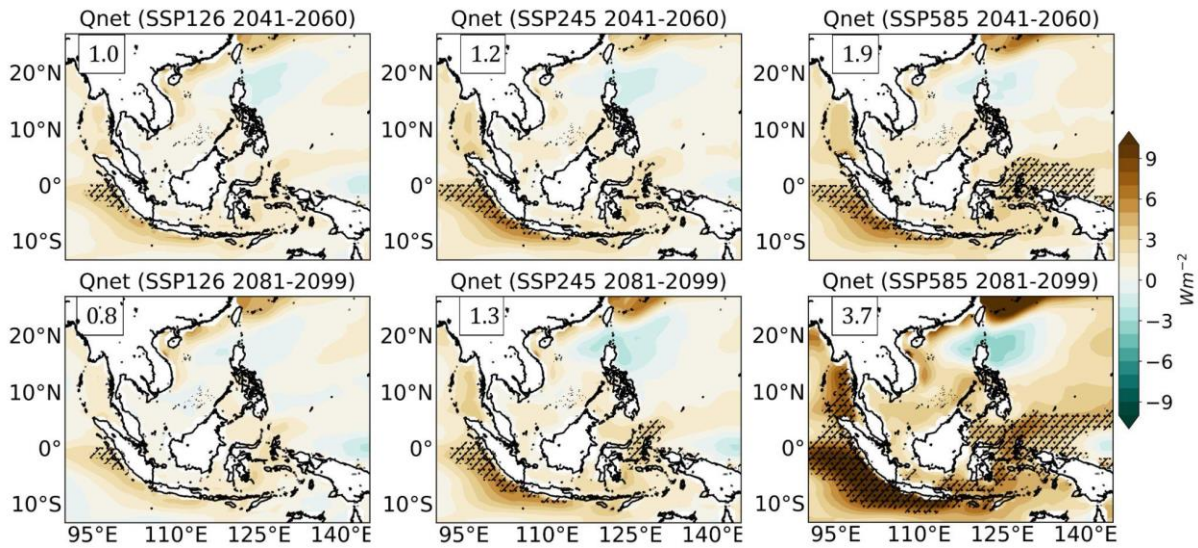
### 4.4 Future projections

#### 4.4.1 Future projections in the multi-model ensemble mean

Projected changes in annual heat fluxes over the SEA region based on the CMIP6 MME under SSP1-2.6, SSP2-4.5, and SSP5-8.5 scenarios are illustrated in Figs. 4.5 and 4.6. In this section, positive (negative) values of heat flux changes ( $\Delta Q_{\text{net}}$ ,  $\Delta SW$ ,  $\Delta LW$ ,  $\Delta LH$ , and  $\Delta SH$ , where  $\Delta$  denotes the difference between the averages over the future and baseline periods) indicate an increase (decrease) relative to the baseline period.

The CMIP6 MME projects an increase in  $Q_{\text{net}}$  across all examined scenarios, with a more pronounced increase in the end-of-century period (2081–2099) compared to the mid-century period (2061–2080) (Fig. 4.5). SSP5-8.5 exhibits the most substantial increase, while SSP1-2.6 demonstrates the weakest increase for both temporal spans. Specifically, CMIP6 MME projects an increase of  $1.0 \text{ W.m}^{-2}$ ,  $1.2 \text{ W.m}^{-2}$ , and  $1.9 \text{ W.m}^{-2}$  in annual  $Q_{\text{net}}$  over the entire SEA for the mid-century under SSP1-2.6, SSP2-4.5, and SSP5-8.5, respectively, and of  $0.8$ ,  $1.3$ , and  $3.7 \text{ W.m}^{-2}$  by the end of the century. These increases are more prominent south of the Maritime region (around  $5^\circ\text{S}$ ), gradually weakening toward the north and exhibiting the smallest (and less significant) changes around  $15^\circ\text{N}$  over the off-Philippine Sea in the end-century under all scenarios. Additionally,  $Q_{\text{net}}$  experiences a weak and statistically insignificant decrease over a small region in the northern SCS and Pacific region. Although the projected changes for  $Q_{\text{net}}$  and its four components in the mid-century period are lower than those in the end-century, the spatial patterns remain similar. Therefore, for all subsequent analyses, we focus on the projected changes at the end of the century.

## Chapter 4. CMIP6 analysis: heat fluxes estimation and the role of the climate change



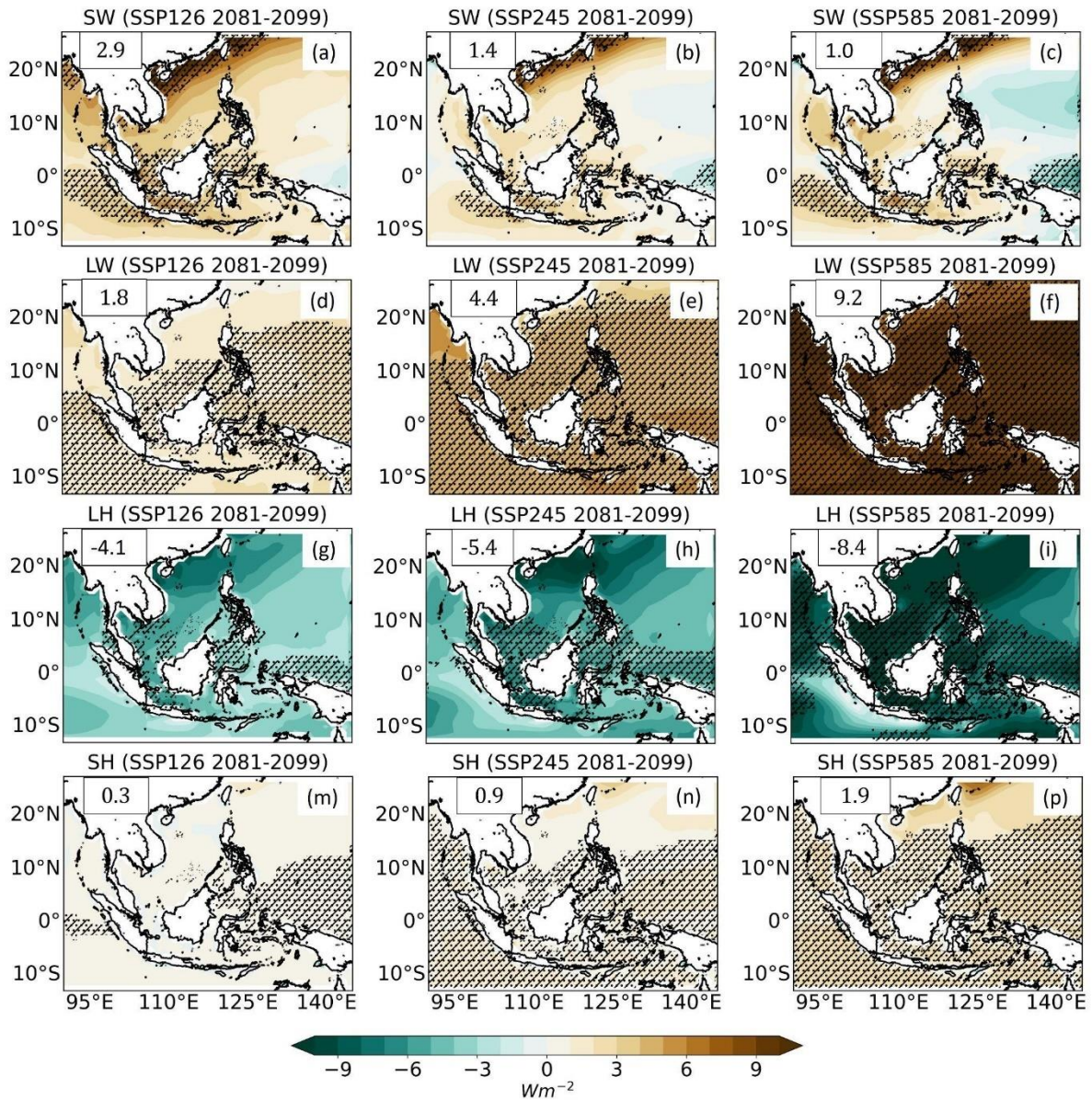
**Figure 4.5.** Projected annual Qnet changes from CMIP6 MME under SSP1-2.6 (left), SSP 2-4.5 (middle) and SSP5-8.5 (right) for the mid-century (upper panel) and the end-century (lower panel) relative to the baseline period. Shading indicates areas where changes are statistically significant at a 95% confidence level based on the student's t-test. The value in the black box shows the average projected change in heat flux over the entire area.

Figure 4.6 depicts the projected changes in the four heat flux components for the end of the century under SSP1-2.6, SSP2-4.5, and SSP5-8.5 relative to the baseline period. Among all components, the LH exhibits the most substantial decrease (i.e., an increase of LH loss) across the entire region under all scenarios compared to the baseline period (Fig. 4.6g-i). The annual LH value is projected to be reduced by  $-4.1 W.m^{-2}$  over the entire SEA region under SSP1-2.6 and  $-5.4 W.m^{-2}$  under SSP2-4.5. These changes are more pronounced under SSP5-8.5 ( $-8.4 W.m^{-2}$ ), particularly over the SCS, where the decrease varies larger than  $-10.0 W.m^{-2}$ .

The SW gain shows an overall increase throughout the entire region under all scenarios, with the largest average increase of  $2.9 W.m^{-2}$  under SSP1-2.6 and the smallest increase of  $1.0 W.m^{-2}$  under SSP5-8.5 (Fig. 4.6a-c). The SW increase is predominantly observed along the southern coast of China, reaching up to  $14.0 W.m^{-2}$  under SSP1-2.6, and  $10.0 W.m^{-2}$ , and  $8.0 W.m^{-2}$  under SSP2-4.5 and SSP5-8.5, respectively. Similar to Qnet, SW also exhibits a significant increase in the southwestern Maritime region under all three scenarios reaching around  $5.0 W.m^{-2}$  by the end of the century under SSP1-2.6. Meanwhile, a significant SW decrease ranging from  $-3.0$  to  $-8.0 W.m^{-2}$  is projected at the equator in the eastern part, close to  $142^{\circ}E$  under SSP1-2.6.

## Chapter 4. CMIP6 analysis: heat fluxes estimation and the role of the climate change

Both LW (Fig. 4.6d–f) and SH (Fig. 4.6m–p) also experience an increase across all scenarios (i.e., a decrease of LW and SH losses). SSP5-8.5 produces the most substantial enhancements in LW and SH, particularly significant over most of the SEA region, with values of  $9.2 \text{ W.m}^{-2}$  and  $1.9 \text{ W.m}^{-2}$ , respectively. SSP1-2.6 produces the smallest increase, with values of  $1.8 \text{ W.m}^{-2}$  and  $0.3 \text{ W.m}^{-2}$ , respectively.



**Figure 4.6.** As in Figure 4.5, but for SW, LW, LH, and SH.

Overall, the projected changes in Qnet, LW, LH, and SH are the highest under SSP5-8.5, followed by SSP2-4.5, and the lowest under SSP1-2.6. However, the projected change in SW exhibits an inverse pattern, with the largest change observed under SSP1-2.6 and the smallest

## Chapter 4. CMIP6 analysis: heat fluxes estimation and the role of the climate change

change under SSP5-8.5. These contrasting changes in SW could be linked to changes in cloud cover and the associated radiative forcing in the atmosphere and at the surface. For instance, previous studies have demonstrated that clouds exert a positive forcing in both SW and LW, leading to a warming in the atmosphere (Ceppi et al. 2017). Concurrently, clouds produce a strong negative SW forcing at the surface during daytime hours and a weakly positive infrared forcing, resulting in a cooling effect (Zelinka and Hartmann 2010, Berry and Mace 2014). Therefore, the offsetting effects between positive and negative radiative forcing by clouds in SW in the atmosphere and at the surface could account for the opposite changes in SW compared to the other heat flux components.

### 4.4.2 Future projections in low and high warming groups

We examine here the relationship between the warming intensity and heat fluxes changes. Figure 4.7 displays the future levels of heat fluxes over SEA compared to the baseline period under three scenarios for the low (L1-2.6, L2-4.5, and L5-8.5) and high (H1-2.6, H2-4.5, and H5-8.5) warming model groups defined in Section 2.c, and for the ensemble average of CMIP6 GCMs (MME1-2.6, MME2-4.5, MME5-8.5). Overall, as observed above for the ensemble mean, Qnet, SW, LW and SH are projected to increase while LH exhibits a downward trend across all options (Fig. 4.7).

When comparing each SSP scenario, and consistently with the discussion about MME from Figs. 4.5 and 4.6 above, the highest emission scenario SSP5-8.5 produces the most substantial heat flux changes for both the low and high warming groups, ranging from 2.0 W.m<sup>-2</sup> to 15.0 W.m<sup>-2</sup> at the end of the century for all components except SW, while the low emission scenario SSP1-2.6 exhibits the lowest changes, with values ranging from 1.0 W.m<sup>-2</sup> to 2.0 W.m<sup>-2</sup>.

In the group-by-group comparison, within a given scenario, the high warming group consistently projects greater changes in heat fluxes compared to the low warming group. Specifically, the H5-8.5 group consistently projects the most substantial changes for Qnet, LH, LW, and SH, with values of 10.0 W.m<sup>-2</sup>, -13.0 W.m<sup>-2</sup>, 15.0 W.m<sup>-2</sup>, and 2.0 W.m<sup>-2</sup>, respectively (Fig. 4.7a, c, d, e). In contrast, the L1-2.6 group projects the smallest changes, with values of 1.0 W.m<sup>-2</sup>, -2.0 W.m<sup>-2</sup>, 2.0 W.m<sup>-2</sup>, and 0.1 W.m<sup>-2</sup>, respectively (Fig. 4.7a, c, d, e). For SW, the H1-2.6 group projects the largest change, with an increase of up to 6.0 W.m<sup>-2</sup> by the end of the century, followed by the H2-4.5 group and, lastly, the H5-8.5 group. Among the lowest model

## Chapter 4. CMIP6 analysis: heat fluxes estimation and the role of the climate change

groups, both the L1-2.6 and L2-4.5 groups show a slight increase, while the L5-8.5 group projects a negligible decrease (approximately  $1.0 \text{ W}\cdot\text{m}^{-2}$ ) by the end of the century (Fig. 4.7b).

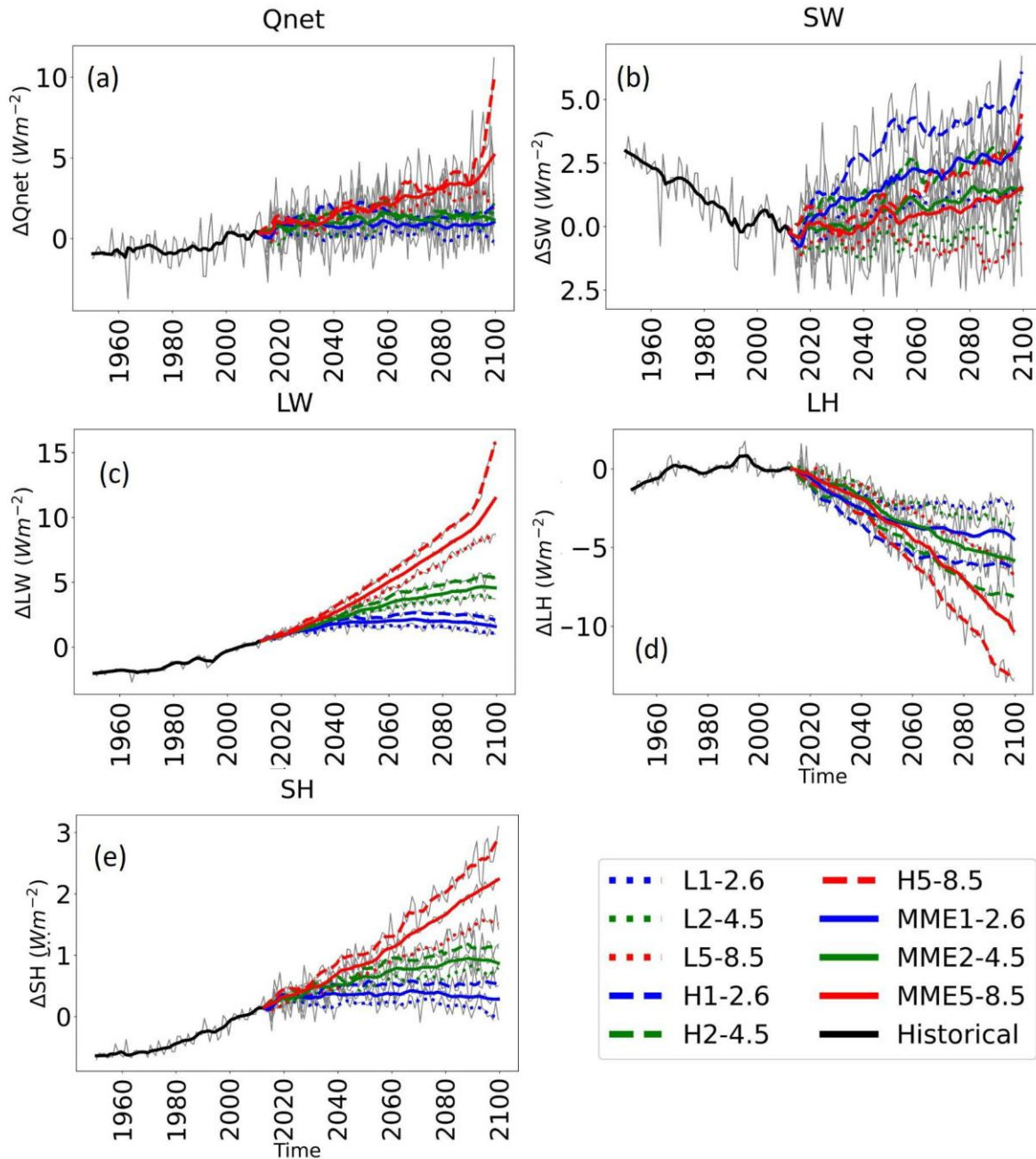


**Figure 4.7.** Time series of projected changes in yearly heat fluxes spatially averaged over the study domain relative to the baseline period 1995-2014 under SSP1-2.6 (blue), SSP2-4.5 (green), and SSP5-8.5 scenario (red) for the low warming group (**L**, dotted line), high warming group (**H**, dashed line) and the ensemble mean of the 30 CMIP6 models (**MME**, solid line). The black solid and color lines depict historical and future heat flux anomalies, respectively.

## Chapter 4. CMIP6 analysis: heat fluxes estimation and the role of the climate change

These lines were obtained using the locally estimated scatterplot smoothing technique (LOESS) (Cleveland et al. 1988). The gray lines indicate the ensemble mean values for each group prior to the use of the LOESS technique.

### 4.5 Models' sensitivity to the magnitude of SST change

This subsection investigates dynamic and thermodynamic processes governing heat fluxes in relation to SST. Future projected changes in SST are expected to correspondingly influence those relationships, and the changes in these components. To ascertain the sensitivity of changes in simulated heat fluxes to changes in SST, Figure 4.8 depicts the average changes in heat fluxes across the entire SEA region against SST changes within each model group under different scenarios, as well as the corresponding linear regression (Fig. 4.8a, e, k, p, s). Both groups exhibit a similar relationship with SST change, featuring ascending patterns in Qnet, LW and SH changes for increasing SST increase, considerable descending trends in LH changes, and a slight descending trend in SW changes.

Pearson correlation coefficients ( $r$ ) between heat flux changes and SST changes exceed the 99% significance test for all components except SW (Fig. 4.8a, e,k,s). The most significant and positive correlations are observed for Qnet, LW and SH changes, ranking between 0.71, 0.96 and 0.92 for the L group and 0.68, 0.93 and 0.86 for the H group, respectively (Fig. 4.8s, k, e). The slope of the linear regression between  $\Delta Q_{net}$  and delta  $\Delta SST$  is equal to  $\sim 1.6 \text{ W}\cdot\text{m}^{-2}\cdot\text{C}^{-1}$  for both groups (Fig. 4.8s). LH changes exhibit significant negative correlations with SST increase, ranging from -0.69 to -0.72 (Fig. 4.8a). The changes of those components therefore show statistically significant linear relationships with change of SST. SW changes do not exhibit correlations significant at 99%, but if the L group exhibits a more robust correlation with SST increase (-0.44, p-value <0.05) compared to the H group (-0.12, p-value > 0.1) (Fig. 4.8p). The plots further illustrate the dispersion of individual models. The L group displays a smaller dispersion than the H group. Across scenarios, the SSP1-2.6 scenario with low emissions demonstrates the smallest dispersion, followed by the SSP2-4.5 scenario, and lastly, the SSP5-8.5 scenario with high emissions exhibits the largest dispersion.

For heat flux components whose change shows a linear relationship with SST change (i.e., LW, LH and SH), we examine which processes explain those relationships. For that, we differentiate Eqs. 4.2, 4.3 and 4.4 with respect to SST, to obtain the slope of this linear relationship. We moreover show the changes of  $W$ ,  $\Delta q$ ,  $\Delta T$  and  $Q_a$  (as defined from Eqs. 4.2

## Chapter 4. CMIP6 analysis: heat fluxes estimation and the role of the climate change

to 4.4) relative to the baseline period 1995-2014 in Fig. 4.8.

For LW, we examine the contributions of changes of longwave radiation directed both downward and upward at the surface, obtaining from Eq. 4.2:

$$\frac{\partial LW}{\partial SST} = \frac{\partial Qa}{\partial SST} - 4\epsilon\sigma SST^3 \quad (\text{Eq. 4.5})$$

Figure 4.8m shows a strong positive correlation between  $\Delta LW$  and  $\Delta Qa$ , with correlation coefficients of  $r_L=0.98$  and  $r_H=0.93$ , both of which are statistically significant (p-value  $<0.01$ ).  $\Delta Qa$  also has a strong positive correlation with  $\Delta SST$ , with correlation coefficients of  $r_L=0.99$  and  $r_H=0.95$  (p-value  $<0.01$ ). An increase in SST therefore leads to an increase in  $\Delta Qa$ , which induces an increase of  $\Delta LW$ , i.e. a stronger decrease of LW loss from the ocean. Eq. 4.5 provides the value of the slope of the linear relationship between  $\Delta LW$  and  $\Delta SST$ . The slope of the linear regression between  $\Delta Qa$  and  $\Delta SST$ , i.e. the first term of the Eq. 4.5, is about  $10.2 \text{ W.m}^{-2}.\text{C}^{-1}$  for both L and H groups (Fig. 4.8n). Meanwhile, for a SST  $\sim 300 \text{ K}$ ,  $-4\epsilon\sigma SST^3 \sim -6.5 \text{ W.m}^{-2}.\text{C}^{-1}$ : a stronger SST increase induces a decrease of  $\Delta LW$ , i.e. an increase of LW loss. We therefore obtain for  $\frac{\partial LW}{\partial SST} = \frac{\partial Qa}{\partial SST} - 4\epsilon\sigma SST^3 = 10.2 - 6.5 = 3.7 \text{ W.m}^{-2}.\text{C}^{-1}$ , exactly the slope of the linear regression line between  $\Delta LW$  and  $\Delta SST$  (Fig. 4.8k). The decrease in LW loss from the ocean is therefore driven by the direct effect of SST increase as well as by its indirect effect on  $Qa$ , which counteracts the direct effect.

For LH and SH, we differentiate Eqs. 4.3 and 4.4 to distinguish the respective contributions of the thermodynamic (related to air humidity and temperature) and dynamic (related to wind speed) processes to the changes of heat fluxes associated with the projected SST change. We obtain:

$$\begin{aligned} \frac{\partial LH}{\partial SST} &= \rho L_v C_E W \frac{\partial \Delta q}{\partial SST} + \rho L_v C_E \Delta q \frac{\partial W}{\partial SST} \\ &= \alpha W \frac{\partial \Delta q}{\partial SST} + \alpha \Delta q \frac{\partial W}{\partial SST} \end{aligned} \quad (\text{Eq. 4.6})$$

$$\begin{aligned} \frac{\partial SH}{\partial SST} &= \rho C_p C_H W \frac{\partial \Delta T}{\partial SST} + \rho C_p C_H \Delta T \frac{\partial W}{\partial SST} \\ &= \beta W \frac{\partial \Delta T}{\partial SST} + \beta \Delta T \frac{\partial W}{\partial SST} \end{aligned} \quad (\text{Eq. 4.7})$$

## Chapter 4. CMIP6 analysis: heat fluxes estimation and the role of the climate change

Where  $\alpha = \rho L_v C_E = 2.379 \text{ J.m}^{-3}$ ;  $\beta = \rho C_P C_H = 1.0176 \text{ J.m}^{-3}.\text{K}^{-1}$ .

The first term on the right-hand side of Eqs. 4.6 and 4.7 is the thermodynamic term:  $\alpha W \frac{\partial \Delta q}{\partial SST}$  and  $\beta W \frac{\partial \Delta T}{\partial SST}$  quantify the humidity and temperature contribution to the LH and SH change, respectively, associated with the SST change. The second term is the dynamic term:  $\alpha \Delta q \frac{\partial W}{\partial SST}$  and  $\beta \Delta T \frac{\partial W}{\partial SST}$  quantify the wind speed contribution to the LH and SH change, respectively, associated with the SST change.

Figure 4.8q shows a weak and non-significant (p-value > 0.05) negative correlation between  $\Delta W$  and  $\Delta SST$ . The slope of the trend line is very small, with  $-0.01 \text{ m.s}^{-1}.\text{°C}^{-1}$  for group L and  $-0.008 \text{ m.s}^{-1}.\text{°C}^{-1}$  for group H. This suggests that wind speed does not change significantly with the sea surface warming, and that the dynamic term in Eqs. 4.6 and 4.7 do not significantly contribute to the relationship between LH and SH changes and SST changes. This is consistent by the weak and non-significant correlation between  $\Delta LH$  and  $\Delta W$  and  $\Delta SH$  and  $\Delta W$  (p-value > 0.1, Fig. 4.8d, h). In the next paragraph, we therefore relate the relationship between  $\Delta LH$ ,  $\Delta SH$  and  $\Delta SST$  to the thermodynamic term that accounts for the contributions of  $\Delta(\Delta q)$  and  $\Delta(\Delta T)$ .

Figure 4.8a shows a positive linear relationship between  $\Delta LH$  and  $\Delta SST$ , with p-value < 0.01 and slopes of  $-1.8 \text{ W.m}^{-2}.\text{°C}^{-1}$  and  $-2.6 \text{ W.m}^{-2}.\text{°C}^{-1}$  for group L and H, respectively. Moreover, Figure 4.8c shows a negative linear relationship between  $\Delta(\Delta q)$  and  $\Delta SST$  ( $r_L = -0.62$ ,  $r_H = -0.73$  with p-value < 0.01) with slopes of  $-0.48 \text{ g.kg}^{-1}.\text{°C}^{-1}$  and  $-0.36 \text{ g.kg}^{-1}.\text{°C}^{-1}$  for group L and H, respectively. The mean W value over the SEA region during the period 2081-2099 is  $1.6 \text{ m.s}^{-1}$  and  $3.10 \text{ m.s}^{-1}$  for the L (which includes all models in group L under three scenarios) and H (which includes all models in group H under three scenarios) group, respectively. The thermodynamic term of Eq. 4.6 is therefore equal to  $\alpha W \frac{\partial \Delta q}{\partial SST} = 2.379 \times 1.6 \times -0.48 \sim -1.8 \text{ W.m}^{-2}.\text{°C}^{-1}$  and  $2.379 \times 3.1 \times -0.36 \sim -2.7 \text{ W.m}^{-2}.\text{°C}^{-1}$  for group L and H, respectively. Those values are consistent with the slope values obtained for the linear regression between  $\Delta LH$  and  $\Delta SST$  on Fig. 4.8a. Therefore, the amplitude of LH decrease (i.e. of LH loss increase) is driven by the thermodynamic term, related to the fact that  $\Delta q$  decreases with increasing SST.

## Chapter 4. CMIP6 analysis: heat fluxes estimation and the role of the climate change

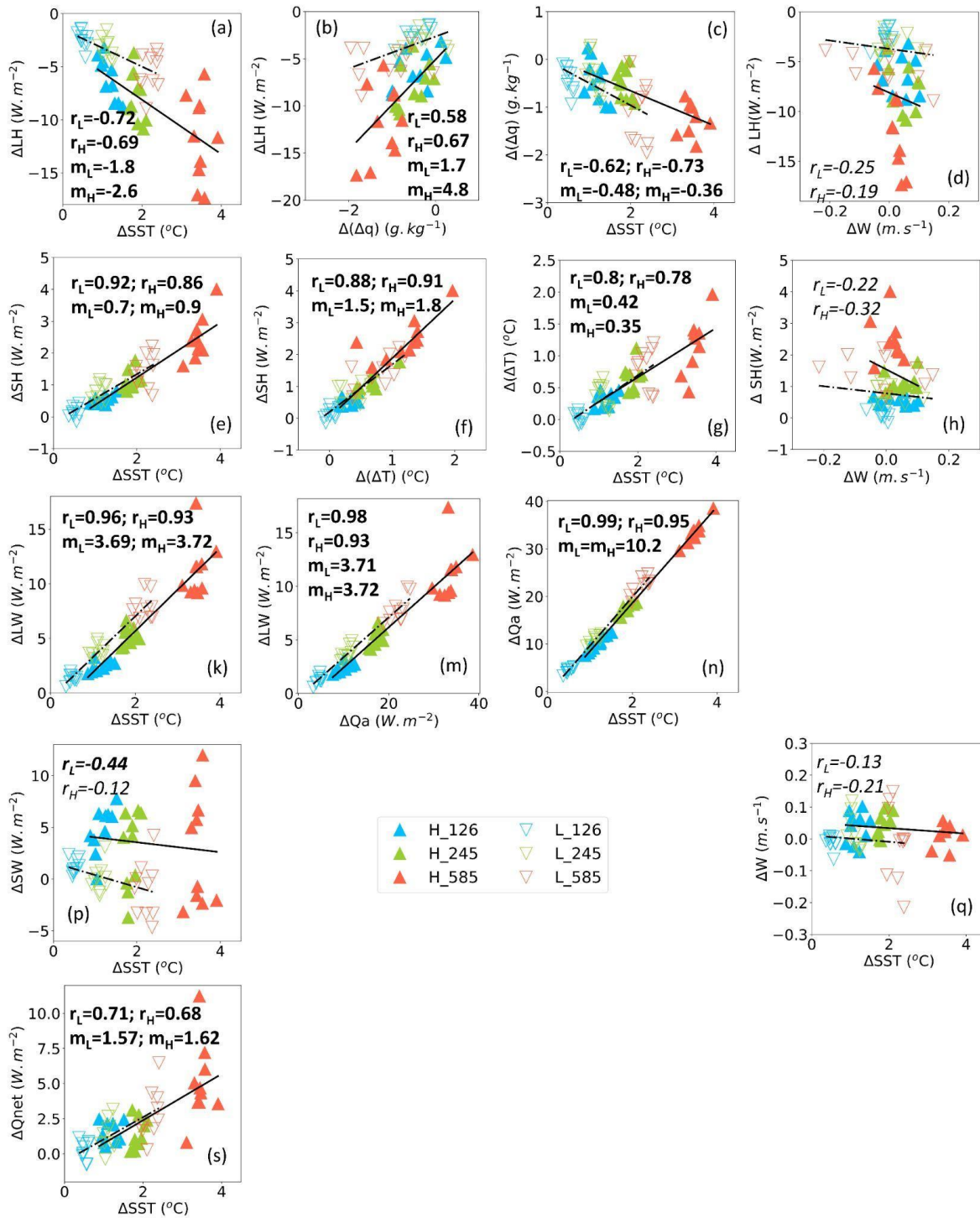


**Figure 4.8.** Projected changes in  $Q_{net}$  and its four components and of  $Q_a$ ,  $W$ ,  $\Delta q = q_a - q_s$ , and  $\Delta T = T_a - T_s$  versus changes in SST by the end of the century compared to the baseline period. Filled upward-pointing triangles represent the high warming (H) group, and non-filled downward-pointing triangles represent the low warming (L) group. Blue, green, and red colors correspond to the scenarios SSP1-2.6, SSP2-4.5, and SSP5-8.5, respectively. Solid and dash-

## Chapter 4. CMIP6 analysis: heat fluxes estimation and the role of the climate change

dotted lines represent trend lines for the H group and the L group, respectively. The Pearson correlation coefficient between changes for the L group and  $\Delta SST$  is denoted as  $r_L$ , while the correlation coefficient between changes for the H group and  $\Delta SST$  is denoted as  $r_H$ , where bold values with p-value  $<0.01$ , bold and italic values with p-value  $<0.05$ , and italic values p-value  $>0.1$ . Values of  $m_L$  and  $m_H$  are slopes for components that show a statistically significant linear relationship (p-value  $<0.01$ ), for group L and H, respectively.

We perform the same analysis for SH. [Figure 4.8e](#) shows a positive linear relationship between  $\Delta SH$  and  $\Delta SST$ : (p-value  $<0.01$  and slopes of  $0.7 \text{ W.m}^{-2}.\text{°C}^{-1}$  and  $0.9 \text{ W.m}^{-2}.\text{°C}^{-1}$  for group L and H, respectively). [Figure 4.8g](#) shows a positive linear relationship between  $\Delta(\Delta T)$  and  $\Delta SST$ : p-value  $<0.01$  with slopes of  $0.42 \text{ °C}.\text{°C}^{-1}$  and  $0.35 \text{ °C}.\text{°C}^{-1}$  for group L and H, respectively. The thermodynamic term of Eq. 4.7 is therefore equal to  $\beta W \frac{\partial \Delta T}{\partial SST} = 1.0176 \times 1.6 \times 0.42 \sim 0.75 \text{ W.m}^{-2}.\text{°C}^{-1}$  and  $1.0176 \times 3.1 \times 0.35 \sim 1.10 \text{ W.m}^{-2}.\text{°C}^{-1}$  for group L and H, respectively, consistent with the slope values obtained for the linear regression between  $\Delta SH$  and  $\Delta SST$ . Therefore, the amplitude of SH increase (i.e., of SH loss decrease) is driven by the thermodynamic term and related to the fact that  $\Delta T = Ta - SST$  increases with increasing SST: the difference between the air temperature and SST decreases when SST increases.

This analysis shows that changes in LH and SH are primarily associated with the thermodynamic effect ( $\Delta T$  and  $\Delta q$ ), which change linearly with SST, rather than the dynamic effect ( $W$ ) that does show a significant change with sea surface warming. It is noteworthy that this observation aligns with the findings of previous studies that showed that CMIP5 models did not produce a significant change of sea surface wind intensity in the SEA region, as reported in [Herrmann et al. \(2020, 2022\)](#).

### 4.6. Conclusions of chapter

In this study, we first assessed the representation of air-sea heat flux over the SEA region in CMIP6 models, comparing a dataset of simulations from 30 models available at the time of data retrieval with ERA5 over the period 1995-2014.

In the annual mean, both ERA5 and CMIP6 MME datasets indicate that the SEA region undergoes a net heat gain for the ocean, with average  $Q_{net}$  values of  $21.3 \pm 11.8 \text{ W.m}^{-2}$  and  $6.8 \pm 11.4 \text{ W.m}^{-2}$ , respectively. The CMIP6 MME values for SW, LW, LH, and SH averaged

## Chapter 4. CMIP6 analysis: heat fluxes estimation and the role of the climate change

over SEA during the baseline period 1995–2014 are  $209\pm 6.6 \text{ W.m}^{-2}$ ,  $-50.8\pm 1.7 \text{ W.m}^{-2}$ ,  $-137.8\pm 7.2 \text{ W.m}^{-2}$ , and  $-13.6\pm 1.1 \text{ W.m}^{-2}$ , respectively, vs.  $201.8\pm 7.3 \text{ W.m}^{-2}$ ,  $-50.8\pm 1.8 \text{ W.m}^{-2}$ ,  $-126.4\pm 6.9 \text{ W.m}^{-2}$  and  $-12.3\pm 1.1 \text{ W.m}^{-2}$  in ERA5. CMIP6 MME underestimates  $Q_{\text{net}}$  by one-third compared to ERA5, primarily attributable to an overestimation of LH loss by  $11.5 \text{ W.m}^{-2}$ . The spatial patterns between the two products however exhibit similarity, with a highly statistically significant spatial correlation of 0.87 for the yearly average of  $Q_{\text{net}}$ . The zonal average of  $Q_{\text{net}}$  in the CMIP6 MME is consistently smaller than in ERA5 with the most substantial disparity occurring near  $2^{\circ}\text{N}$ . For all components, the highest biases emerge during the DJF season, while the least biases are observed during MAM. The primary contributors to biases in seasonal  $Q_{\text{net}}$  are LH and SW. SW consistently exhibits lower values than that from ERA5 within the  $0^{\circ}\text{N}$  to  $20^{\circ}\text{N}$  range, and the most significant bias in LH manifests around the equator. The CMIP6 MME reproduces well the seasonal cycle of all components of air-sea heat fluxes over the SEA region. The semiannual cycle of  $Q_{\text{net}}$  is well depicted, with a primary maximum in April and a secondary maximum in October, consistent with the minimum LH loss in April, secondary minimum LH loss in October, and maximum HL loss in January.

CMIP6 models and MME are thus capable of capturing the spatial variability and seasonal cycle of heat fluxes well, but with large biases in magnitude. In numerical modeling, air-sea fluxes are commonly estimated from bulk flux parameterization using flux-related near-surface meteorological variables (wind speed, sea and air temperatures, and humidity) (Bonino et al. 2022). Previous studies have shown that the uncertainty in the parameterizations in bulk formulae for heat fluxes can lead to significant biases (Weare 1989, Planton et al. 1991, Wang et al. 2017, Zhou et al. 2020). The biases in the near-surface specific humidity and wind speed in the products are the primary sources of the biases in their respective LH. Zhou et al (2020) found that near-surface humidity has a greater contribution to the bias in LH than wind speed, while air temperature has a greater contribution to the bias in SH than wind speed. Meanwhile the biases in LH are thought to contribute to 75% of the biases in  $Q_{\text{net}}$  over tropical oceans (Jo et al. 2004). This results in a wide and varied performance range for each individual model within CMIP6 concerning each component of heat flux. Consequently, when employing a multiple model's ensemble (MME), the negative bias in  $Q_{\text{net}}$  compared to ERA5 arises from CMIP6 MME overestimating LH loss and slightly underestimating SW. The disparities in SW and LH are the primary causes of bias in  $Q_{\text{net}}$ , followed by disparity in LW and SH. Therefore, understanding both the capabilities of a model to simulate surface heat flux and the sources of its biases is important and necessary.

## Chapter 4. CMIP6 analysis: heat fluxes estimation and the role of the climate change

Second, we used these CMIP6 model outputs to examine the impact of climate change on air-sea heat flux in the SEA region. All CMIP6 models considered here produce a  $Q_{net}$  increase over the 21st century for the SEA region, pronounced at the mid-century and intensified further by the end of the century under all scenarios. The results show that the projected changes in  $Q_{net}$ , LH, LW, and SH are highest under SSP5-8.5 (3.7, -8.4, 9.2, and 1.9  $W.m^{-2}$ , respectively) and lowest under SSP1-2.6 (0.8, -4.1, 1.8 and 0.3  $W.m^{-2}$ , respectively). SW exhibits an opposite trend, with the highest change under SSP1-2.6 (2.9  $W.m^{-2}$ ) and the lowest under SSP5-8.5 scenarios (1.0  $W.m^{-2}$ ).

To assess the sensitivity of heat flux to SST changes in the model, we curated two distinct groups of models: the Low warming models group (L) and the High warming models group (H), determined by the lowest and highest projected SST changes in the future. Across scenarios, the models producing strong warming consistently projected more pronounced changes in heat flux compared to models producing lower warming, except for SW, where the trend is reversed.

We have further shown that there is a linear relationship between the change of SST and the change of  $Q_{net}$ , related to linear relationships between changes of LW, LH and SH and change of SST. The thermodynamic component related to changes of humidity and temperature drives the changes of LH and SH with respect to SST change, and the dynamic term related to change of wind intensity is negligible. With increasing SST in the future, the decrease of  $\Delta q$  will lead to an increase in LH loss from the ocean, and the increase of  $\Delta T$ , that corresponds to a stronger warming of air than of sea surface, will lead to a decrease in SH loss.

Further, the errors in each model depend on various factors, including differences in utilizing different heat flux bulk formulas to estimate the components of heat flux. This issue needs to be considered in other future studies.

## Chapter 5. Conclusions and perspectives

### Contents

5.1 Conclusions.....	131
5.1.1 Impact of ENSO/ENSO Modoki on rainfall variability .....	132
5.1.2 Estimation, variability, and evolution of air-sea heat fluxes .....	133
5.1.2.1 Estimating air-sea heat fluxes over the SEA region.....	133
5.1.2.2 Representation and climate projection of SEA air-sea heat fluxes in CMIP6 models.....	134
5.2 Perspectives.....	135
<i>Relationship between SST and heat fluxes</i> .....	136

### Conclusion and perspectives in English

#### 5.1 Conclusions

The atmosphere and ocean act as a coupled system, interacting in various ways, including ocean-surface wind stresses, downward radiation fluxes, and exchanges of surface heat, energy and water. These interactions drive ocean currents and large-scale circulation patterns, modulate upper-ocean dynamics and thermodynamics, control atmospheric cloud development, and shape climate and weather phenomena (Cronin et al. 2019, Yu 2019, Zhang 2005). This intricate interaction has multifaceted impacts that extend across different scales and aspects of the Earth's climate system.

In Southeast Asia (SEA), El Niño Southern Oscillation (ENSO), a coupled ocean-atmosphere phenomenon in the tropical Pacific, is one of the main factors that influences precipitation patterns across the region through remote atmospheric teleconnections. Notably, there exists a distinction between ENSO and a more recently identified ENSO variant known as ENSO Modoki. The impact of ENSO Modoki on SEA climate, in particular precipitation, remains insufficiently explored. Therefore, the primary objective of this thesis was to employ updated datasets to assess the impacts of both ENSO and ENSO Modoki on precipitation variability in Southeast Asia and its subregions, discerning the differential impacts of Modoki events compared to typical ENSO events, and identifying the associated circulation mechanisms.

Furthermore, understanding how heat fluxes at the air-sea interface vary across different spatial and temporal scales is also crucial for detecting and comprehending the consequences of climate variability and change, both at the global and regional scales (Trenberth et al. 2009). However, estimates of air-sea heat fluxes still exhibit significant uncertainties, in particular in the SEA region, due in particular to limitations in observational data. Hence, the second objective of this thesis was to estimate the net heat flux  $Q_{net}$  and its four components over SEA and examine their spatial and temporal variability and long-term evolution using available datasets and state-of-the-art CMIP6 climate models. We first established a benchmark value for air-sea heat flux in the SEA region, which can be utilized for the assessment of various available datasets (analysis and reanalysis, climate modeling, observations, etc.). We then evaluated the performance of CMIP6 models in representing air-sea heat fluxes over SEA and used those models to examine SEA air-sea heat fluxes response to climate change.

The primary outcomes of this thesis are as follows:

### 5.1.1 Impact of ENSO/ENSO Modoki on rainfall variability

We conducted an analysis of the impacts of ENSO and ENSO Modoki on rainfall during December-February (DJF) and June-August (JJA), the main wet seasons in the southeastern and northern SEA regions, respectively. Over the period 1979–2019, seven El Niño (EN), six La Niña (LN), five El Niño Modoki (EM), and five La Niña Modoki (LM) events were identified.

During the summer (JJA) and winter (DJF) of EN events, reduced rainfall occurred over the Maritime Continent and the Philippines, except for Western Philippines in JJA and West Kalimantan in DJF. Similar but drier/wetter conditions were identified during EM events. In LN events, increased rainfall was observed in most subregions except for Western Philippines and parts of the Indochina Peninsula in JJA and DJF in certain areas southward, such as South Sumatra, West Kalimantan, and Papua. Compared to LN, LM events typically exhibited wetter/drier conditions in JJA for most subregions and wetter conditions in DJF over much of the Maritime Continent.

The decrease (increase) in rainfall over SEA during Modoki ENSO events compared to classic ENSO events is explained by reduced (enhanced) moisture transport into the region and the weakening (strengthening) of the ascending branch of the Walker circulation. For instance, during EN, negative anomalies of the ascending branch of the Walker circulation are situated southwest and southeast of SEA in JJA and DJF, thereby reducing rainfall and leading to drier conditions in the area. The negative anomalies of the ascending branch weaken progressively in EM, resulting in weaker rainfall reduction compared to EN over the Philippines and Papua in JJA and over Southeast Asia in DJF. The rainfall deficit in LM compared to LN in JJA originates from reduced moisture transport into northern SEA and a strong upper-level convergence anomaly leading to the weakening of the ascending motion below, thereby inhibiting rainfall. Meanwhile, the rainfall surplus in LM compared to LN in DJF in southern subregions is due to enhanced moisture transport by the Pacific easterlies and equatorial westerlies into the area, resulting in excess rainfall.

Our findings indicate that droughts during EM events may exhibit less severity than those during EN events across nearly all subregions in JJA, while floods during LM events could intensify compared to LN events, particularly in the southern regions of SEA during DJF.

### 5.1.2 Estimation, variability, and evolution of air-sea heat fluxes

#### 5.1.2.1 Estimating air-sea heat fluxes over the SEA region.

We first examined air-sea heat fluxes produced by 5 analysis and reanalysis datasets over the period 2017-2018: ERA5, ECMWF, MERRA-2, JRA-55 and CFSv2. The ECMWF and CFSv2 analyses, as well as reanalysis of MERRA-2, JRA-55, and ERA5, were evaluated for their spatial distribution, seasonal cycle, and annual mean values. In general, the higher (and positive)  $Q_{net}$  estimates (ERA5, ECMWF, CFSv2) are due to stronger SW (shortwave radiation) gain and weaker LH (latent heat) loss (especially CFSv2), while the negative  $Q_{net}$  (net heat flux) estimates (MERRA-2 and JRA-55) are due to weaker SW and stronger LH loss. The difference in SW and LH are the two main causes of the difference in  $Q_{net}$ , followed by the difference in LW (longwave radiation).

We then used the three-dimensional hydrostatic ocean circulation model SYMPHONIE to conduct six short-term simulations for the period 2017-2018 using two methods, bulk and flux, to investigate the sensitivity of the model sea surface temperature (SST) to different heat flux forcings. The simulated SST from the SYMPHONIE simulation using bulk formulae (CTL) was the closest to observations, with an annual mean bias of  $-0.28\text{ }^{\circ}\text{C}$  for 2018. For simulations using prescribed fluxes (and not computing them from bulk formulae), the smallest SST bias was obtained from the simulation using CTL fluxes ( $0.39\text{ }^{\circ}\text{C}$  for 2018), followed by the bias from simulations based on ECMWF and MERRA-2 fluxes (respectively  $1.05\text{ }^{\circ}\text{C}$  and  $-1.13\text{ }^{\circ}\text{C}$ ). CFSv2 produced a significant overestimation of SST over the entire region ( $4.46\text{ }^{\circ}\text{C}$ ), while JRA-55 underestimated SST ( $-2.59\text{ }^{\circ}\text{C}$ ). The time correlation coefficient of daily SST between CTL and OSTIA over 2017-2018 is the highest ( $>0.95$  in most regions), while low and nearly uncorrelated correlation coefficients in the equatorial region were observed in simulations based on MERRA-2, CFSv2 and JRA-55. Fluxes computed from the CTL simulations showed a  $\sim -6\text{ W}\cdot\text{m}^{-2}$  difference compared to ERA5 over 2017-2018. The relationship between SST bias and the average net heat flux prescribed to the model over 2017-2018 has been shown to be strongly linear and significant. We extended our analysis by running a 10-year simulation over

## Chapter 5. Conclusions and perspectives

2009-2018 using bulk formulas, still obtaining a  $\sim -6 \text{ W.m}^{-2}$  difference between fluxes computed from this simulation and ECMWF and ERA5. The main cause of this systematic net heat flux difference is the difference in LH and SH (sensible heat), which may be due to internal model errors and different parameterizations in the bulk heat flux formulae. Those heat fluxes estimates were compared to a variety of other heat flux products, which showed a large uncertainty in the estimation of air-sea exchange over the SEA region. ERA5 and ECMWF, although possibly overestimating the net heat flux by  $\sim 6 \text{ W.m}^{-2}$ , appear to be the best products in terms of air-sea heat flux values.

### *5.1.2.2 Representation and climate projection of SEA air-sea heat fluxes in CMIP6 models*

We used a dataset of 30 climate models from the Coupled Model Intercomparison Project Phase 6 (CMIP6), which were available at the time of data retrieval. We first assessed the representation of air-sea heat fluxes over the SEA region in this dataset through a comparative analysis with the ERA5 reanalysis dataset over the historical period. Overall, the CMIP6 models reproduce well the spatial distribution and seasonal cycle of air-sea heat fluxes, as evidenced by a high spatial correlation coefficient of 0.87 for the annual mean  $Q_{\text{net}}$  in CMIP6 multi-model ensemble (MME). However, the models exhibit significant biases in magnitude, with the CMIP6 MME underestimating  $Q_{\text{net}}$  by two-third compared to ERA5 in the annual mean ( $6.8 \text{ W.m}^{-2}$  on average over 1995-2014 vs.  $21.3 \text{ W.m}^{-2}$ ). Both the zonal mean and seasonal cycle indicate that the primary contributors to biases in seasonal  $Q_{\text{net}}$  values are the seasonal biases in LH loss and SW gain. [This is consistent with results from Jo et al. \(2004\)](#) who highlighted that the biases in LH contribute to 75% of the biases in  $Q_{\text{net}}$  estimates over the tropical ocean. Biases in CMIP6 models but also in regional climate models can be related to intrinsic errors and uncertainties in the physics and parameterizations of processes involved in air-sea heat fluxes (clouds, convection, ...). Therefore, it is essential to assess the ability of those models to simulate surface heat fluxes and identify the sources of their biases.

All CMIP6 models considered here project an increase in  $Q_{\text{net}}$  over the 21st century for the SEA region in all scenarios. The projected changes in  $Q_{\text{net}}$ , LH, LW, and SH are highest in SSP5-8.5 (3.7, -8.4, 9.2, and  $1.9 \text{ W.m}^{-2}$ , respectively), followed by SSP2-4.5 (1.3, -5.4, 4.4, and  $0.9 \text{ W.m}^{-2}$ , respectively) and lowest under SSP1-2.6 (0.8, -4.1, 1.8, and  $0.3 \text{ W.m}^{-2}$ , respectively). SW exhibits the opposite trend, with the largest change under SSP1-2.6 ( $2.9 \text{ W.m}^{-2}$ ) and the smallest in the SSP5-8.5 scenarios ( $1.0 \text{ W.m}^{-2}$ ). To assess the sensitivity of heat

## Chapter 5. Conclusions and perspectives

flux to SST changes in models, we selected two distinct model groups: a Low warming (L) model group and a High warming (H) model group, defined by the lowest and highest projected SST changes in the future. For all scenarios, the models producing stronger warming consistently projected more pronounced changes in heat flux compared to models producing lower warming, except for SW, where the trend is reversed. We obtained a linear relationship between the change of SST and the change of  $Q_{net}$ , related to linear relationships between changes of LW, LH and SH and change of SST. The thermodynamic effect related to changes of humidity and temperature drive the changes of LH and SH with respect to SST change, and the dynamic term related to change of wind intensity is negligible.

### 5.2 Perspectives

In the investigation about the impact of ENSO/ENSO Modoki on SEA rainfall outlined in Chapter 2, the role of air-sea heat transfer has remained unexplored. Given the established correlation between latent and sensible heat fluxes and rainfall (Gao et al., 2015, Juneng et al., 2016), we underscore the crucial need to examine the impact of both ENSO and ENSO Modoki phenomena on oceanic heat transport and budget across the entire SEA region. For this, the potential of regional models to reproduce both types of ENSO and their associated effects should be subjected to careful scrutiny in future studies. Furthermore, an alternative perspective for studying ENSO and its variants involves leveraging CMIP6 data. Based on the long-term availability of this dataset, we can analyze changes in the intensity of ENSO events and projected variations in their intensity. Additionally, examining how ENSO interacts with other climate factors would provide a more comprehensive understanding of its influence on various global climate patterns.

The results of chapters 3 and 4 improved our understanding of the dynamics of heat fluxes in the SEA region through the utilization of the latest datasets including CMIP6 outputs. Our findings highlighted the importance of considering model biases in heat flux simulations when assessing future climate projections. Due to the lack of a comprehensive dataset for estimating air-sea fluxes in the region, we relied on the latest reanalysis (ERA5), based on the conclusions of simulations that did not exceed 10 years. Further analysis over longer periods should be considered in the future to increase the robustness of our analysis and detect trends and changes in ocean and atmosphere conditions. Some processes, such as the Atlantic Multidecadal Oscillation (AMO) or the Pacific Decadal Oscillation (PDO), indeed operate on decadal

## Chapter 5. Conclusions and perspectives

timescales. Those annual, decadal, and long-term variations affect the ocean's ability to absorb and release heat. Further, the model outputs from CMIP6 effectively illustrate the relationships among various components of heat flux and the dynamic processes with SST. This demonstrates the interaction and feedback between the ocean and the atmosphere, as captured by the models. Furthermore, the results contribute to an enhanced understanding of the models' biases in heat flux estimation over the SEA region, thus opening up the possibility of refining these inaccuracies in future studies.

Applying over the SEA the same analysis as done by [Trinh et al. \(2023\)](#) over the South China Sea using a fully closed budget model over the area would contribute to an improved understanding of air-sea heat fluxes over the region. This would in particular allow to examine consistently surface atmospheric fluxes, river fluxes and lateral fluxes through interocean straits, as well as internal variations, thus, to better understand water masses transfer through the SEA region (SCSTF and ITF) and their role in the ocean thermohaline circulation and climate. Finally, using a ocean-atmosphere regional coupled model as presently developed from SYMPHONIE and RegCM will also improve our understanding of air-sea interactions in the area. Those outcomes are essential to improve predictions of extreme events as well as predictions of climate phenomena such as El Niño and La Niña and their variants, and of course for climate projections.

### *Relationship between SST and heat fluxes*

We did a preliminary analysis of the relationship between heat fluxes and wind speed and SST over the historical period ([Fig. 5.1](#)). [Figure 5.1](#) shows the existence of a tipping point in SST values at which the relationships between  $Q_{net}$ , each heat flux component, as well as wind speed, on one side and SST on the other side change sharply. SW gains, LH loss, and W exhibit similar trends: they increase with SST until reaching their respective tipping points (around 28.2°C, 27.6°C, and 27.0°C, respectively), then decrease with further SST increase. Regarding SH and LW losses, they decrease as SST increases up to the tipping points of 28.3°C and 28.7°C, respectively. Beyond these points, SH and LW losses increase with increasing SST values. The trend of LW loss after the tipping point shows a smaller increase compared to the increase of SH loss.

$Q_{net}$  is the balance of net SW gain and net LW, LH, and SH losses. Therefore, the variation of  $Q_{net}$  as a function of SST reveals the compensating effect of the different trends in the four

flux components: below the  $\sim 28^\circ\text{C}$  threshold,  $Q_{\text{net}}$  increases with respect to SST due to the strong increasing trend in SW gain and decreasing trend in LW and SH losses, which compensates and exceeds the increasing trend in LH loss. Above this threshold, the decrease in LH loss largely dominates SW gain decrease and SH and LW losses increase, and  $Q_{\text{net}}$  still increases with SST.

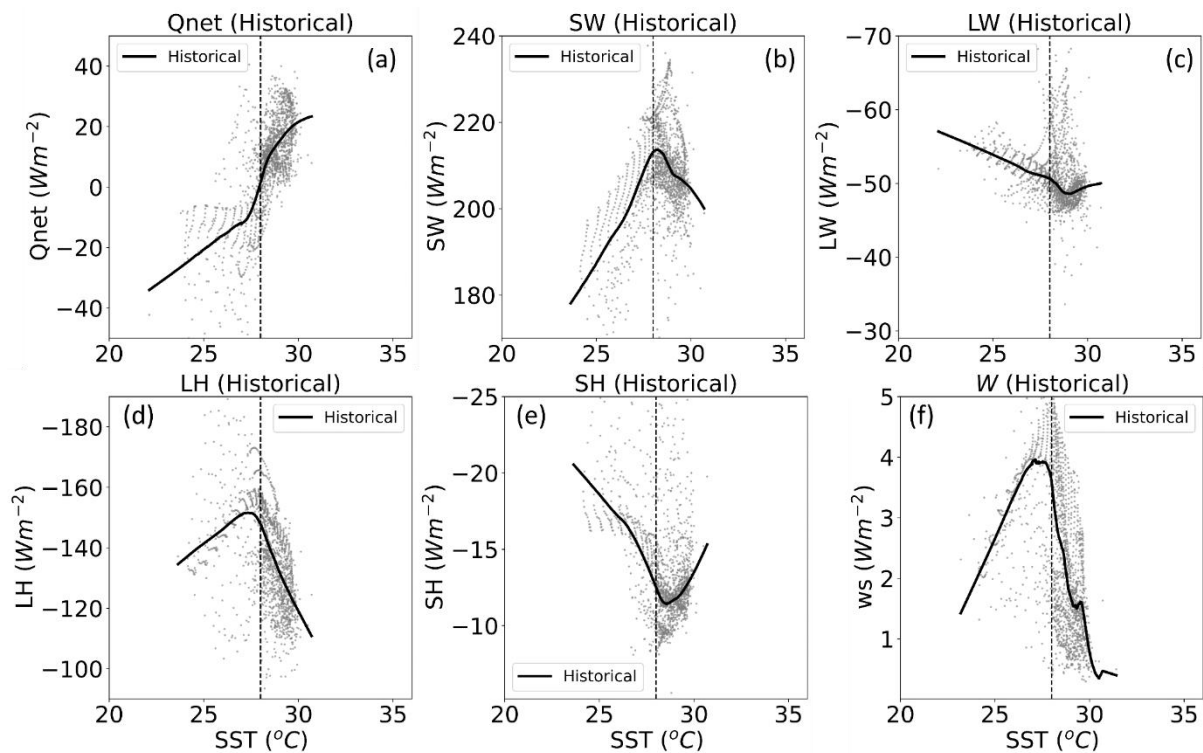


**Figure 5.1.** Scatter plots showing the relationships of (a)  $Q_{\text{net}}$ , (b) SW, (c) LW, (d) LH, (e) SH, and (f) W vs. SST for the period 1995–2014. Each dot on the plot represents a distinct grid point in the study domain. The curves fitted through the set of data points were obtained using the LOESS technique. The vertical dashed line corresponds to SST at  $28^\circ\text{C}$ .

Our results therefore show that the relationships between heat fluxes, wind speed, and SST over the SEA oceanic region are pronounced, and that those trends change above at a tipping threshold of around  $27^\circ\text{C} - 28.7^\circ\text{C}$ . Previous studies revealed that above a certain SST threshold, the air becomes more moist and less dense, resulting in a convectively unstable surface air layer (Ramanathan and Collins 1992; Zhang et al. 1995). Neelin and Held (1987) moreover demonstrated that convectively unstable regions on a large-scale experience low-level convergence, characterized by low wind speeds. Lower wind speeds when SST exceeds a certain threshold would then become a limiting factor for LH loss (Liu 1988, Zhang et al.

## Chapter 5. Conclusions and perspectives

1995, Kumar et al. 2017). Indeed, Liu (1988) confirmed that regions with surface convergence experience a decrease in LH loss due to a decrease in wind speeds. Given that the SST threshold for onset of convection falls within a similar temperature range (Graham and Barnett 1987; Johnson and Xie 2010), our results suggest that convection is a dominant factor causing these tipping points. Hence, the tipping points displayed for wind speeds (Fig. 5.1f) and LH (Fig. 5.1d) can be explained by those dynamic factors: SST values above 28°C lead to unstable atmosphere and stronger convection which in turn increases low-level convergence, resulting in weaker surface wind speeds and, consequently, weaker LH loss. On the other hand, stronger convection generates more clouds associated with convective systems, which block SW from reaching the surface, thus reducing surface SW (Fig. 5.1b). Meanwhile, the increasing LW and SH losses are accelerated above the SST tipping thresholds, acting to restore SST to lower values, i.e. cool the ocean. In brief, all four components of heat flux provide feedback on SST variations over the SEA region.

Projected SST changes vary with future SSP scenarios (Figure 4.A1). As SST increases in the future, a question arises: do the relationships between heat flux components and wind speed and SST, such as the tipping points identified in Fig. 5.1, also change? Figure 5.2 displays these projected relationships for the end of the century for the L and H model groups under the three SSP scenarios. Although the projected heat flux components and wind speed follow the same trends as for the historical period, the SST tipping thresholds shift to higher values, all the more so as the SST warming is greater. For instance, the L1-2.6 group, with the smallest projected SST increase, exhibits a threshold value of around 28°C for SW (Fig. 5.2b). The L2-4.5 and H1-2.6 groups have threshold values of around 29–29.5°C, followed by the L5-8.5 and H2.4-5 groups, both having threshold values of approximately 30°C. Finally, the H5-8.5 group, with the largest SST increase, has a tipping threshold value of about 32°C. Similar tendencies in the shift of tipping thresholds are observed for LW, LH, SH and wind speed.

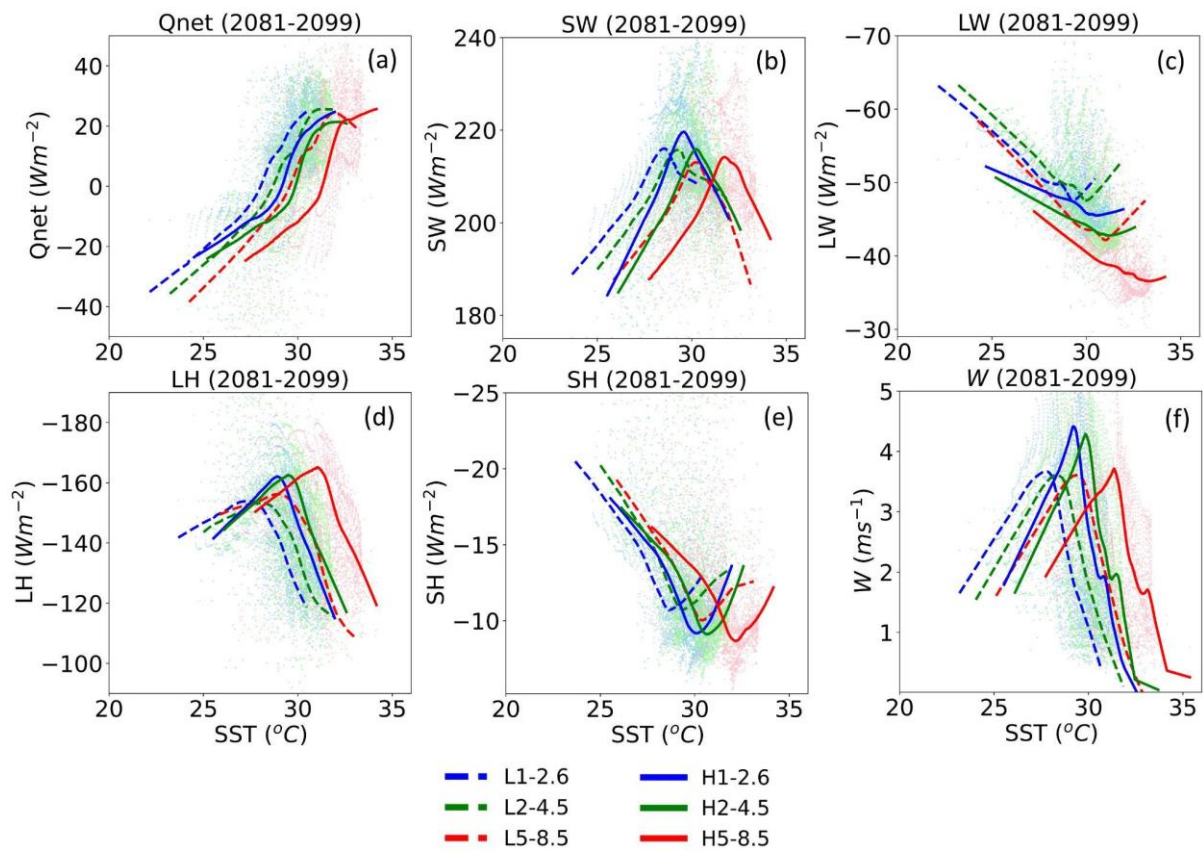


**Figure 5.2.** Same as Figure 5.1 for the L (dashed curve) and H (solid curve) groups under SSP1-2.6 (blue color), SSP2-4.5 (green color), and SSP5-8.5 (red color) scenarios for the period 2081–2099.

# CONCLUSION GÉNÉRALE

## I. Conclusions

L'atmosphère et l'océan agissent comme un système couplé, interagissant de diverses manières, incluant la friction du vent à la surface de l'océan, les flux de rayonnement et les échanges de chaleur, d'énergie et d'eau en surface. Ces interactions déterminent les courants océaniques et la circulation à grande échelle, modulent la dynamique et la thermodynamique de la couche supérieure de l'océan, contrôlent le développement des nuages atmosphériques et façonnent les phénomènes climatiques et météorologiques (Cronin et al. 2019, Yu 2019, Zhang 2005). Cette interaction complexe a des impacts à multiples facettes qui s'étendent à différentes échelles et à différents aspects du système climatique terrestre.

En Asie du Sud-Est (SEA), l'oscillation australe El Niño (ENSO), un phénomène couplé océan-atmosphère dans le Pacifique tropical, est l'un des principaux facteurs qui influencent les régimes de précipitations dans la région par le biais de téléconnexions atmosphériques. Il existe notamment une distinction entre ENSO et une variante d'ENSO identifiée plus récemment, connue sous le nom d'ENSO Modoki. L'impact d'ENSO Modoki sur le climat de SEA, en particulier sur les précipitations, n'a pas été suffisamment étudié. Par conséquent, l'objectif principal de cette thèse était d'utiliser des ensembles de données actualisées pour évaluer les impacts d'ENSO et d'ENSO Modoki sur la variabilité des précipitations en Asie du Sud-Est et dans ses sous-régions, en discernant les impacts différentiels des événements Modoki par rapport aux événements ENSO typiques, et en identifiant les mécanismes de circulation associés.

Il est également essentiel de comprendre comment les flux de chaleur à l'interface air-mer varient à différentes échelles spatiales et temporelles pour détecter et comprendre les conséquences de la variabilité et du changement climatiques, tant à l'échelle mondiale que régionale (Trenberth et al. 2009). Cependant, les estimations des flux de chaleur air-mer présentent encore des incertitudes significatives, en particulier dans la région SEA, en raison notamment des limitations des données d'observation. Par conséquent, le deuxième objectif de cette thèse était d'estimer le flux de chaleur net  $Q_{net}$  et ses quatre composantes dans la région SEA et d'examiner leur variabilité spatiale et temporelle ainsi que leur évolution à long terme en utilisant les ensembles de données disponibles et les modèles climatiques CMIP6. Nous

avons d'abord établi une valeur de référence pour le flux de chaleur air-mer dans la région SEA, qui peut être utilisée pour l'évaluation de divers ensembles de données disponibles (analyse et réanalyse, modélisation climatique, observations, etc.) Nous avons ensuite évalué la performance des modèles CMIP6 dans la représentation des flux de chaleur air-mer dans la région SEA et nous avons utilisé ces modèles pour examiner la réponse au changement climatique des flux de chaleur air-mer dans la région SEA.

Les principaux résultats de cette thèse sont les suivants:

### **I.1 Impact d'ENSO/ENSO Modoki sur la variabilité des précipitations**

Nous avons effectué une analyse des impacts d'ENSO et d'ENSO Modoki sur les précipitations pendant les mois de décembre-février (DJF) et de juin-août (JJA), les principales saisons des pluies dans les régions du sud-est et du nord de la SEA, respectivement. Sur la période 1979-2019, sept événements El Niño (EN), six La Niña (LN), cinq El Niño Modoki (EM) et cinq La Niña Modoki (LM) ont été identifiés.

Au cours de l'été (JJA) et de l'hiver (DJF) des événements EN, les précipitations sont réduites sur le continent maritime et les Philippines, à l'exception de l'ouest des Philippines (JJA) et de l'ouest du Kalimantan (DJF). Des conditions similaires mais plus sèches/humides ont été identifiées lors des événements EM. Lors des événements LN, une augmentation des précipitations a été observée dans la plupart des sous-régions, à l'exception de l'ouest des Philippines et de certaines parties de la péninsule indochinoise lors de la JJA et de la DJF dans certaines zones vers le sud, telles que le sud de Sumatra, l'ouest du Kalimantan et la Papouasie. Par rapport aux événements LN, les événements LM présentent généralement des conditions plus humides/sèches en JJA pour la plupart des sous-régions et des conditions plus humides en DJF sur la majeure partie du continent maritime.

La diminution (augmentation) des précipitations sur SEA pendant les événements ENSO Modoki par rapport aux événements ENSO classiques s'explique par la réduction (augmentation) du transport de l'humidité dans la région et l'affaiblissement (renforcement) de la branche ascendante de la circulation de Walker. Par exemple, pendant EN, des anomalies négatives de la branche ascendante de la circulation de Walker sont situées au sud-ouest et au sud-est de SEA en JJA et DJF, réduisant ainsi les précipitations et conduisant à des conditions plus sèches dans la région. Les anomalies négatives de la branche ascendante s'affaiblissent progressivement sur EM, entraînant une réduction des précipitations plus faible que sur EN sur

les Philippines et la Papouasie en JJA et sur l'Asie du Sud-Est en DJF. Le déficit pluviométrique dans LM par rapport à LN dans JJA provient d'une réduction du transport d'humidité dans le nord de l'Asie du Sud-Est et d'une forte anomalie de convergence en altitude conduisant à l'affaiblissement du mouvement ascendant en dessous, ce qui inhibe les précipitations. Par ailleurs, l'excédent pluviométrique dans LM par rapport à LN dans DJF dans les sous-régions méridionales est dû au transport accru d'humidité par les vents d'est du Pacifique et les vents d'ouest équatoriaux dans la région, ce qui entraîne des précipitations excessives.

Nos résultats indiquent que les sécheresses pendant les événements El Niño Modoli peuvent être moins sévères que celles pendant les événements El Niño dans presque toutes les sous-régions de la JJA, tandis que les inondations pendant les événements La Niña Modoki pourraient s'intensifier par rapport aux événements La Niña, en particulier dans les régions méridionales de la SEA pendant l'hiver boréal.

### **I.2 Estimation, variabilité et évolution des flux de chaleur air-mer**

#### *I.2.1 Estimation des flux de chaleur air-mer sur la région SEA*

Nous avons tout d'abord examiné les flux de chaleur air-mer produits par 5 analyses et réanalyses atmosphériques sur la période 2017-2018: ERA5, ECMWF, MERRA-2, JRA-55 et CFSv2. Les analyses ECMWF et CFSv2, ainsi que les réanalyses MERRA-2, JRA-55 et ERA5, ont été évaluées pour leur distribution spatiale, leur cycle saisonnier et leurs valeurs moyennes annuelles. Les estimations plus élevées (et positives) de  $Q_{net}$  (ERA5, ECMWF, CFSv2) sont dues à un gain plus important de SW (rayonnement à ondes courtes) et à une perte plus faible de LH (chaleur latente) (en particulier CFSv2), tandis que les estimations négatives de  $Q_{net}$  (flux de chaleur net) dans (MERRA-2 et JRA-55) sont dues à un gain plus faible de SW et à une perte plus importante de LH. Les différences de SW et LH sont les deux principales causes de la différence de  $Q_{net}$ , suivies par la différence de LW (rayonnement de grande longueur d'onde).

Nous avons ensuite utilisé le modèle tridimensionnel de circulation océanique SYMPHONIE pour effectuer six simulations sur la période 2017-2018 en utilisant deux méthodes, "bulk" et "flux", afin d'étudier la sensibilité de la température de surface de la mer (SST) du modèle à différents forçages de flux de chaleur. La SST simulée par SYMPHONIE via la méthode bulk (CTL) était la plus proche des observations, avec un biais moyen annuel

de  $-0,28$  °C pour 2018. Pour les simulations utilisant des flux prescrits (et ne les calculant pas à partir de formules bulk), le plus petit biais de SST a été obtenu à partir de la simulation utilisant les flux CTL ( $0,39$  °C pour 2018), suivi par le biais des simulations basées sur les flux ECMWF et MERRA-2 (respectivement  $1,05$  °C et  $-1,13$  °C). La simulation produite à partir de CFSv2 a produit une surestimation significative de la SST sur l'ensemble de la région ( $4,46$  °C), tandis que celle produite à partir de JRA-55 a sous-estimé la SST ( $-2,59$  °C). Le coefficient de corrélation temporelle de la SST journalière entre CTL et OSTIA sur 2017-2018 est le plus élevé ( $>0,95$  dans la plupart des régions), tandis que des coefficients de corrélation faibles et non significatifs dans la région équatoriale ont été observés dans les simulations basées sur MERRA-2, CFSv2 et JRA-55. Les flux calculés à partir des simulations CTL ont montré une différence d'environ  $-6$  W.m<sup>-2</sup> par rapport à ERA5 sur 2017-2018. La relation entre le biais de SST et le flux de chaleur net moyen prescrit au modèle sur 2017-2018 s'est avérée fortement linéaire et significative. Nous avons étendu notre analyse en effectuant une simulation de 10 ans en utilisant des formules globales, obtenant toujours une différence de  $\sim -6$  W.m<sup>-2</sup> entre les flux calculés à partir de cette simulation et l'ECMWF et l'ERA5. La principale cause de cette différence systématique de flux de chaleur nette est la différence entre LH et SH (chaleur sensible), qui peut être due à des erreurs internes du modèle et à des paramétrisations différentes dans les formules de flux bulk. Ces estimations de flux de chaleur ont été comparées à une variété d'autres produits, qui ont montré une grande incertitude dans l'estimation de l'échange air-mer dans la région SEA. ERA5 et ECMWF, bien que surestimant probablement le flux de chaleur net de quelques W.m<sup>-2</sup>, semblent être les meilleurs produits en termes de valeurs de flux de chaleur air-mer.

### *1.2.2 Représentation et projection climatique des flux de chaleur air-mer de l'ESE dans les modèles CMIP6*

Nous avons enfin utilisé un ensemble de données de 30 modèles climatiques de la phase 6 du projet de comparaison des modèles couplés (CMIP6) disponibles au moment de l'extraction des données. Nous avons tout d'abord évalué la représentation des flux de chaleur air-mer sur la région SEA dans cet ensemble de données via une analyse comparative avec ERA5 sur la période historique. Dans l'ensemble, les modèles CMIP6 reproduisent bien la distribution spatiale et le cycle saisonnier des flux de chaleur air-mer, comme le montre un coefficient de corrélation spatiale élevé de  $0,87$  pour la moyenne annuelle de  $Q_{net}$  dans la moyenne d'ensemble multi-modèle (MME) CMIP6. Cependant, les modèles présentent des biais

importants en termes de magnitude, la MME sous-estimant le Qnet de deux tiers par rapport à ERA5 dans la moyenne annuelle ( $6,8 \text{ W.m}^{-2}$  en moyenne sur 1995-2014 vs.  $21,3 \text{ W.m}^{-2}$ ). La moyenne zonale et le cycle saisonnier indiquent que les principaux facteurs de biais dans les valeurs saisonnières de Qnet sont les biais saisonniers dans la perte de LH et le gain de SW. Ceci est cohérent avec les résultats de Jo et al. (2004) qui ont mis en évidence que les biais de LH contribuent à 75% des biais dans les estimations de Qnet au-dessus de l'océan tropical. Les biais dans les modèles CMIP6 mais aussi dans les modèles climatiques régionaux peuvent être liés à des erreurs intrinsèques et à des incertitudes dans la physique et les paramétrisations des processus impliqués dans les flux de chaleur air-mer (nuages, convection, ...). Il est essentiel d'évaluer la capacité de ces modèles à simuler les flux de chaleur en surface et d'identifier les sources de leurs biais.

Tous les modèles CMIP6 examinés ici prévoient une augmentation de Qnet tout au long du 21ème siècle pour la région SEA dans tous les scénarios. Les changements projetés de Qnet, LH, LW et SH sont les plus élevés dans le scénario SSP5-8.5 (3,7, -8,4, 9,2 et 1,9  $\text{W.m}^{-2}$ , respectivement), suivis par le scénario SSP2-4.5 (1,3, -5,4, 4,4 et 0,9  $\text{W.m}^{-2}$ ) et les plus faibles dans le scénario SSP1-2.6 (0,8, -4,1, 1,8 et 0,3  $\text{W.m}^{-2}$ ). Le SW présente la tendance inverse, avec le changement le plus important dans le cadre du scénario SSP1-2.6 (2,9  $\text{W.m}^{-2}$ ) et le plus faible dans le cadre du scénario SSP5-8.5 (1,0  $\text{W.m}^{-2}$ ). Pour évaluer la sensibilité du flux de chaleur aux changements de SST dans les modèles, nous avons sélectionné deux groupes de modèles distincts: un groupe de modèles à faible réchauffement de surface de l'océan (L) et un groupe de modèles à réchauffement élevé (H). Pour tous les scénarios, les modèles à fort réchauffement prévoient systématiquement des changements de flux de chaleur plus prononcés que les modèles à faible réchauffement, sauf pour le SW, où la tendance est inversée.

Notre analyse a montré une claire relation entre les flux de chaleur et la SST, avec une bifurcation claire de cette relation autour d'un seuil de 27-28,7 °C. Ce mécanisme peut être élucidé à travers le rôle de la convection et son impact sur les vents, les nuages et les flux LH et SW. Alors que la relation entre les flux de chaleur et la SST présente une forme similaire à celle de la période historique, le seuil de température augmente à l'avenir, avec une ampleur qui dépend de l'ampleur prévue de réchauffement : les modèles et les scénarios produisant un réchauffement de surface plus important (groupe H et SSP5-8.5) présentent également un seuil de TSM plus chaud (31-32 °C contre 28-29 °C pour le groupe L et le scénario SSP1-2.6).

### II. Perspectives

Lors de l'étude de l'impact d'ENSO/ENSO Modoki sur les précipitations en SEA décrite au chapitre 2, le rôle du transfert de chaleur air-mer n'a pas été exploré. Etant donné la corrélation établie entre les flux de chaleur latente et sensible et les précipitations (Gao et al., 2015, Juneng et al., 2016), nous soulignons le besoin crucial d'examiner l'impact des phénomènes ENSO et ENSO Modoki sur le transport et le bilan de chaleur océanique dans l'ensemble de la région SEA. Pour cela, le potentiel des modèles régionaux à reproduire les deux types d'ENSO et leurs effets associés devrait être soumis à un examen minutieux. En outre, une perspective pour l'étude d'ENSO et de ses variantes consisterait à exploiter les données CMIP6: grâce à la disponibilité à long terme de cet ensemble de données, nous pourrions analyser les changements dans l'intensité des événements ENSO et les variations prévues de leur intensité. En outre, l'examen de l'interaction d'ENSO avec d'autres facteurs climatiques permettrait de mieux comprendre son influence sur les différents modèles climatiques mondiaux.

Les résultats des chapitres 3 et 4 ont permis d'améliorer notre compréhension de la dynamique des flux de chaleur dans la région SEA grâce à l'utilisation d'ensembles de données récents, y compris les résultats de CMIP6. Nos résultats ont mis en évidence l'importance de prendre en compte les biais des modèles dans les simulations de flux de chaleur lors de l'évaluation des projections climatiques futures. En raison de l'absence d'un ensemble de données complet pour l'estimation des flux air-mer dans la région, nous nous sommes appuyés sur la dernière réanalyse (ERA5), sur la base de simulations qui n'ont pas dépassé 10 ans. D'autres analyses sur des périodes plus longues devraient être envisagées à l'avenir afin d'accroître la robustesse de notre analyse et de détecter les tendances et les changements dans les conditions océaniques et atmosphériques. Certains processus, tels que l'oscillation multidécennale de l'Atlantique (AMO) ou l'oscillation décennale du Pacifique (PDO), opèrent en effet sur des échelles de temps décennales. Ces variations annuelles, décennales et à long terme affectent la capacité de l'océan à absorber et à libérer de la chaleur.

L'application à la SEA de la même analyse que celle effectuée par Trinh et al. (2023) sur la mer de Chine méridionale en utilisant un modèle de bilan entièrement fermé sur la région contribuerait à une meilleure compréhension des flux de chaleur. Cela permettrait en particulier d'examiner de manière cohérente les flux atmosphériques de surface, les flux fluviaux et les flux latéraux à travers les détroits interocéaniques, ainsi que les variations internes, et donc de mieux comprendre le transfert des masses d'eau à travers la région SEA (SCSTF et ITF) et leur

## **Conclusion générale**

rôle dans la circulation thermohaline de l'océan et le climat. Enfin, l'utilisation d'un modèle régional couplé océan-atmosphère tel que développé actuellement à partir de SYMPHONIE et RegCM permettra également d'améliorer notre compréhension des interactions air-mer dans la région. Ces résultats sont essentiels pour améliorer les prévisions d'événements extrêmes ainsi que les prévisions de phénomènes climatiques tels que El Niño et La Niña et leurs variantes, et bien sur pour les projections climatiques.

# Reference

- Abid MA et al (2020) Tropical Indian Ocean mediates ENSO influence over Central Southwest Asia during the wet season. *Geophys Res Lett* 47: e2020GL089308. <https://doi.org/10.1029/2020GL089308>.
- Acosta, L. A., Eugenio, E. A., Macandog, P. B. M., Magcale-Macandog, D. B., Lin, E. K. H., Abucay, E. R., et al. (2016). Loss and damage from typhoon-induced floods and landslides in the Philippines: Community perceptions on climate impacts and adaptation options. *International Journal of Global Warming*, 9(1), 33– 65. <https://doi.org/10.1504/ijgw.2016.074307>
- Aldrian, E. and Dwi Susanto, R., 2003. Identification of three dominant rainfall regions within Indonesia and their relationship to sea surface temperature. *Int. J. Climatol.*, 23(12), pp.1435-1452.
- Alsepan G, Minobe S (2020) Relations between interannual variability of regional-scale Indonesian precipitation and large-scale climate modes during 1960–2007. *J Clim* 33:5271–5291. <https://doi.org/10.1175/jcli-d-19-0811.1>
- An S-I, Wang B (2001) Mechanisms of locking the El Nino and La Nina mature phases to boreal winter. *J Clim* 14:2164–2176
- APEC Climate Center. (2017). Disaster management research roadmap for the ASEAN region: ASEAN science-based disaster management platform (ASDMP) project. In (pp. 18– 19). Busan, Republic of Korea: The Republic of Korea government.
- Arakawa U and Lamb VR. 1977. Computational design of the basic dynamical processes of the UCLA general circulation model. in: *General Circulation Models of the Atmosphere, Methods in Computational Physics*. edited by: Chang J. 17. Berlin. 173–265.
- Arakawa, A., and M. J. Suarez, Vertical differencing of the primitive equations in sigma coordinates, *Monthly Weather Review*, 111, 34–45, 1983.
- Ashok, K., Behera, S.K., Rao, S.A., Weng, H., Yamagata, T., 2007: El Niño Modoki and its possible teleconnection. *J. Geophys. Res.* **112**, C11007. Available from: <https://doi.org/10.1029/2006JC003798>.

## References

- Ashok, K., Yamagata, T. The El Niño with a difference. *Nature* 461, 481–484 (2009).  
<https://doi.org/10.1038/461481a>
- Auclair, F., Estournel, C., Floor, J.W., Herrmann, M., Nguyen, C., Marsaleix, P., 2011. A nonhydrostatic algorithm for free-surface ocean modeling. *Ocean Model* 36:49-70.  
<http://dx.doi.org/10.1016/j.ocemod.2010.09.006>.
- Bani, P., Oppenheimer, C., Tsanev, V. et al. Modest volcanic SO<sub>2</sub> emissions from the Indonesian archipelago. *Nat Commun* 13, 3366 (2022). <https://doi.org/10.1038/s41467-022-31043-7>
- Barnier, B., Siefridt, L., Marchesiello, P., 1995. Surface thermal boundary condition for a global ocean circulation model from a three-year climatology of ECMWF analyses. *J. Mar. Syst.* 6, 363–380.
- Barr, B. W., S. S. Chen, and C. W. Fairall, 2023: Sea-State-Dependent Sea Spray and Air–Sea Heat Fluxes in Tropical Cyclones: A New Parameterization for Fully Coupled Atmosphere–Wave–Ocean Models. *J. Atmos. Sci.*, 80, 933–960,  
<https://doi.org/10.1175/JAS-D-22-0126.1>.
- Barsugli, J. J., and D. S. Battisti, 1998: The basic effects of atmosphere–ocean thermal coupling on midlatitude variability. *J. Atmos. Sci.*, **55**, 477–493, [http://doi.org/10.1175/1520-0469\(1998\)055%3C0477:TBEOAO%3E2.0.CO;2](http://doi.org/10.1175/1520-0469(1998)055%3C0477:TBEOAO%3E2.0.CO;2)
- Behera SK, Doi T, Luo JJ., 2021. Air–sea interaction in tropical Pacific: the dynamics of El Niño/Southern Oscillation. In *Tropical and Extratropical Air-Sea Interactions*. In *Tropical and Extratropical Air-Sea Interactions*. Elsevier, 61-92.
- Bell, G.D., Chelliah, M., 2006. Leading tropical modes associated with interannual and multi-decadal fluctuations in North Atlantic hurricane activity. *J. Clim.* 19, 590-612.
- Berry, D. I., and E. C. Kent, 2009: A New Air–Sea Interaction Gridded Dataset from ICOADS With Uncertainty Estimates. *Bull. Amer. Meteor. Soc.*, **90**, 645–656,  
<https://doi.org/10.1175/2008BAMS2639.1>.
- Berry, E., and Mace, G. G. 2014: Cloud properties and radiative effects of the Asian summer monsoon derived from A-Train data, *J. Geophys. Res. Atmos.*, **119**, 9492–9508,  
<https://doi.org/10.1002/2014JD021458>.

## References

- Bjerknes J (1969) Atmospheric teleconnections from the equatorial Pacific. *Mon Weather Rev* 97(3):163–172. [https://doi.org/10.1175/1520-0493\(1969\)097%3c0163:ATFTEP%3e2.3.CO;2](https://doi.org/10.1175/1520-0493(1969)097%3c0163:ATFTEP%3e2.3.CO;2)
- Bo L, Ren HL (2019) ENSO Features, Dynamics, and Teleconnections to East Asian Climate as Simulated in CAMS-CSM. *J Meteorol Res* 33:46-65. <https://doi.org/10.1007/s13351-019-8101-6>
- Bonino, G., Iovino, D., Brodeau, L., & Masina, S. 2022: The bulk parameterizations of turbulent air-sea fluxes in NEMO4: The origin of sea surface temperature differences in a global model study. *Geoscientific Model Development Discussion*. <https://doi.org/10.5194/gmd-2021-436>
- Bosilovich, M. (2008), NASA's modern era retrospective-analysis for research and applications: Integrating earth observations, *Earthzine*, 26 Sept.
- Boyd, J. P. (2018). *Dynamics of the equatorial ocean*. Berlin: Springer.
- Bressan, A, and Constantin, A. (2019). The deflection angle of surface ocean currents from the wind direction. *Journal of Geophysical Research: Oceans*, 124, 7412– 7420. <https://doi.org/10.1029/2019JC015454>
- Brunke, M. A., Zeng, X., and Anderson, S. (2002). Uncertainties in sea surface turbulent flux algorithms and data sets. *J. Geophys. Res.* 107, 3141. [doi: 10.1029/2001JC000992](https://doi.org/10.1029/2001JC000992)
- Brunke, M. A., C. W. Fairall, X. Zeng, L. Eymard, and J. A. Curry, 2003: Which bulk aerodynamic algorithms are least problematic in computing ocean surface turbulent fluxes? *J. Climate*, **16**, 619–635. [http://doi.org/10.1175/1520-0442\(2003\)016%3C0619:WBAAAL%3E2.0.CO;2](https://doi.org/10.1175/1520-0442(2003)016%3C0619:WBAAAL%3E2.0.CO;2)
- Bryden, H. L., and S. Imawaki (2001), Ocean transport of heat, in *Ocean Circulation and Climate*, edited by G. Siedler, J. Church, and J. Gould, pp. 455–475, Academic, San Diego, Calif.
- Cai, W., Cowan, T., 2009. La Niña Modoki impacts Australia autumn rainfall variability. *Geophys. Res. Lett.* 36, L12805. Available from: <https://doi.org/10.1029/2009GL037885>.
- Cai, W., McPhaden, M.J., Grimm, A.M., et al., 2020. Climate impacts of the El Niño Southern Oscillation on South America. *Nat. Rev. Earth Environ.* 1, 215231. Available from: <https://doi.org/10.1038/s43017-020-0040-3>.

## References

- Cao, N., B. Ren, and J. Zheng, 2015: Evaluation of CMIP5 climate models in simulating 1979–2015 oceanic latent heat flux over the Pacific. *Adv. Atmos. Sci.* **32**, 1603–1616, <https://doi.org/10.1007/s00376-015-5016-8>.
- Camargo, S.J., Sobel, A.H., 2005. Western North Pacific tropical cyclone intensity and ENSO. *J. Clim.* 18 (15), 2996-3006.
- Capotondi A et al (2015) Understanding ENSO Diversity. *Bull Ame Meteorol Soc* 96(6): 921-938. <https://doi.org/10.1175/BAMS-D-13-00117.1>
- Carton, J. A. and Zhou, Z.: Annual cycle of sea surface temperature in the tropical Atlantic Ocean, *J. Geophys. Res.-Oceans*, 102, 27813–27824, <https://doi.org/10.1029/97JC02197>, 1997.
- Cayan, D. R., 1992: Latent and Sensible Heat Flux Anomalies over the Northern Oceans: Driving the Sea Surface Temperature. *J. Phys. Oceanogr.*, **22**, 859–881, [https://doi.org/10.1175/1520-0485\(1992\)022<0859:LASHA>2.0.CO;2](https://doi.org/10.1175/1520-0485(1992)022<0859:LASHA>2.0.CO;2).
- Ceppi, P. Brient F., Zelinka, M.D., and Hartmann, D.L. 2017: Cloud feedback mechanisms and their representation in global climate models, *WIREs Clim Change*, e465. [doi: 10.1002/wcc.465](https://doi.org/10.1002/wcc.465).
- Chao, S. Y., Shaw, P. T., and Wu, S. Y. 1996: El Niño modulation of the South China Sea circulation, *Prog. Oceanogr.*, 38, 51–93, [https://doi.org/10.1016/S0079-6611\(96\)00010-9](https://doi.org/10.1016/S0079-6611(96)00010-9).
- Chan, J.C.L., 2000. Tropical cyclone activity over the Western North Pacific associated with El Niño and La Niña Events. *J. Clim.* 13, 2960-2972. [doi:https://doi.org/10.1175/1520-0442\(2000\)013%3C2960:TCAOTW%3E2.0.CO;2](https://doi.org/10.1175/1520-0442(2000)013%3C2960:TCAOTW%3E2.0.CO;2)
- Chang CP, Zhang Y, Li T. 2000: Interannual and interdecadal variations of the East Asian Summer Monsoon and tropical Pacific SSTs. Part I: roles of the subtropical ridge, *J. Clim.* **13**: 4310-4325.
- Chang CP, Harr PA, McBride J, Hsu HH. 2004. The Maritime Continent monsoon. Chapter 3, in East Asian monsoon, Chang CP (ed).World Scientific Publishing, Hackensack, New Jersey, USA 107–150.
- Chang, CP, Wang, Zhuo; McBride, John; Liu, Ching-Hwang 2005. Annual Cycle of Southeast Asia—Maritime Continent Rainfall and the Asymmetric Monsoon Transition. *Journal of Climate*, 18(2), 287–301. [doi:10.1175/jcli-3257.1](https://doi.org/10.1175/jcli-3257.1)

## References

- Chang, C.P., Wang, Z., Hendon, H. (2006). The Asian winter monsoon. In: The Asian Monsoon. Springer Praxis Books. Springer, Berlin, Heidelberg. [https://doi.org/10.1007/3-540-37722-0\\_3](https://doi.org/10.1007/3-540-37722-0_3)
- Chelton DB, 1982. Large-scale response of the California Current to forcing by the wind stress curl. CalCOFI Rep, 23, 30-148.
- Chen, A., Giese, M., & Chen, D. (2020). Flood impact on Mainland Southeast Asia between 1985 and 2018—the role of tropical cyclones. 13(2), e12598. <https://doi.org/10.1111/jfr3.12598>
- Chen, C., Z. Lai, R. C. Beardsley, Q. Xu, H. Lin, and N. T. Viet (2012), Current separation and upwelling over the southeast shelf of Vietnam in the South China Sea, J. Geophys. Res. 117 (3), C03033, [doi:10.1029/2011JC007150](https://doi.org/10.1029/2011JC007150)
- Chen, G., Tam, C.Y., 2010. Different impact of two kinds of Pacific Ocean warming on tropical cyclone frequency over western North Pacific. Geophys. Res. Lett. 37, L01803. Available from: <https://doi.org/10.1029/2009GL041708>
- Chen H, Jin F (2020) Fundamental Behavior of ENSO Phase Locking. J Clim 33(5):1953–1968
- Chen, T., W. B. Rossow, and Y. Zhang 2000: Radiative effects of cloud type variations, *J. Clim.*, **13**, 264–286.
- Chen, TC., Tsay, J.-D., Yen, M.-C. and Matsumoto, J. (2013) The winter rainfall of Malaysia. *Journal of Climate*, 26(3), 936–958. <https://doi.org/10.1175/JCLI-D-12-00174.1>.
- Chenoli, S. N., Diong, J. Y., Mohd Nor, M. F. F., Yip, W. S., Xavier, P., Chang, N. K., & Abu Samah, A. (2022). Objective determination of the winter monsoon onset dates and its interannual variability in Malaysia. *International Journal of Climatology*, 42(16), 10238–10252. <https://doi-org.proxyiub.uits.iu.edu/10.1002/joc.7895>
- Chiang, J.C.H., Bitz, C.M., 2005. Influence of high latitude ice cover on the marine Intertropical Convergence Zone. *Climate Dynamics* 25, 477–496. <https://doi.org/10.1007/s00382-005-0040-5>
- Chokngamwong R, Chiu LS (2008) Thailand daily rainfall and comparison with TRMM products. *J Hydrometeorol* 9:256–266

## References

- Chronis, T., V. Papadopoulos, and E. I. Nikolopoulos, 2011: QuickSCAT observations of extreme wind events over the Mediterranean and Black Seas during 2000–2008. *Int. J. Climatol.*, **31**, 2068–2077, [doi:10.1002/joc.2213](https://doi.org/10.1002/joc.2213)
- Chuan, Goh Kim 2005, The Climate of Southeast Asia, The Physical Geography of Southeast Asia (Oxford, 2005; online edn, Oxford Academic, 12 Nov. 2020), <https://doi.org/10.1093/oso/9780199248025.003.0015>
- Cleveland, W. S., Devlin, S. J., and Grosse, E., 1988: Regression by local fitting. *J. Econometrics*, **37**(1), 87–114. [https://doi.org/10.1016/0304-4076\(88\)90077-2](https://doi.org/10.1016/0304-4076(88)90077-2)
- Cronin, M. F., Gentemann, C. L., Edson, J., Ueki, I., Bourassa, M., Brown, S., Zhang, D. (2019). Air-Sea Fluxes with a Focus on Heat and Momentum. *Frontiers in Marine Science*, **6**. [doi:10.3389/fmars.2019.00430](https://doi.org/10.3389/fmars.2019.00430)
- Cruz, F. T., Narisma, G. T., Dado, J. B., Singhruck, P., Tangang, F., Linarka, U. A., Aldrian, E. (2017). Sensitivity of temperature to physical parameterization schemes of RegCM4 over the CORDEX-Southeast Asia region. *International Journal of Climatology*, **37**(15), 5139–5153. [doi:10.1002/joc.5151](https://doi.org/10.1002/joc.5151)
- D'Arrigo R, Smerdon JE (2008) Tropical climate influences on drought variability over Java, Indonesia. *Geophys Res Lett* **35**: L05707. <https://doi.org/10.1029/2007GL032589>
- Da, N. D., Herrmann, M., Morrow, R., Niño, F., Huan, N. M., and Trinh, N. Q. 2019: Contributions of Wind, Ocean Intrinsic Variability, and ENSO to the Interannual Variability of the South Vietnam Upwelling: A Modeling Study, *J. Geophys. Res.-Ocean.*, **124**, 6545–6574, <https://doi.org/10.1029/2018JC014647>
- De Blij HJ, Muller PO, Williams RS, 2004. *Physical geography: the global environment*. Oxford University Press.
- Dee, D.P., et al, 2011. The ERAinterim reanalysis: configuration and performance of the data assimilation system. *Q. J. R. Meteorolog. Soc.* **137** (656), 553–597.
- Deser C, Guo R, Lehner F (2017) The relative contributions of tropical Pacific Sea surface temperatures and atmospheric internal variability to the recent global warming hiatus. *Geophys Res Lett* **44**:7945–7954. <https://doi.org/10.1002/2017gl074273>
- Dilley, Maxx, and Barry N. Heyman. 1995. “ENSO and Disaster: Droughts, Floods and El Niño/Southern Oscillation Warm Events.” *Disasters* **19**(3):181–93.

## References

- Du, Y., Qu, T., 2010. Three inflow pathways of the Indonesian throughflow as seen from the Simple Ocean Data Assimilation. *Dyn. Atmos. Oceans*, 50, 233-256.
- Dukhovskoy, D.S., Morey, S.L., Martin, P.J., O'Brien, J.J., Cooper, C., 2009. Application of a vanishing, quasi-sigma, vertical coordinate for simulation of high-speed, deep currents over the Sigsbee Escarpment in the Gulf of Mexico. *Ocean Modelling* 28, 250–265.
- Duvel, J. P., R. Roca, and J. Vialard, 2004: Ocean Mixed Layer Temperature Variations Induced by Intraseasonal Convective Perturbations over the Indian Ocean. *J. Atmos. Sci.*, 61, 1004–1023, [https://doi.org/10.1175/1520-0469\(2004\)061<1004:OMLTVI>2.0.CO;2](https://doi.org/10.1175/1520-0469(2004)061<1004:OMLTVI>2.0.CO;2).
- England, M. H., and F. Huang, 2005: On the interannual variability of the Indonesian Throughflow and its linkage with ENSO. *J. Climate*, 18, 1435–1444, <https://doi.org/10.1175/JCLI3322.1>.
- Efron B and Tibshirani R J (1993) *An Introduction to the Bootstrap*. New York: Chapman & Hall, 436pp.
- Estournel, C., et al. (2016), High resolution modeling of dense water formation in the north-western Mediterranean during winter 2012–2013: Processes and budget, *J. Geophys. Res. Oceans*, 121, 5367–5392, [doi:10.1002/2016JC011935](https://doi.org/10.1002/2016JC011935).
- Eyring, V., Bony, S., Meehl, G. A., Senior, C. A., Stevens, B., Stouffer, R. J., & Taylor, K. E., 2016: Overview of the coupled model intercomparison project phase 6 (CMIP6) experimental design and organization. *Geoscientific Model Development*, 9, 1937–1958. <https://doi.org/10.5194/gmd-9-1937-2016>.
- Fang, G., Wei, Z., Choi, B.-H., Wang, K., Fang, Y., Wei, L., 2002. Interbasin volume, heat and salt transport through the boundaries of the East and South China Seas from a variable-grid global ocean circulation model. *Sci. China (Ser. D)* 32 (12), 969–977(in Chinese)
- Fang, G., Wang, Y., Wei, Z., Fang, Y., Qiao, F., Hu, X., 2009. Interocean circulation and heat and freshwater budgets of the South China Sea based on a numerical model, *Dyn. Atmos. Oceans*, 47, 55-72.
- Farmer, B. (2012). *Evaluation of bulk heat fluxes from atmospheric datasets* (dissertation). Tallahassee, FL: Florida State University Libraries.
- Fasullo J, Webster PJ (2003) A hydrological definition of Indian Monsoon onset and withdrawal. *J Clim* 16:3200–3211. <https://doi.org/10.1175/1520-0442>

## References

- Fang, Y., and coauthors, 2010. A regional air-sea coupled model and its application over East Asia in the summer of 2000. *Adv. Atmos. Sci.* 27, 583–593. <https://doi.org/10.1007/s00376-009-8203-7>
- Feng J et al (2010) Different impacts of two types of Pacific Ocean warming on Southeast Asian rainfall during boreal winter. *J Geophys Res* 115:D24122. <https://doi.org/10.1029/2010JD014761>
- Feng, J., Chen, W., Tam, C.Y., Zhou, W., 2011. Different impacts of El Niño and El Niño Modoki on China rainfall in the decaying phases. *Int. J. Climatol.* 31 (14), 2091-2101.
- Feng S, Hu Q (2004) Variations in the teleconnection of ENSO and summer rainfall in northern China: A role of the Indian summer monsoon. *J Clim* 17:4871–4881. <https://doi.org/10.1175/JCLI-3245.1>
- Fioux, M. (2017). *The planetary ocean* (1st ed.). EDP Sciences. Retrieved from <https://www.perlego.com/book/3058250/the-planetary-ocean-pdf> (Original work published 2017)
- Francisco RV et al (2006) Regional model simulation of summer rainfall over the Philippines: effect of choice of driving fields and ocean flux schemes. *Theor Appl Climatol* 86:215–227
- Gao, S., L. S. Chiu, and C. L. Shie, 2013: Trends and variations of ocean surface latent heat flux: Results from GSSTF2c data set. *Geophys. Res. Lett.*, **40**, 380–385, <https://doi.org/10.1029/2012GL054620>.
- Gao Y et al (2015) Assessing and improving noah-MP land model simulations for the central Tibetan plateau. *J Geophys Res Atmos* 120:9258-9278, <https://doi.org/10.1002/2015JD023404>
- Gan, J., Li, H., Curchitser, E.N., Haidvogel, D.B., 2006. Modeling South China Sea circulation: response to seasonal forcing regimes. *J. Geophys. Res.* 111, C06034, [doi:10.1029/2005JC003298](https://doi.org/10.1029/2005JC003298).
- Ganopolski, A. (2008). *Encyclopedia of Ecology Ocean Currents and Their Role in the Biosphere.* , (), 2553–2559. [doi:10.1016/b978-008045405-4.00751-5](https://doi.org/10.1016/b978-008045405-4.00751-5)
- Gelaro, R., and Coauthors, 2017: The Modern-Era Retrospective Analysis for Research and Applications, version 2 (MERRA-2). *J. Climate*, **30**, 5419–5454, <https://doi.org/10.1175/JCLI-D-16-0758.1>.

## References

- Goh, A. Z.-C., & Chan, J. C. L. (2010). Interannual and interdecadal variations of tropical cyclone activity in the South China Sea. *International Journal of Climatology*, 30(6), 827–843. <https://doi.org/10.1002/joc.1943>
- Gordon, A. L., & Fine, R. A. (1996). Pathways of water between the Pacific and Indian oceans in the Indonesian seas. *Nature*, 379(6561), 146–149. [doi:10.1038/379146a0](https://doi.org/10.1038/379146a0)
- Gordon, Arnold. (2005). Oceanography of the Indonesian Seas and Their Throughflow. *Oceanography*. 18. 14-27. [10.5670/oceanog.2005.01](https://doi.org/10.5670/oceanog.2005.01).
- Gordon, A. L., J. Sprintall, H. van Aken, R. D. Susanto, S. Wijffels, R. Molcard, A. Field, and W. Pranowo (2010), The Indonesian Throughflow during 2004–2006 as observed by the INSTANT program, *Dyn. Atmos. Oceans*, 50, 115–128, [doi:10.1016/j.dynatmoce.2010.04.003](https://doi.org/10.1016/j.dynatmoce.2010.04.003).
- Gordon AL, Huber BA, Metzger EJ, Susanto RD, Hurlburt HE, Adi TR. 2012. South China Sea throughflow impact on the Indonesian throughflow. *Geophys Res Lett*. 39(11).[doi:10.1029/2012GL052021](https://doi.org/10.1029/2012GL052021).
- Graham, N. E., and T. P. Barnett, 1987: Observations of sea surface temperature and convection over tropical oceans. *Science*, **238**, 657–659.
- Gutjahr, Oliver & Jungclaus, J. & Brüggemann, N. & Haak, Helmuth & Marotzke, J.. (2022). Air-Sea Interactions and Water Mass Transformation During a Katabatic Storm in the Irminger Sea. *Journal of Geophysical Research: Oceans*. 127. e2021JC018075. [10.1029/2021JC018075](https://doi.org/10.1029/2021JC018075).
- Hamed MM, Nashwan MS, Shahid S, bin Ismail T, Wang XJ, Dewan A, Asaduzzaman M (2022) Inconsistency in historical simulations and future projections of temperature and rainfall: A comparison of CMIP5 and CMIP6 models over Southeast Asia. *Atmospheric Research*, 265, p.105927. <https://doi.org/10.1016/j.atmosres.2021.105927>
- Halpert, M S and Ropelewski, C F 1992: Surface Temperature Patterns Associated with the Southern Oscillation, *J. Clim.*, 5, 577–593.
- Harger JRE (1995) Air-temperature variations and ENSO effects in Indonesia, the Philippines, and El Salvador: ENSO patterns and changes from 1866–1993. *Atmos Environ* 29:1919–1942
- Harlow FH and Welch JE. 1965. Numerical calculation of time-dependent viscous incompressible flow of fluid with free surface. *Phys. Fluids* 8: 2182–2189.

## References

- Harris I, Osborn T J, Jones P, Lister D (2020). Version 4 of the CRU TS monthly high-resolution gridded multivariate climate dataset. *Sci Data*, 7(1), 109–. <https://doi:10.1038/s41597-020-0453-3>
- Hein, H. (2008), Vietnam Upwelling, Hamburg.
- Helmholtz H (1867) On Integrals of the hydrodynamical equations, which express vortex-motion. *The London, Edinburgh, and Dublin Philosophical Magazine and J Science* 33(226): 485–512. <https://doi.org/10.1080/14786446708639824>
- Hendon HH (2003) Indonesia rainfall variability: Impacts of ENSO and local air-sea interaction. *J Clim* 16:1775–1790
- Hendrawan IG, Asai K, Triwahyuni A, Lestari DV (2019) The interannual rainfall variability in Indonesia corresponding to El Niño Southern Oscillation and Indian Ocean Dipole. *Acta Oceanologica Sinica* 38(7):57–66. <https://doi.org/10.1007/s13131-019-1457-1>
- Herrmann, M. J., and S. Somot (2008), Relevance of ERA40 dynamical downscaling for modeling deep convection in the Mediterranean Sea, *Geophys. Res. Lett.*, 35, L04607, [doi:10.1029/2007GL032442](https://doi.org/10.1029/2007GL032442).
- Herrmann, M., S. Somot, F. Sevault, C. Estournel, and M. Déqué (2008), Modeling the deep convection in the northwestern Mediterranean Sea using an eddy-permitting and an eddy resolving model: Case study of winter 1986 – 1987, *J. Geophys. Res.*, 113,C04011, [doi:10.1029/2006JC003991](https://doi.org/10.1029/2006JC003991)
- Herrmann, M., T. Ngo-Duc, L. Trinh-Tuan, 2020: Impact of climate change on sea surface wind in Southeast Asia, from climatological average to extreme events: results from a RegCM4 dynamical downscaling of CNRM-CM5 in the CORDEX-SEA framework. *Climate Dynamics*, 54, 2101–2134. <https://doi.org/10.1007/s00382-019-05103-6>.
- Herrmann, M., T. Nguyen-Duy, T. Ngo-Duc, F. Tangang, 2022: Climate change impact on sea surface winds in Southeast Asia. *International Journal of Climatology*, 42, 3571-3595. <https://doi.org/10.1002/joc.7433>
- Hersbach, H., and Dee, D., 2016: ERA5 reanalysis is in production. *ECMWF Newsl.*, 147, 7. <https://cir.nii.ac.jp/crid/1370009142734268815>
- Hersbach H, Bell B, Berrisford P, et al. (2020) The ERA5 global reanalysis. *Q J R Meteorol Soc.* 146: 1999– 2049. <https://doi.org/10.1002/qj.3803>

## References

- Hijioka Y, and coauthors 2014: impacts, adaptation, and vulnerability. Part B: regional aspects. Contribution of working group II to the fifth assessment report of the intergovernmental panel on climate change. Cambridge University Press, Cambridge, United Kingdom and New York, NY, p 1327–1370.
- Hogg, N. G., and Johns, W. E. (1995), Western boundary currents, *Rev. Geophys.*, 33(S2), 1311–1334, [doi:10.1029/95RG00491](https://doi.org/10.1029/95RG00491).
- Hosking JS et al. (2012). Tropical convective transport and the Walker circulation. *Atmos Chem Phys* 12:9791–9797. <http://doi.org/10.5194/acp-12-9791-2012>
- Hu D, and coauthors, (2015). Pacific western boundary currents and their roles in climate. *Nature*, 522(7556), 299–308. [doi:10.1038/nature14504](https://doi.org/10.1038/nature14504)
- Hu, S, and J. Sprintall, 2016: Interannual variability of the Indonesian Throughflow: The salinity effect. *J. Geophys. Res. Oceans*, 121, 2596–2615, <https://doi.org/10.1002/2015JC011495>.
- Huang, R.X., 2015: Thermohaline Circulation, Editor(s): Gerald R. North, John Pyle, Fuqing Zhang, *Encyclopedia of Atmospheric Sciences (Second Edition)*, Academic Press, 315–328. <https://doi.org/10.1016/B978-0-12-382225-3.00281-4>.
- Huang, J., and coauthors, 2023: Role of air-sea heat flux on the transformation of Atlantic Water encircling the Nordic Seas. *Nat Commun* 14, 141. <https://doi.org/10.1038/s41467-023-35889-3>
- Huber, Markus & Zanna, Laure. (2017). Drivers of uncertainty in simulated ocean circulation and heat uptake: AIR-SEA FLUXES AND OCEAN CIRCULATION. *Geophysical Research Letters*. 44. [10.1002/2016GL071587](https://doi.org/10.1002/2016GL071587).
- Hughes, T.M.C., Weaver, A.J., 1996. Sea surface temperature evaporation feedback on the ocean's thermohaline circulation. *J. Phys. Oceanogr.* 26, 644–654
- Imawaki S, Bower AS, Beal L, Qiu B (2013). [International Geophysics] *Ocean Circulation and Climate - A 21st Century Perspective Volume 103 Western Boundary Currents*. 305–338. [doi:10.1016/B978-0-12-391851-2.00013-1](https://doi.org/10.1016/B978-0-12-391851-2.00013-1)
- IPCC (2013) *Climate change 2013: the physical science basis*. In: Contribution of working group I to the fifth assessment report of the intergovernmental panel on climate change. Cambridge University Press, Cambridge. <https://doi.org/10.1017/CBO9781107415324>

## References

- IPCC, 2021: Climate Change 2021: The Physical Science Basis. Contribution of Working Group I to the Sixth Assessment Report of the Intergovernmental Panel on Climate Change (Masson-Delmotte, V., and Coauthors). Cambridge University Press, Cambridge, United Kingdom and New York, NY, USA. <https://doi.org/10.1017/9781009157896>
- Ishii, M., A. Shouji, S. Sugimoto, and T. Matsumoto, 2005: Objective analyses of sea-surface temperature and marine meteorological variables for the 20th century using ICOADS and the Kobe collection. *Int. J. Climatol.*, 25, 865–879.
- Jacobs, Z. L., Grist, J. P., Marsh, R., Sinha, B., & Josey, S. A. 2020. The major role of air-sea heat fluxes in driving interannual variations of gulf stream transport. *Journal of Geophysical Research: Oceans*, 125. <https://doi.org/10.1029/2019JC016004>
- Jiang, F., & Zhang, W. (2022). Understanding the complicated relationship between ENSO and wintertime North Tropical Atlantic SST variability. *Geophysical Research Letters*, 49, e2022GL097889. <https://doi.org/10.1029/2022GL097889>
- Jin J, et al. 2022. The effects of redistributed heat flux on ocean climate change in FAFMIP heat flux anomaly experiments, *Ocean Modelling*, 176, 102063. <https://doi.org/10.1016/j.ocemod.2022.102063>
- Jo, YH, Yan XH, Pan JY, Liu WT, He MX 2004: Sensible and latent heat flux in the tropical Pacific from satellite multi-sensor data. *Remote Sens Environ.* **90**:166–177
- Johnson, R.H., 1987. Precipitating cloud systems of the Asian monsoon. *Mons. Meteorol.*
- Johnson, R. H., and C. P. Chang, 2007: Winter MONEX: A quarter-century and beyond. *Bull. Amer. Meteor. Soc.*, **88**, 385–388, [doi:10.1175/BAMS-88-3-385](https://doi.org/10.1175/BAMS-88-3-385).
- Johnson, N., Xie, S.P. 2010: Changes in the sea surface temperature threshold for tropical convection. *Nature Geosci* 3, 842–845. <https://doi.org/10.1038/ngeo1008>
- Jordà, G., and coauthors, 2017: The Mediterranean Sea heat and mass budgets: Estimates, uncertainties, and perspectives. *Prog. Oceanogr.*, 156, 174–208.
- Josey, S., and Coauthors, 2019: Extreme Variability in Irminger Sea Winter Heat Loss Revealed by Ocean Observatories Initiative Mooring and the ERA5 R. *Geos Res Lett.* **46**. <https://doi.org/10.1029/2018GL080956>.
- Julian R, Chervin RM (1978) A Study of the Southern Oscillation and Walker Circulation Phenomenon. *Mon Weather Rev* 106(10):1433–1451. [https://doi.org/10.1175/1520-0493\(1978\)106<1433:asotso>2.0.co;2](https://doi.org/10.1175/1520-0493(1978)106<1433:asotso>2.0.co;2)

## References

- Juneng, L. and Tangang, F.T., 2005. Evolution of ENSO-related rainfall anomalies in Southeast Asia region and its relationship with atmosphere–ocean variations in Indo-Pacific sector. *Clim.Dyn.*, 25(4), pp.337-350.
- Juneng, L., Tangang, F.T. and Reason, C.J.C. (2007) Numerical case study of an extreme rainfall event during 9–11 December 2004 over the east coast of Peninsular Malaysia. *Meteorology and Atmospheric Physics*, 98, 81–98. <https://doi.org/10.1007/s00703-006-0236-1>
- Juneng L et al (2016) Sensitivity of the Southeast Asia Rainfall Simulations to Cumulus and Ocean Flux Parameterization in RegCM4. *Clim Res* 69:59-77. <https://doi.org/10.3354/cr01386>
- Kao HY, Yu JY (2009) Contrasting Eastern-Pacific and Central-Pacific Types of ENSO. *J Clim* 22(3):615–632. <https://doi.org/10.1175/2008jcli2309.1>
- Kalnay, E., et al., 1996. The Ncep/Ncar 40-year reanalysis project. *Bull. Am. Meteorol. Soc.* 77 (3), 437–471. [https://doi.org/10.1175/1520-0477\(1996\)077<0437:TNYRP>2.0.CO;2](https://doi.org/10.1175/1520-0477(1996)077<0437:TNYRP>2.0.CO;2).
- Kanamitsu, M., and Coauthors, 2002: NCEP–DOE AMIP-II reanalysis (R-2). *Bull. Am. Meteorol. Soc.* **83**, 1631–1644.
- Kannad, A., Goodkin, N. F., Murty, S. A., Ramos, R. D., Samanta, D., and Gordon, A. L.: Paleoclimate drivers of the Indonesian and South China Sea throughflows, the curious case of the IOD, EGU General Assembly 2020, Online, 4–8 May 2020, EGU2020-6484, <https://doi.org/10.5194/egusphere-egu2020-6484, 2020>
- Kara, A.B., Hurlburt, H.E., Rochford, P.A., 2000. Efficient and accurate bulk parameterizations of air–sea fluxes for use in general circulation models. *J. Atmos. Ocean. Technol.* 17, 1421–1438
- Karori MA, Li J, Jin F (2013) The Asymmetric Influence of the Two Types of El Niño and La Niña on Summer Rainfall over Southeast China. *J Clim* 26(13):4567–4582. <https://doi.org/10.1175/jcli-d-12-00324.1>
- Kashino Y, Ishida, A, and Kuroda Y 2005 Variability of the Mindanao Current: mooring observation results. *Geophys. Res. Lett.* 32, L18611
- Kashino Y, N. Espana, F. Syamsudin, K.J. Richards, T. Jensen, P. Dutrieux, A 2009 Ishida Observations of the North Equatorial Current, Mindanao Current, and the Kuroshio Current system during the 2006/07 El Niño and 2007/08 La Niña *J. Oceanogr.*, 65, pp. 325-333

## References

- Khan, N., Pour, S.H., Shahid, S., Ismail, T., Ahmed, K., Chung, E.S., Nawaz, N., Wang, X., 2019. Spatial distribution of secular trends in rainfall indices of Peninsular Malaysia in the presence of long-term persistence. *Meteorol. Appl.* 26, 655–670. <https://doi.org/10.1002/met.1792>
- Kido, S., Richter, I., Tozuka, T. et al. Understanding the interplay between ENSO and related tropical SST variability using linear inverse models. *Clim Dyn* 61, 1029–1048 (2023). <https://doi.org/10.1007/s00382-022-06484-x>
- Kiehl J. T., Trenberth K. E., 1997: Earth's annual global mean energy budget. *Bull. Am. Meteorol. Soc.*, **78**, 197–208. [https://doi.org/10.1175/1520-0477\(1997\)078<0197:EAGMEB>2.0.CO;2](https://doi.org/10.1175/1520-0477(1997)078<0197:EAGMEB>2.0.CO;2).
- Kim, D.W., Choi, K.S., Byun, H.R., 2012. Effects of El Niño Modoki on winter precipitation in Korea. *Clim. Dyn.* 38, 13131324. Available from: <https://doi.org/10.1007/s00382-011-1114-1>.
- Kiguchi, M. and Matsumoto, J. (2005) The rainfall phenomena during the pre-monsoon period over the Indochina peninsula in the GAME-IOP year, 1998. *Journal of the Meteorological Society of Japan*, 83, 89– 106. <https://doi.org/10.2151/jmsj.83.89>.
- Kiguchi, M., Matsumoto, J., Kanae, S. and Oki, T. (2016) Pre-monsoon rain and its relationship with monsoon onset over the Indochina peninsula. *Frontiers in Earth Science*, 4, 42. <https://doi.org/10.3389/feart.2016.00042>.
- Kim, Y.Y., Qu, T., Jensen, T., Miyama, T., Mitsudera, H., Kang, H.W., Ishida, A., 2004. Seasonal and interannual variations of the North Equatorial Current bifurcation in a high-resolution OGCM. *J. Geophys. Res.* 109, [doi:10.1029/2003JC002013](https://doi.org/10.1029/2003JC002013).
- Kim, H.M., Webster, P.J., Judith, A.C., 2009. Impact of shifting patterns of Pacific Ocean warming on North Atlantic tropical cyclones. *Science* 325, 7780 [DOI:10.1126/science.1174062](https://doi.org/10.1126/science.1174062).
- Kleeman R, McCreary JP, Klinger BA. 1999. A mechanism for generating ENSO decadal variability. *Geophys. Res. Lett.* 26(12): 1743-1746. <https://doi.org/10.1029/1999GL900352>

## References

- Kobayashi, S., et al., 2015. The JRA-55 reanalysis: general specifications and basic characteristics. *J. Meteorol. Soc. Jpn. Ser. II* 93 (1), 5–48. <https://doi.org/10.2151/jmsj.2015-001>
- Konda, M., H. Ichikawa, H. Tomita, and M. F. Cronin, 2010: Surface heat flux variations across the Kuroshio Extension as observed by surface flux buoys. *J. Climate*, 23, 5206–5221
- Kubota, M., Iwabe, N., Cronin, M. F., and Tomita, H. (2008). Surface heat fluxes from the NCEP/NCAR and NCEP/DOE reanalyses at the Kuroshio Extension Observatory buoy site. *J. Geophys. Res. Ocean.* 113, 1–14. [doi: 10.1029/2007JC004338](https://doi.org/10.1029/2007JC004338)
- Kudryavtsev, V., Chapron, B., and Makin, V. (2014), Impact of wind waves on the air-sea fluxes: A coupled model, *J. Geophys. Res. Oceans*, 119, 1217–1236, [doi:10.1002/2013JC009412](https://doi.org/10.1002/2013JC009412).
- Kumar, B. P., M. F. Cronin, S. Joseph, M. Ravichandran, and N. Sureshkumar, 2017: Latent Heat Flux Sensitivity to Sea Surface Temperature: Regional Perspectives. *J. Climate*, 30, 129–143, <https://doi.org/10.1175/JCLI-D-16-0285.1>.
- Kug J S, Jin FF, An SI (2009) Two Types of El Niño Events: Cold Tongue El Niño and Warm Pool El Niño. *J Clim* 22(6):1499–1515. <https://doi.org/10.1175/2008jcli2624.1>
- Landsea, C. W., 2000: El Niño-Southern Oscillation and the seasonal predictability of tropical cyclones. In press in *El Niño: Impacts of Multiscale Variability on Natural Ecosystems and Society*, edited by H. F. Diaz and V. Markgraf.
- Large, W. G., & Yeager, S. (2004). Diurnal to decadal global forcing for ocean and sea-ice models: The data sets and flux climatologies. [doi:10.5065/D6KK98Q6](https://doi.org/10.5065/D6KK98Q6)
- Large, W. G., and S. G. Yeager (2009), The global climatology of an inter annually varying air-sea flux data set, *Clim. Dyn.*, 33, 341–364, [doi:10.1007/s00382-008-0441-3](https://doi.org/10.1007/s00382-008-0441-3).
- Larkin NK, Harrison DE (2005) Global seasonal temperature and precipitation anomalies during El Niño autumn and winter. *Geophys Res Lett* 32: L13705. <https://doi.org/10.1029/2005GL022738>
- Lau, K.M. and Chan, P.H., 1983. Short-term climate variability and atmospheric teleconnections from satellite-observed outgoing longwave radiation. Part I: Simultaneous relationships. *Journal of the atmospheric sciences*, 40(12), pp.2735-2750.
- Lau KM, Yang S. 1997. Climatology and interannual variability of the Southeast Asian summer monsoon. *Advances in Atmospheric Sciences* 14: 141–162

## References

- Lau K, Yang S., 2003: Walker circulation. *Encycloped Atmos Sci.* <https://doi.org/10.1016/B0-12-227090-8/00450-4>
- Lau, N.C. and Wang, B., 2006. Interactions between the Asian monsoon and the El Niño - Southern oscillation. In *The Asian Monsoon* (pp. 479-512). Springer, Berlin, Heidelberg.
- L'Ecuyer, T. S., Beaudoin, H. K., Rodell, M., Olson, W., Lin, B., Kato, S., et al. (2015). The observed state of the energy budget in the early twenty-first century. *J. Clim.* 28, 8319–8346. <https://doi.org/10.1175/JCLI-D-14-00556.1>
- Lee TN, W.E. Johns, C.-T. Liu, D. Zhang, R. Zantopp, Y. Yang, 2001. Mean transport and seasonal cycle of the Kuroshio east of Taiwan with comparison to the Florida Current *J. Geophys. Res.*, 106, pp. 22,143-22,158
- Lestari S et al (2016) ENSO Influences on Rainfall Extremes around Sulawesi and Maluku Islands in the Eastern Indonesian Maritime Continent. *SOLA* 12(0):37–41. <https://doi.org/10.2151/sola.2016-008>
- Li LM et al (2011) The recycling rate of atmospheric moisture over the past two decades (1988-2009). *Environ Res Lett* 6:034018. <https://doi.org/10.1088/1748-9326/6/3/034018>
- Li, Z., Tam, C.-Y., Li, Y., Lau, N.-C., Chen, J., Chan, S. T., et al. (2022). How does air-sea wave interaction affect tropical cyclone intensity? An atmosphere-wave-ocean coupled model study based on super typhoon Mangkhut (2018). *Earth and Space Science*, 9, e2021EA002136. <https://doi.org/10.1029/2021EA002136>
- Lim, T.J. and Samah, A.A. 2004. *Weather and Climate of Malaysia.* Kuala Lumpur: University of Malaya Press.
- Lind, R. and Katsaros, K. 1986 Radiation measurements and model results from R/V Oceanographer during STREX 1980, *J. Geophys. Res.* 91, 13308-13314
- Liu, C., Allan, R. P., Berrisford, P., Mayer, M., Hyder, P., Loeb, N., et al. (2015). Combining satellite observations and reanalysis energy transports to estimate global net surface energy fluxes 1985–2012. *Journal of Geophysical Research: Atmospheres*, 120(18), 9374–9389. <https://doi.org/10.1002/2015jd023264>
- Liu, K. S., & Chan, J. C. L. (2003). Climatological characteristics and seasonal forecasting of tropical cyclones making landfall along the south China coast. *Monthly Weather Review*, 131(8), 1650–1662. <https://doi.org/10.1175//2554.1>

## References

- Liu, W. T. (1988), Moisture and latent heat flux variabilities in the tropical Pacific derived from satellite data, *J. Geophys. Res.*, 93(C6), 6749–6760, doi:[10.1029/JC093iC06p06749](https://doi.org/10.1029/JC093iC06p06749).
- Loo, Yen Yi; Billa, Lawal; Singh, Ajit (2014). Effect of climate change on seasonal monsoon in Asia and its impact on the variability of monsoon rainfall in Southeast Asia. *Geoscience Frontiers*, (), S167498711400036X–. doi:[10.1016/j.gsf.2014.02.009](https://doi.org/10.1016/j.gsf.2014.02.009)
- Longhurst, A., 1993. Seasonal cooling and blooming in tropical oceans. *Deep Sea Research Part I: Oceanographic Research Papers*, 40(11-12), pp.2145-2165. [https://doi.org/10.1016/0967-0637\(93\)90095-K](https://doi.org/10.1016/0967-0637(93)90095-K)
- Lu, Y., Qin, X.S. and Mandapaka, P.V., 2015. A combined weather generator and K-nearest-neighbour approach for assessing climate change impact on regional rainfall extremes. *Int. J. Climatol.*, 35(15), pp.4493-4508.
- Lyard, F. H., Allain, D. J., Cancet, M., Carrère, L., and Picot, N. (2021): FES2014 global ocean tide atlas: design and performance, *Ocean Sci.*, 17, 615–649, doi:[10.5194/os-17-615-2021](https://doi.org/10.5194/os-17-615-2021)
- Ma T et al (2022) Different ENSO Teleconnections over East Asia in Early and Late Winter: Role of Precipitation Anomalies in the Tropical Indian Ocean and Far Western Pacific. *J Clim* 35(24): 4319-4335. <https://doi.org/10.1175/JCLI-D-21-0805.1>
- Ma, Z., J. Fei, X. Huang, and X. Cheng, 2015: Contributions of Surface Sensible Heat Fluxes to Tropical Cyclone. Part I: Evolution of Tropical Cyclone Intensity and Structure. *J. Atmos. Sci.*, 72, 120–140, <https://doi.org/10.1175/JAS-D-14-0199.1>.
- Macdonald AM, Wunsch C, 1996. An estimate of global ocean circulation and heat fluxes. *Nature* 382.6590: 436-439.
- Madden, R. A., and P. R. Julian, 1994: Observations of the 40–50-day tropical oscillation—A review. *Mon. Wea. Rev.*, 122, 814–837. [https://doi.org/10.1175/1520-0493\(1994\)122<0814:OOTDTP>2.0.CO;2](https://doi.org/10.1175/1520-0493(1994)122<0814:OOTDTP>2.0.CO;2).
- Magee, A. D., Verdon-Kidd, D. C., Diamond, H. J. & Kiem, A. S, 2017. Influence of ENSO, ENSO Modoki and the IPO on tropical cyclogenesis: a spatial analysis of the southwest Pacific region. *Int. J. Climatol.* 37, 1118–1137
- Mahrt, L., D. Vickers, P. Frederickson, K. Davidson, and A. Smedman (2003), Sea-surface aerodynamic roughness, *J. Geophys. Res.*, 108(C6), 3171, doi:[10.1029/2002JC001383](https://doi.org/10.1029/2002JC001383).
- Mandapaka, P.V., Qin, X. and Lo, E.Y., 2017. Analysis of spatial patterns of daily precipitation and wet spell extremes in Southeast Asia. *Int. J. Climatol.*, 37, pp.1161-1179.

## References

- Maltrud, M.E., Smith, R.D., Semtner, A.J., Malone, R.C., 1998. Global eddy-resolving ocean simulations driven by 1985–1995 atmospheric winds. *J. Geophys. Res.* 103, 30, 825–30,853.
- Marathe S, Ashok K, Swapna P, Sabin TP (2015) Revisiting El Niño Modokis. *Clim Dyn* 45:3527–3545. <https://doi.org/10.1007/s00382-015-2555-8>
- Marsaleix P., Auclair F., Floor J. W., Herrmann M. J., Estournel C., Pairaud I., Ulses C., 2008. Energy conservation issues in sigma-coordinate free-surface ocean models. *Ocean Modelling.* 20, 61-89. <http://dx.doi.org/10.1016/j.ocemod.2007.07.005>
- Marsaleix P., Auclair F., Estournel C., 2009. Low-order pressure gradient schemes in sigma coordinate models: The seamount test revisited. *Ocean Modelling.* 30, 169-177. <http://dx.doi.org/10.1016/j.ocemod.2009.06.011>
- Marsaleix P., Auclair F., Duhaut T., Estournel C., Nguyen C., Ulses C. (2012) Alternatives to the Robert-Asselin filter. *Oc. Modell.*, 41, 53-66, [doi: 10.1016/j.ocemod.2011.11.002](http://dx.doi.org/10.1016/j.ocemod.2011.11.002).
- Marsaleix, P., Michaud, H., Estournel, C., 2019. 3D phase-resolved wave modeling with a nonhydrostatic ocean circulation model. *Ocean Modelling.* 136, 28-50. <https://doi.org/10.1016/j.ocemod.2019.02.002>
- Matsumoto J. 1997. Seasonal transition of summer rainy season over Indochina and adjacent region. *Advances in Atmospheric Sciences* 14: 231–245.
- Mayer, J., Haimberger, L., and Mayer, M. 2023: Changes in air-sea fluxes over the North Atlantic during 1950-2019 as derived from ERA5 data, EGU General Assembly 2023, Vienna, Austria, 24–28 Apr 2023, EGU23-14080, <https://doi.org/10.5194/egusphere-egu23-14080>, 2023.
- McPhaden, M.J., 2002. El Niño and La Niña: causes and global consequences. *Encyclopedia of global environmental change*, 1, pp.353-370.
- McPhaden MJ, Zebiak SE, Glantz MH (2006) ENSO as an Integrating Concept in Earth Science. *Science* 314(5806):1740–1745. <https://doi.org/10.1126/science.1132588>
- Mei, W., & Xie, S.-P. (2016). Intensification of landfalling typhoons over the northwest Pacific since the late 1970s. *Nature Geoscience*, 9(10), 753–757. <https://doi.org/10.1038/ngeo2792>
- Meehl GA. 1994. Influence of the land surface in the Asian Summer monsoon: external conditions versus internal feedback. *J. Clim.* 7: 1033-1049.

## References

- Meyers, G., 1996: Variation of Indonesian Throughflow and the El Niño–Southern Oscillation. *J. Geophys. Res.*, 101, 12 255–12 263, <https://doi.org/10.1029/95JC03729>.
- Michaud, H., Marsaleix, P., Leredde, Y., Estournel, C., Bourrin, F., Lyard, F., Mayet, C., Arduin, F., 2011. Three-dimensional modeling of wave-induced current from the surf zone to the inner shelf. *Ocean Sci. Discuss.* 8:2417–2478. <http://dx.doi.org/10.5194/osd-8-2417-2011>.
- Millot, C., Taupier-Letage, I. (2005). Circulation in the Mediterranean Sea. In: Saliot, A. (eds) *The Mediterranean Sea. Handbook of Environmental Chemistry*, vol 5K. Springer, Berlin, Heidelberg. <https://doi.org/10.1007/b107143>
- Misra, V. and DiNapoli, S., 2014. The variability of the Southeast Asian summer monsoon. *Int. J. Climatol.*, 34(3), pp.893-901
- Mitsuguchi, Takehiro and Dang XP & Kitagawa, Hiroyuki & Yoneda, Minoru & Shibata, Yasuyuki. (2007). Tropical South China Sea Surface 14C Record in an Annually Banded Coral. *Radiocarbon*. 49. [10.1017/S0033822200042776](https://doi.org/10.1017/S0033822200042776).
- Mizuta R, Arakawa O, Ose T, Kusunoki S, Endo H, Kitoh A. 2014: Classification of CMIP5 Future Climate Responses by the Tropical Sea Surface Temperature Changes. *SOLA* 10(1): 167–171. <https://doi.org/10.2151/sola.2014-035>.
- Molod, A., Takacs, L., Suarez, M., Bacmeister, J., 2015. Development of the geos-5 atmospheric general circulation model: evolution from MERRA to MERRA2. *Geosci. Model Dev.* 8 (5), 1339–1356. <https://doi.org/10.5194/gmd-8-1339-2015>
- Mori, N., Kato, M., Kim, S., Mase, H., Shibutani, Y., Takemi, T., et al. (2014). Local amplification of storm surge by Super Typhoon. Haiyan in Leyte Gulf, 41(14), 5106– 5113.
- Myhre, G.; Shindell, D.; Pongratz, J. Anthropogenic and Natural Radiative Forcing. In *Climate Change 2013: The Physical Science Basis Working Group I Contribution to the Fifth Assessment Report of the Intergovernmental Panel on Climate Change*; Stocker, T., Ed.; Cambridge University Press: Cambridge, UK, 2014; pp. 659–740.
- Norman H. Zide (1968). *Studies in comparative Austroasiatic linguistics. Indo-Iranian Monographs, Vol V.* Mouton & Co., London, The Hague, Paris, 1966. 229 pp., Preis: f 42., 19(1-2), 86–93. [doi:10.1016/0024-3841\(69\)90110-7](https://doi.org/10.1016/0024-3841(69)90110-7)

## References

- Ngai, S.T., and Coauthors, 2022: Projected Mean and Extreme Precipitation Based on Bias-Corrected Simulation Outputs of CORDEX Southeast Asia. *Weather and Climate Extremes*, 100484. <https://doi.org/10.1016/j.wace.2022.100484>
- Ngo-Duc, T., and coauthors., 2017: Performance evaluation of RegCM4 in simulating extreme rainfall and temperature indices over the CORDEX-Southeast Asia region. *Int. J. Climatol.*, 37(3), pp.1634-1647.
- Ngo-Thanh H, Ngo-Duc T, Nguyen-Hong H, Baker P, Phan-Van T. 2018: A distinction between rainy season and summer season over the Central Highlands of Vietnam. *Theoretical and Applied Climatology*, **132**: 1237. <http://doi.org/10.1007/s00704-017-2178-6>.
- Nguyen DT., 2022. Variability of the Red River plume in the Gulf of Tonkin from stochastic modeling and cluster analysis. *Ocean, Atmosphere*. Université Paul Sabatier - Toulouse III, 2022. English. (NNT: 2022TOU30089). (tel-03828544)
- Nguyen-Le D, Matsumoto J, Ngo-Duc T. 2015: Onset of the rainy seasons in the eastern Indochina Peninsula. *J. Clim.* **28(14)**: 5645-5666. <http://doi.org/10.1175/JCLI-D-14-00373.1>.
- Nguyen-Thanh, H., Ngo-Duc, T. & Herrmann, M., 2023: The distinct impacts of the two types of ENSO on rainfall variability over Southeast Asia. *Clim Dyn* 61, 2155–2172. <https://doi.org/10.1007/s00382-023-06673-2>
- Nguyen-Thi HA, Matsumoto J, Ngo-Duc T, Endo N (2012) A climatological study of tropical cyclone rainfall in Viet- nam. *SOLA* 8:41–44
- Nisha, P. G., P. M. Muraleedharan, M. G. Keerthi, P. V. Sathe, and M. Ravichandran, 2012: Does sea level pressure modulate the dynamic and thermodynamic forcing in the tropical Indian Ocean? *Int. J. Remote Sens.*, **33**, 1991–2002. <https://doi.org/10.1080/01431161.2011.604653>.
- Neelin, J.D. and Held, I.M., 1987: Modeling tropical convergence based on the moist static energy budget. *Mon. Wea. Rev.*, **315**, 3-12. [https://doi.org/10.1175/1520-0493\(1987\)115<0003:MTCBOT>2.0.CO;2](https://doi.org/10.1175/1520-0493(1987)115<0003:MTCBOT>2.0.CO;2)
- NOAA-CPC (2022)  
[https://origin.cpc.ncep.noaa.gov/products/analysis\\_monitoring/ensostuff/ONI\\_v5.php](https://origin.cpc.ncep.noaa.gov/products/analysis_monitoring/ensostuff/ONI_v5.php)  
(last accessed in June 2022)

## References

- Ooi, S.H., Samah, A.A., Chenoli,S.N., Subramaniam, K. and AhmadMazuki, M.Y. (2017) Extreme rainstorms that caused devastatingflooding across the East Coast of Peninsular Malaysia duringNovember and December 2014. *Weather and Forecasting*, 32(3),849–872. <https://doi.org/10.1175/WAF-D-16-0160.1>.  
[CHENOLIET AL.10251.](https://doi.org/10.1175/WAF-D-16-0160.1)
- Pang X, Bassinot F, Sepulcre S (2021). Indonesian Throughflow variability over the last two glacial-interglacial cycles: Evidence from the eastern Indian Ocean. *Quaternary Science Reviews*, (), –. [doi:10.1016/j.quascirev.2021.106839](https://doi.org/10.1016/j.quascirev.2021.106839)
- Page SE et al (2002) The amount of carbon released during peat and forest fires in Indonesia during 1997. *Nature* 420:61–65
- Papadopoulos, V. P., A. Bartzokas, T. Chronis, D. Georgopoulos, and G. Ferentinos, 2012: Factors Regulating the Air–Sea Heat Fluxes Regime over the Aegean Sea. *J. Climate*, 25, 491–508, <https://doi.org/10.1175/2011JCLI4197.1>.
- Park, S., C. Deser, and M. A. Alexander, 2005: Estimation of the Surface Heat Flux Response to Sea Surface Temperature Anomalies over the Global Oceans. *J. Climate*, 18, 4582–4599, <https://doi.org/10.1175/JCLI3521.1>.
- Planton S, Deque M, Bellevaux C, 1991: Validation of an annual cycle simulation with a T42–L20 GCM. *Clim Dyn* 5:189–200
- Pennington, J.T., Mahoney, K.L., Kuwahara, V.S., Kolber, D.D., Calienes, R. and Chavez, F.P., 2006. Primary production in the eastern tropical Pacific: A review. *Progress in oceanography*, 69(2-4), pp.285-317. <https://doi.org/10.1016/j.pocean.2006.03.012>
- Phan VT, Ngo-Duc T, Ho TMH (2009) Seasonal and interannual variations of surface climate elements over Vietnam. *Clim Res* 40: 49-60
- Piton, V., 2019. Du Fleuve Rouge au Golfe du Tonkin: dynamique et transport sédimentaire le long du continuum estuaire-zone côtière. Doctoral dissertation. Université de Toulouse, Toulouse, France.
- Pokhrel, S., Dutta, U., Rahaman, H., Chaudhari, H., Hazra, A., Saha, S. K., & Veeranjanyulu, C. (2020). Evaluation of different heat flux products over the tropical Indian Ocean. *Earth and Space Science*, 7, e2019EA000988. <https://doi.org/10.1029/2019EA000988>
- Pond Stephen (1971). *Air-sea interaction*. *Eos, Transactions American Geophysical Union*, 52(6), IUGG389–. [doi:10.1029/eo052i006piu389](https://doi.org/10.1029/eo052i006piu389)

## References

- Power S, Casey T, Folland C, Colman A, Mehta V (1999) Inter-decadal modulation of the impact of ENSO on Australia. *Clim Dyn* 15(5):319–324. <https://doi.org/10.1007/s003820050284>
- Power SB, Smith IN (2007) Weakening of the Walker Circulation and apparent dominance of El Niño both reach record levels, but has ENSO really changed? *Geophys Res Lett* 34(18):L18702. <https://doi.org/10.1029/2007g1030854>
- Pradhan, P.K., Preethi, B., Ashok, K., Krishnan, R., Sahai, A.K., 2011. Modoki, Indian Ocean Dipole, and western North Pacific typhoons: possible implications for extreme events. *J. Geophys. Res.* 116, D18108. <https://doi.org/10.1029/2011JD015666>.
- Preethi, B., et al., 2015. Impacts of the ENSO Modoki and other tropical IndoPacific climate-drivers on African rainfall. *Sci. Rep.* 5, 16653. Available from: <https://doi.org/10.1038/srep16653>.
- Pullen, J., A. L. Gordon, M. Flatau, J. D. Doyle, C. Villanoy, and O. Cabrera, 2015: Multiscale influences on extreme winter rainfall in the Philippines. *J. Geophys. Res. Atmos.*, **120**, 3292–3309, [doi:10.1002/2014JD022645](https://doi.org/10.1002/2014JD022645).
- Qiu B, S. Chen Interannual-to-decadal variability in the bifurcation of the North Equatorial Current off the Philippines *J. Phys. Oceanogr.*, 40 (2010), pp. 2525-2538
- Qian W, Yang S. 2000. Onset of the regional monsoon over Southeast Asia. *Meteorology and Atmospheric Physics* 75: 29–38.
- Qu, T., Mitsudera, H., Yamagata, T., 2000. Intrusion of the North Pacific waters into the South China Sea, *J. Geophys. Res.*, 105, C3, 6,415-6,424.
- Qu, T. and Lukas, R. The bifurcation of the North Equatorial Current in the Pacific. *J. Phys. Oceanogr.* 33, 5–18 (2003)
- Qu, T., Y. Y. Kim, M. Yaremchuk, T. Tozuka, A. Ishida, and T. Yamagata (2004), Can the Luzon Strait transport play a role in conveying the impact of ENSO to the South China Sea?, *J. Clim.*, 17, 3644–3657, [doi:10.1175/1520-0442\(2004\)017<3644:CLSTPA>2.0.CO;2](https://doi.org/10.1175/1520-0442(2004)017<3644:CLSTPA>2.0.CO;2).
- Qu, T., Du, Y., Meyers, G., Ishida, A., Wang, D., 2005. Connecting the tropical Pacific with Indian Ocean through South China Sea. *Geophys. Res. Lett.* 32, L24609, [doi:10.1029/2005GL024698](https://doi.org/10.1029/2005GL024698).

## References

- Qu, T., Girton, G., Whitehead, J., 2006. Deepwater overflow through Luzon strait. *J. Geophys. Res.* 111, C01002, [doi:10.1029/2005JC003139](https://doi.org/10.1029/2005JC003139).
- Qu, T., Du, Y., Sasaki, H., 2006. South China Sea throughflow: a heat and freshwater conveyor. *Geophys. Res. Lett.* 33, L23617, [doi:10.1029/2006GL028350](https://doi.org/10.1029/2006GL028350)
- Qu, T., Du, Y., Gan, J., Wang, D., 2007. Mean seasonal cycle of isothermal depth in the South China Sea. *J. Geophys. Res.* 112, C02020, [doi:10.1029/2006JC003583](https://doi.org/10.1029/2006JC003583).
- Qu T; Y. Tony Song; Toshio Yamagata (2009). An introduction to the South China Sea throughflow: Its dynamics, variability, and application for climate, 47(1-3), 0–14. [doi:10.1016/j.dynatmoce.2008.05.001](https://doi.org/10.1016/j.dynatmoce.2008.05.001)
- Raghavan, S.V., Liu, J., Nguyen, N.S., Vu, M.T. and Liong, S.Y., 2017. Assessment of CMIP5 historical simulations of rainfall over Southeast Asia. *Theor. Appl. Climatol.*, pp.1-14
- Ramanathan, V., and Collins, W. 1992: Thermostat and global warming. *Nature*, **357**, 649. <https://doi.org/10.1038/357649a0>.
- Räsänen, T.A., Lindgren, V., Guillaume, J.H., Buckley, B.M. and Kummu, M., 2016. On the spatial and temporal variability of ENSO precipitation and drought teleconnection in mainland Southeast Asia. *Clim. of the Past*, 12(9), pp.1889-1905.
- Rasmusson, E.M., Carpenter, T.H., 1982. Variations in tropical sea surface temperature and surface wind fields associated with the Southern Oscillation/El Niño. *Mon. Weather Rev.* 110, 354384.
- Rasmusson EM, Wallace JM (1982) Meteorological aspects of the El Niño/Southern Oscillation. *Science* 222(4629):1195– 1202.
- Rasmusson EM, Carpenter TH (1983) The relationship between Eastern equatorial Pacific sea surface temperatures and rainfall over India and Sri Lanka. *Mon Weather Rev* 111:517– 528
- Rayner NA et al (2003) Global analyses of SST, sea ice and night marine air temperature since the late nineteenth century. *J Geophys Res* 108: <https://doi.org/10.1029/2002JD002670>
- Ratna SB, Ratnam JV, Behera SK, Tangang FT, Yamagata T (2017). Validation of the WRF regional climate model over the subregions of Southeast Asia: climatology and interannual variability. *Climate Research*, 71(3), pp.263-280.

## References

- Reeves E J. E. Jack, Zeng X., Zhang K, 2021: Ocean Surface Flux Algorithm Effects on Earth System Model Energy and Water Cycles, *Frontiers in Marine Science* 8,2296-7745. [DOI:10.3389/fmars.2021.642804](https://doi.org/10.3389/fmars.2021.642804)
- Rhein, M., Rintoul, S., Aoki, S., Campos, E., Chambers, D., Feely, R., et al. (2013). “Observations: ocean,” in *Climate Change 2013: The Physical Science Basis. Contribution of Working Group I to the Fifth Assessment Report of the Intergovernmental Panel on Climate Change*, eds T. Stocker, D. Qin, G.-K. Plattner, M. Tignor, S. Allen, J. Boschung, A. Nauels, Y. Xia, V. Bex, and P. Midgley (Cambridge; New York, NY: Cambridge University Press, 255–316.
- Rienecker, M. M., et al. (2011), MERRA—NASA’s modern-era retrospective analysis for research and applications, *J. Clim.*, 24, 3624–3648
- Robertson, A.W., Moron, V., Qian, J.-H., Chang, C.-P., Tangang, F., Aldrian, E., Koh, T.Y. and Liew, J. (2011) The Maritime Continent monsoon. In: *The Global Monsoon System. World Scientific Series on Asia-Pacific Weather and Climate*. Singapore: WorldScientific, pp. 85–98. [https://doi.org/10.1142/9789814343411\\_0006](https://doi.org/10.1142/9789814343411_0006).
- Robertson, F. R., and Coauthors, 2020: Uncertainties in Ocean Latent Heat Flux Variations over Recent Decades in Satellite-Based Estimates and Reduced Observation Reanalyses. *J. Climate*, 33, 8415–8437, <https://doi.org/10.1175/JCLI-D-19-0954.1>.
- Roxy M. 2014. Sensitivity of precipitation to sea surface temperature over the tropical summer monsoon region – and its quantification. *Clim. Dyn.* 43: 1159–1169. <https://doi.org/10.1007/s00382-013-1881-y>.
- Rudolf B, Hauschild H, Reuth W, Schneider U (1994) Terrestrial precipitation analysis: Operational method and required density of point measurements. *Global Precipitation and Climate Change* (M. Desbois, F. Desalmond, eds.), NATO ASI Series I, 26:173-186
- Saji, N. H., Goswami, B. N., Vinayachandran, P. N., & Yamagata, T. (1999). A dipole mode in the tropical Indian Ocean. *Nature*, 401(6751), 360–363. <https://doi.org/10.1038/43854>
- Salimun E et al (2013) Differential impacts of conventional El Niño versus El Niño Modoki on Malaysian rainfall anomaly during winter monsoon. *Int J Climatol* 34(8):2763–2774. <https://doi.org/10.1002/joc.3873>
- Schopf, P.S., Lough, A., 1995. A reduced gravity isopycnal ocean model: hindcasts of El Niño. *Mon. Weather Rev.* 123, 2839–2863

## References

- Sea-Air Interactions. (2017). In United Nations (Ed.), *The First Global Integrated Marine Assessment: World Ocean Assessment I* (pp. 105-118). Cambridge: Cambridge University Press. [doi:10.1017/9781108186148.008](https://doi.org/10.1017/9781108186148.008)
- Shaw, P.-T., Chao, S.-Y., Fu, L.-L., 1999. Sea surface height variations in the South China Sea from satellite altimetry. *Oceanol. Acta* 22, 1–17.
- Shinoda T, Hurlburt HE, Metzger EJ (2011) Anomalous tropical ocean circulation associated with La Niña Modoki. *J Geophys Res Atmos* 116:C12001. <https://doi.org/10.1029/2011JC007304>
- Shukla RP, Tripathi KC, Pandey AC, Das IML (2011) Prediction of Indian summer monsoon rainfall using Niño indices: A neural network approach. *Atmos Res* 102(1-2):99–109. <https://doi.org/10.1016/j.atmosres.2011.06.013>
- Siddorn J.R., Furner R., 2013. An analytical stretching function that combines the best attributes of geopotential and terrain-following vertical coordinates. *Ocean Modelling* 66, 1–13
- Sikka DR, and R. Narasimha, 1995: Genesis of the Monsoon Trough Boundary Layer Experiment (MONTBLEX). *Proc. Indian Acad. Sci.*, 104, 157–187.
- Singh, V., Sharma, A. and Goyal, M.K., 2019. Projection of hydro-climatological changes over eastern Himalayan catchment by the evaluation of RegCM4 RCM and CMIP5 GCM models. *Hydrol. Res.*, 50(1), pp.117-137.
- Song, X., and Yu, L., 2013: How much net surface heat flux should go into the Western Pacific Warm Pool?, *J. Geophys. Res. Oceans*, **118**, 3569– 3585, <https://doi.org/10.1002/jgrc.20246>.
- Song, X., and Yu, L. 2017: Air-sea heat flux climatologies in the Mediterranean Sea: Surface energy balance and its consistency with ocean heat storage, *J. Geophys. Res. Oceans*, 122, 4068–4087, [doi:10.1002/2016JC012254](https://doi.org/10.1002/2016JC012254).
- Sprintall, J., A. L. Gordon, T. Lee, J. T. Potemra, K. Pujiana, and S. E. Wijffels (2014), The Indonesian seas and their role in the couple ocean-climate system, *Nat. Geosci.*, 7, 487–492, [doi:10.1038/ngeo2188](https://doi.org/10.1038/ngeo2188).
- Sun, X., Renard, B., Thyer, M., Westra, S. and Lang, M., 2015. A global analysis of the asymmetric effect of ENSO on extreme precipitation. *J. Hydrol.*, 530, pp.51-65.

## References

- Supari, E., and Coauthors, 2020: Multi-model Projections of Precipitation Extremes in Southeast Asia based on CORDEX-Southeast Asia simulations. *Environmental Research*, **184**, 109350, <https://doi.org/10.1016/j.envres.2020.109350>.
- Susanto R. D., A. Ffield, A. L. Gordon, and T. R. Adi (2012), Variability of Indonesian throughflow within Makassar Strait throughflow: 2004 to 2009, *Geophys Res. Lett.*, 117, C09013, [doi:10.1029/2012JC008096](https://doi.org/10.1029/2012JC008096).
- Susanto, R. Dwi; Song, Y. Tony (2015). Indonesian throughflow proxy from satellite altimeters and gravimeters. *Journal of Geophysical Research: Oceans*, 120(4), 2844–2855. [doi:10.1002/2014JC010382](https://doi.org/10.1002/2014JC010382)
- Stommel, H. and Arons, A.B., 1959. On the abyssal circulation of the world ocean—II. An idealized model of the circulation pattern and amplitude in oceanic basins. *Deep Sea Research* (1953), 6, 217-233. [https://doi.org/10.1016/0146-6313\(59\)90075-9](https://doi.org/10.1016/0146-6313(59)90075-9)
- Stephens GL et al. (2012). An update on Earth's energy balance in light of the latest global observations. *Nature Geoscience*, 5(10), 691–696. [doi:10.1038/ngeo1580](https://doi.org/10.1038/ngeo1580)
- Stern ME, 1965. Interaction of a uniform wind stress with a geostrophic vortex. In *Deep Sea Research and Oceanographic Abstracts*, 12, 3, 55-367, Elsevier. [https://doi.org/10.1016/0011-7471\(65\)90007-0](https://doi.org/10.1016/0011-7471(65)90007-0)
- Strobach E, Molod A, Forget G, Campin JM, Hill C, Menemenlis D, Heimbach P (2018). Consequences of different air-sea feedback on ocean using MITgcm and MERRA-2 forcing: Implications for Coupled Data Assimilation Systems. *Ocean Modelling*. 132. [doi:10.1016/j.ocemod.2018.10.006](https://doi.org/10.1016/j.ocemod.2018.10.006).
- Tanaka M. 1994. The onset and retreat dates of the Austral summer monsoon over Indonesia, Australia, and New Guinea. *Journal of the Meteorological Society of Japan* 72: 255–267.
- Tanaka HL, Ishizaki N, Kitoh A (2004) Trend and interannual variability of Walker, monsoon and Hadley circulations defined by velocity potential in the upper troposphere. *Tellus A* 56(3): 250–269. <https://doi.org/10.1111/j.1600-0870.2004.00049.x>
- Takaura, N., Uchiyama, Y., Kajikawa, Y., and Nakayama, A. 2020 “Impact of the ENSO on oceanic heat transport in the South China Sea and the Indonesian Seas”, vol. 2020.
- Tangang, F. T., L. Juneng, E. Salimun, P. N. Vinayachandran, K. S. Yap, C. J. C. Reason, S. K. Behera, and T. Yasunari, 2008: On the roles of the northeast cold surge, the Borneo vortex, the Madden–Julian oscillation, and the Indian Ocean dipole during the extreme

## References

- 2006/2007 flood in southern Peninsular Malaysia. *Geophys. Res. Lett.*, **35**, L14S07, [doi:10.1029/2008GL033429](https://doi.org/10.1029/2008GL033429).
- Tangang FT et al (2017) Characteristics of precipitation extremes in Malaysia associated with El Niño and La Niña events. *International Journal of Climatology*. <https://doi.org/10.1002/joc.5032>
- Tangang, F., and coauthors, 2020. Projected future changes in rainfall in Southeast Asia based on CORDEX–SEA multi-model simulations. *Clim Dyn* **55**, 1247–1267. <https://doi.org/10.1007/s00382-020-05322-2>
- Taschetto, A. S., and M. H. England, 2009: El Niño Modoki Impacts on Australian Rainfall. *J. Climate*, **22**, 3167–3174, <https://doi.org/10.1175/2008JCLI2589.1>.
- Taschetto, A.S., Ummenhofer, C.C., Sen Gupta, A., England, M.H., 2009. Effect of anomalous warming in the central Pacific on the Australian monsoon. *Geophys. Res. Lett.* **36**, L12704. <https://doi.org/10.1029/2009GL038416>
- Taylor, K. E., Stouffer, R. J., and Meehl, G. A., 2012: An overview of CMIP5 and the experiment design. *Bull. Am. Meteorol. Soc.*, **93** (4), 485–498. <https://doi.org/10.1175/BAMS-D-11-00094.1>
- Taylor, P.K., 2015: AIR SEA INTERACTIONS | Momentum, Heat, and Vapor Fluxes, Editor(s): Gerald R. North, John Pyle, Fuqing Zhang, *Encyclopedia of Atmospheric Sciences (Second Edition)*, Academic Press, 129-135. <https://doi.org/10.1016/B978-0-12-382225-3.00064-5>.
- Tillinger D, Gordon AL, 2010. Transport weighted temperature and internal energy transport of the Indonesian throughflow, *Dynamics of Atmospheres and Oceans*, **50**(2),224-232. <https://doi.org/10.1016/j.dynatmoce.2010.01.002>.
- Timmermann A et al (2018) El Niño–Southern Oscillation complexity. *Nature* **559**:535–545. <https://doi.org/10.1038/s41586-018-0252-6>
- Tebaldi, C., Debeire, K., Eyring, V., Fischer, E., Fyfe, J., Friedlingstein, P., & Ziehn, T. 2021: Climate model projections from the scenario model intercomparison project (scenarioMIP) of CMIP6. *Earth System Dynamics*, **12**(1), 253–293. <https://doi.org/10.5194/esd-12-253-2021>
- Terray, P., Kamala, K., Masson, S., Madec, G., Sahai, A.K., Luo, J.J., Yamagata, T., 2012: The role of the intra-daily SST variability in the Indian monsoon variability and monsoon-

## References

- ENSO-IOD relationships in a global coupled model. *Climate Dyn.*, **39**, 729–754. <https://doi.org/10.1007/s00382-011-1240-9>.
- Tetzner D, Thomas E, Allen C., 2019: A Validation of ERA5 Reanalysis Data in the Southern Antarctic Peninsula—Ellsworth Land Region, and Its Implications for Ice Core Studies. *Geosciences*; **9(7)**: 289. <https://doi.org/10.3390/geosciences9070289>
- To D.T (2022). Interannual to intraseasonal variability of the South Vietnam Upwelling: the role of high-frequency atmospheric forcing, mesoscale dynamics, coastal circulation, and intrinsic variability. Doctoral dissertation. Université de Toulouse, Toulouse, France.
- Tokinaga, H., Y. Tanimoto, and S.-P. Xie (2005), SST-induced surface wind variations over the Brazil-Malvinas Confluence: Satellite and in situ observations, *J. Clim.*, **18**, 3470–3482.
- Tomita H., Kutsuwada K., Kubota M., Hihara T., 2021. Advances in the Estimation of Global Surface Net Heat Flux Based on Satellite Observation: J-OFURO3 V1.1. *Frontiers in Marine Science*, **8**. [DOI=10.3389/fmars.2021.612361](https://doi.org/10.3389/fmars.2021.612361)
- Tozuka, T., T. Kagimoto, Y. Masumoto, and T. Yamagata, 2002: Simulated multiscale variations in the western tropical Pacific: The Mindanao Dome revisited. *J. Phys. Oceanogr*, **32**, 1338–1359.
- Tozuka, T., Qu, T., Yamagata, T., 2007. Dramatic impact of the South China Sea on the Indonesian Throughflow. *Geophys. Res. Lett.* **34**, [doi:10.1029/2007GL030420](https://doi.org/10.1029/2007GL030420).
- Tozuka T, Qu T, Masumoto Y, Yamagata T (2009). Impacts of the South China Sea Throughflow on seasonal and interannual variations of the Indonesian Throughflow. *J. Geophys. Res.* **114**, 47(1-3), 0–85. [doi:10.1016/j.dynatmoce.2008.09.001](https://doi.org/10.1016/j.dynatmoce.2008.09.001)
- Tran TL, Ritchie EA, Perkins-Kirkpatrick SE 2022. A 50-year tropical cyclone exposure climatology in Southeast Asia. *Journal of Geophysical Research: Atmospheres*. **127**(4), e2021JD036301. <https://doi.org/10.1029/2021JD036301>
- Trenberth KE (1997) The definition of El Niño. *Bull Amer Meteorol Soc* **78**(12):2771–2777. [https://doi.org/10.1175/1520-0477\(1997\)078%3c2771:tdoen%3e2.0.co;2](https://doi.org/10.1175/1520-0477(1997)078%3c2771:tdoen%3e2.0.co;2)
- Trenberth, K.E., et al., 1998. Progress during TOGA in understanding and modeling global teleconnections associated with tropical sea surface temperatures. *J. Geophys. Res.* **103**, 1429114324.

## References

- Trenberth, Kevin E.; Fasullo, John T.; Kiehl, Jeffrey (2009). *Earth's Global Energy Budget. Bulletin of the American Meteorological Society*, 90(3), 311–323. [doi:10.1175/2008BAMS2634.1](https://doi.org/10.1175/2008BAMS2634.1)
- Trinh BN, 2020 Water, heat and salt cycles over the South China sea, from seasonal to interannual variability: a closed budget and high-resolution ocean modelling approach. Oceanography. Université Paul Sabatier - Toulouse III, 2020. English. (NNT : 2020TOU30290). (tel-03332193)
- Trinh, N. B., Herrmann, M., Ulses, C., Marsaleix, P., Duhaut, T., To Duy, T., Estournel, C., and Shearman, R. K.: Studying multi-scale ocean dynamics and their contribution to water, heat and salt budgets in the South China Sea: evaluation of a high-resolution configuration of an online closed-budget hydrodynamical ocean model (SYMPHONIE version 249), EGUsphere [preprint], <https://doi.org/10.5194/egusphere-2023-547>, 2023.
- Tyrlis, E., Lelieveld, J. and Steil, B., 2013. The summer circulation over the eastern Mediterranean and the Middle East: influence of the South Asian monsoon. *Clim. Dyn.*, 40(5-6), pp.1103-1123
- Valdivieso, M., Haines, K., Balmaseda, M., Chang, Y.-S., Drevillon, M., Ferry, N., et al. (2017). An assessment of air–sea heat fluxes from ocean and coupled reanalyses. *Clim. Dyn.* 49, 983–1008. [doi: 10.1007/s00382-015-2843-3](https://doi.org/10.1007/s00382-015-2843-3)
- van Sebille, E., J. Sprintall, F. Schwarzkopf, A. Sen Gupta, A. Santoso, M. H. England, C. Boning, and A. Biastoch, 2014: Pacific-to-Indian Ocean connectivity: Tasman leakage, Indonesian Throughflow and the role of ENSO. *J. Geophys. Res. Oceans*, 119, 1365–1382, <https://doi.org/10.1002/2013JC009525>.
- Villafuerte, M.Q. and Matsumoto, J., 2015. Significant influences of global mean temperature and ENSO on extreme rainfall in Southeast Asia. *J. Clim.*, 28(5), pp.1905-1919.
- Vecchi GA et al (2006) Weakening of tropical Pacific atmospheric circulation due to anthropogenic forcing. *Nature* 441: 73-76
- Uppala, S. M., et al. (2005), The ERA-40 re-analysis, *Q. J. R. Meteorol. Soc.*, 131, 2961–3012, [doi:10.1256/qj.04.176](https://doi.org/10.1256/qj.04.176).
- Waldman, R., et al. (2016), Estimating dense water volume and its evolution for the year 2012–2013 in the Northwestern Mediterranean Sea: An observing system simulation experiment approach, *J. Geophys. Res. Oceans*, 121, 6696–6716, [doi:10.1002/2016JC011694](https://doi.org/10.1002/2016JC011694)

## References

- Waliser DE, Gautier C (1993) A satellite-derived climatology of the ITCZ. *J Clim* 6:2162–2174. [https://doi.org/10.1175/1520-0442\(1993\)006<2162:Asdcot>2.0.Co;2](https://doi.org/10.1175/1520-0442(1993)006<2162:Asdcot>2.0.Co;2)
- Wallcraft A, Kara A, Hurlburt H, Chassignet E, and Halliwell G (2008). Value of bulk heat flux parameterizations for ocean SST prediction. *Journal of Marine Systems - J MARINE SYST.* 74. 241-258. [doi:10.1016/j.jmarsys.2008.01.009](https://doi.org/10.1016/j.jmarsys.2008.01.009).
- Wang, B., 2004: *The Asian Monsoon*. Springer/Praxis, 787 pp
- Wang, B., Chan, J.C.L., 2002. How strong ENSO events affect tropical storm activity over the Western North Pacific. *J. Clim.* 15, 1643-1658. [https://doi.org/10.1175/1520-0442\(2002\)015%3C1643:HSEEAT%3E2.0.CO;2](https://doi.org/10.1175/1520-0442(2002)015%3C1643:HSEEAT%3E2.0.CO;2)
- Wang B, LinHo (2002) Rainy season of the Asian–Pacific summer monsoon. *J Climate* 15: 386–398
- Wang, B., Yim, SY., Lee, JY. *et al.*, 2014 Future change of Asian-Australian monsoon under RCP 4.5 anthropogenic warming scenario. *Clim Dyn* 42, 83–100 . <https://doi.org/10.1007/s00382-013-1769-x>
- Wang B, Wu R, Fu X (2000) Pacific –East Asian teleconnection: how does ENSO affect East Asian climate. *J Clim* 13:1517–1536
- Wang B, Ding Q, Fu X, Kang I.-S, Jin K, Shukla J, Doblas-Reyes F. 2005. Fundamental challenge in simulation and prediction of summer monsoon rainfall. *Geophys. Res. Lett.*, **32(15)**: L15711. <https://doi.org/10.1029/2005GL022734>.
- Wang C (2002) Atmospheric circulation cells associated with the El Nino Southern Oscillation. *J Clim* 15:399–419
- Wang, C and Picaut, J. 2004: Understanding ENSO physics—A review. *Earth's Climate: The Ocean–Atmosphere Interaction*, *Geophys. Monograph*, 147, 21–48.
- Wang, Y., Fang, G., Wei, Z., Qiao, F., and Chen, H. 2006: Interannual variation of the South China Sea circulation and its relation to El Niño, as seen from a variable grid global ocean model, *J. Geophys. Res.-Ocean.*, 111, 1–15, <https://doi.org/10.1029/2005JC003269>.,.
- Wang, D., Liu, Q., Huang, R., Du, Y., Qu, T., 2006. Interannual variability of the South China Sea throughflow inferred from wind data and an ocean data assimilation product. *Geophys. Res. Lett.* 33, L14605, [doi:10.1029/2006GL026316](https://doi.org/10.1029/2006GL026316).

## References

- Wang D, Wang H, Li M, Liu G and Wu X, 2013. Role of Ekman transport versus Ekman pumping in driving summer upwelling in the South China Sea. *J. Ocean Univ. China* 12, 355–365. <https://doi.org/10.1007/s11802-013-1904-7>
- Wang, D.X., Zhou, F.X., Li, Y.P., 1997. Annual cycle of sea surface temperature and sea surface heat budget. *Acta Oceanol. Sin.* 19,35–44 (in Chinese).
- Wang X, Zhang R., Huang J., Zeng L., Huang F., 2017: Biases of five latent heat flux products and their impacts on mixed-layer temperature estimates in the South China Sea. *Journal of Geophysical Research: Oceans*. 122. 5088–5104. <https://doi.org/10.1002/2016JC012332>.
- Wang, Y., and Coauthors, 2019: Seasonal variation of water transport through the Karimata Strait. *Acta Oceanol. Sin.*, **38**, 47–57. <https://doi.org/10.1007/s13131-018-1224-2>.
- Wang Yan, Xu Tengfei, Li Shujiang, Susanto R. Dwi, Agustiadi Teguh, Trenggono Mukti, Tan Wei, Wei Zexun. 2019. Seasonal variation of water transport through the Karimata Strait. *Acta Oceanologica Sinica*, 38(4): 47–57, [doi: 10.1007/s13131-018-1224-2](https://doi.org/10.1007/s13131-018-1224-2)
- Wang Z. and Chang, C.P., 2012. A numerical study of the interaction between the large-scale monsoon circulation and orographic precipitation over South and Southeast Asia. *J. Clim.*, 25(7), pp.2440-2455.
- Wang W, Chen M, Kumar A, Xue Y (2011) How important is intraseasonal surface wind variability to real-time ENSO prediction? *Geophys Res Lett* 38(13). <https://doi.org/10.1029/2011gl047684>
- Ward, P.J., Eisner, S., Flörke, M., Dettinger, M.D. and Kummerow, M., 2014. Annual flood sensitivities to El Niño–Southern Oscillation at the global scale. *Hydrol. Earth System Sci.*, 18(1), pp.47-66.
- Weare BC. 1989: Uncertainties in estimates of surface heat flux derived from marine reports over the tropical and subtropical oceans. *Tellus Ser A Dyn Meteorol Oceanogr* 41:357–370
- Webster, P. J., and G. L. Stephens, 1984: Cloud–radiation interaction and the climate problems, in *The Global Climate*, edited by J. T. Houghton, 63–78, Cambridge Univ. Press, New York.
- Webster PJ, Magana VO, Palmer TN, Shukla J, Tomas RA, Yanai M, Yasunari T. 1998. Monsoons: processes, predictability, and the prospects for prediction. *Journal of Geophysical Research* 103: 14451–14510.

## References

- Webster, P. J., Moore, A. M., Loschnigg, J. P., & Leben, R. R. 1999. Coupled ocean-atmosphere dynamics in the Indian Ocean during 1997–98. *Nature*, 401(6751), 356–360. <https://doi.org/10.1038/43848>
- Welander P, 1957. Wind action on a shallow sea: some generalizations of Ekman's theory. *Tellus*, 9, 45-52. <https://doi.org/10.1111/j.2153-3490.1957.tb01852.x>
- Weng, H., K. Ashok, S. K. Behera, and S. A. Rao, 2007: Impacts of recent El Niño Modoki on dry/wet conditions in the Pacific Rim during boreal summer. *Climate Dyn.*, 29, 113–129.
- Weng, H., Behera, S.K., Yamagata, T., 2009. Anomalous winter climate conditions in the Pacific rim during recent El Niño Modoki and El Niño events. *Clim. Dyn.* 32, 663-674.
- Weng S, Behera K and Yamagata T (2009) Anomalous winter climate conditions in the Pacific rim during recent El Niño Modoki and El Niño events. *Clim Dyn.* 32:663–674. <https://doi.org/10.1007/s00382-008-0394-6>
- Wild M, Folini D, Schar C, Loeb N, Dutton EG, König-Langlo G (2013a) The global energy balance from a surface perspective. *Clim Dyn* 40(11–12):3107–3134. [doi:10.1007/S00382-012-1569-8](https://doi.org/10.1007/S00382-012-1569-8)
- Wild M, Folini D, Schar C, Loeb N, Dutton EG, König-Langlo G(2013b) A new diagram of the global energy balance. *AIP Conf Proc* 1531:628–631. [doi:10.1063/1.4804848](https://doi.org/10.1063/1.4804848)
- Wild, M., 2020. The global energy balance as represented in CMIP6 climate models. *Clim Dyn* 55, 553–577. <https://doi.org/10.1007/s00382-020-05282-7>
- Woodruff, J. D., Irish, J. L., & Camargo, S. J. (2013). Coastal flooding by tropical cyclones and sea-level rise. *Nature*, 504(7478), 44– 52. <https://doi.org/10.1038/nature12855>
- Wu, M., Chang, W., & Leung, W. (2004). Impacts of El Niño–southern oscillation events on tropical cyclone landfalling activity in the Western North Pacific. *Journal of Climate*, 17(6), 1419–1428. [https://doi.org/10.1175/1520-0442\(2004\)017<1419:IOENOE>2.0.CO;2](https://doi.org/10.1175/1520-0442(2004)017<1419:IOENOE>2.0.CO;2)
- Wu, P., M. Hara, H. Fudeyasu, M. D. Yamanaka, J. Matsumoto, F. Syamsudin, R. Sulistyowati, and Y. S. Djajadihardja, 2007: The impact of trans-equatorial monsoon flow on the formation of repeated torrential rains over Java Island. *SOLA*, 3, 93–96, [doi:10.2151/sola.2007-024](https://doi.org/10.2151/sola.2007-024).
- Wu G, Zhang Y. 1998. Tibetan Plateau forcing and timing of the monsoon onset over South Asia and South China Sea. *Monthly Weather Review* 126: 913–927.

## References

- Wu R, Hu ZZ, Kirtman BP (2003) Evolution of ENSO-related rainfall anomalies in East Asia and the processes. *J Clim* 16: 3742–3758
- Wu R, Wang B. 2000. Interannual variability of summer monsoon onset over the western North Pacific and the underlying processes. *Journal of Climate* 13: 2483–2501.
- Wu, R., B. P. Kirtman, and K. Pegion, 2007: Surface latent heat flux and its relationship with sea surface temperature in the National Centers for Environmental Prediction Climate Forecast System simulations and retrospective forecasts. *Geophys. Res. Lett.*, **34**, L17712, <https://doi.org/10.1029/2007GL030751>.
- Wu, R., and G. Chen, 2021: Contrasting Cloud Regimes and Associated Rainfall over the South Asian and East Asian Monsoon Regions. *J. Climate*, **34**, 3663–3681, <https://doi.org/10.1175/JCLI-D-20-0992.1>.
- Wyrtki, K., 1961. Physical oceanography of the Southeast Asian waters, Naga Report 2, Scripps Inst. of Oceanogr., La Jolla, CA, 195 pp.
- Xavier, P., Rahmat, R., Cheong, W.K. and Wallace, E., 2014. Influence of Madden-Julian Oscillation on Southeast Asia rainfall extremes: observations and predictability. *Geophys. Res. Lett.*, 41(12), pp.4406-4412.
- Xie, S.P., Xie, Q., Wang, D., and Liu, W. T. (2003), Summer upwelling in the South China Sea and its role in regional climate variations, *J. Geophys. Res.*, 108, 3261, <https://doi.org/10.1029/2003JC001867>, C8.
- Xie, S.-P. (2004), Satellite observations of cool ocean-atmosphere interaction, *Bull. Am. Meteorol. Soc.*, **85**, 195–208.
- Xie S-P, Deser C, Vecchi GA, Ma J, Teng H, Wittenberg AT. 2010: Global warming pattern formation: sea surface temperature and rainfall. *J. Clim.* **23(4)**: 966–986. <https://doi.org/10.1175/2009JCLI3329.1>.
- Xu K et al (2017) CMIP5 Projections of Two Types of El Niño and Their Related Tropical Precipitation in the Twenty-First Century. *J Clim* 30(3):849–864. <https://doi.org/10.1175/jcli-d-16-0413.1>
- Xue F, Liu CZ (2008) The influence of moderate ENSO on summer rainfall in eastern China and its comparison with strong ENSO (in Chinese). *Chin Sci Bull* 53(5):791–800. <https://doi.org/10.1007/s11434-008-0002-5>

## References

- Xue, P., Malanotte-Rizzoli, P., Wei, J., & Eltahir, E. A. B. (2020). Coupled ocean-atmosphere modeling over the Maritime Continent: A review. *Journal of Geophysical Research: Oceans*, 125, e2019JC014978. <https://doi.org/10.1029/2019JC014978>
- Yamagata, T., Masumoto, Y., 1992. Interdecadal natural climate variability in the western pacific and its implication in global warming. *J. Meteor. Soc. Japan* 70, 167–175.
- Yan J et al (2020) Temporal Convolutional Networks for the Advance Prediction of ENSO. *Sci Rep* 10:8055. <https://doi.org/10.1038/s41598-020-65070-5>
- Yang, H., Liu, Q., Jia, X., 1999. On the upper oceanic heat budget in the South China Sea: annual cycle. *Adv. Atmos. Sci.* 16 (4),619–629.
- Yang S, Lau K-M. 1998: Influences of Sea Surface Temperature and Ground Wetness on Asian Summer Monsoon. *J. Clim.* 11(12): 3230–3246. [https://doi.org/10.1175/1520-0442\(1998\)011<3230:IOSSTA>2.0.CO;2](https://doi.org/10.1175/1520-0442(1998)011<3230:IOSSTA>2.0.CO;2).
- Yang, S., Wu, R., Jian, M., Huang, J., Hu, X., Wang, Z., Jiang, X., 2021. *Climate Change in Southeast Asia and Surrounding Areas*. Springer Climate
- Yatagai, A., K. Kamiguchi, O. Arakawa, A. Hamada, N. Yasutomi, and A. Kito, 2012: APHRODITE: Constructing a long-term daily gridded precipitation dataset for Asia based on a dense network of rain gauges. *Bull. Amer. Meteor. Soc.*, 93, 1401–1415, <https://doi.org/10.1175/BAMS-D-11-00122.1>.
- Yoneyama, K., & Zhang, C. (2020). Years of the Maritime Continent. *Geophysical Research Letters*, 47, e2020GL087182. <https://doi.org/10.1029/2020GL087182>
- Yu JY, Kao HY (2007) Decadal changes of ENSO persistence barrier in SST and ocean heat content indices: 1958–2001. *J Geophys Res* 112: D13106. <https://doi.org/10.1029/2006JD007654>
- Yu, J.Y., Zou, Y., Kim, S.T., Lee, T., 2012. The changing impact of El Niño on US winter temperatures. *Geophys. Res. Lett.* 39, L15702. Available from: <https://doi.org/10.1029/2012GL052483.1>
- Yu JY, Zou Y (2013) The enhanced drying effect of central-Pacific El Niño on US winter. *Environ Res Lett* 8:014019. <https://doi.org/10.1088/1748-9326/8/1/014019>
- Yu, L., Jin, X., & Weller, R. A. 2006. Role of net surface heat flux in seasonal variations of sea surface temperature in the tropical Atlantic Ocean. *Journal of Climate*, 19(23), 6153–6169. <https://doi.org/10.1175/jcli3970.1>

## References

- Yu, L., Jin, X., & Weller, R. A. 2007. Annual, seasonal, and interannual variability of air–sea heat fluxes in the Indian Ocean. *Journal of Climate*, 20(13), 3190–3209. <https://doi.org/10.1175/jcli4163.1>
- Yu, L., Jin, X., and Weller, R. A. 2008: Multi Decade Global Flux Datasets from the Objectively Analyzed Air-sea Fluxes (OAFlux) Project: Latent and Sensible Heat Fluxes, Ocean Evaporation, and Related Surface Meteorological Variables. Massachusetts: Woods Hole Oceanographic Institution. OAFlux Project Technical Report. OA-2008-01.
- Yu, L. 2009: Sea Surface Exchanges of Momentum, Heat, and Fresh Water Determined by Satellite Remote Sensing. *Encyclopedia of Ocean Sciences*, 202–211. [doi:10.1016/b978-012374473-9.00800-6](https://doi.org/10.1016/b978-012374473-9.00800-6)
- Yu, L., 2019: Global air–sea fluxes of heat, fresh water, and momentum: energy budget closure and unanswered questions. *Annual review of marine science*, **11**, pp.227-248.
- Yu, L., Weller, R.A., 2007. Objectively Analyzed air-sea heat Fluxes for the global ice-free oceans (1981–2005). *Bull. Am. Meteor. Soc.* 88, 527–539. <https://doi.org/10.1175/bams-88-4-527>
- Yu, L., Weller, R.A and B. Sun, 2004: Improving latent and sensible heat flux estimates for the Atlantic Ocean (1988–1999) by a synthesis approach. *J. Climate*, **17**, 373–393. [https://doi.org/10.1175/1520-0442\(2004\)017<0373:ILASHF>2.0.CO;2](https://doi.org/10.1175/1520-0442(2004)017<0373:ILASHF>2.0.CO;2)
- Yeh SW et al (2009) El Niño in a changing climate. *Nature* 461:511–514
- Yu, Z., Shen, S., McCreary, J.P., Yaremchuk, M., Furue, R., 2007. South China Sea throughflow as evidenced by satellite images and numerical experiments. *Geophys. Res. Lett.* 34, L01601, [doi:10.1029/2006GL028103](https://doi.org/10.1029/2006GL028103).
- Zelinka, M. D., and D. L. Hartmann 2010: Why is longwave cloud feedback positive? *J. Geophys. Res.*, **115**, D16117. <https://doi.org/10.1029/2010JD013817>.
- Zhang, C. 2005: Madden-Julian Oscillation. *Reviews of Geophysics*, **43**, RG2003. <https://doi.org/10.1029/2004RG000158>
- Zhang, G. J., and M. J. McPhaden, 1995: The relationship between sea surface temperature and latent heat flux in the equatorial Pacific. *J. Climate*, **8**, 589–605, [https://doi.org/10.1175/1520-0442\(1995\)008<0589:TRBSST>2.0.CO;2](https://doi.org/10.1175/1520-0442(1995)008<0589:TRBSST>2.0.CO;2).

## References

- Zhang, G. J., V. Ramanathan, and M. J. McPhaden, 1995: Convection-Evaporation Feedback in the Equatorial Pacific. *J. Climate*, **8**, 3040–3051, [https://doi.org/10.1175/1520-0442\(1995\)008<3040:CEFITE>2.0.CO;2](https://doi.org/10.1175/1520-0442(1995)008<3040:CEFITE>2.0.CO;2).
- Zhang, Y., W. B. Rossow, A. A. Lacis, V. Oinas, and M. I. Mishchenko (2004), Calculation of radiative fluxes from the surface to top of atmosphere based on ISCCP and other global data sets: Refinements of the radiative transfer model and the input data, *J. Geophys. Res.*, **109**, D19105, [doi:10.1029/2003JD004457](https://doi.org/10.1029/2003JD004457)
- Zhang, R., X. Wang, and C. Wang, 2018: On the Simulations of Global Oceanic Latent Heat Flux in the CMIP5 Multimodel Ensemble. *J. Climate*, **31**, 7111–7128, <https://doi.org/10.1175/JCLI-D-17-0713.1>.
- Zhou, S.; Zhai, X.; Renfrew, I.A., 2018: The Impact of High-Frequency Weather Systems on SST and Surface Mixed Layer in the Central Arabian Sea. *J. Geophys. Res. Ocean*, **23**, 1091–1104. <https://doi.org/10.1002/2017JC013609>.
- Zhou TJ, Yu RC (2005) Atmospheric water vapor transport associated with typical anomalous summer rainfall patterns in China. *J Geophys Res* **110**:D08104. <https://doi.org/10.1029/2004JD005413>
- Zhou, X., and Coauthors, 2020: Understanding the bias in surface latent and sensible heat fluxes in contemporary AGCMs over tropical oceans. *Clim Dyn*, **55**, 2957–2978. <https://doi.org/10.1007/s00382-020-05431-y>

# Appendix A

## Supplemental Tables

**Table 2.A1.** List of ENSO and ENSO Modoki months over the period of 1979–2019. Results are obtained with the Niño3 index. Slightly different results obtained with the Niño3.4 index are indicated in the parentheses. The last row shows the total number of months for each event.

El Niño	El Niño Modoki	La Niña	La Niña Modoki
04(05)/1982–06(05)/1983			
			09/1983–05/1984
		10(09)/1984–08/1985	
09/1986–11/1987(01/1988)			
		04(05)/1988–10/1988	11/1988–05/1989
	08/1991–02/1992		
	05/1994–05/1995		
		08(09)/1995–03(02)/1996	
05/1997–05/1998			06/1998–05/1999
		06/1999–03(05)/2000	
	07/2002–03/2003		
	06/2004–03/2005		
09/2006–01/2007			
		07/2007–12/2007	01/2008–03/2009
	10/2009–03/2010		
		06/2010–05/2011	
			10/2011–03/2012
11/2014–04/2016			
		10(09)/2017–04(03)/2018	
	06/2018–10/2018		
11/2018–06/2019			

	07/2019–12/2019		
<b>74 (74)</b>	<b>56 (56)</b>	<b>61 (61)</b>	<b>49 (49) (months)</b>

**Table 4.A1.** Annual mean value of SST, Qnet and its four components for individual models in CMIP6 during baseline 1995-2014 over the SEA region.

No.	Models	Historical				Qnet	SST
		SW	LW	LH	SH		
1	ACCESS-CM2	212.4	-50.4	-151.6	-8.5	1.9	28.6
2	ACCESS-ESM1-5	220.7	-50.5	-153.8	-8.3	8.1	28.9
3	BCC-CSM2-MR	216.3	-51.9	-147.6	-9.2	7.7	29.1
4	CAMS-CSM1-0	207.9	-54.2	-136.7	-11.2	5.8	28.3
5	CanESM5	208.2	-49.1	-138.3	-13.3	7.4	28.9
6	CAS-ESM2-0	194.6	-48.4	-125.8	-9.3	11.2	28.3
7	CESM2-WACCM	206.1	-47.6	-135.8	-13.2	9.5	29.0
8	CIESM	209.4	-45.5	-143.2	-11.0	9.6	28.5
9	CMCC-CM2-SR5	206.7	-45.7	-143.6	-12.3	5.1	29.0
10	CMCC-ESM2	209.2	-46.3	-144.8	-12.1	6.0	28.8
11	EC-Earth3	204.3	-54.6	-129.1	-13.6	6.9	28.1
12	EC-Earth3-Veg	203.9	-54.3	-128.7	-13.6	7.3	28.2
13	EC-Earth3-Veg-LR	201.0	-55.3	-125.5	-13.7	6.5	27.6
14	FGOALS-f3-L	223.1	-51.6	-147.1	-17.0	7.5	27.8
15	FGOALS-g3	218.0	-55.8	-140.2	-13.6	8.4	28.5
16	FIO-ESM-2-0	202.8	-43.8	-137.4	-12.5	9.2	28.1
17	GFDL-ESM4	206.6	-54.9	-134.5	-12.6	4.6	28.1
18	IITM-ESM	206.0	-58.6	-136.7	-5.9	4.7	26.9
19	INM-CM4-8	211.7	-50.8	-142.7	-12.6	5.6	28.2
20	INM-CM5-0	209.7	-51.2	-144.5	-12.5	1.5	27.7
21	IPSL-CM6A-LR	207.0	-52.0	-138.5	-14.8	1.7	28.3
22	KACE-1-0-G	217.5	-52.0	-144.3	-8.1	13.0	28.4
23	MIROC6	192.6	-44.2	-140.8	-7.4	0.2	28.1
24	MPI-ESM1-2-HR	225.4	-54.7	-138.7	-20.0	12.1	27.8
25	MPI-ESM1-2-LR	220.7	-53.1	-138.3	-21.3	8.0	27.4
26	MRI-ESM2-0	212.2	-51.9	-134.2	-11.4	14.7	28.1
27	NESM3	192.9	-46.5	-121.1	-19.8	5.5	27.3
28	NorESM2-LM	205.0	-47.7	-140.2	-15.0	2.1	29.1
29	NorESM2-MM	208.6	-50.3	-138.9	-14.9	4.5	28.9
30	TaiESM1	206.3	-46.9	-140.7	-11.6	7.1	28.4

**Table 4.A2.** Annual mean value of SST, Qnet and its four components for individual models in CMIP6 under SSP1-2.6 during 2015-2099.  $\Delta$ SST is the difference in SST during the period 2015-2099 compared to the baseline period 1995-2014.

No.	Models	SSP1-2.6						
		SW	LW	LH	SH	Qnet	SST	$\Delta$ SST
1	ACCESS-CM2	217.3	-47.9	-157.8	-7.9	3.7	30.0	1.408
2	ACCESS-ESM1-5	222.6	-48.7	-159.4	-8.0	6.4	29.8	0.884
3	BCC-CSM2-MR	217.7	-50.6	-150.7	-8.9	7.5	29.4	0.283
4	CAMS-CSM1-0	207.9	-52.7	-138.3	-11.1	5.7	28.7	0.426
5	CanESM5	209.6	-46.9	-142.2	-12.7	7.8	29.9	0.963
6	CAS-ESM2-0	199.0	-46.5	-130.5	-9.0	13.0	29.3	0.975
7	CESM2-WACCM	211.1	-45.7	-140.7	-12.7	12.1	30.0	1.044
8	CIESM	212.2	-44.3	-147.1	-11.0	9.8	29.3	0.793
9	CMCC-CM2-SR5	209.5	-43.9	-149.8	-11.8	4.0	29.8	0.829
10	CMCC-ESM2	212.5	-44.8	-148.3	-11.7	7.7	29.7	0.919
11	EC-Earth3	205.9	-52.5	-131.8	-13.2	8.4	29.0	0.85
12	EC-Earth3-Veg	205.5	-52.5	-131.6	-13.3	8.1	29.0	0.791
13	EC-Earth3-Veg-LR	202.8	-53.7	-128.0	-13.3	7.8	28.3	0.734
14	FGOALS-f3-L	222.2	-49.5	-148.6	-16.6	7.5	28.3	0.488
15	FGOALS-g3	214.3	-54.8	-141.9	-13.5	4.1	28.8	0.332
16	FIO-ESM-2-0	203.7	-42.6	-141.2	-12.0	7.9	28.8	0.712
17	GFDL-ESM4	207.5	-53.8	-136.7	-12.3	4.7	28.7	0.636
18	IITM-ESM	206.9	-57.3	-139.0	-5.9	4.7	27.2	0.303
19	INM-CM4-8	211.9	-49.7	-144.2	-12.4	5.6	28.6	0.462
20	INM-CM5-0	210.3	-50.1	-146.0	-12.1	2.2	28.2	0.49
21	IPSL-CM6A-LR	205.3	-49.3	-140.4	-14.2	1.4	29.0	0.72
22	KACE-1-0-G	221.7	-49.6	-150.6	-7.5	14.0	29.5	1.114
23	MIROC6	193.4	-42.8	-142.9	-7.4	0.4	28.6	0.52
24	MPI-ESM1-2-HR	225.2	-52.7	-140.5	-19.7	12.3	28.6	0.78
25	MPI-ESM1-2-LR	220.7	-51.4	-139.8	-21.1	8.4	28.0	0.656
26	MRI-ESM2-0	216.8	-50.6	-138.4	-11.0	16.7	28.9	0.841
27	NESM3	192.7	-44.5	-124.0	-19.5	4.7	28.0	0.731
28	NorESM2-LM	207.0	-46.3	-142.4	-14.7	3.6	29.8	0.663
29	NorESM2-MM	208.6	-48.3	-142.1	-14.4	3.8	29.6	0.731
30	TaiESM1	211.2	-44.8	-147.2	-11.0	8.3	29.7	1.271

**Table 4.A3** As the same Table 4.A2 but for SSP2-4.5

No.	Models	SSP245						
		SW	LW	LH	SH	Qnet	SST	$\Delta$ SST
1	ACCESS-CM2	216.9	-46.8	-158.6	-7.7	3.8	30.0	1.408
2	ACCESS-ESM1-5	221.7	-47.3	-160.1	-7.8	6.5	30.1	1.188
3	BCC-CSM2-MR	216.5	-49.1	-150.9	-8.6	8.0	29.7	0.631
4	CAMS-CSM1-0	207.2	-51.6	-138.6	-10.8	6.2	29.0	0.695
5	CanESM5	208.1	-45.0	-142.4	-12.1	8.6	30.3	1.383

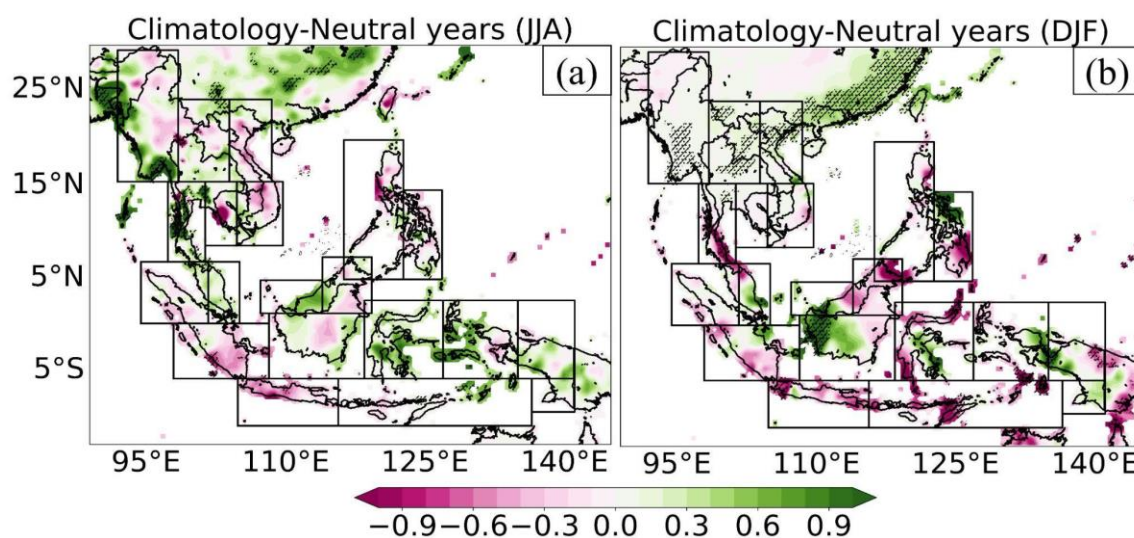
6	CAS-ESM2-0	197.0	-45.5	-129.5	-8.6	13.4	29.5	1.201
7	CESM2-WACCM	210.4	-44.8	-140.7	-12.4	12.4	30.3	1.266
8	CIESM	212.1	-43.0	-148.4	-10.5	10.2	29.8	1.277
9	CMCC-CM2-SR5	208.5	-43.0	-149.6	-11.5	4.4	30.1	1.036
10	CMCC-ESM2	210.9	-43.7	-148.0	-11.4	7.8	29.9	1.156
11	EC-Earth3	203.9	-51.0	-132.0	-12.9	8.1	29.3	1.185
12	EC-Earth3-Veg	203.9	-51.0	-131.7	-12.9	8.3	29.3	1.107
13	EC-Earth3-Veg-LR	200.6	-52.0	-128.2	-13.0	7.4	28.7	1.112
14	FGOALS-f3-L	222.9	-48.5	-149.4	-16.3	8.7	28.6	0.79
15	FGOALS-g3	212.4	-53.2	-141.3	-13.2	4.7	29.1	0.615
16	FIO-ESM-2-0	204.3	-41.8	-142.2	-11.7	8.6	29.1	1.012
17	GFDL-ESM4	205.5	-52.4	-136.4	-12.1	4.6	29.0	0.93
18	IITM-ESM	205.6	-56.1	-139.0	-5.7	4.9	27.4	0.575
19	INM-CM4-8	211.9	-48.6	-145.4	-12.1	5.8	28.6	0.44
20	INM-CM5-0	209.6	-49.0	-146.8	-11.9	1.9	28.4	0.742
21	IPSL-CM6A-LR	204.3	-47.6	-140.7	-13.8	2.2	29.5	1.138
22	KACE-1-0-G	220.7	-48.4	-150.9	-7.3	14.1	29.7	1.369
23	MIROC6	192.8	-41.9	-142.8	-7.2	1.0	28.8	0.725
24	MPI-ESM1-2-HR	223.2	-51.2	-140.4	-19.3	12.2	28.9	1.064
25	MPI-ESM1-2-LR	219.3	-50.1	-139.2	-20.5	9.6	28.3	0.949
26	MRI-ESM2-0	215.1	-49.3	-138.2	-10.7	16.9	29.2	1.115
27	NESM3	189.6	-43.1	-123.3	-19.1	4.2	28.3	1.047
28	NorESM2-LM	206.6	-45.4	-142.4	-14.3	4.5	30.0	0.88
29	NorESM2-MM	207.4	-47.1	-141.8	-14.1	4.5	29.9	0.949
30	TaiESM1	210.4	-43.9	-147.2	-10.7	8.6	29.9	1.466

Table 4.A4 As the same Table 4.A2 but for SSP5-8.5

No.	Models	SSP585						$\Delta$ SST
		SW	LW	LH	SH	Qnet	SST	
1	ACCESS-CM2	218.8	-45.1	-160.9	-7.3	5.5	30.6	2.005
2	ACCESS-ESM1-5	221.9	-45.7	-161.5	-7.4	7.2	30.6	1.625
3	BCC-CSM2-MR	215.9	-47.0	-152.4	-8.3	8.2	30.2	1.164
4	CAMS-CSM1-0	206.9	-50.1	-139.5	-10.5	6.8	29.4	1.047
5	CanESM5	207.6	-42.1	-144.5	-11.2	9.8	31.1	2.221
6	CAS-ESM2-0	196.4	-43.5	-130.2	-8.2	14.4	30.1	1.745
7	CESM2-WACCM	210.3	-42.6	-143.0	-11.9	12.9	31.0	1.995
8	CIESM	212.7	-39.2	-150.2	-9.7	13.6	30.4	1.9
9	CMCC-CM2-SR5	207.7	-41.1	-150.6	-11.1	5.0	30.6	1.56
10	CMCC-ESM2	209.8	-41.8	-149.2	-11.1	7.8	30.4	1.612
11	EC-Earth3	203.4	-48.5	-133.1	-12.3	9.5	30.0	1.895
12	EC-Earth3-Veg	203.6	-48.6	-133.0	-12.3	9.7	30.0	1.811
13	EC-Earth3-Veg-LR	200.3	-49.8	-129.3	-12.3	8.9	29.3	1.724
14	FGOALS-f3-L	222.7	-46.5	-150.8	-15.8	9.6	29.1	1.319
15	FGOALS-g3	211.0	-51.0	-141.9	-12.9	5.1	29.6	1.094
16	FIO-ESM-2-0	204.2	-40.1	-143.4	-11.4	9.4	29.6	1.528
17	GFDL-ESM4	204.1	-50.6	-136.6	-11.7	5.3	29.4	1.369

18	IITM-ESM	205.6	-54.6	-139.9	-5.4	5.6	27.9	1.037
19	INM-CM4-8	212.3	-46.9	-147.9	-11.9	5.5	29.4	1.249
20	INM-CM5-0	210.1	-47.4	-148.6	-11.6	2.5	28.9	1.21
21	IPSL-CM6A-LR	203.8	-45.4	-141.6	-13.3	3.6	30.2	1.836
22	KACE-1-0-G	222.5	-46.5	-153.7	-7.0	15.3	30.4	2.01
23	MIROC6	193.2	-40.5	-143.4	-7.0	2.4	29.3	1.238
24	MPI-ESM1-2-HR	222.5	-49.3	-140.3	-18.7	14.2	29.3	1.47
25	MPI-ESM1-2-LR	217.7	-48.0	-139.5	-20.0	10.2	28.8	1.43
26	MRI-ESM2-0	214.8	-47.2	-139.2	-10.0	18.4	29.7	1.649
27	NESM3	188.5	-40.6	-124.1	-18.5	5.3	29.0	1.763
28	NorESM2-LM	207.3	-43.9	-143.5	-13.9	6.0	30.5	1.373
29	NorESM2-MM	208.2	-45.5	-143.0	-13.6	6.1	30.4	1.457
30	TaiESM1	209.3	-41.7	-148.2	-10.2	9.2	30.5	2.092

Supplemental Figures



**Figure 2.A1.** Differences between climatology and neutral values for (a) JJA and (b) DJF. Units in mm/day. The dot pattern indicates areas where differences are statistically significant at 90% based on the Student's t-test.

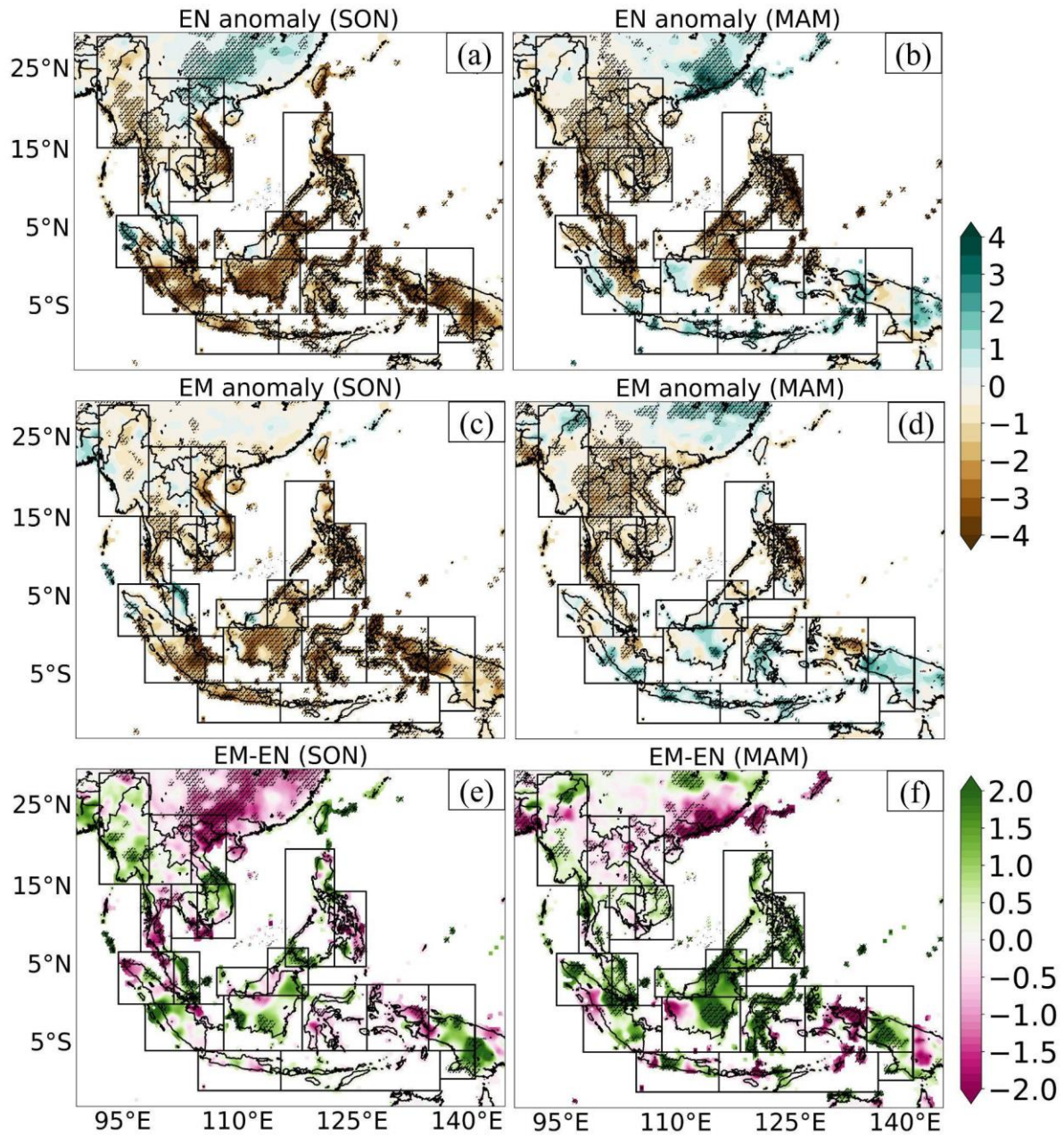


**Figure 2.A2** Composites of SON and MAM rainfall anomalies (units: mm/day) for (a, b) EN, (c, d) EM, and (e, f) the differences between EN and EM. The dot pattern indicates areas where differences are statistically significant at 90% based on the bootstrap test.

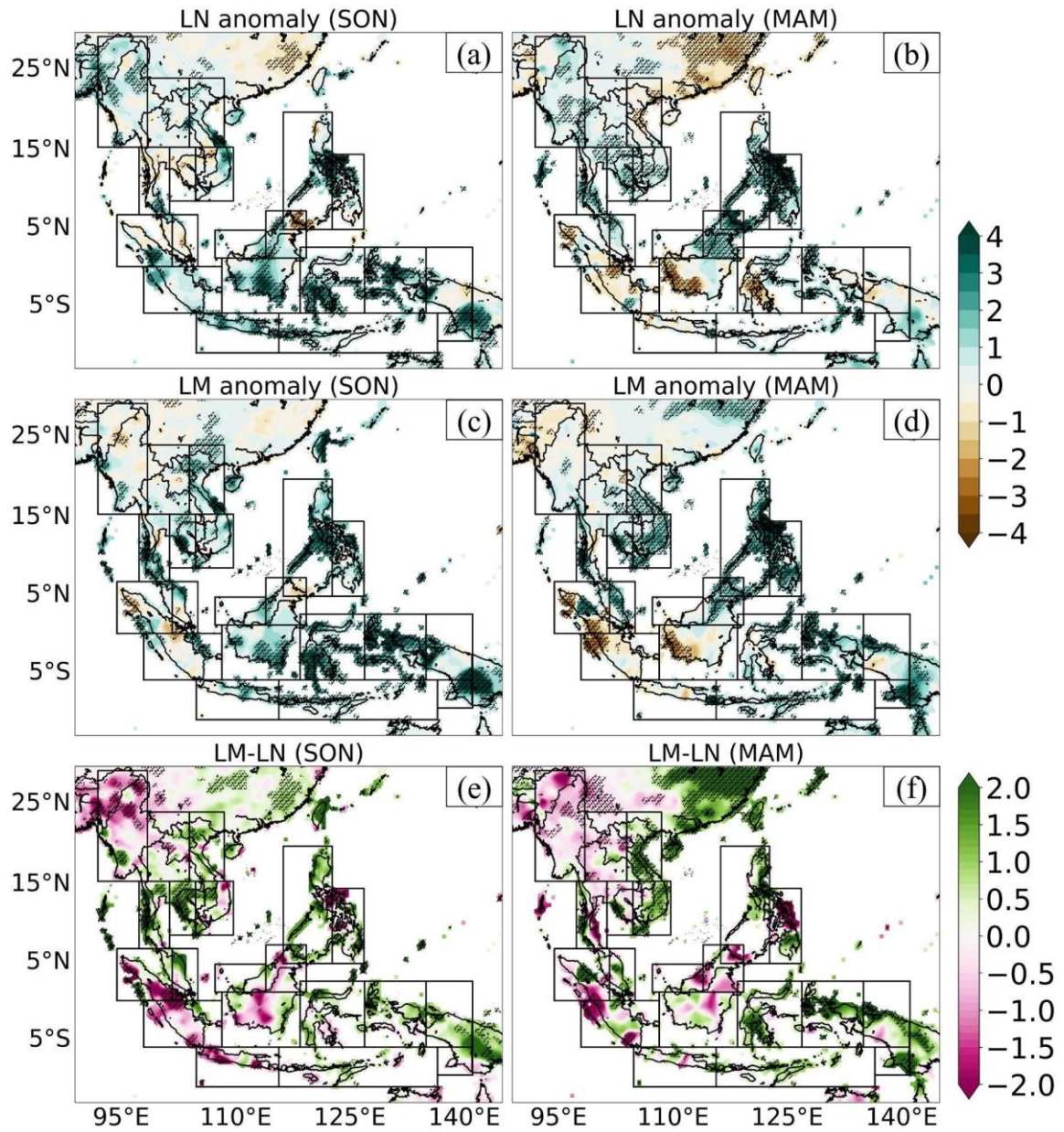


**Figure 2.A3.** As in SFig. 2 but for LN and LM.

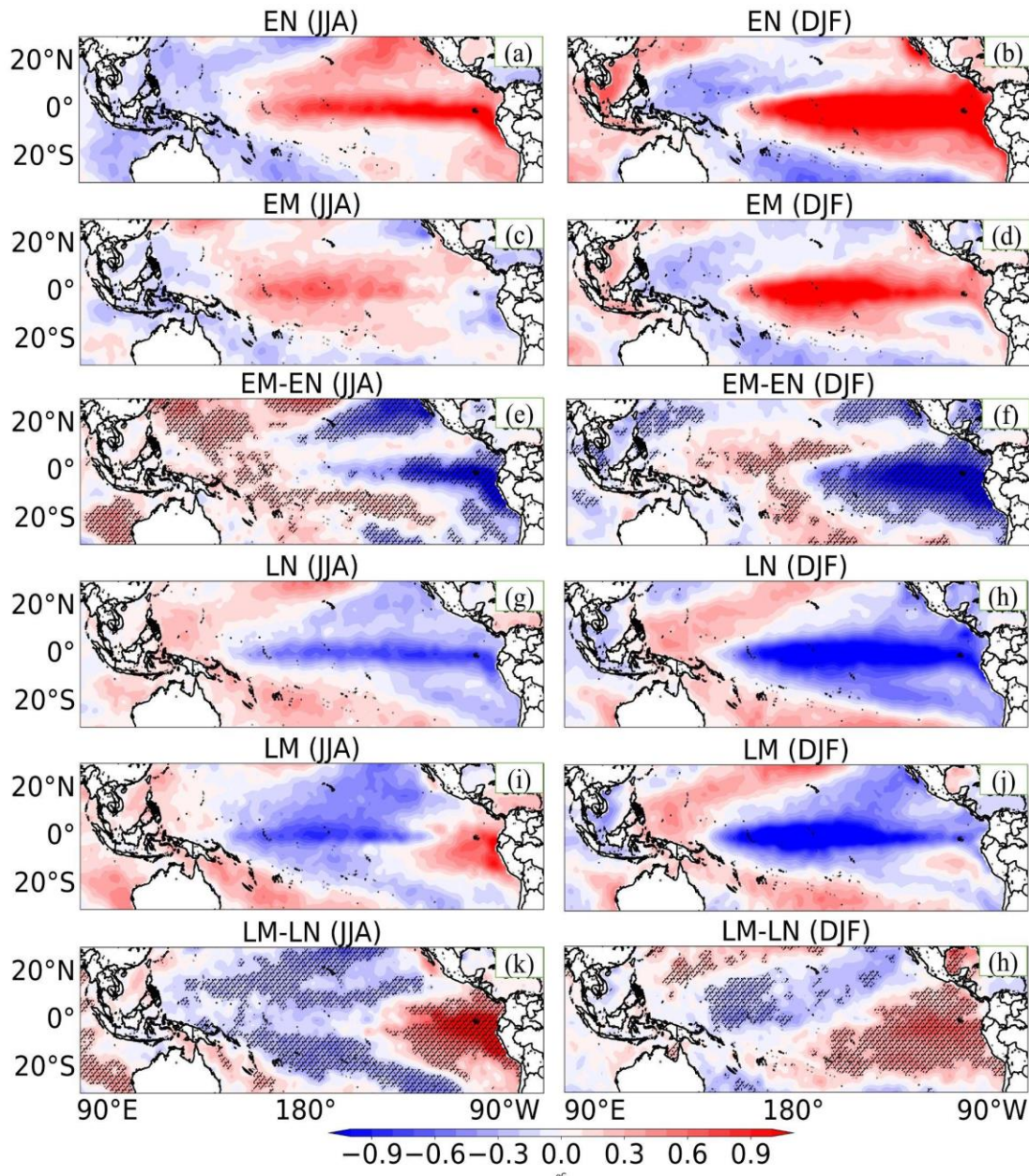


**Figure 2.A4** Composites of JJA and DJF sea surface temperature anomalies (SSTA) (units: °C) for (a, b) EN, (c, d) EM, and (e, f) the differences between EN and EM; (g, h) LN, (i, j) LM, and (k, l) the differences between LN and LM. The dot pattern indicates areas where differences are statistically significant at 90% based on the bootstrap test.

**AUTEUR:** Hue Thi Thanh NGUYEN

**TITRE:** Interactions air-mer en Asie du Sud-Est: Évaluation de l'impact d'ENSO canonique et/ENSO Modoki sur la variabilité des précipitations et caractérisation des échanges thermiques air-mer sur les périodes historiques et futures

**DIRECTEUR DE THESE:** Marine HERRMANN

**LIEU ET DATE DE SOUTENANCE:** LEGOS, TOULOUSE, Le 18 Décembre 2023

---

**RÉSUMÉ:** Cette thèse porte sur les interactions air-mer dans le climat d'Asie du Sud-Est. L'impact sur les précipitations d'ENSO et de sa variante, ENSO Modoki, est d'abord étudié. La diminution (augmentation) des précipitations observée pendant les événements Modoki par rapport aux événements canoniques est expliquée par une réduction (augmentation) du transport d'humidité dans la région et un affaiblissement (renforcement) de la branche ascendante de la circulation de Walker. L'évaluation des flux de chaleur air-mer à partir des jeux de données disponibles révèle ensuite une large plage d'incertitude. Des expériences numériques de sensibilité estiment le gain net de chaleur océanique à  $+12,5 \text{ W.m}^{-2}$  sur la période 2009-2018 et montrent qu'ERA5 peut être utilisé comme référence. La moyenne d'ensemble des modèles CMIP6 reproduit bien la variabilité spatiale mais sous-estime le gain de chaleur net. Celui-ci devrait augmenter au cours du siècle, en particulier dans les modèles et scénarios produisant un fort réchauffement de la surface océanique.

---

**TITLE:** Air-sea interactions in Southeast Asia: Evaluating the impact of ENSO/ENSO Modoki on rainfall variability and characterizing historical and future surface air-sea heat exchanges

**SUMMARY:** This thesis aims to better understand air-sea interactions in Southeast Asia climate. First, the impact on rainfall of ENSO and its variant, ENSO Modoki, is investigated. The observed rainfall decreases (increase) during Modoki events compared to canonical events is explained by a reduced (enhanced) moisture transport into the region and a weakening (strengthening) of the ascending branch of the Walker circulation. Second, air-sea heat fluxes assessment from available datasets reveals a wide uncertainty range. Numerical sensitivity experiments estimate a  $+12.5 \text{ W.m}^{-2}$  net ocean heat gain over 2009-2018 and show that ERA5 can be used as a reference. The ensemble average of CMIP6 models reproduces well air-sea heat fluxes spatial variability but underestimates the net heat gain. This gain is projected to increase during the century, in particular in models and scenarios producing strong sea surface warming.

**Mots-cles:** Interaction air-mer, Asie du Sud-Est, ENSO, CMIP6, SYMPHONIE, flux de chaleur.

**INTITULE ET ADRESSE DU LABORATOIRE:** LEGOS, 14, avenue Édouard Belin  
31400 TOULOUSE